# Hybrid Metal Oxide Nanostructures for Solar Water Splitting and Inorganic Perovskite Photovoltaics


Daniel Commandeur

Supervisor: Dr Qiao Chen

Submitted to the University of Sussex in part fulfilment of the

requirements of the degree of Doctor of Philosophy

September 2019

# Declaration

I hereby declare that all work described in this thesis was carried out at the University of Sussex under the supervision of Dr Qiao Chen from October 2015 to September 2019. The work presented in this thesis is my own unless otherwise stated. This thesis conforms to an 'article format'. Following from the general introduction in Chapter 1, and materials characterisation in Chapter 2; Chapters 3 and 4 consist of articles written and published in peer-reviewed journals. Chapters 5, 6 and 7 contain articles that have been submitted for peer-review. Chapter 8 are manuscripts currently under preparation for submission. Chapter 9 contains the conclusions and suggestions for future directions.

Chapter 3 is published in *ACS Applied Nanomaterials* as: D. Commandeur, G. Brown, E. Hills, J. Spencer and Q. Chen, *ACS Appl. Nano Mater.*, 2019, **2**, 1570–1578.

The author contributions were as follows: The research topic was conceptualised by Daniel Commandeur and Qiao Chen. Daniel Commandeur conducted the full experimental chemistry, data collection, data analysis and the preparation of the manuscript. Grant Brown performed follow up tests on the samples, while Edward Hills and John Spencer provided guidance on microwave synthesis of nano materials. Qiao Chen gave feedback on manuscript preparation, experimental design and data interpretation.

Chapter 4 is published in *Journal of Physical Chemistry C* as: D. Commandeur, G. Brown, P. McNulty, C. Dadswell, J. Spencer and Q. Chen, *J. Phys. Chem. C*, 2019, **123**, 18187–18197.

The author contributions were as follows: The research topic was conceptualised by Daniel Commandeur and Qiao Chen. Daniel Commandeur conducted the primary experimental chemistry, data collection, manuscript preparation and analysis. Grant Brown performed scanning electron microscopy on the samples and varied potential electrical impedance spectroscopy which were subsequently fitted by Daniel Commandeur. Peter McNulty synthesised samples

by hydrothermal method for comparison. John Spencer provided guidance on microwave synthesis of nano materials. Qiao Chen gave feedback on manuscript preparation, experimental design and data interpretation.

Chapter 5 is accepted in *Nanotechnology* with the following authors: D. Commandeur, J. McGuckin and Q. Chen.

The author contributions were as follows: The research topic was conceptualised by Daniel Commandeur and Qiao Chen. Daniel Commandeur conducted the primary experimental chemistry, data collection, data analysis and manuscript preparation. Joshua McGuckin performed follow up tests on the samples. Qiao Chen gave feedback on manuscript preparation, experimental design and data interpretation.

Chapter 6 is submitted to *Chemistry of Materials* with the following authors: D. Commandeur, J. McGuckin and Q. Chen.

The author contributions were as follows: The research topic was conceptualised by Daniel Commandeur and Qiao Chen. Joshua McGuckin performed initial investigations of the deposition on the samples. Daniel Commandeur conducted the continued experimental chemistry, data collection, data analysis and manuscript preparation. Qiao Chen gave feedback on manuscript preparation, experimental design and data interpretation.

Chapter 7 is submitted to *ACS Applied Nanomaterials* with the following authors: D. Commandeur, H. Morrissey and Q. Chen.

The author contributions were as follows: The research topic was conceptualised by Daniel Commandeur and Qiao Chen. Harry Morrissey investigated the initial deposition of perovskite on ZnO nanorods. Daniel Commandeur conducted the continued experimental chemistry, synthesised graphite ink, optimised device architecture, data collection, data analysis and manuscript preparation. Qiao Chen gave feedback on manuscript preparation, experimental design and data interpretation.

Chapter 8 will be submitted to *Nature Communications* with the following authors: D. Commandeur, T. Draper and Q. Chen.

The author contributions were as follows: The research topic was conceptualised by Daniel Commandeur and Qiao Chen. Daniel Commandeur conducted the experimental chemistry, data collection, data analysis and manuscript preparation. Thomas Draper provided insight for the manuscript. Qiao Chen gave feedback on manuscript preparation, experimental design and data interpretation.

I hereby declare that this thesis has not been and will not be, submitted in whole or in part for the award of any other degree.

# Acknowledgements

Firstly, I would like to sincerely thank my main supervisor Dr Qiao Chen for his tireless support and help through the last few years. I am deeply appreciative for all his patient efforts to help me embrace chemistry after my physics degree. Secondly I would like to thank Dr Mark Osborne, my second supervisor, for all his guidance with my project. Thanks as well for taking me along for some fantastic sessions of 'Spectroscopy in a Suitcase', and stimulating discussions about photophysics.

Most importantly would like to thank Jesus Christ, my Lord and Saviour, for His sustaining hand. My hope in dark places, when nothing seemed to work; my joy in times of celebration and breakthrough. Through it all He has fuelled my love of science and sense of wonder, gazing down at the surface of new worlds smaller than a micron. I could not have done any of the past few years without Him.

I would like to thank my wife, Gail Holt Commandeur, the love of my life, for her constant encouragement and support. I could not have weathered the frustration and tears without your gentle voice, and relentless loving kindness.

Many thanks to my family, I am proud to follow in my father's footsteps to PhD, and even prouder of his bravery, love and strength I've seen over the last 27 years. Thanks Mum, for all your help and love, you gave me the best possible start in life and for better or for worse, are the reason I am who I am today. Thanks to wonderful Elle for all your encouragement along the way, and for the inspiration of how you live your life following God. I also couldn't have done this without my legendary in-laws. Firstly, Pete Harrison, thank you for imparting your love of birds and running to me. Thanks Mel, Bert, Nick and Charlotte Commandeur for your enthusiastic support, welcoming me into your family and believing in me.

I also must thank my brothers, who have remained faithful and supportive through this

time: Dan White, Errol Tshabalala, Nick French, Will Emmett and Anthony Bligh. Thanks to my wonderful friends, Louis Lepper, Sarah El-Baghdady, Martin Suttle, Rob Taylor-Jones, Caroline Taylor-Jones, Sam Tranter, Dave Ashcroft, Ben Vessey, Lizzy Pymm, Nick Whiteway, Ben Congdon, Samuel Hatfield and Joseph Forestier-Walker. Thanks to my beautiful church family, the prayers of whom led me to thesis submission, Zoë Benjafield, Caroline Oliveira, Abi Slade, Sarah Hart, Dom Hart and Jonathan Murray to name just a few.

I would finally specially like to thank all those at the University of Sussex who made my time so rewarding. Above all, the talented and amazing nanolab group members and alumni. Many thanks to Emmanuel Kamba and Munirah Alhar, for your friendship that saw me cross the finish line. A huge thanks to the old hands who taught me everything I know, whom I hold in the highest esteem: Dr Thomas Draper, Dr Giacomo Canciani and Dr Yuanxing Fang. Many thanks to the ancient council of Matts, firstly Dr Matthew Molloy who always brightened my day. Secondly, Dr Matthew Leech, my best friend at Sussex, thank you for your strength and assistance in my battle with imposter syndrome, I treasure your friendship. Also, I can't forget Grant Brown, many thanks for your warm friendship, I am thrilled and proud to see you start your PhD in the near future. A sincere thank you to Victor Zdorichenko and Stavroula Sampani for brightening up the office and lab 10 south, respectively.

I would also like to thank the brilliant MChem students who spent time with us in the lab, Peter McNulty, Benjamin Fry, Jone-Him Tsang, Harry Morrissey, Geoffrey Nash and Jack Davies. I would also like to thank Deniz Gulercan for her assistance and stimulating collaboration. I also can't forget our summer students whom it was a pleasure to work alongside: Gioia Rossini, Joshua McGuckin, Raman Yachi, Celso Delatorre, Boaz Chan and Teodora Vasile. I would finally like to thank Professor John Spencer for your continuous encouragement, Alex Burns for fixing all manner of problems, Chris Dadswell for help with ICP-MS, Verity Holmes and Christopher Davis for kind help from the teaching lab.

# Abstract

The conversion and storage of solar energy is already a strategic pillar of global strategy to reduce emissions and fight climate change. Despite showing major promise in application to solar water splitting and photovoltaic cells, hybrid metal oxide nanostructures have not been widely adopted as commercial energy materials. This is largely due to their infancy, requiring extensive research for further optimisation and performance enhancement. The aim of this thesis is to explore the beneficial properties of these materials such as high n-type doping and stability in water, and improve them using various strategies. Ultimately, to test their validity by first measuring water splitting photocurrent, and second incorporating the materials into inorganic perovskite solar cells and measuring power conversion efficiency.

The first strategy implemented in this thesis was the novel synthesis of vertically aligned zinc oxide nanorods. By utilising microwave heating, growth duration of the high surface area material was cut down from the conventional method's 16 hours to under three hours. The resistive heating of the conductive glass substrate led to defect rich structures with higher n-type doping as measured by electrical impedance spectroscopy. The quantity of these defects was then reduced in order to restrict surface recombination by thermal annealing in air. The second strategy went a step further, adding extrinsic yttrium atom dopants to the nanorods. This finely tuned defect population with greater control, resulting in increased electron mobility due to the neutralisation of transport restrictive traps. These strategies led to a fourfold and 23% enhancement in solar water splitting photocurrent for microwave synthesis and yttrium doping respectively. Furthermore, such dopants led to resistance to photo-corrosion, a critical problem for zinc oxide photoanodes.

Despite these improvements, the critical issue of large band gap energy renders zinc oxide unable to generate photoelectrons when exposed to most visible light. In order to overcome this

problem, $\alpha$-$Fe_2O_3$ (hematite) was applied as a surface coating on the nanorods. This material has a low band gap of 2.1 $\mathrm{eV}$, capable of absorbing visible light. Electrochemical deposition was chosen for this application due to high control of layer thickness along with various electrolytes compatible with ZnO. Initially cathodic deposition was applied, wherein $Fe^{3+}$ ions were reduced at the nanorod surface from a low concentration solution. Following annealing, the presence of both $\alpha$-$Fe_2O_3$ phase and $ZnFe_2O_4$ interphase layers were confirmed. External quantum efficiency measurement indicated the success of the photoanode; achieving 8.96% at 400 nm irradiation, in comparison to zero activity for uncoated ZnO. The critical limitation of $\alpha$-$Fe_2O_3$, sluggish charge transportation, is overcome using the novel three dimensional structure, forming nanoparticles on the surface of conductive yttrium doped ZnO. Utilising the cores as electron highways in conjunction with visible light sensitisation led to the highest water splitting photocurrent achieved in this thesis, 1.59 $\mathrm{mA\,cm^{-2}}$ at 1.23 $V_{RHE}$. Furthermore, an anodic current deposition led to the growth of hematite nanosheets on the surface of the wires. This too, led to greater water splitting performance with added surface area for increased charge transfer.

Photolysis of water may have the advantage of storing solar energy in chemical bonds, but thus far has achieved limited commercialisation and wide application. This is due to the complex material requirements resulting in either low power conversion efficiency or expensive device construction. Therefore the previously employed strategies were applied to photovoltaic devices for high efficiency solar energy generation. Inorganic $CsPbBr_3$ perovskite allows ambient synthesis and long term stability, it was selected as light absorber due to remarkable optoelectronic properties and visible light sensitive band gap of 2.4 $\mathrm{eV}$. Devices were constructed by applying a layer of the material upon ZnO nanorod arrays, followed by drop casting of liquid phase exfoliated graphite ink produced by sonication. The suitable work function of the final material formed a Schottky junction yielding a hole selective contact, completing the photovoltaic device. Optimisation and enhancement was achieved by applying yttrium doping, NR

length control and finally $TiO_2$ coating for surface passivation and recombination reduction. The success of the enhanced device yielded quantum efficiency of 77.8% at 400 nm illumination, and a champion power conversion efficiency of 5.8%. In nearly all cases the performance of said cells improved as time passed under dark ambient storage conditions. Therefore this thesis is concluded with a final investigation into the potential causes after storage in various conditions.

# Contents

# List of Abbreviations

| | |
|---|---|
| $\alpha$ | Absorption coefficient |
| AM 1.5G | Air mass |
| AC | Alternating Current |
| Å | Angstrom |
| $E_g$ | Band gap energy |
| $k$ | Boltzmann constant |
| $C$ | Capacitance |
| CBD | Chemical bath deposition |
| CVD | Chemical vapour deposition |
| CB | Chlorobenzene |
| CB | Conduction band |
| $J$ | Current |
| $D$ | Crystalline domain size |
| DoH | Degree of hysteresis |
| DI | Deionised |
| $\epsilon$ | Dielectric constant |
| $\theta$ | Diffraction angle |
| DC | Direct Current |
| $N_D$ | Dopant density |
| DSSC | Dye sensitised solar cell |
| EIS | Electrochemical impedance spectroscopy |
| $e$ | Electron charge |
| $\sigma_n$ | Electron conductivity |
| $m$ | Electron mass |
| $\mu_n$ | Electron mobility |
| ETM | Electron transport material |

| | |
|---|---|
| eV | Electron volt |
| $E$ | Energy |
| EDX | Energy dispersive x-ray spectroscopy |
| EQE | External quantum efficiency |
| $f_{FE}$ | Faradaic efficiency |
| FFT | Fast Fourier transform |
| $E_F$ | Fermi energy |
| FF | Fill factor |
| FTO | Fluorine doped tin oxide |
| $\nu$ | Frequency of light |
| FWHM | Full width half maximum |
| HMT | Hexamethylenetetramine |
| HRTEM | High resolution transmission electron microscopy |
| HTM | Hole transport material |
| IPCE | Incident photon-to-current conversion efficiency |
| ICP-MS | Inductively coupled plasma mass spectrometry |
| $Z$" | Imaginary impedance |
| ITO | Indium tin oxide |
| LEDs | Light emitting diode |
| LCAO | Linear combination of atomic orbitals |
| LSV | Linear sweep voltammetry |
| LPE | Liquid phase exfoliated |
| mp-$TiO_2$ | Mesoporous $TiO_2$ |
| MeOH | Methanol |
| MAPI | methyl-ammonium lead iodide |
| MW | Microwave |
| $p$ | Momentum |
| M-S | Mott-Schottky |

| | |
|---|---|
| NRs | Nanorods |
| NWs | Nanowires |
| NTs | Nanotubes |
| NSs | Nanosheets |
| NBE | Near band edge emission |
| $V_{oc}$ | Open circuit voltage |
| $\epsilon_0$ | Permittivity of free space |
| PSC | Perovskite solar cell |
| PL | Photoluminescence |
| PCE | Photoconversion efficiency |
| PEC | Photoelectrochemical |
| PV | Photovoltaic |
| $V_{RHE}$ | Potential vs Reversible Hydrogen Electrode |
| $P$ | Power |
| $\eta$ | Power conversion efficiency |
| SEM | Scanning electron microscopy |
| $c$ | Speed of light |
| $\eta_{STH}$ | Solar to hydrogen efficiency |
| TTIP | Titanium tetra isopropoxide |
| TEM | Transmission electron microscopy |
| TCO | Transparent conducting oxide |
| QDSSC | Quantum dot sensitised solar cell |
| $R_{CT}$ | Charge transfer resistance |
| $Z'$ | Real impedance |
| $j_{rec}$ | Recombination current |
| $R_R$ | Recombination resistance |
| $\hbar$ | Reduced Planck Constant |

| | |
|---|---|
| n | refractive index |
| $R_T$ | Transport resistance |
| $R_s$ | Series resistance |
| SSSC | Semiconductor sensitised solar cell |
| $J_{sc}$ | Short circuit current |
| RPM | Revolutions per minute |
| $\lambda$ | Wavelength |
| XRD | X-ray diffractometer |
| XPS | X-ray photoelectron spectroscopy |
| URMAD | Ultra-rapid microwave assisted deposition |
| UV | Ultraviolet light |
| VB | Valence band |
| Vis | Visible light |

# Chapter 1

# Introduction

## 1.1 Solar Energy

Dramatic increases in the frequency of extreme weather events and an increase in human disease linked to climate fluctuations have made anthropogenic climate change impossible to ignore as the most important challenge facing our time.[1] With 150,000 lives lost annually as a direct result,[2] the urgency to reduce emissions and turn to renewable energy sources is high and solar energy harnessed by photovoltaic cells and photoelectrochemical hydrogen generation is emerging as a vital solution. As a resource solar energy is nearly inexhaustible, with quantities of energy arriving in one hour the same order of magnitude as the entire Earth's annual energy demand ($4.3\times10^{20}$ J), there has been much progress in harvesting this energy.[3] Photovoltaic (PV) panels save the carbon dioxide emitted in their construction within one to two years, providing an alternative to fossil fuels, paving the way to a future built upon sustainable energy.[4]

Throughout the world this crisis has received urgent attention, with 185 countries out of 197 having ratified the historic Paris climate agreement.[5] The commitment to limit global warming to well below 2°C demands a reduction in $CO_2$ levels, involving the inevitable switch to renewable energy, change in human behaviour, electrification and investment in carbon capture

technology.[1] Photovoltaics have occupied a growing portion of the energy market, predicted to grow substantially in the USA, Brazil and India.[6–8] In the United Kingdom, renewable energy use grew 230% from 2009 to 2017, 33.1% of electricity generated in 2018 was from such sources.[9] Over 6% of all power used was from PV, an increase from 20 GWh in 2009 to 4,500 GWh last year due to subsidies and the falling price of modules.[10] This growing market has fuelled a wide range of research, with the aim of driving the price of solar cells down, whilst increasing their performance.[11–13]

Other than PV technology, more methods of capturing solar energy are in commercial use today, including solar water heating and concentrating solar power. The former tackles the excessive energy required to heat water, necessary for maintaining modern hygiene standards. Methods such as the flat plate and the evacuated tube collectors are capable of heating water using light from the sun up to 80 and 100°C respectively.[14] Concentrating solar power allows even higher temperatures to be generated, reflecting light from a larger area to a focal point or line using planar or parabolic mirrors. Commercial solar towers reaching temperatures as high as 850°C resist the intermittency of cloud coverage for a 50 MW power output using a gas turbine,[15] with future application to molten salt reactors a possibility.[16] Despite much progress the problem of 24 hour energy demand persists.

A possible solution is the hydrogen economy, replacing fossil fuels with $H_2$ gas allows far easier storage than electricity, at high energy densities.[17] Currently, the most common source of the gas is steam reforming of natural gas, using high temperatures and a catalyst in a process that emits $CO_2$.[18] Despite the low cost of this method, a renewable alternative is strongly desired, particularly as countries such as Japan begin to invest heavily in the hydrogen economy.[19] The commercialisation of production by electrolysis of water is already under way with several sources available, but the direct conversion of solar energy to chemical hydrogen bonds from water would be preferable. The photolysis of water was already widely achieved by nature

in the form of photosynthesis, inspiring research into solar water splitting.[20] This is achieved predominantly using photo-electrochemistry to overcome the redox potentials associated with the reaction.

$$2\,H_2O \xrightarrow{\text{sunlight}} 2\,H_2(g, 1\,\text{atm}) + O_2(g, 1\,\text{atm}) \qquad E^o = 1.23V \tag{1.1}$$

This process occurs within the leaf itself, then stored through the production of carbohydrates.[21] Photoelectrochemical water splitting is the application of focus in this thesis, with increased efficiency achieved by various strategies in the first four experimental chapters. An alternate method is to use solar thermal energy to perform splitting, $800^{\circ}\text{C}$ concentrated heat is sufficient to split $H_2O$ to form $H_2$ in a thermochemical reaction.[22] Relatively new, this technology requires a high set up cost but with promising results, including efficiencies exceeding $25\%$.[23]

## 1.2 Photoelectrochemical Water Splitting

The genesis of research into photodegradation and artificial photosynthesis occurred in 1972 where Fujishima and Honda used the wide band gap semiconductor $TiO_2$ to perform photoelectrochemical water splitting.[24] The photoactivity of metal oxides such as $TiO_2$ can be attributed to the nature of their semiconductor properties; their band gaps and the positions of their conduction and valence bands. The electronic band structure was first theorised to exist using two different models. The nearly free electron model,[25] where a weak positive lattice is imposed upon a gas of free electrons, is solved using degenerate perturbation theory. Unimpeded free electron gas with no atomic lattice consideration is modelled by the simple Drude model. The tight binding model of electronic structure confines the electrons to each atom with their wave functions perturbed by neighbouring nuclei,[26] closely linked to Linear Combination of Atomic Orbitals (LCAO).

Both theories use the Bloch Theorem for electrons in a repeating lattice; which applies the

following eigenstate

$$\psi_k^\alpha(\overline{r}) = e^{i\overline{k}\cdot\overline{r}} u_k^\alpha(\overline{r}) \tag{1.2}$$

where $e^{i\overline{k}\cdot\overline{r}}$ corresponds to the free electron wavefunction which leads to the familiar energy eigenvalues.

$$E = \frac{\hbar^2 k^2}{2m} \tag{1.3}$$

Where energy $E$ is proportional to momentum $k$ squared; $\hbar$ is plank's constant and $m$ is the electron mass. $u_k^\alpha(\overline{r})$ corresponds to the periodic potential of the eigenstates in each unit cell, where $\alpha$ is the discrete band index.

$$u_k^\alpha(\overline{r}) = u_k^\alpha(\overline{r} + \overline{a}) \tag{1.4}$$

the repeating potential of the positive atomic lattice is indistinguishable from one unit cell to the next. This allows aliasing to occur where electrons with high enough momentum can leave a unit cell in momentum space only to find themselves in effectively the same cell, transferring momentum to the crystal lattice. This renders the wavefunctions indistinguishable from unit cell to neighbouring cell. Where $a$ is the lattice constant of the unit cell.

Remarkably the dispersion relations of bound states, where the energy of electrons is plotted against momentum in k space, predict the same features using either model. Forbidden regions open up where certain energy states become impossible to attain for electrons, the electronic band gap.[27] The introduction of the Fermi level, the highest electron energy level occupied at absolute zero, allows the electronic properties of a material to be predicted. If the Fermi level lies in the forbidden zone between bands the material will be either a semiconductor or insulator; this depends on either a comparatively narrow zone (or band gap) or wide zone respectively. The Fermi level intersecting one of the bands will produce a conductor, where electric fields can easily affect the net momentum of electrons in a particular direction.[28] This model is summarised in Figure 1.1.

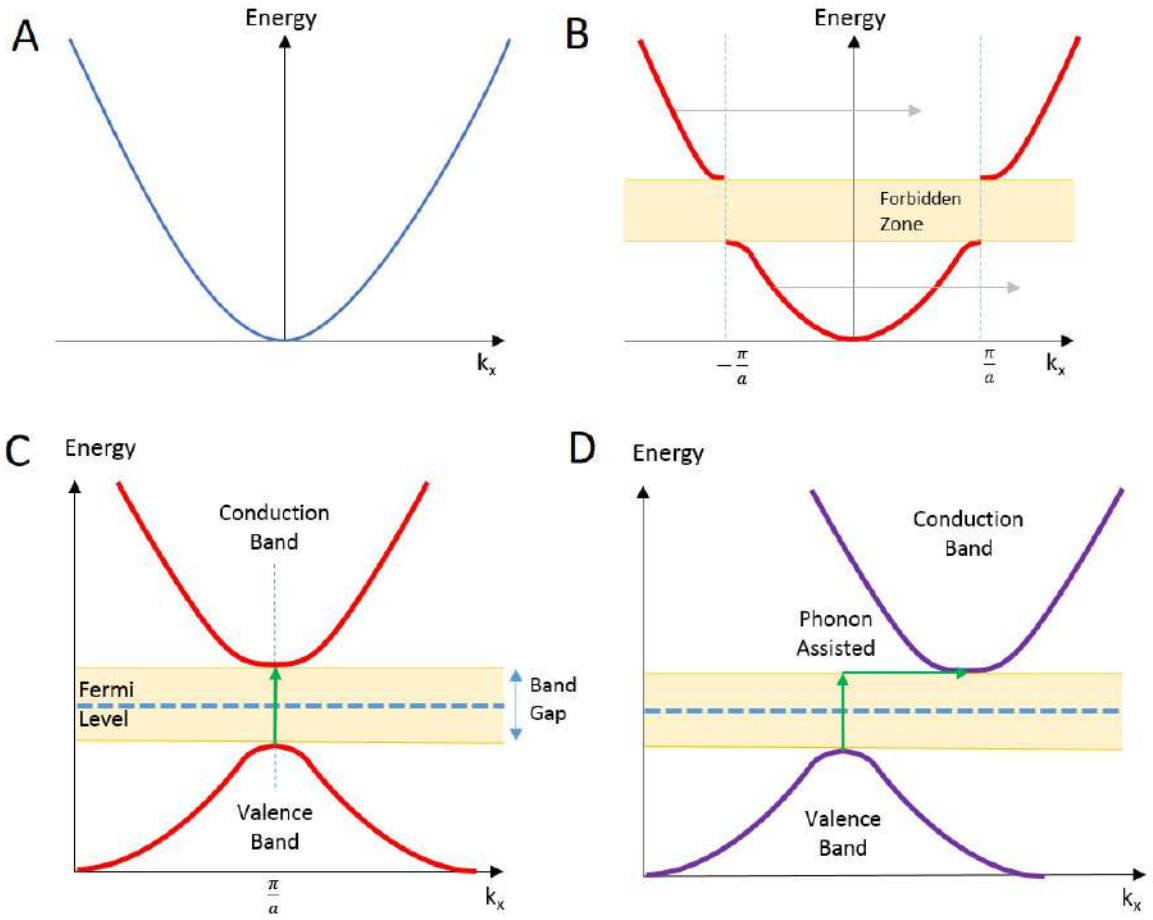


Figure 1.1: A) The Drude model dispersion relation of free electrons, $k_x$ corresponds to the momentum in the $x$ direction; B) displays the result of the Nearly Free Electron Model and Tight Binding Model, where the light grey arrows transform the curve into the familiar band gap diagram found in C) due to the process of aliasing. In C) the position of the Fermi Level indicates an intrinsic semiconductor, the green arrow indicates the transition of an electron from the valence band into the conduction band due to the absorption of a photon. D) Displays an indirect band gap with transitions assisted by phonons.

The bands below and above the forbidden zone in semiconductors are referred to as the valence and conduction band respectively; in order to produce a net flow of electrons, sufficient energy and momentum must be provided to the valence electrons to reach the conduction band. Both $TiO_2$ and ZnO are referred to as direct band gap semiconductors as the minima of their conduction bands and maxima of their valence bands lie at the same point in momentum space.[29] This is a useful property for the absorption of photons, as the photon momentum $p$ transferred is insignificant compared to the energy supplied. This produces a near vertical transition in the dispersion relation. The simple equation $E = pc$ describes photon dispersion where $c$ is the speed of light. For indirect band gap semiconductors additional momentum is required in the form of phonons, slowing the rate of transitions and therefore photon absorption.[30]

The energy from light absorbed can be stored in the process of water splitting provided two conditions are met. The conduction band of the semiconductor must lie above the reduction potential of hydrogen; and the valence band must lie below the oxidation potential of oxygen in water. Naturally this requires a band gap of greater than 1.23 eV as displayed in Figure 1.2. Upon excitation of electrons to the conduction band, the fermions move to the counter electrode to reduce hydrogen and the valence band holes in turn, oxidise the water.[31]

The most effective method of measuring photoelectrochemical water splitting ability is through solar-to-hydrogen efficiency, $\eta_{STH}$, calculated using the following equation.

$$\eta_{STH} = \frac{J_{op} E_{rxn} f_{FE}}{P_{in}} \tag{1.5}$$

Where $J_{op}$ is defined as the operating current, $E_{rxn}$ is the redox potential equal to 1.23 eV, $f_{FE}$ is the Faradaic efficiency and $P_{in}$ is the illumination power density.[32] Thus far, the highest performance PEC water splitting devices have incorporated several layers including a photovoltaic cell providing potential bias and various catalysts. An early example of such a system used a GaAs photovoltaic cell linked to a $GaInP_2$ photocathode, achieving a 12.4% value of $\eta_{STH}$ at 11

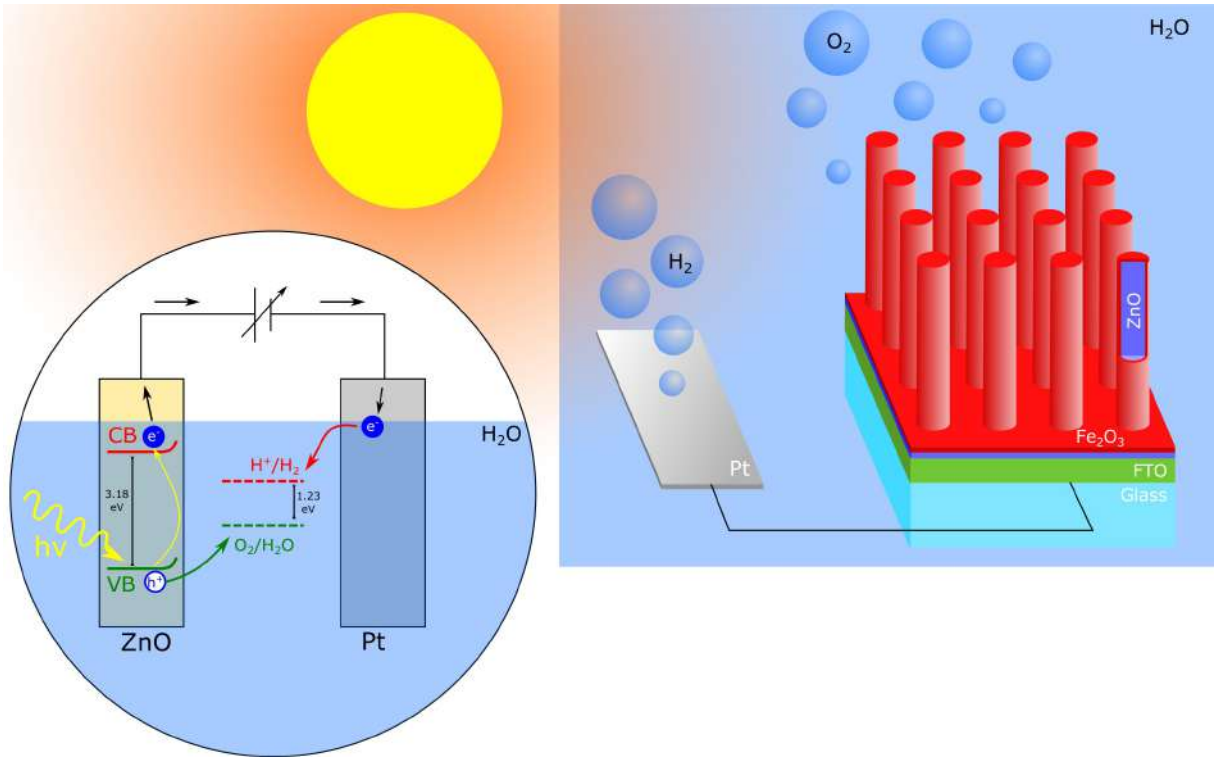


Figure 1.2: Diagram showing the band gap of ZnO in relation to the redox potential of water, transitions occur when photons of visible light are absorbed, allowing the photolysis of water.

sun illumination in 2002.[33] In 2012 Nocera produced a free standing artificial leaf combining cobalt and NiMoZn as oxygen and hydrogen evolution catalysts respectively, with a triple junction amorphous silicon photovoltaic for 6.7% efficiency.[21] Further records were broken by driving photolysis with methylammonium lead halide perovskite photovoltaics, achieving 12.3% efficiency with 1 sun illumination.[34] In more recent examples further enhancement has been achieved by optimising the tandem photovoltaics driving the reaction, May *et al.* achieved 14% efficiency and Young *et al.* produced a device capable of 16% solar to hydrogen conversion.[35,36] The highest performance photovoltaic PEC water splitting device utilised ruthenium oxide and rhodium as evolution catalysts, yielding 19.3% efficiency.[37]

Despite these impressive performances, these devices suffer from complex fabrication methods along with expensive catalysts. Therefore, the investigation of novel materials and simple junctions that can be directly submerged in water without degradation, to act as photoanode or photocathode, has been continuous since the first use of $TiO_2$.[24] This forms the majority of PEC water splitting literature, with metal oxides such as ZnO and $Fe_2O_3$ commonly applied due to suitable band edge positions and good stability, using an external potentiostat for testing.[38–40] Typically performance and efficiency are measured using generated photocurrents from a three electrode set up. In this way, selected anodes or cathodes can be built and tested at a fraction of the cost, with potential to be linked in tandem with PVs in future for higher performance. Many of these materials feature more prominently in the construction of PVs themselves, particularly in modern perovskite solar cells, the second application in this thesis.

## 1.3 Photovoltaic Cells

Despite the discovery of the photovoltaic effect by Edmond Becquerel in 1839,[41] it was 38 years before this principle was applied to the solid state by Adams and Day during their investigation of the photoconductivity of selenium.[42] This material remarkably formed the base

of the first thin-film solar cell completed with gold foil on top.[43] This led to the investigation of other materials such as $CuO_2$ and $Tl_2S$, selected for the ability to grow $\sim$ 10 nm thick barrier layers by oxidation and sulphurization on metal supports.[44,45] The foundational silicon p-n junction, the most familiar photovoltaic technology today, was discovered as a naturally occurring phenomenon in commercial ingots of high purity recrystallized silicon in 1941,[46] due to the segregation of impurities during melting. This was several years before the invention of the transistor, where each end of the material cut from the ingot were labelled 'N' and 'P' based on the positive or negative potential observed when illuminated. Subsequent advancements in efficiency and production of such cells occurred through using purer silicon, an intrinsic semiconductor, followed by controlled extrinsic doping through ion beam bombardment.[47,48]

The inclusion of small populations of impurities have a profound effect on the electronic properties of semiconductors, as only a small proportion of electrons have sufficient energy at thermal levels to reach the conduction band. Therefore even low band gap materials such as silicon, are highly resistive to electron transport, due to low numbers of delocalised charge carriers. Doping with either donor or acceptor impurities gives rise to the previously mentioned n or p type material respectively, forming the junction in Figure 1.3. These extrinsic dopant atoms reduce the resistivity by introducing new electronic states into the band gap, typically within thermal energies of the conduction or valence bands that donate electrons or holes respectively. This will not only affect the charge carrier density, but also the position of the Fermi-level, $E_F$, shifting it towards the conduction band in the case of n-type doping and valence band for p-type. When the junction is formed, as the $E_F$ reaches equilibrium donated electrons flow to fill into the p-type conductor to fill the holes at the interface and vice versa, driven by concentration gradient. This results in a depletion region, with a built in a diodic electric field which allows the separation of charge neutral electron hole pairs, excitons, generated by the absorption of photons. This is how photocurrent is generated; conversely when excitons recombine without

charge separation the absorbed photon is re-emitted, and the energy lost. However, the majority of recombination occurs at the junction due to the proximity of photogenerated electrons to holes.

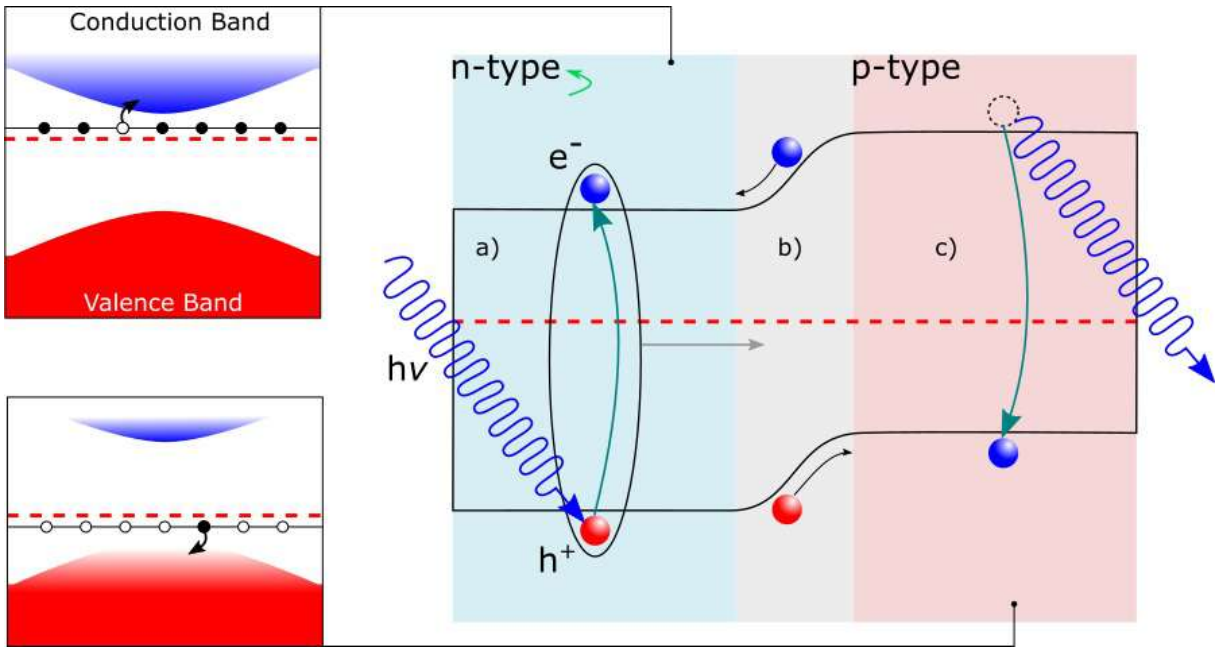


Figure 1.3: The function of the pn junction: a) Bound charge neutral electron hole pairs, excitons, are generated through the absorption of a photon. b) Exciton diffuses to the junction between p and n doped semiconductors where charge separation occurs. c) Example of energy loss through exciton recombination, the photon is re-emitted as the electron drops down from the conduction band to the valence.

Dye Sensitised Solar Cells, (DSSCs) rely on a different form of band structure engineering and hold a considerable share of the frontier research into solar energy.[49] Using a variety of light sensitive compounds, wide band gap metal oxide semiconductors can be manipulated to absorb photons with energy far lower than their band gaps.[50] The first DSSCs used organic dyes which donate electrons to the conduction band of the metal oxide upon photoexcitation leading to research into developing new dyes.[11,51–53] These devices effectively divide the processes occurring in traditional p n junction solar cells, drawing upon inspiration from the natural world.

Rather than exciton generation as previously described; where charge separation and charge

transport all occur within the semiconductor bulk; photoelectrons are generated in the dye, charge separation occurs at the dye/semiconductor interface and the semiconductor is used for charge transport.[54] This is a bio-memetic approach to harvesting solar power, a concept which was first reported in 1971, when a small photocurrent density was observed, sensitising ZnO with chlorophyll extracted from bacteria and dissolved in electrolyte.[55] This invention has evolved since its conception to include Semiconductor Sensitised Solar Cells (SSSCs) in order to both overcome the photoinstability of organic dyes and provide more accurate optical band structure tuning.[12,56,57] The demand for even higher precision electronic structuring led to QDSSCs, the quantum dot equivalent, utilising quantum confinement and multiple exciton generation.[58–61] This effect arises in semiconductor crystals with dimensions less than 10 nm as the size of the crystal becomes comparable to the wavelength of the exciton, causing a splitting of energy levels and the ability to tune the band gaps.[62] These cells show strong efficiency due to nanoscale engineering.[63–65] The different generations of this branch of solar technology are displayed in Figure 1.4.

Representing a modern leap forward in photovoltaic technology, perovskite solar cells (PSCs) are the newest evolution of the DSSC. Named after its crystal structure, perovskite is cheap to synthesise and solution processable, which will lead to commercialisation in the near future.[66] Most commonly referring to methyl-ammonium lead iodide, MAPI, the term represents a wide range of materials following the same chemical formula of $ABX_3$, A and B referring to a singularly and doubly charged cation respectively, alongside a halide anion X. Swapping component atoms, and introducing mixtures of cations and halides have a great influence on the stability and band gap energy of the material. Most commonly the A cation is comprised of methyl-ammonium, formamidinium or cesium, the B cation is tin or lead and finally X can be iodide, bromide or chloride. Currently they are constructed as n-i-p (intrinsic semiconductor layer) junction cells where the tunable band gap material performs the actions of photon absorption

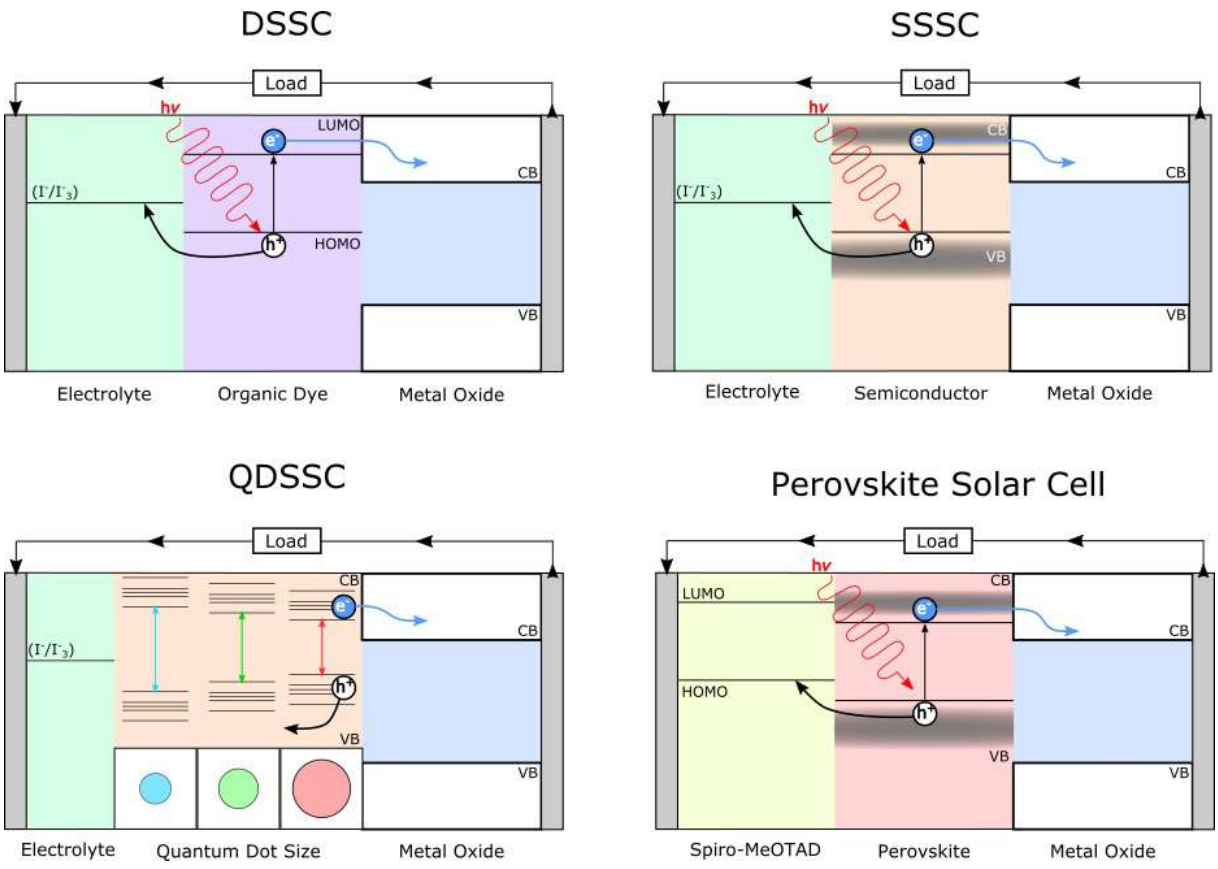


Figure 1.4: The DSSC and subsequent generations of cell: Black arrows to the load indicate the path of electrons, grey boxes indicate electrodes. Top right, the dye is replaced with an optical semiconductor, gradient shading indicates continuous levels of electronic bands. Bottom left displays the quantisation of bands due to quantum confinement and the size dependant band gap found in QDs. Bottom right, electrolyte replaced with solid phase hole transport material.

as well as charge separation due to the low exciton binding energy.[67–70] Typically the n-type layer, or electron transport material, is made of mesoporous $TiO_2$ or ZnO with a compact layer for hole blocking on a transparent conducting oxide. After perovskite layer deposition the cell is capped off with a state of the art solid state hole transport layer, which is usually doped 2,2',7,7'-tetrakis [N,N-di(4-methoxyphenyl)amino]- 9,9'-spirobifluorene, spiro-MeOTAD, followed by thermally evaporated gold. Needless to say, these final two layers add the greatest cost, spurring interest in the reverse p-i-n structures, along with hole transport free perovskite solar cells.

These cells no longer resemble their parent DSSCs, however organic-inorganic hybrid lead halide perovskite began as just another semiconductor used to sensitise mesoporous $TiO_2$.[71] From this point in time several key discoveries ensured the materials meteoric rise in efficiency over the last 10 years. Improvement to the device performance was first enabled by using the aforementioned solid state hole transport material, cutting out the liquid phase.[72] Great enhancement was next achieved through improved film deposition, which began with the sequential method developed by Burschka *et al.*, increasing efficiency up to 13%.[68] Further improvement to perovskite film quality using anti-solvent methods and compositional changes have led to efficiencies greater than 20%,[73,74] with the current highest efficiency single junction cell giving 23.7%.[75] A limitation of the typical MAPI cells is poor long term stability in humid air, and sensitivity to moisture during the synthetic process. Several methods have been used to negate this effect, including encapsulation and using mixed halides. By cutting out the organic cation altogether far higher stability can be achieved, leading to the growing field of inorganic PSCs typically made using $CsPbBr_3$. Furthermore, these devices often utilise a hole transport free conductive carbon back contact for so-called 'all-inorganic' cells. High purity and lanthanide doped $CsPbBr_3$ PSCs recently achieved 9.72 and 10.14% efficiency respectively,[76,77] nearly doubling performance after just a few years of development.[78] For this reason, all-inorganic

architecture formed the base of the PSCs reported in this thesis.

## 1.4 Metal Oxide Nanomaterials

Both photoelectrochemical water splitting and photovoltaics benefit from wide ranging advancement in nanotechnology, which is also responsible for Moore's law; whereby the number of components on an integrated circuit doubles every 18 months largely due to the miniaturisation of transistor size.[79] Now transistors have reached sizes below 5 nm,[80] it is no surprise that engineering at the nanoscale has become a vibrant field of research. Nanomaterials have subsequently been used to build negative electrodes for lithium ion batteries; to form antibacterial layers using silver nanoparticles and to even enhance the colour display of televisions using quantum dots.[81–83] Furthermore, photocatalytic nanoparticles of $TiO_2$ have been incorporated into glass and building materials to act as self cleaning layers.[84,85] This uses radical generation from UV absorption in the wide band gap material, the radicals break apart the molecular bonds binding grime to the surface, to be washed away by the rain. Finally, nanotechnology has received great attention in medicine, where biocompatible magnetic nanoparticles have been applied for controlled drug delivery and cancer diagnosis and treatment.[86]

Inorganic nanomaterials have been widely applied to solar energy due to their exotic optical and electronic properties. Utilising quanta of energy excited through the physical oscillating displacement of charge clouds, plasmonic nobel metal nanoparticles have been widely applied to both PEC water splitting and photovoltaic cells. This energy is transferred to the light absorbing medium by either near field optical coupling, far field scattering or hot electron injection into the conduction band.[87,88] Significant enhancement was achieved by coupling ZnO nanowires to gold nanoparticles (NPs) for oxygen evolution,[89] meanwhile Au-Ag alloyed NPs were incorporated into PSCs for significantly increased efficiency.[90] This is one example of light trapping methods used to elongate the optical path length through thin film solar cells,[91] others include

lambertian back scattering,[92] inverse opal photonic crystals and silicon nanowires (NWs) acting as optical waveguides.[93,94] Noble metal NWs have also been applied as transparent conductors in PVs, replacing typical fluorine doped tin oxide (FTO) or indium tin oxide (ITO).[95]

By far the most common use of nanomaterials in solar energy technology is the use of nanostructured metal oxides as electron transport materials or photoelectrodes in PVs or PEC water splitting respectively. The most common structures applied are nanowires, nanotubes and nanoparticle films forming mesoporous contacts,[96–100] each are advantageous due to increased surface area.[32] Vital when applied to PEC and DSSC devices, larger surface area boosts the efficiency due to greater contact area with water, electrolyte or solid perovskite photoabsorbing layer, allowing a faster rate of charge transfer.[101] However too high a surface area can be detrimental to power conversion efficiency (PCE) due to surface recombination, accelerated by the presence of surface electronic states.[102] For this reason good charge transportation properties are favourable, allowing the photogenerated charge to be transferred away from the interface. Fortunately, water stable metal oxides such as $TiO_2$, ZnO and $Fe_2O_3$ are relatively simple to grow into nanostructures for the photolysis of $H_2O$.

These nanoscale structures also exhibit beneficial electronic properties for the collection of charge in solid state cells. In PV cells excitons must meet an interface or p-n junction in order to separate the charges within the lifetime of the exciton to avoid recombination.[103] The charge is then free to flow around the circuit producing a photocurrent. This is vital to the 2D nano geometry of the thin film solar cell and the nanoscale domain widths of the interpenetrating network involved in bulk heterojunction polymer solar cells.[104] Generally lead halide perovskites have a longer charge carrier path length, and exciton separation occurs at room temperature energies. Therefore, the vast majority of devices capture photoelectrons using high surface area mesoporous $TiO_2$ for charge extraction. The disadvantage of this is slow transportation due to the relatively poor connectivity of the NPs, limiting the thickness of the solar cell. Conversely

NWs and NTs have lower surface area, but more favourable transportation properties. Their application has yielded good performance PSCs, but thus far fall short of the benchmark mp-$TiO_2$. ZnO represents a suitable alternative and thus is the material focus of this thesis. The three most important crystal structures used are found in Figure 1.5.

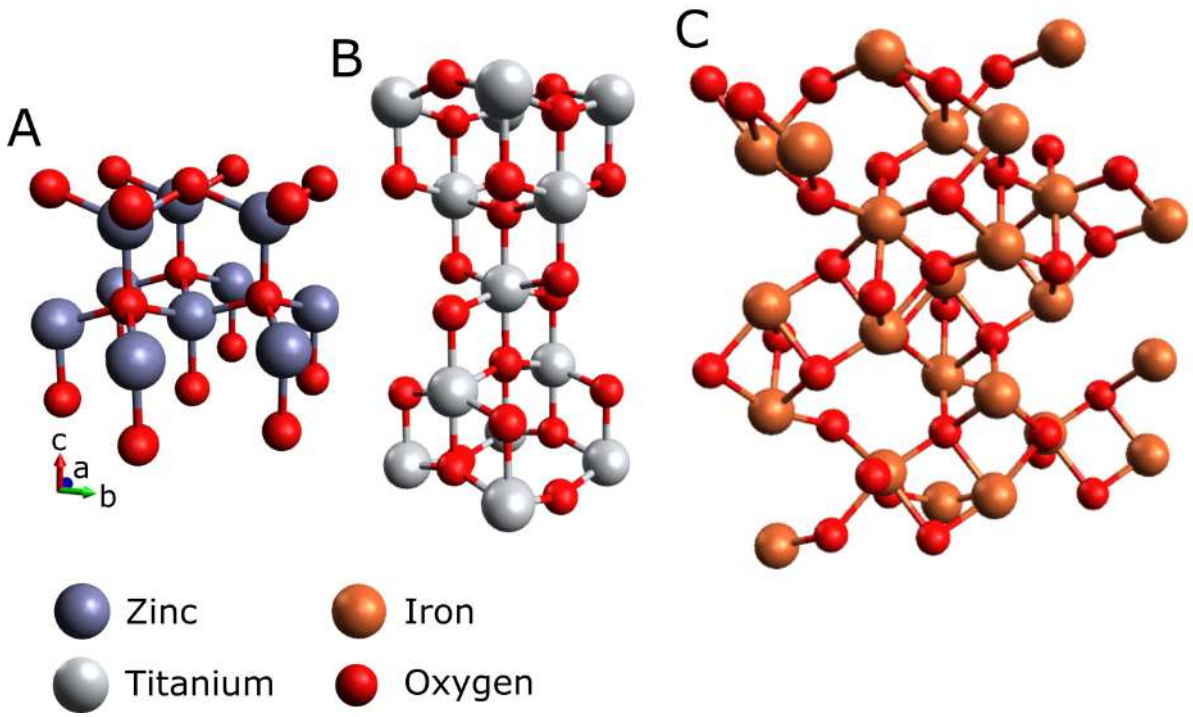


Figure 1.5: A) Shows the crystal structure of wurtzite ZnO, B) anatase $TiO_2$ and finally C) $\alpha$-$Fe_2O_3$

## 1.5 Zinc Oxide

### 1.5.1 Properties

Interest in zinc oxide grew steadily from the 1950s onwards, but only in the last two decades have the materials remarkable properties led to an explosion in publications. The wide direct band gap of 3.37 eV lends itself to UV optical applications which along with high exciton bind-

ing energy of 60 $\mathrm{meV}$ gives photoluminescence of greater quantum yield.[105] Not only useful for optical purposes, the semiconductor also boasts favourable electronic properties with single crystals displaying electron mobility, $\mu_e$, of 200 $\mathrm{cm^2\,V^{-1}}$ in Hall effect measurements.[106] Furthermore it typically displays high n-type doping upon synthesis for high conductivity, $\sigma$, defined by $\sigma = ne\mu_e$, where $n$ is electron concentration increased by doping.[107] This can be further enhanced through extrinsic dopants. The material has also shown ferromagnetic properties when doped with Mn for spintronic applications, alongside strong ability to tune the band gap with divalent atoms. A key drawback of ZnO is the difficulty in controlling the naturally occurring donor defects and impurities, a problem confronted in this work by annealing in air and novel synthesis. Common crystal defects are displayed in Figure 1.6.

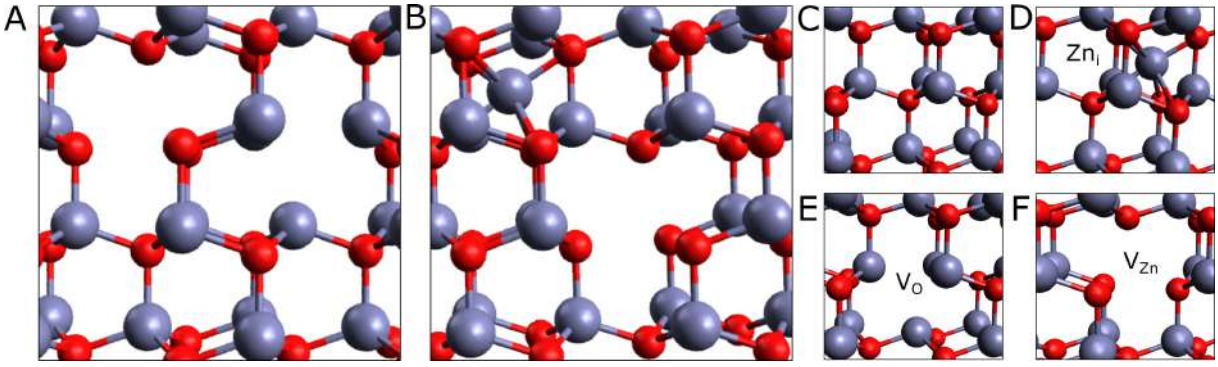


Figure 1.6: A) shows the ZnO wurtzite lattice with a Schottky defect, B) a Frenkel defect, C) the complete lattice, and D) through F) various native point defects found in ZnO.

The origin of n-type doping in the lattice has been the centrepiece of much discussion, in the past it has been attributed solely to oxygen vacancies and zinc interstitials ($V_O$ and $Zn_i$ respectively). Photoluminescence (PL) and dielectric spectroscopies in conjunction with theoretical models have shed light on the defect state positions in relation to the band gap. It is clear that the most likely candidates for n-type doping are $Zn_i$ and hydrogen impurities, which both introduce states close enough to the conduction band for electron injection. From such analysis the presence of $V_{Zn}$ likely behaves as an accepter defect, arising with $V_O$ during the formation

of Schottky defects, defined by charge cancelling vacancy pairs. The presence of $Zn_i$ and $V_{Zn}$ confirms the genesis of Frenkel defects, occurring from displaced interstitial atoms paired with vacancies,[108] while hydrogen impurities are likely present due to the precursors used to synthesise ZnO in basic media. High quantities of defects are beneficial for high doping, but have a negative effect on charge mobility acting as traps and scattering points. They also act as recombination centres, particularly at the surface of the ZnO, and therefore their population must be controlled.

Defect population can be greatly affected by methods of synthesis, typically rapid crystal growth forms greater concentration, compared with slower techniques which yield high quality structures. The characteristic crystal structure of ZnO is hexagonal wurtzite, with lattice parameters of 3.25 and 5.20 Å for a and c respectively.[105] The highly ionic lattice has O atoms tetrahedrally coordinated to four Zn, alternating the local charge when stacked and leading to polarised surfaces responsible for the plethora of ZnO nanostructures. This typically favours growth in the c axis direction by the attraction of anions due to the partial positive charge of the $Zn^{2+}$ terminated 001 plane. The adsorbed anions will reverse the polarity, accelerating the growth process leading to vertically aligned nanorod arrays (NRs) orientated along the specified axis.[109] This mechanism is exploited through various synthetic methods, such as chemical bath, hydrothermal and electrochemical depositions.

Electrochemical deposition uses the reduction of $O_2$ to $OH^-$ in an oxygen saturated bath, which subsequently reacts with $Zn^{2+}$ to form $Zn(OH)_2$.[110] At elevated temperatures this species forms ZnO at the surface of a substrate.[111] The advantages of this method are rapid growth (10 to 60 minutes) and morphological control, but the set up requires three electrodes and the use of gas saturation, leading many to favour more simple synthesis. Rather than the local raising in pH achieved by the previous method, chemical bath deposition uses the slow decomposition of hexamethylenetetramine (HMT) at 85 °C to provide $OH^-$ for $Zn(OH)_2$ generation leading

to ZnO precipitation.[112] The slow pace is required for nucleation and growth on the substrate, rather than the formation of ZnO powder in the solution. Typically requiring 16 hours or more, this process yields high quality NRs with low quantities of defects due to the slow reaction rate. hydrothermal growth offers a compromise, by using a high pH ($\sim$10) adjusted with ammonia, leading to the formation of a sol-gel, cloudy with $Zn(OH)_2$, which is left at a higher temperature of 95 $^{\circ}\mathrm{C}$ at high pressure in an autoclave. Such methods form highly favourable morphology after two to six hours, but with one critical disadvantage. High quantities of $Zn(OH)_2$ form surface OH groups which cause rapid recombination in solar applications, such impurities must be removed by vacuum annealing at 700 $^{\circ}\mathrm{C}$.[113] Novel synthesis of ZnO NRs using microwave heating gave rapid growth while increasing solar water splitting performance, is outlined in chapter 3.[114]

Using these various methods and more, nanostructures other than NRs have been produced, such as nano platelets,[115] nano flowers and nano trees.[116,117] ZnO nanoparticles can also be synthesised and used to make mesoporous films,[118] with great surface areas suitable for solar application. Post treatment of NRs leads to exotic structures such as nanopencils carved out using L-ascorbic acid,[119] and nanotubes etched with KCl,[120] increasing surface area whilst maintaining good transport properties. Some common structures are shown in Figure 1.7. Subsequently, using various templates, ZnO can be grown into porous layers,[121] and inverse opal structures acting as photonic crystals for light trapping.[122] Finally, the use of zinc oxide thin films is rife,[123] for use in a rich field of applications to be outlined in the next section.

### 1.5.2 Application

The favourable optoelectronic properties of ZnO have led to its use in several emerging fields, such as utilising its rapid electron mobility and UV/blue emission for ultra-fast photonics.[124] In this field it has been used to make lasers and LEDs,[125] Figure 1.8. Doping with aluminium

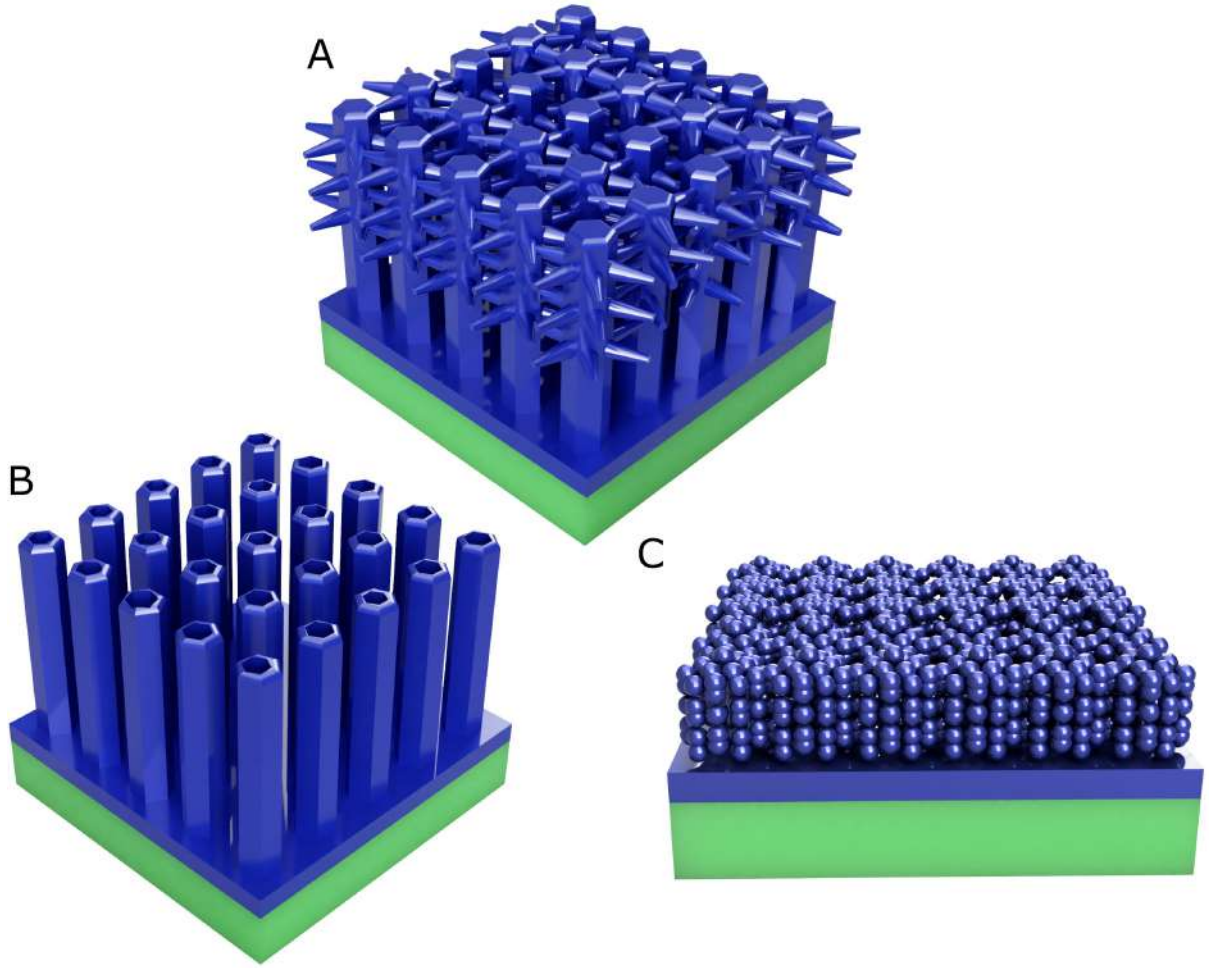


Figure 1.7: A) Shows cartoons of zinc oxide nanotrees, B) nanotubes and C) mesoporous nanoparticle films.

and yttrium can significantly increase the conductivity of thin films, leading to experimental trial as a transparent conducting oxide to replace fluoride doped tin oxide or indium tin oxide.[126,127] Electrical energy storage represents another serious challenge, which has led to the use of nanostructured ZnO as anode material in lithium ion batteries,[128] along with incorporation into supercapacitors.[129] Furthermore the material has found use in both biosensors,[130] able to detect molecules such as urea,[131] as well as gas sensors.[132] The latter rely on significant changes in conductivity in the presence of various gases, reduced breakdown voltages can be achieved using yttrium doping.[133] Finally, highly sensitive pressure sensors were built using ZnO using its piezoelectric properties for biological applications.[134]

Due to similar band edge alignment to $TiO_2$, zinc oxide has been proposed as an alternative to the effective gold standard of photocatalysis. A process mimicking the breakdown of organic pollutants in water, the photodegradation of methylene blue has been achieved by modified ZnO on several occasions. Faster reaction rate was observed using microwave crystallisation of NRs;[135] decorating nanopowders with silver;[136] and finally yttrium doping of ZnO nanoflowers.[116] Encasing ZnO micro-ferns with ZnS led to increased photo degradation of further species, including Rhodamine B and 4-nitrophenol,[137] meanwhile boron doping assisted in the decomposition of aqueous cyanide.[138] Not only useful in degradation, when combined with Cu nano particles, ZnO was able to perform $CO_2$ reduction under solar illumination and atmospheric pressure.[139] This technology, when combined with solar generated $H_2$ can produce a completely photosynthesised liquid fuel, methanol.[140] Finally, hydrophobic porous layers of ZnO have been applied to self-cleaning glass showing a strong UV response.[121]

Solar energy application represents one of the most prevalent uses of the wide band gap semiconductor, particularly in the field of photoelectrochemical water splitting. ZnO is stable in neutral and caustic conditions with suitable band edge positions for water oxidation, acting as a photoanode. Comparing pristine ZnO for this application shows that structure, synthesis and

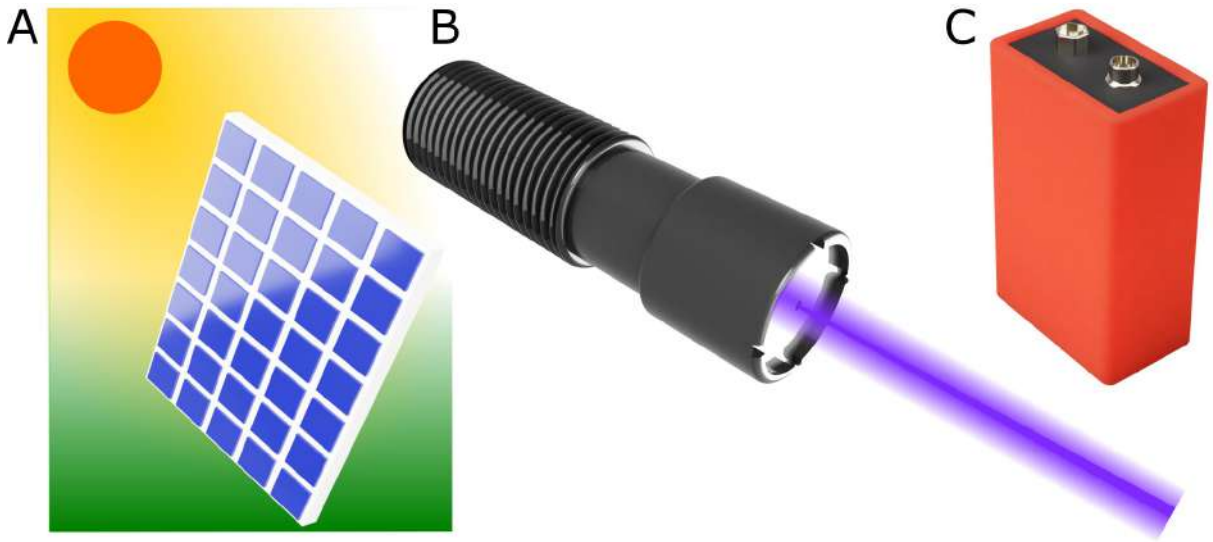


Figure 1.8: The various applications of zinc oxide.

post treatment play a vital role in anode performance. hydrothermal NRs grown by Vuong *et al.*, using repeated four hour reactions along with 2 hours calcining, achieved the highest pristine ZnO performance as measured by current density at 1.23 $V_{RHE}$, valued to be 0.9 $\mathrm{mA\,cm^{-2}}$.[141] The aforementioned nanopencils also performed efficiently at $>$0.6 $\mathrm{mA\,cm^{-2}}$, due to their optimised morphology.[119] These performances greatly fall short of solar water splitting achieved by lower band gap materials sensitive to visible light.[142]

This material shortcoming is defeated by two major strategies, extrinsic doping and by sensitising with other light absorbing materials. Significant band gap reduction occurs when doping with particular atoms, such as sodium or nitrogen, leading to a photocurrent of 1.4 $\mathrm{mA\,cm^{-2}}$ at 1.23 $V_{RHE}$.[100,143,144] Other effects of doping are greater conductivity from hydrogen atoms achieving $\sim$ 1.3 $\mathrm{mA\,cm^{-2}}$;[141] more favourable morphology increasing surface contact from yttrium doping and finally ferroelectric polarisation at the interface with lithium inclusion yielding optimised band bending.[133,145] Even greater enhancement is achieved through sensitisation with other materials, such as low band gap CdS and CdTe, boasting performances of 6.0 and 1.6

$\mathrm{mA\,cm^{-2}}$ respectively.[141,146] Other impressive results utilise both plasmonic and semiconductor absorption effects, such as silver/silver phosphate core/shell nano particle decoration of ZnO NRs.[147] As well as decorating ZnO nanotubes with low band gap $ZnFe_2O_4$ nanosheets and Au nanoparticles for an initial photocurrent value of $\sim 4.0\ \mathrm{mA\,cm^{-2}}$.[148] Recently ZnO NRs have even been coated with mixed metal organic frameworks for enhanced watersplitting, cementing sensitisation as a powerful tool for solar energy generation with zinc oxide. Doping with yttrium as described in chapter four of this thesis, and then coating with hematite as described in chapters five and six, all displayed substantial improvement in water splitting.

Zinc oxide has been applied in a variety of photovoltaic technologies, including bulk heterojunction polymer solar cells. Generally used as electron transport layers, aluminium doped ZnO formed the base of PTB7-Th:$PC_{71}BM$* cells which achieved 10.42% PCE.[149] NRs functionalised by 2-(2-Methoxyethoxy) acetic acid and small molecule coating reduced aggregation to form transparent electron selective layers, capable of 7.38% efficiency.[150] In another example, extremely thin absorber cells were constructed upon $TiO_2$ coated ZnO NRs, utilising $Sb_2S_3$ and P3HT† light absorbing layers for reasonable performance.[151] Most commonly ZnO is applied to DSSC type cells, with great success in utilising low temperature carved nanotubes for 2.87% efficiency.[120] Other material nanostructures such as mesoporous ZnO and long whiskers have been incorporated into this architecture with great success.[152,153] Furthermore, ZnO has been applied with $TiO_2$ to QDSSCs, performing well with PCE values up to 5.92%.[154,155]

Far higher performance can be found in application to emerging perovskite solar cells, where ZnO has became a serious contender to rival the most commonly used mesoporous-$TiO_2$. Early examples of ZnO incorporation both used NR arrays with typical processing techniques achieving reasonable efficiency in MAPI cells as high as 8.9%.[156,157] Once again through doping and

*PTB7-Th: poly[4,8-bis(5-(2-ethylhexyl)thiophen-2-yl)benzo[1,2- b;4,5- b']dithiophene-2,6-diyl- alt-(4-(2-ethylhexyl)-3-fluorothieno[3,4- b]thiophene-)-2-carboxylate-2-6-diyl]
$PC_{71}BM$: [6,6]-Phenyl C71 butyric acid methyl ester

†P3HT: Poly(3-hexylthiophene-2,5-diyl)

coating great enhancement was observed, a thin layer of $TiO_2$ enabled the cells to reach 13.49% efficiency,[158] whilst N doping achieved 16.1% with conductivity and surface passivation the key aims.[159] The highest performance ZnO based cell was constructed by Cao *et al.*, using a mesoporous layer with MgO coating in a mixed perovskite cell yielding a summit performance of 21.1% efficiency. The material has been incorporated in other architectures, including a bulk heterojunction of ZnO and MAPI(Cl) and as low temperature processed counter electrodes for flexible solar cells.[160,161] As for inorganic PSCs the semiconductor has only been applied twice to mixed halide cells, achieving 4.8% and 13.3%.[162,163] A description of how ZnO was applied to $CsPbBr_3$ PSCs for the first time is in chapter seven of this thesis.

## 1.6 Hematite

### 1.6.1 Properties

Though found in many forms, the most thermodynamically stable mineral of iron oxide is hematite ($\alpha$-$Fe_2O_3$). Synthesised at a low cost, this particular "rust" has been extensively studied for application to solar energy due to its low band gap energy (1.9-2.2 $\mathrm{eV}$) betrayed by its vibrant red-orange pigment. Although not quite the ideal value for photoelectrochemical water splitting, an average band gap of 2.1$\mathrm{eV}$ yields a theoretical solar to hydrogen conversion efficiency of 15%.[164] Despite the ability to absorb a great proportion of the visible light spectrum, it has an indirect band gap and therefore a low absorption coefficient. Therefore, thicker layers of the material must be employed in order to achieve significant absorption, especially at near band gap energies.

The crystal structure consists of trivalent iron atoms in a trigonal-hexagonal arrangement with oxygen, characterised by space group $R\overline{3}c$. It exhibits weak ferromagnetism at room temperature.[165] This structure protects the material in a wide range of pH, including strongly basic conditions. One of the key disadvantages of $\alpha$-$Fe_2O_3$ is associated with electronic trans-

portation, affecting water oxidation kinetics and charge carrier collection. Transport occurs within the crystal following a small polaron model, whereby moving charge distorts neighbouring atoms as it hops from site to site.[166] This means low electron mobility of $\sim 10^{-2}\ \mathrm{cm^2\,V^{-1}\,s}$ and poor charge separation efficiency, due to short excitation lifetime (3-10 ps), which leads to a minority carrier mean free path length of 2-4 nm. This critically high recombination rate fuels the need for large overpotentials to drive the oxygen evolution reaction in order to generate sufficient holes. Furthermore, the mechanism is complicated by the extensive charging of prevalent surface states with holes under illumination, which aids the solar water splitting process.[167] The fundamental obstacle to surmount in the utilisation of hematite is how to increase light absorption limited by indirect band gap, whilst maintaining short crystalline domains for hole transfer.

A natural solution is presented by nanostructuring, where chemical methods have been widely used to synthesise a variety of morphologies. For example ultra-thin films of the material have been grown on conductive substrates, allowing rapid injection of holes into the solution.[168] However, this does not combat the problem of poor light absorption achieving only $\sim 0.3\ \mathrm{mA\,cm^{-2}}$ at 1.23 $V_{RHE}$, unlike three dimensional designs. Architecture such as nanorods,[169] nanotubes,[170] nanodendrites and mesoporous layers offer far higher surface area films while increasing layer thickness.[164,171] The development of such designs led to far higher performance, with the final two mentioned achieving photocurrents of $2.2$ and $1.4\ \mathrm{mA\,cm^{-2}}$ respectively. Higher performance anodes nearly universely rely upon surface modification with catalytic materials such as cobalt for reducing harsh overpotentials.[171,172] Despite these gains, electrical connectivity is still a limiting factor insulating electron flow to the counter electrode.

In order to surmount said issue, various dopants have been incorporated into the hematite structure in order to achieve improved transportation. Most commonly this is achieved by n-type doping with ions such as $Si^{4+}$ and $Ti^{4+}$, widely reported previously.[171,173,174] This achieved some

of the highest water splitting rates in literature, with Ti doped $Fe_2O_3$ yielding $4.1\ \mathrm{mA\,cm^{-2}}$ at 1.23 $V_{RHE}$ with the help of surface catalytic Ti−FeOOH.[175] Forming hybrid structures with other materials is an another fertile route to enhancement, several aiming to boost conductivity. Utilising conductive mesoporous scaffolds of antimony doped tin oxide gave a performance of $0.9\ \mathrm{mA\,cm^{-2}}$.[176] Analogously, coating indium tin oxide or zinc oxide nanowires with hematite, forming core-shell structures gave higher performance, still.[177,178] Other hybrid material hybrids aim to overcome the low light absorption, such as coating iron oxide on silicon nanowires.[179,180] Finally, plasmonic enhancement using the decoration of noble metal nanostructures can also lead to greater light absorption by exploiting surface plasmon resonance.[181] However, $Fe_2O_3$ has seen a variety of different applications other than just photoelectrochemical water splitting.

### 1.6.2 Application

The use of hematite by human kind dates back far earlier than modern science, the earliest example of which is attributed to the *pinnacle point man* who lived 164,000 years ago.[182] He used the vibrant red chalk to paint and remarkably it is still used in art today, as its hydrated form is responsible for yellow ochre and unhydrated for the red counterpart. The catalytic properties observed have led to application in environmental protection, first to remove carbon monoxide via oxidation reactions and second to clean pentachlorophenol contamination from waste water.[183,184] Not only suitable for the degradation of poisons, the material has been used to synthesis useful products, such as the conversion of ethylbenzene to styrene.[185] Aside from catalysis, highly controllable morphology at the goethite growth stage allows effective incorporation into gas sensors within a porous capsule.[186] Such devices are capable of high sensitivity to the detection of ethanol, formaldehyde and acetic acid.[187] Electrical properties such as n-type doping and high stability, demanded testing as an anode in lithium ion batteries, a key technology critical to solving the problem of energy storage.[188] Hematite nanocones boasted an

excellent capacity alongside 86% retention after 1000 cycles.[189]

Although the material was not applied to photovoltaic cells in this thesis, a wide number of examples show suitability for the task.[190–193] Firstly, $Fe_2O_3$ was applied to dye sensitised solar cells as a nanostructured counter electrode achieving efficiency of 4.6%.[192] Other examples incorporate into perovskite solar cells as an electron selective layer as a replacement to $TiO_2$, resulting in reduced current voltage hysteresis.[193] This device yielded an efficiency of 10.8% in MAPI cells and superior stability over 30 days. Once again though, high recombination rate was a limiting factor which was alleviated by mixing with the fullerene phenyl-C61-butyric acid methyl ester (PCBM).[190] The composite electron transport layer was able to reach 14.2%, still falling short of the sky-rocketing efficiencies achieved by the persistent bench mark, titanium dioxide.

## 1.7 Titanium Dioxide

### 1.7.1 Properties

The champion material of photocatalysis, titanium dioxide has been explored as a green alternative for chemical processes and energy generation since its photoabsorbing properties were first discovered in the 1950s.[194] Active under UV illumination, the two most common crystal phases of $TiO_2$, anatase and rutile are tetragonal structures with electronic band gaps of 3.2 and 3.0 $\mathrm{eV}$ respectively.[40] Due to the defect states introduced by oxygen vacancies $V_O$ the semiconductor is n-type, with suitable band edge positions to become the first recorded solar water splitting photoanode.[24] Reasonable electron mobility values measured by the Hall effect of 0.4 $\mathrm{cm^2\,V^{-1}\,s}$ (greater than hematite, $10^{-2}$, less than zinc oxide, $10^2\ \mathrm{cm^2\,V^{-1}\,s}$), allow transportation to the platinum counter electrode, while holes remain at the surface to oxidise adsorbed species.[195] While charge mobility is an order of magnitude higher than hematite, the material is still resistive, particularly in nanoparticle films where electrons must frequently cross crys-

tal grain boundaries.[196] Finally, $TiO_2$ is once again chemically stable and therefore ideal as an anode in photoelectrochemical cells with long lasting performance.[197]

Limited charge transportation and the surface catalytic mechanism require $TiO_2$ with high surface area, leading to a large number of different structures. The semiconductor has been grown, templated and chemically etched into many forms, including nanorods which achieved a power conversion efficiency, PCE, of 6.4%,[198] or higher surface area still, oriented nanotubes incorporated into DSSCs.[199] Despite poorer connectivity, high surface area remains the most important factor when building photovoltaics with$TiO_2$, allowing greater quantities of dye to be anchored to the surface for oxidation.[196] Therefore, mesoporous (mp) films have commanded the highest performance and greatest attention, beginning in 1991 with O'Regan and Grätzel.[200] It was this high surface area, high band gap semiconductor that was first sensitised to visible light with an organic dye inventing the DSSC. The staple consists of networks of nanoparticles forming a film and more recently achieved a PCE of 12.3% using a porphyrin sensisiter and cobalt electrolyte.[201] Further improvements to the metal oxides structure itself include making porous single crystal $TiO_2$ using an $SiO_2$ template, improving charge transport whilst maintaining high surface area.[202] Finally, forming various layers of larger nanoparticles ($\sim$ 200 nm) alongside typical anatase films ($\sim$ 20 nm), with additional nanorods improves light scattering effects for greater efficiency.[203]

The large band gap of 3.2 $\mathrm{eV}$ has not only been overcome by the adsorption of organic dyes, but also the conjunction with lower band gap semiconductors for visible light absorption. Mp-$TiO_2$ has been combined with low band gap CdS,[204] CdSe and PbS for quantum dot sensitised solar cells,[205,206] as well as carbon QDs and long persistance phosphors for all weather cells.[207] However the most successful combination has been with hybrid organic-inorganic perovskites, the mesoscopic oxide forms the vast majority of electron transport layers for PSCs.[39,68,208–210] This is due to the well aligned $TiO_2$ conduction band with the MAPI perovskite, along with the

deeply positive valence band position blocking holes from recombination.[211] This hole blocking function is vital due to the material properties of the perovskite, allowing rapid charge separation and mobility within its bulk,[212] therefore a compact layer (c-$TiO_2$) is added to stop holes recombining at the FTO interface.[68] This effectively passivates the electrical contact, acting as an insulating layer, which is the purpose of the $TiO_2$ surface treatment used in this thesis. This strategy has been previously employed to improve the performance of QDSSCs and ZnO used in PSCs.[158,213] The success of mp and c-$TiO_2$ has led to all the highest landmark efficiencies in solar cells, with the 3D scaffold adding light absorption unavailable to planar cells topping 21.3% PCE.[75,214]

### 1.7.2 Application

Other than use in solar cells and solar water splitting $TiO_2$ is once again widely used as a pigment, titanium white, and is the active ingredient in sunscreen.[215,216] The materials photocatalytic properties garner much attention and wide ranging commercialisation in forms such as the anatase/rutile mixed nanopowder, P25.[217] Alongside environmental protection such as the degradation of methylene blue,[218] the semiconductor is used to make self cleaning glass and buildings. In this case, oxidised radical species generated when the immobilised powder is exposed to sunlight attack the chemical bonds binding dirt to surfaces, subsequently washed away in the rain.[219] Finally titanium dioxide has a key role in lithium ion battery technology, employed as a high surface area anode for swift lithium ion intercalation.[220] In this case, nanorods prove to be an effective structure for high capacity, especially when doped with niobium.[221] In fact, niobium titanate is currently at the frontier of high voltage, high capacity, long life materials, already incorporated into electric vehicle batteries.[222]

## 1.8 Junction Properties

In order to best increase the performance of ZnO in both PEC water splitting and photovoltaic cells, the electronic nature of the junctions involved must be understood. These fall into two different categories, the solid/liquid junction that occurs between the electrolyte and ZnO, and the solid/solid junction existing between ZnO and any other semiconductor material. In the former upon contact with liquid the Fermi level, $E_F$, in the ZnO will equilibrate with the effective redox $E_F$ of the solution, forming a space charge region in the solid as electrons are injected into the solution. In the liquid a double layer will form, typically a localised negative Helmholtz single layer of ions will counteract the ZnO positive depletion region, followed by a diffuse layer attracted to the first, screening out the Coulombic charge. Without external bias ZnO will not spontaneously split water due to slight misalignment of band edges, increasing the bias up to the flat band potential removes the depletion zone.[223] Increasing the bias further begins the net flow of holes into the solution at the interface as electrons are free to reduce at the counter electrode. Doping with donor type defects raises the position of the Fermi-level with respect to the conduction band, causing more negative flat band potential and advantageously, lower voltage onset, Figure 1.9.[32]

When selecting secondary solid materials to functionalise ZnO, electronic band position is of utmost importance. Architectures that either trap holes before their injection to the electrolyte, or prevent electrons access to the counter electrode stifle device performance. The ideal junction is known as type II introducing a material with a small increase in valence and conduction band energies between the ZnO and solution, will cause net flow of electrons into the former and holes into the latter.[224] Of course the initial position of $E_F$ in the new material will also affect the junction, with electron flow causing band bending and new depletion zones as the materials form equilibrium.[225] Any surface states will cause further complication which

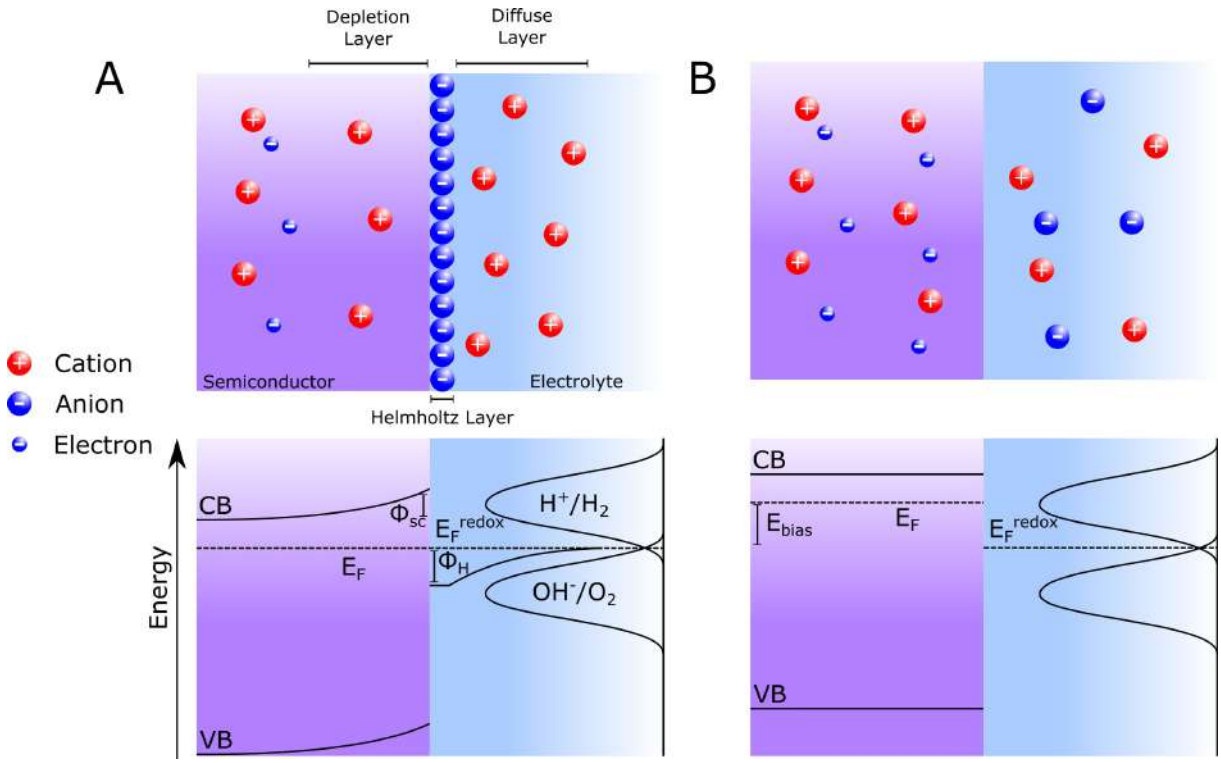


Figure 1.9: Electronic junction physics at A) the depletion zone of n doped ZnO, space charge condition and B) at flat band potential condition. $\Phi_{sc}$ is defined as the space charge potential and $\Phi_H$ the Helmholtz potential.

can lead to Fermi level pinning, preventing free charge flow.[226] other solid/solid junction type utilised in this thesis is the Schottky barrier, where a semiconductor is paired to a metal contact with drastically different work-function.[227] Such a barrier is utilised to produce hole-transport-layer free perovskite solar cells applying carbon or gold directly to the light absorbing layer.[228] Here, so great an injection of electrons into the metal occurs that band bending becomes severe producing a high potential barrier for electrons to cross.[229] This bending is beneficial for the valence band which can transfer holes without friction, enabling charge selectivity. In chapters seven and eight there is a description of how graphite forms this interface with $CsPbBr_3$. These solid / solid junctions along with Fermi-level pinning effect are shown in Figure 1.10.

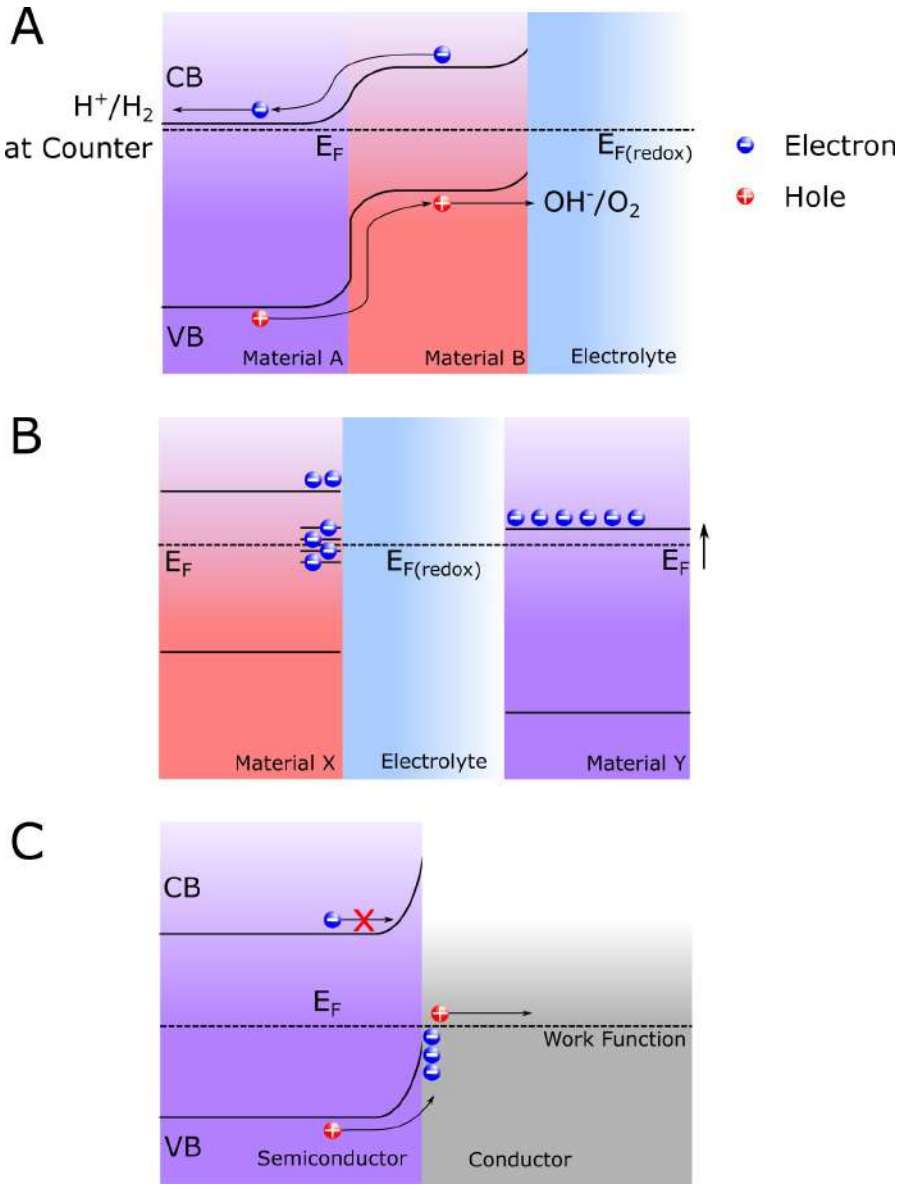


Figure 1.10: A) The junction physics of a type II heterojunction junction suitable for photo-charge generation and separation; B) Fermi-level pinning where $E_F$ is fixed to surface states within the band gap of Material X; and finally C) the Schottky junction showing severe band bending resulting in a hole selective conductive layer.

### 1.8.1 Iron Oxide Hybrids

The type II heterojunctions formed in this thesis used hematite, $\alpha$-$Fe_2O_3$, as a coating on ZnO. This form of rust has many useful properties, a low indirect band gap of 1.9-2.2 $\mathrm{eV}$ allows the absorption of visible light, also its highly stable in alkali media.[230] For this reason it has been applied to great effect in solar water splitting using structures such as nanoparticles, nanorods and nanotubes to achieve high performance.[231] $\alpha$-$Fe_2O_3$ can be synthesised using a variety of techniques, such as hydrothermal,[164] electrochemical and microwave assisted depositions.[232,233] The major drawbacks of the material, are summed up by poor charge transportation, and non-ideal band positioning.[171] The former is due to the slow polaron exchange, whereby electron charge is screened by the collective motion of the atomic lattice decreasing mobility, leading to extremely short minority carrier path lengths causing critical recombination rates.[180] The conduction band and Fermi-level positions are typically far more positive than ZnO, requiring higher onset potentials in some cases even greater than 1.23 $V_{RHE}$. These shortcomings have been tackled in the past using very fine nanostructures with high penetration of electrolyte to shorten the path the hole travels before reaching the interface.[234] Secondly, doping has been widely employed to raise $E_F$ in order to lower the onset potential.[235]

Upon first glance the conduction and valence band positions appear unsuitable for hybridisation with ZnO, however the junction has been used with great success in photocatalysis and PEC water splitting. The explanation is controversial in literature, firstly because the absolute band positions don't shift at all, leading to a favourable environment for both electron and hole flow into $\alpha$-$Fe_2O_3$.[236] This explanation is unlikely as it would cause the photo generated electrons to be trapped in the outer layer at photon energies lower than the ZnO band gap. This is countered by evidence of IPCE showing increased photocurrent generated at wavelengths greater than the iron oxide band edge. The second explanation involves dramatic $E_F$ shift, while retaining the difference between conduction band and $E_F$ forming a type II heterojunction as

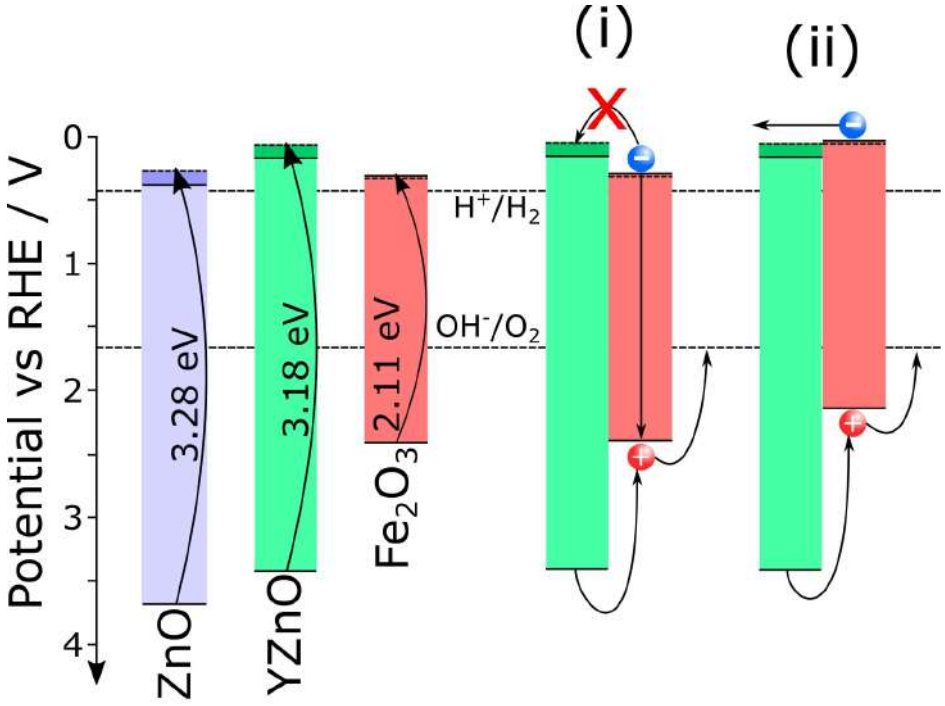


Figure 1.11: Various band gap positions and energies of the semiconductors that form the ZnO/$\alpha$-$Fe_2O_3$ junctions in this thesis. (i) Displays the Fermi-level pinned junction, halting the flow of electrons for hydrogen evolution, (ii) displays Fermi level equilibrium whereby electrons and holes are free to perform both reduction and oxidation reactions, respectively.

ZnO is far more n-doped, and so the difference will be smaller.[178] This explanation confirms the incident photon to current conversion efficiency, IPCE, however in reality great shifts in $E_F$ occur due to the filling of available band states by the net electron flow. This will reduce the conduction band / $E_F$ energy difference in the hematite.[237] This model explains the full picture confirmed in this thesis, shown in Figure 1.11, alongside new observations of flat band shifts in the heterojunction iron oxide.

### 1.8.2 Titanium Dioxide Hybrids

A much larger share of literature is devoted to the construction of ZnO / $TiO_2$ hybrids.[238–240] Previously mentioned as the gold standard for perovskite electron transport and general photocatalysis,[196,241] nano structured $TiO_2$ is synthesised using a variety of methods. Hydrothermal synthesis is typical for high surface area nanoparticles,[54] anodisation of a titanium plate yields nanotube structures and successive ionic layer adsorption and reaction enable the growth of thin films at an atomic scale.[39,242] Nearly indestructible in chemical solution, $TiO_2$ has a wide band gap with reasonable n-doping,[243] with charge transportation qualities finding the middle ground between ZnO and $\alpha$-$Fe_2O_3$.[236] Its high density of conduction band states allows a high electron selectivity and hole blocking,[244] ideal as a compact layer in many PSC devices.[245–247] Although incurring a similar disadvantage as ZnO in low visible light absorption, this can be improved by the optimised inclusion of lower band gap rutile crystal phases amongst the usual anatase.[248] $E_F$ level is similar but more negative than ZnO, and less donor dopants mean a conduction band even more negative still.[249]

This electronic similarity has led to the abundance of research, with ZnO / $TiO_2$ interchangeably used as the electrolyte facing material.[240] For example growing ZnO NRs on hollow hemispheres of $TiO_2$ allowed electrons to flow from the former into the latter yielding high PEC performance.[250] More commonly however it is the other way around, where ZnO acts like a

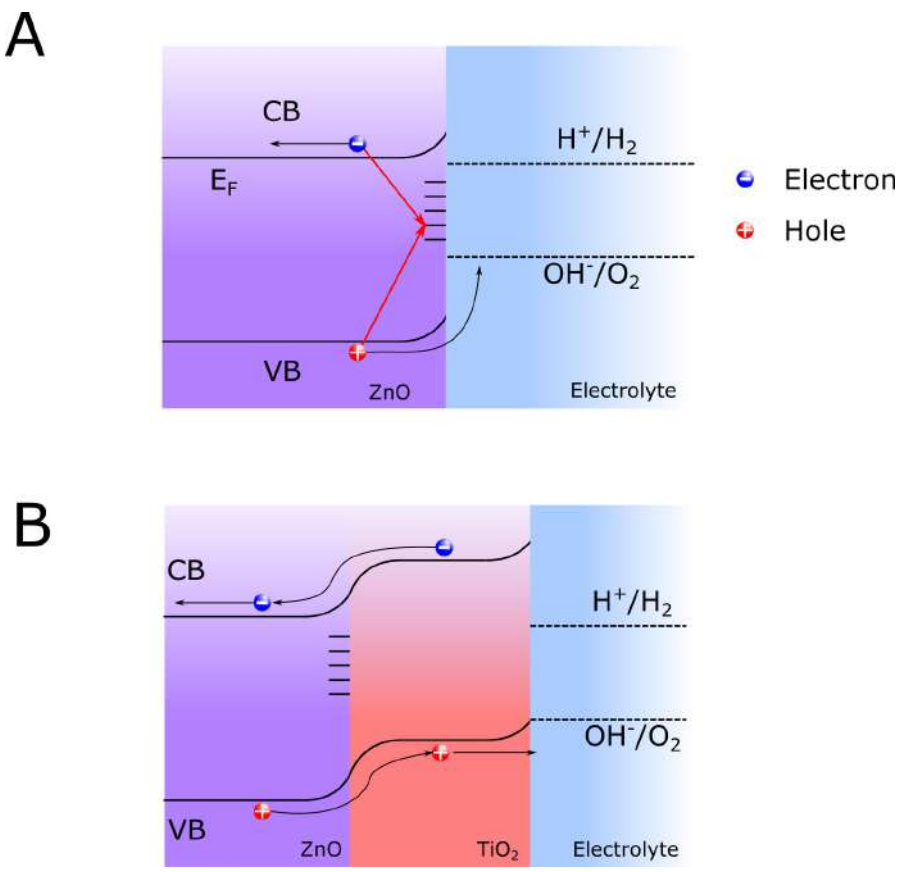


Figure 1.12: A) Naked ZnO suffering electron hole recombination via surface trap states, B) the function of the passivating $TiO_2$ layer. The less conductive annealed $TiO_2$, is less likely to allow surface states to act as charge traps.

conductive core to an immobilised highly active $TiO_2$ photocatalyst.[154,239,251] The benefits of this junction are only slightly due to increased visible light absorption. Passivation plays a far more significant role, by coating with a more insulating material, the recombination at the ZnO surface is reduced.[151] In PSCs without this coating, current can easily flow backward as conduction band electrons recombine with holes in the perovskite, Figure 1.12.[252] Therefore chapters seven and eight describe how the ZnO was coated with $TiO_2$ as an additional hole blocking layer.

## 1.9 Thesis Overview

This thesis aims to further realise the potential of zinc oxide nanostructures in their application to solar energy generation, through novel synthesis, doping and hybridisation with other metal oxides. Therefore chapter one presents a literature review of the current state of solar energy research, focussing on photoelectrochemical water splitting and photovoltaic cells. Subsequently the properties of ZnO and its suitability to both these applications is presented, along with a review of several methods used to enhance its light harvesting abilities. Of these strategies extrinsic doping is explored in great detail alongside synthetic methods used to increase populations of native point defects acting as dopants. Finally, a review of other metal oxides, specifically iron oxide and titanium dioxide, was undertaken in order to assess their suitability for hybridisation with ZnO. Chapter two details the various characterisation techniques used to analyse the materials in this thesis.

Chapter three describes how the novel synthetic method was developed to rapidly grow ZnO NWs using microwave heating. Evidence showed that both dielectric and resistive heating occurred during the process leading to highly defected material in comparison to the NWs grown by conventional CBD. The native point defects generated acted as n-type dopants, increasing the conductivity of the NRs through the bulk whilst detrimentally causing surface recombination.

The population of the defects and therefore donor density was reduced by thermal annealing in air at various temperatures allowing for optimisation at 500°C. Overall the PEC water splitting efficiency MW NWs vastly outperformed the CBD sample, and were further enhanced by annealing.

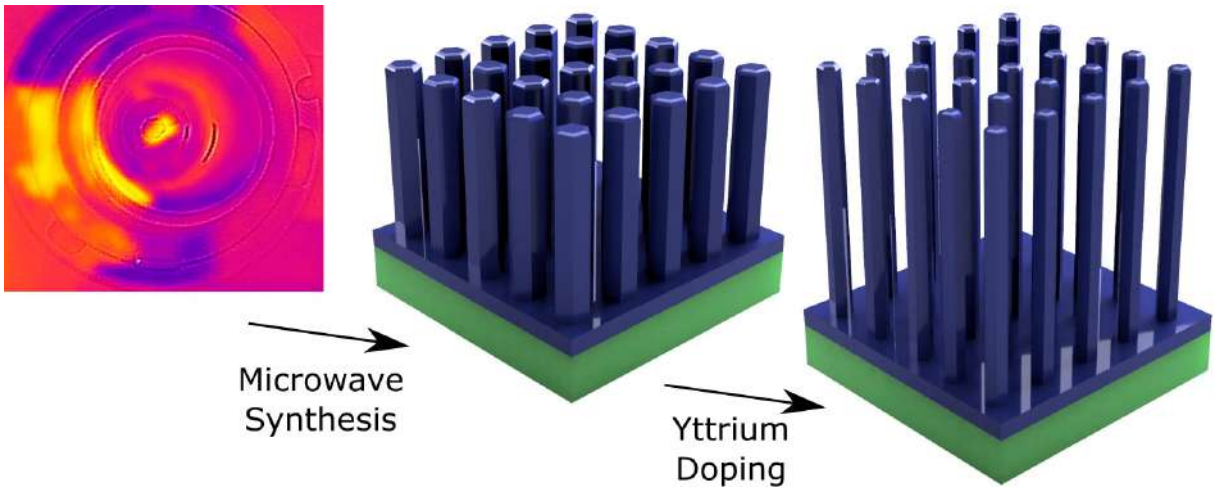


Figure 1.13: Thermal image of resistive heating of FTO glass during microwave irradiation (left), scheme of ZnO nanorods (centre) alongside increased aspect ratio yttrium doped samples (right).

The MW NRs were further investigated in chapter four through the use of extrinsic doping. Yttrium doping was performed during the growth process of the NRs, having been previously confirmed as an n-type dopant. The concentration of yttrium nitrate in the growth solution was varied to 0.5, 1 and 2% and compared with pristine ZnO, real Y concentrations determined by ICP-MS were 0.04, 0.1 and 0.15% respectively. The dopant ions had a positive effect on morphology, increasing the aspect ratio of the NWs and therefore surface area. They also had a strong effect on the conductivity of the NRs, increasing both donor density and electron mobility as measured by Mott-Schottky and transmission line analysis of impedance spectroscopy respectively. The increase in mobility was likely due to trap mediated charge mechanisms and the reduction of other defect populations. The optimised dopant content was found to be 0.1%

Y, which gave a significant improvement in water photolysis (from 0.71 to 0.84$\mathrm{mA\,cm^{-2}}$ at 1.23 $V_{RHE}$). Chapters three and four are summarised in Figure 1.13.

Taking a different approach, ZnO NRs were then sensitised to visible light using a cathodic electrochemical deposition of hematite, $\alpha$-$Fe_2O_3$, as described in chapter five. The new coating layer had a lower direct band gap of 2.11 $\mathrm{eV}$ and allowed the ZnO NRs to absorb light as low energy as 575 nm, as measured by IPCE. The morphology of the hybrid showed nanoparticle decoration on the surface of the wires, agglomerating into mesoporous layers that grew thicker with deposition current, likely the $\alpha$-$Fe_2O_3$ as confirmed by pXRD. The wires also showed a thin 8 nm layer coating which is likely $ZnFe_2O_4$ formed by contact with $FeCl_3$, present on the sample. The combination of three n-type layers formed an efficient junction for charge generation, separation and transportation, the latter improved further by Y doping. The result after optimisation of thickness and thermal annealing duration yielded a far higher rate of water cleavage (1.59 $\mathrm{mA\,cm^{-2}}$ at 1.23 $V_{RHE}$).

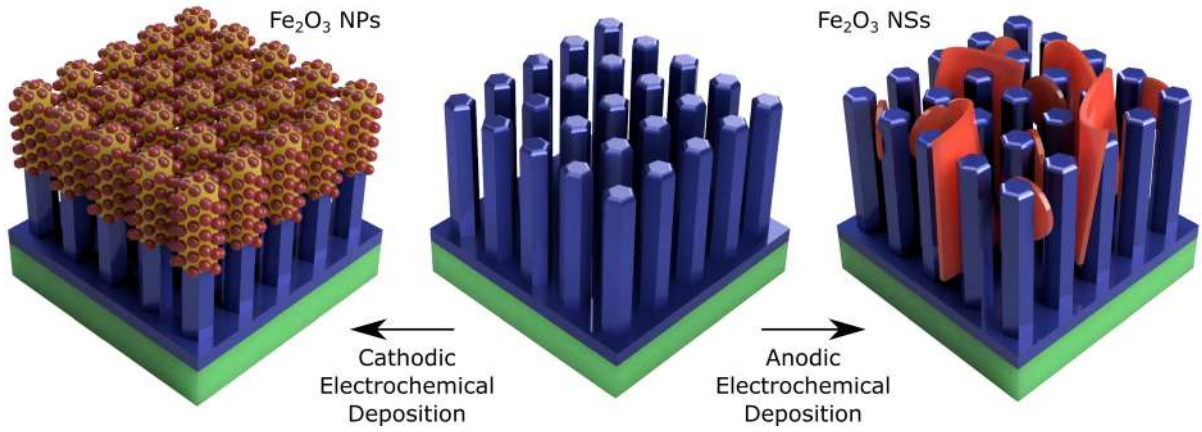


Figure 1.14: Coating with iron oxide using electrochemical deposition, yielding nanoparticle decoration with cathodic potential and nanosheets with anodic.

More exotic structures of $\alpha$-$Fe_2O_3$ were used to decorate ZnO as described in chapter six, where hematite nanosheets were grown in situ. The NSs were grown using an anodic electrochemical deposition, using a potential specific to the oxidation reaction of $Fe^{2+}$ to form

α-FeOOH, goethite. This material was then annealed to form hematite with a much greater surface area due to novel morphology. The deposition process was simply controlled using varied duration, yielding NSs of regular thickness and width that grew linearly with time. The geometry of the samples were optimised for the PEC water splitting process, showing a reasonable photocurrent density of 0.91 $\mathrm{mA\,cm^{-2}}$ at 1.23 $V_{RHE}$. This accompanied a great reduction in charge transfer resistance as determined by EIS, indicating favourable delivery of photogenerated charge to ZnO electron highways. Chapters five and six are summarised in Figure 1.14.

In chapter seven the previously explored NWs were applied to inorganic perovskite solar cells, utilising a novel architecture of $CsPbBr_3$ as light absorber and sonication exfoliated graphite as the back contact for hole transfer. The light absorbing layer was not only effective as in the visible range with a band gap of 2.30 eV, but also had impressive charge separation and delivery to the ZnO. This material was well embedded between the NWs giving a thick absorbing layer, the low cost and ease with which to synthesise graphite gave effective hole extraction in this hole transport material free device. Photocurrents generated by the solar cells were an order of magnitude greater than those achieved by water splitting, enhanced by the dual strategy of yttrium doping and $TiO_2$ coating. This coating acted as a passivation layer, showing strongly reduced electron hole recombination at the interface. The devices were highly reproducible and showed competitive power conversion efficiencies with other inorganic perovskite devices.

Finally, chapter eight explains the anomalous maturing effect that was observed in the optimised solar cells. After storage on a two week time scale the performance of the cells reproducibly increased, and the causes were explored using various characterisation techniques. The devices were stored in several different environments, including methanol, water, chlorobenzene, air and $N_2$ to determine the cause of maturation, the latter two had devices stored in both illumination and darkness. It was proposed that three different mechanisms were at work, the crystal phase ratio of $CsPbBr_3$ : $CsPb_2Br_5$ was strongly varied by residual solvents. Per-

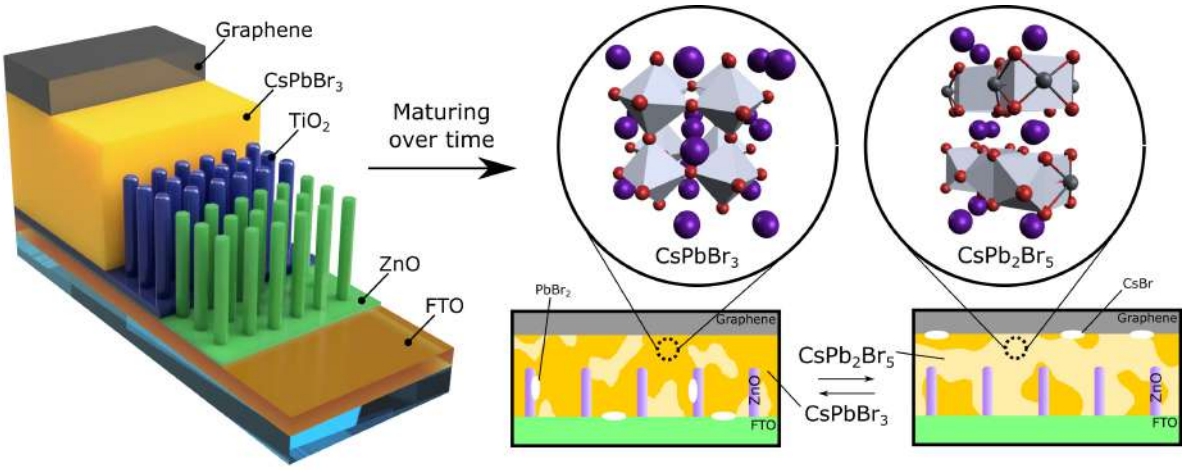


Figure 1.15: 3D image of ZnO NR based perovskite solar cell and the effects of maturation altering the phase ratio of crystal structures.

ovskite crystal grains were seen to shrink as they fit between NWs increasing electrical contact. The final explanation was that ionic diffusion rates cause more rapid degradation or more effective charge separation depending on the storage conditions. Chapters seven and eight are summarised in Figure 1.15.

# Chapter 2

# Materials Characterisation

## 2.1 Abstract

This chapter provides a relatively brief summary of the characterisation techniques used in this thesis. The information obtained by these methods was critical to understand the qualities of the synthesised nanostructured hybrids, both their structures and photoresponse. This provided the basis for comparison with other materials, to the wide array of examples in literature and those found within this work. The three techniques that provided structural and morphological information were scanning and transmission electron microscopy as well as x-ray diffraction. The optical excitation of samples using ultra violet, visible and x-ray photons yielded crucial data and elucidated the materials' electronic structure via UV-Vis, photoluminescence and x-ray photoelectron spectroscopy. In order to understand the fundamental processes at work in the application of materials to photoelectrochemical water splitting and photovoltaic cells, electrical characterisation was required, using potentiostatic curves and electrical impedance spectroscopy.

## 2.2 Structure and Morphology

### 2.2.1 Scanning Electron Microscopy

SEM provides a visual image of the morphology of the sample prepared upon the substrate at a higher resolution than that possible using an optical microscope. Electrons are accelerated to high energies (around 20 keV), giving them a far shorter wavelength than visible light; therefore a far higher resolution limit is achievable following the Rayleigh criterion for a circular aperture.[253]

$$\theta_R = 1.22\frac{\lambda}{D} \tag{2.1}$$

$\theta_R$ refers to the angular resolution limit between two points, $\lambda$ the wavelength of the imaging wave and $D$ the diameter of the lens. However, even the highest specification SEM will not reach this resolution; due to the scanning nature of this method.[102]

Rather than using the primary electrons to image; the core function of an SEM uses secondary electrons emitted through the inelastic collision of the beam with k shell electrons in the atoms, displayed in Figure 2.1A. These low energy electrons are emitted in all directions from within nanometres of the surface of the sample, they are captured by a detector situated above the sample. By focusing the emitted electron beam onto a small diameter probe which is scanned across the sample, the surface morphology of thick samples can be imaged. Scanning in two perpendicular directions simultaneously covers a small rectangular area of the sample, collecting the secondary electrons from each point forms the image.[254]

Many SEM instruments have the ability to measure other useful signals such as Back Scattered Electrons (BSE) or Energy Dispersive X-ray (EDX) spectroscopy. BSE are generated by the elastic interaction of the beam with the atomic nuclei of the sample, Figure 2.1B, resulting in high energy deflected electrons at high angles.[255] For this reason BSE detectors are situated near to the incident beam. The advantages include generating images sensitive to nuclear

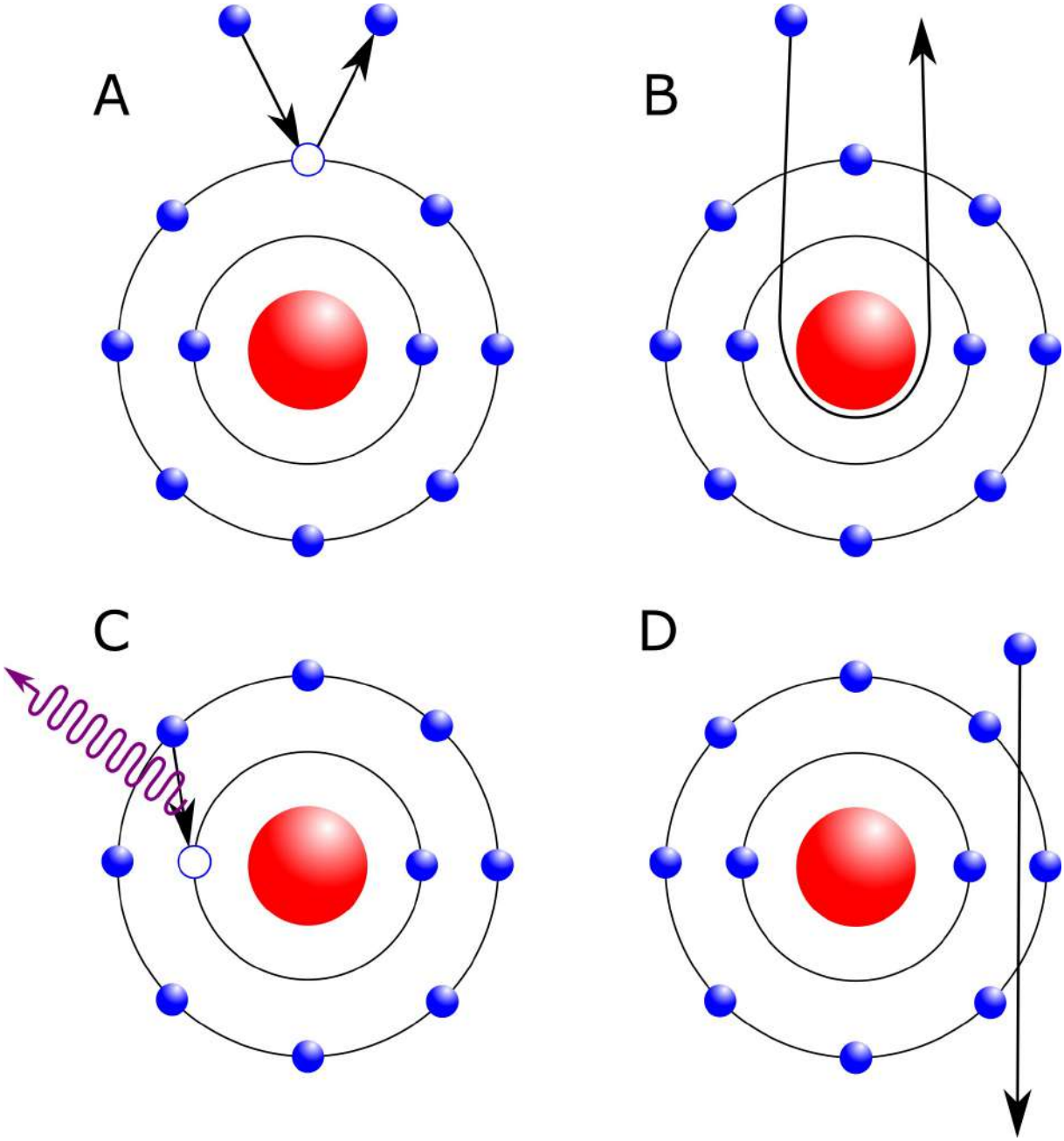


Figure 2.1: The various processes leading to imaging and mapping within electron microscopy, A) is the inelastic release of secondary electrons, the primary detector used in SEM. B) Shows the process of back scattered electron generation; C) displays characteristic x-rays used for elemental analysis with EDX, and finally D) displays transmitted electrons used in TEM.

mass, able to differentiate structures rich in particular elements controlled by contrast. Also, morphology below the surface can be imaged as the electrons are highly penetrative. The key disadvantage is that back scattering is a rarer event, leading to lower resolution than secondary electron imaging.

EDX spectroscopy utilises the characteristic x-rays released from the sample, when outer shell electrons relax into inner vacancies left by the excitation, which emits photons of the fixed transition energy, Figure 2.1C. This allows qualitative elemental analysis of the sample, as well as mapping of elemental concentrations.[256]

### 2.2.2 Transmission Electron Microscopy

Higher resolution can be obtained using Transmission Electron Microscopy (TEM) which captures primary electrons after they are attenuated and scattered whilst travelling through the sample, Figure 2.1D. The incident electron beam is treated as a forward scattered wave. These effects are so strong that it is unsuitable to image samples thicker than 100 nm. Due to the comparative low loss of signal and high acceleration voltage, the resolution is an order of magnitude higher than SEM. Voltages of 120 kV can be used to image coatings and particles on the order of single nanometres, whilst 200 kV (High Resolution Transmission Electron Microscopy, HRTEM) allows the resolving of crystal lattice spacing and individual atoms. The final resolution however, is mainly determined by the objective lens.

By measuring these distances, likely crystal structures can be determined, and fast fourier transforms (FFT) can be used as an image processing technique to view such structures in reciprocal space. This leads to bright spots corresponding to Fraunhofer diffraction patterns further confirming the crystal structure on a particular zone axis. Once again, EDX is often available, as well as selected area electron diffraction (SAED), for even greater confidence in phase identification.[257]

### 2.2.3 X-ray Diffraction

X-ray diffraction occurs upon incidence with solid crystals due to the similar wavelength of the electromagnetic radiation to the distance between lattice planes in the crystal. The atoms in the crystal will act like a diffraction grating as the x-rays couple to the electrons, resulting in spherical wavefronts which positively interfere, provided the Bragg condition is satisfied.[258]

$$n\lambda = 2d\sin\theta \tag{2.2}$$

The equation describes how the wavelength of the x-rays $\lambda$ relates to the spacing of the lattice $d$ and the incident angle $\theta$ is equal to half the angle of reflection ($n$ is a positive integer due to the periodicity of the wave).

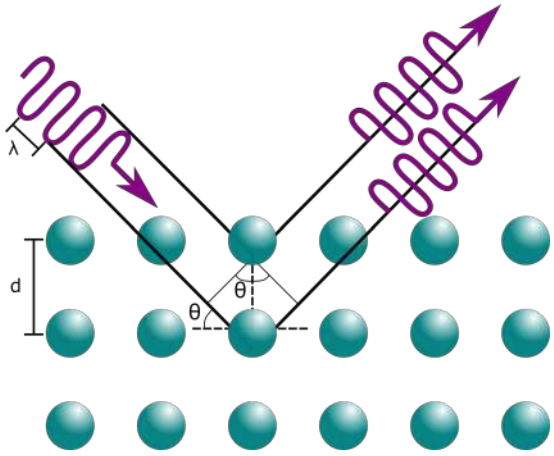


Figure 2.2: The geometric description of Bragg's law of diffraction.

Powder XRD scans through $\theta$ in one dimension of rotation, relying on the random orientation of a ground-up crystal powder. The peaks are then cross referenced with a catalogue of known crystal spectra using the software X'pert Highscore Plus.

Crystallinity can also be measured by looking into the full width half maximum of diffraction peaks. Peak broadening occurs when the sample is less crystalline, either due to a higher quantity of crystal defects, or the crystal domain size of nanometre dimensions. The latter value

can be quantified using the Scherrer equation, 2.3, though broadening can occur due to either reason, limiting the accuracy.[259]

$$D_{hkl} = \frac{K\lambda}{B_{hkl}cos\theta} \tag{2.3}$$

Briefly, $D_{hkl}$ refers to the crystal domain size which is perpendicular to the specific lattice plane selected using Miller indices. The shape factor $K$, is typically valued at 0.9, $B_{hkl}$ is the full width half maximum of the selected peak.[259] The diffractometer used in this thesis used a reflected angle, flat plate set up and a copper source, with $K\alpha$ wavelength of 1.5406 Å. The flat plate set up allowed the determination regarding preferential orientation, as nanostructures grown on a solid glass substrate did not need to be removed and ground up. The opposite is the case for transmission foil mode XRD.

## 2.3 Optical Characterisation

### 2.3.1 UV-Visible Spectroscopy

UV-Vis absorption spectroscopy has been used to measure the light absorbing ability of the ZnO NRs synthesised. In this technique, the path of a visible UV pulse of light to a detector is interrupted by the translucent sample, Figure 2.3A. After passage through the sample, unabsorbed light is split into constituent wavelengths by a diffraction grating. This spread beam is then incident upon a photodiode array which can measure the intensity against the wavelength. The relation between the intensity of light emitted through a blank reference sample $I_0$, and the light detected $I_s$, will give the resulting absorbance A, of the sample using the following simple relation.

$$A = -\log \frac{I_s}{I_0} \tag{2.4}$$

.

Precise values of the energy of the band gap can be calculated firstly by using the path length

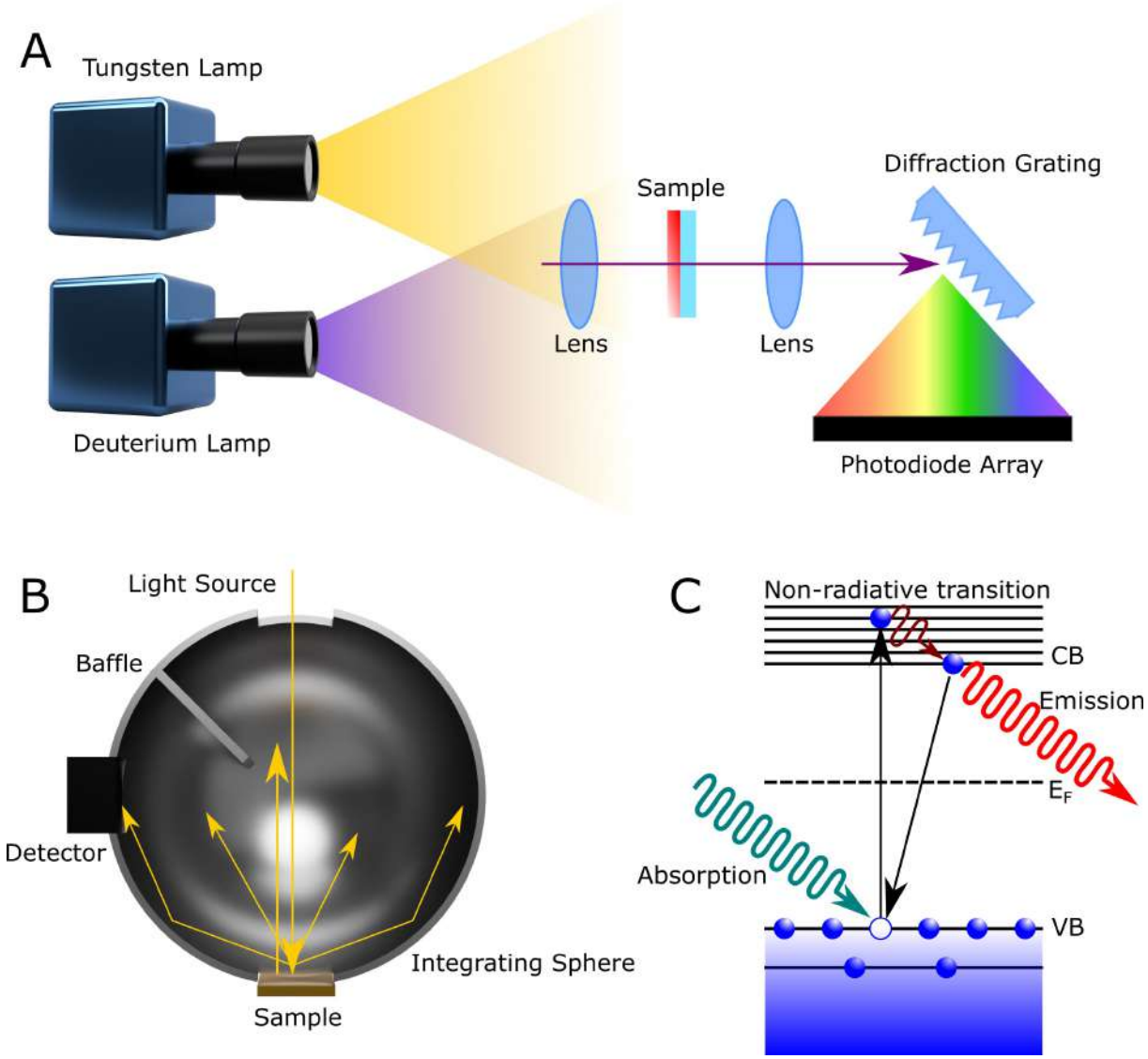


Figure 2.3: The two different UV-Vis spectrometers used in this thesis, A) shows UV-Vis absorption spectroscopy with photodiode array detector. Diffuse reflectance measurements of UV-Vis using an integrating sphere are shown in B), and the physical semiconductor response to this excitation is shown in C) alongside photoluminescent emission.

of light through the array, film thickness $b$, and the absorbance of the material $A$ to calculate the molar absorptivity $\alpha$.[260]

$$\alpha = \frac{A}{b} \ln 10 \tag{2.5}$$

This value is then used in the Tauc function in order to find the absorption edge and therefore band gap energy of the sample.[261]

$$(\alpha h\nu)^{\frac{1}{n}} = A_0(h\nu - E_g) \tag{2.6}$$

From this relation it is clear that plotting $(\alpha h\nu)^{\frac{1}{n}}$ against $h\nu$ and extrapolating any linear relationships to the x intercept will provide band gap energy $E_g$. $h\nu$ refers to photon energy; $A_0$ is a constant based on the electron hole mobility of the material and finally $n$ describes the nature of the transition; equal to $\frac{1}{2}$ for direct, and 2 for indirect.[262,263]

In some cases samples can be too thick for UV-Vis absorption spectroscopy, this leads to saturated values of $A$, requiring the use of reflection spectroscopy, Figure 2.3B. In these cases the sample is once again illuminated from by a suitable light source, and an integrating sphere is used to determine the resulting diffuse reflectance. This is a near perfect sphere with a matt white surface, to conserve optical power whilst losing spatial information. In this way the spectral reflectance is removed, and the light source is blocked from directly entering the detector through the use of a baffle. In order to calculate spectra in terms of the fraction of reflected light, a white reference material must be used as an assumed 100% reflection. In this thesis MgO powder was used to normalise the spectra.

In the same way light with sufficient energy to excite valence electrons to the conduction band is absorbed, lower energy light is reflected. The most commonly used model to calculate an analogous Tauc plot from said spectra is the Kubelka Munk function, $F(R)$.[262]

$$F(R) = \frac{(1-R)^2}{2R} \propto (\alpha h\nu) \tag{S6}$$

Where $R$ is the value of the fractional reflectance at any specific wavelength, and calculated plots can yield the band gaps of materials with the appropriate exponent of $(\alpha h\nu)$ as described previously.

### 2.3.2 Photoluminescence Spectroscopy

Using a similar light source as UV-Vis spectroscopy, this method of characterisation introduces a 90° angle between light source and detector. The light source is monochromated and held at a constant wavelength, above the band gap energy of the ZnO allowing the excitation of electrons into the conduction band. The excited electrons will then dissipate this energy by vibrational means to the conduction band minimum, followed by radiative transitions either directly to the valence band (near band edge emission) or via any defect states, Figure 2.3C. The detector then scans through wavelengths measuring the emission of the sample placed on the stage; as 90° geometry minimizes the detection of scattered light from the excitation source, intending for only the photoluminescence of the sample to be measured.[264]

Although usually samples are suspended in solution and measured, solid substrates can be characterised by placing them in the stage at a 45° angle. There is a danger of some reflected light entering the detector. Therefore, a high energy excitation was chosen at 320 nm, with a detection range that was significantly lower (350-600 nm). The intensity of the fluorescent peaks show the general rate of electron hole recombination as an undesired property in the semiconductor. The intermediate peaks falling within the forbidden zone show impurity states, which indicates the presence of crystal defects such as oxygen and zinc vacancies.[265,266] Peaks can be tested to be real emissions by altering the energy of the excitation, if some intensity is lost or gained they are likely genuine electronic states. If the peak begins to shift with the excitation, it is likely to be a ghost generated by nodes of reflected wavelength. These spectra were normalised in this thesis to the absorbance value at the excitation wavelength.

### 2.3.3 X-ray Photoelectron Spectroscopy

X-ray photoelectron spectroscopy, XPS, is a powerful technique of surface analysis to determine the elemental composition, ionisation states and electronic structure of a material. This uses Einstein's photoelectric effect to release bound electrons from the sample using monochromatic x-ray illumination. The energy with which these electrons are bound can be determined by measuring the kinetic energy of the released electrons.

$$E_B = h\nu - E_K - \phi \tag{2.7}$$

The Einstein equation describes this, 2.7, $E_B$ is the binding energy, $h\nu$ is the photon energy, $E_K$ is the kinetic energy and finally $\phi$ is the work function of the material. Rapid electron absorption means that this instrumentation yields information within 10 nm of the surface, unless the sample is sputter etched using an $Ar^+$ beam for depth profile analysis.[267]

This process yields spectra which map the electronic structure of the material, where single peaks reveal orbitals, unique to specific elements. Peaks are assigned according to principle quantum number as the first integer, followed by the angular momentum quantum number according to their orbital labels. These typical photoelectrons are described in Figure 2.4A; a different labelling convention is used for two electron events described as Auger electrons. Following photoelectron release from the inner shell, electrons from less bound states are free to transition into the space releasing a photon, Figure 2.4B. This energy can be subsequently absorbed by another electron, now unbound and emitted to the vacuum Figure 2.4C. These signals are unique to each element and are described using x-ray notation, where principle quantum number is replaced by letter K, L, M; and angular momentum quantum number is defined by integer.[268]

The relative abundances of elements can be determined by integrating the signal peaks, and dividing by relative sensitivity factor. Finally, valence band position can be determined using

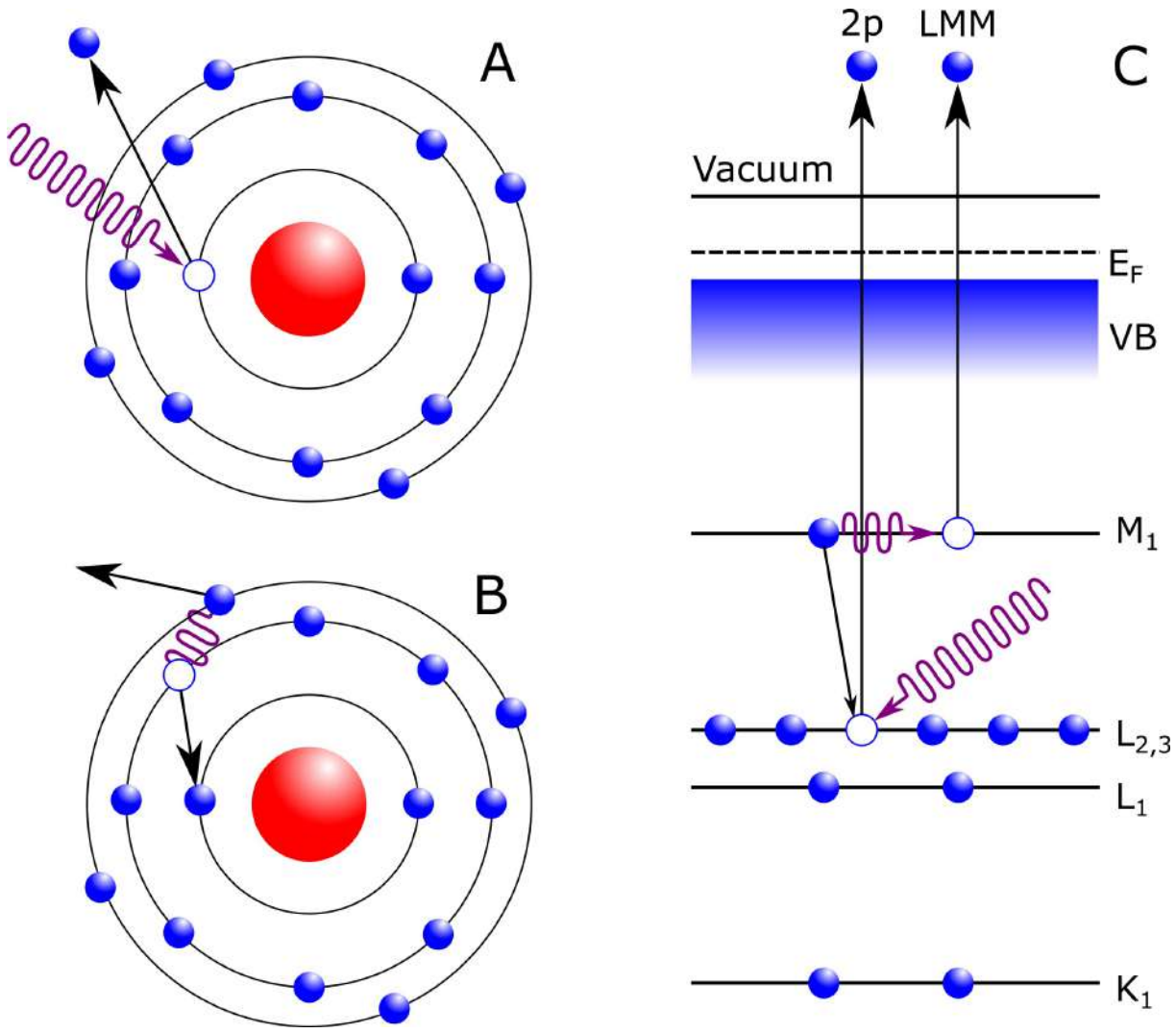


Figure 2.4: The processes involved in XPS, the release of a photoelectron is shown in A) from X-ray excitation. B) Displays the release of a typical Auger electron in a two electron process. The energy diagram of XPS is shown in C), including its relation to the valence band maximum and the occurrence of an LMM Auger electron.

this technique, exploring the low end of the binding energy spectrum (0-10 eV). The onset of electron excitation can be extrapolated from the linear region to the baseline, this value can be transformed to vacuum energy by adding an additional +4.44 eV.[237]

## 2.4 Electrical Characterisation

### 2.4.1 Potentiostatic Curves

The majority of electrical characterisation performed in this thesis required the use of a potentiostat, for varied input potential bias whilst measuring output current. A simplified diagram of how the potentiostat works is shown in Figure 2.5A, alongside its connection to the working, counter and reference electrode. Briefly, the voltage signal is generated based on software input, examples shown are linear sweep voltammetry (LSV, top); chronoamperometry (CA, middle) and cyclic voltammetry (CV, bottom). This voltage $V_{sig}$ leads to a current through the left resistor and a potential difference with opamp i, as its positive terminal is grounded and so $V_{in,i,-} = 0$. As opamp i has nearly 0 current, it flows to opamp ii set up as a voltage follower; therefore $V_{out,ii} = -V_{sig} = V_{RE}$ at the reference electrode. At the same time working electrode voltage is grounded and held at zero, therefore the potential across the system will be $V_{WE} - V_{RE} = V_{sig}$. Output current can be read at the resistor closest to the computer. Finally the connection of $V_{sig}$ to the negative terminal of opamp i, means that $V_{out,i}$ will always have the reverse sign to the working electrode vs reference electrode.[269]

When performing photoelectrochemical water splitting, a standard three electrode cell was set up with the potentiostat, Figure 2.5B (top). The synthesised sample was the working electrode, plantinum foil was the counter electrode and a KCl saturated Ag/AgCl was the reference electrode. The light source was a solar simulator with an AM1.5 G filter calibrated to produce 100 mW/cm$^2$ flux at a distance of 25 cm; imitating solar light post atmospheric absorption. The light source had to be calibrated using a reference solar cell with a known short circuit current.

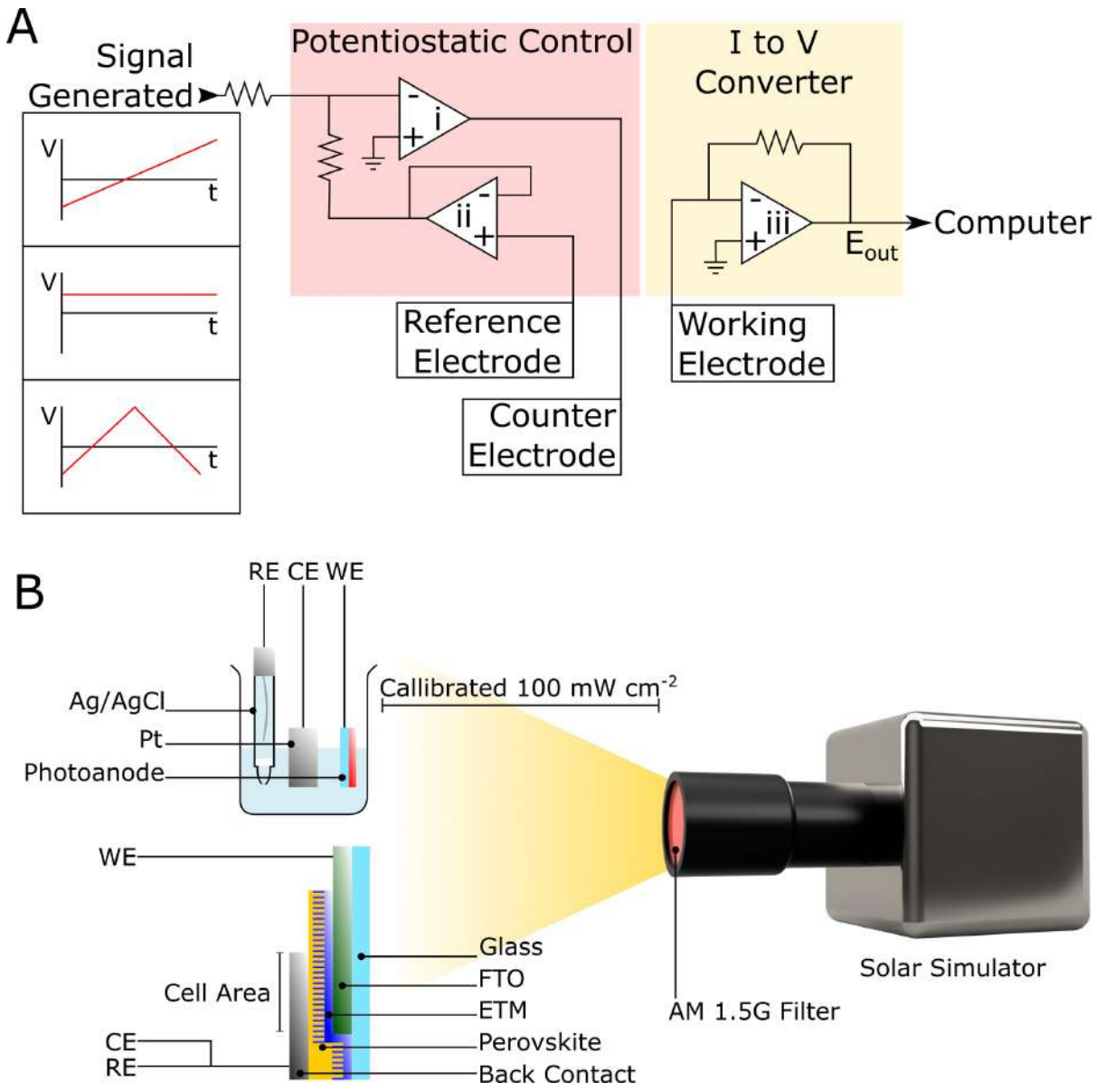


Figure 2.5: A simplified circuit diagram of a potentiostat is shown in A), displaying the logic used for three electrode analysis. Typical signals used in the thesis are shown on the left including linear sweep voltammetry (top); chronoamperometry (middle) and cyclic voltammetry (bottom). The physical connection for the measurement of photoelectrochemical water splitting (top) and photovoltaic IV curve (bottom) is shown in B).

The electrodes were immersed in both 0.5 M $Na_2SO_4$ and 1 $\mathrm{mol\,dm^{-3}}$ KOH electrolytes depending on the chapter, giving pH values of 6.8 and 13.6 respectively. This meant the hydrogen and oxygen evolution potentials were transformed from their places according to the Nernst equation.[270]

$$E_{RHE} = E_{Ag/AgCl} + 0.059pH + E^{o}_{Ag/AgCl} \tag{2.8}$$

$E_{RHE}$ refers to the potential versus RHE; $E_{Ag/AgCl}$ was the measured potential versus the reference electrode and $E^{o}_{Ag/AgCl}$ was the oxidation potential versus the reference electrode (equal to 0.1976 at 25°C). Measured photocurrents via the 3 electrode system could then be converted to power conversion efficiency, PCE, though this is controversial in literature.[32]

$$\eta(\%) = \frac{J_p(E^{o}_{rev} - E_{app})}{I_0} \times 100 \tag{2.9}$$

PCE is referred to as $\eta$, $J_p$ is the photocurrent density (mA cm$^{-}2$) and $E^{o}_{rev}$ is the oxygen evolution potential (1.23 V). The applied voltage $E_{app}$ is calculated by transforming the three electrode potential to its two electrode equivalent; $E_{app}$ is the approximated potential vs the platinum counter electrode.

$$E_{app} = E_{meas} - E_{oc} \tag{2.10}$$

Where $E_{meas}$ is the measured working electrode potential vs reference electrode and $E_{oc}$ is the open circuit potential under the condition, $J_p$ is equal to 0 $\mathrm{mA\,cm^{-2}}$. $I_0$ is the incident power density from the lamp and the PCE (%) is numerically equivalent to the power output due to $I_0$ holding the value of 100 mW cm$^{-2}$.[263] It was also useful to use a shadow mask to confine a more accurate illumination area of the photoanode, especially when comparing currents to those achieved by incident photon to current conversion efficiency tests (IPCE).

Photovoltaic cells were tested in an analogous way using a two electrode set up, by connecting counter and reference electrodes together, Figure 2.5B bottom. The working electrode was connected to the electron transport layer side of the cell, where all layers had been removed

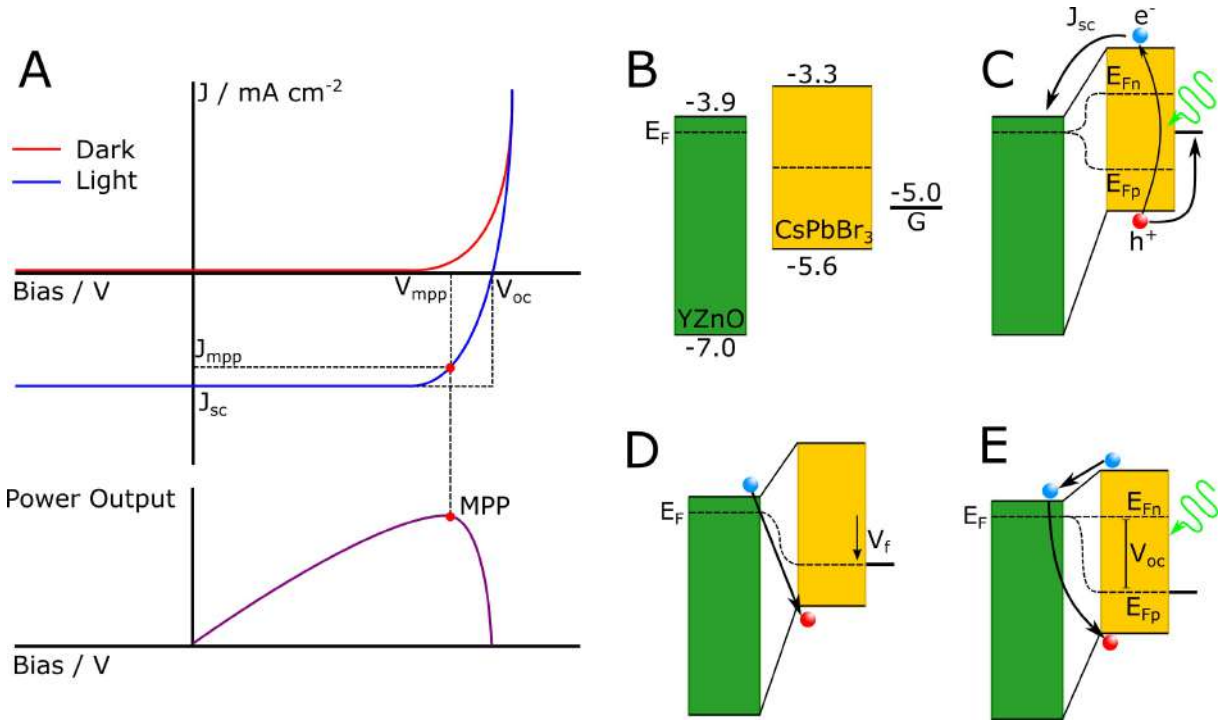


Figure 2.6: A) shows a typical photovoltaic IV curve under dark and illuminated conditions. The isolated material work functions and band positions of separated materials are found in B). Illumination under the short circuit condition is shown in C) leading to maximum photocurrent. The effect of forward Bias is shown in D) leading to electron injection from YZnO CB to $CsPbBr_3$ VB. D) shows the illuminated $V_{oc}$ condition where electron injection is equal to photogeneration, netting zero current.

exposing the FTO. The counter electrode was connected to the graphite layer on top of the cell, below which the FTO had been etched away prior to cell construction. The overlapping area of FTO and graphite defined the solar cell area, approximating 'lateral' motion of electrons to be negligible. Three cells were printed on each device, defined by the three strips of drop cast graphite.

A cartoon of the output IV curve of a typical solar cell is shown in Figure 2.6A, as well as the corresponding power output curve. Within, key solar cell parameters are determined when illuminated, the point of the y intercept is the short circuit current, $J_{sc}$ and the x intercept is the $V_{oc}$. The current and voltage values at maximum power point (MPP) are defined by $J_{mpp}$, and $V_{mpp}$; allowing the calculation of fill factor, FF.[193]

$$FF = \frac{J_{mpp}V_{mpp}}{J_{sc}V_{oc}} \tag{2.11}$$

A useful value for determining the quality of the cell versus its theoretical performance, usually hindered by recombination rate. This leads to two simple equations of calculating the solar cell power conversion efficiency.

$$\eta = \frac{P_{mpp}}{I_0} = \frac{FFJ_{sc}V_{oc}}{I_0} \tag{2.12}$$

The value $P_{mpp}$ is the MPP power. Typical band energy positions along with Fermi levels are shown in Figure 2.6B of the materials used in all the devices in this thesis. When brought together in junction with a potential bias of 0 V and illumination by solar simulator, the resulting $J_{sc}$ condition is shown in Figure 2.6C. Illumination leads to Fermi-level splitting to two quasi levels due to dynamic populations of photo-generated electrons and holes.[271] Meanwhile the Fermi levels of the YZnO and graphite are equal; driving electrons into the the conduction band of the former, and holes into the latter. Figure 2.6D shows the dark junction under a forward bias, which leads to electron injection from the YZnO conduction band, into the perovskite valence band according to typical diodic behaviour. This is reflected in the dark scan of Fig-

ure 2.6A; where given sufficient bias injection takes over leading to positive current.[272]

Figure 2.6E displays finally the $V_{oc}$ condition, where forward bias and illumination are applied. When the bias matches the difference in quasi Fermi levels determined by ETM and HTM, the forward current, due to electron injection, matches the reverse current generated by photocharge. This results in a net charge of zero.[273] This model explains the shape of the photovoltaic IV curve, though it is a simplified picture; quasi Fermi levels are also formed in the YZnO. However, due to the position of the YZnO p-level it is unfavourable for any photogenerated holes to be transferred. It also worth noting that for perovskite cells, it is worth performing a CV rather than LSV, in order to measure the current voltage hysteresis common to such devices.[274]

Fermi level splitting in the YZnO is, on the other hand, crucial to understanding the process of solar water splitting utilised in this work. A typical LSV cartoon is shown in Figure 2.7A, with explanations of the processes involved in B - F. This data varies fundamentally from the PV system due to the three electrode nature of the potential bias, along with the role of oxygen and hydrogen evolution potentials ($V_{OE}$ and $V_{HE}$) in the electrolyte. Once again, the wide band gap semiconductor, YZnO is represented on the left. At negative bias position the reaction is unable to occur, Figure 2.7B, as the potential is uphill for hydrogen reduction at the platinum electrode. Also, holes are unable to oxidise oxygen due to the downward band bending in the semiconductor. At less negative potential, the flat band condition ($V_{FB}$) is satisfied, Figure 2.7C, where the depletion zone in the material is removed as the Fermi level is equilibrated to the $V_{HE}$.[275] This allows the determination of this level against the reference electrode using Mott-Schottky plots.[276]

Forward bias results in upward band bending in the semiconductor in the dark, Figure 2.7D, and light, Figure 2.7E, splitting the Fermi level once more. Illumination results in the raising of both semiconductor and platinum $E_F$ with respect to the solution level, as it is transparent. If

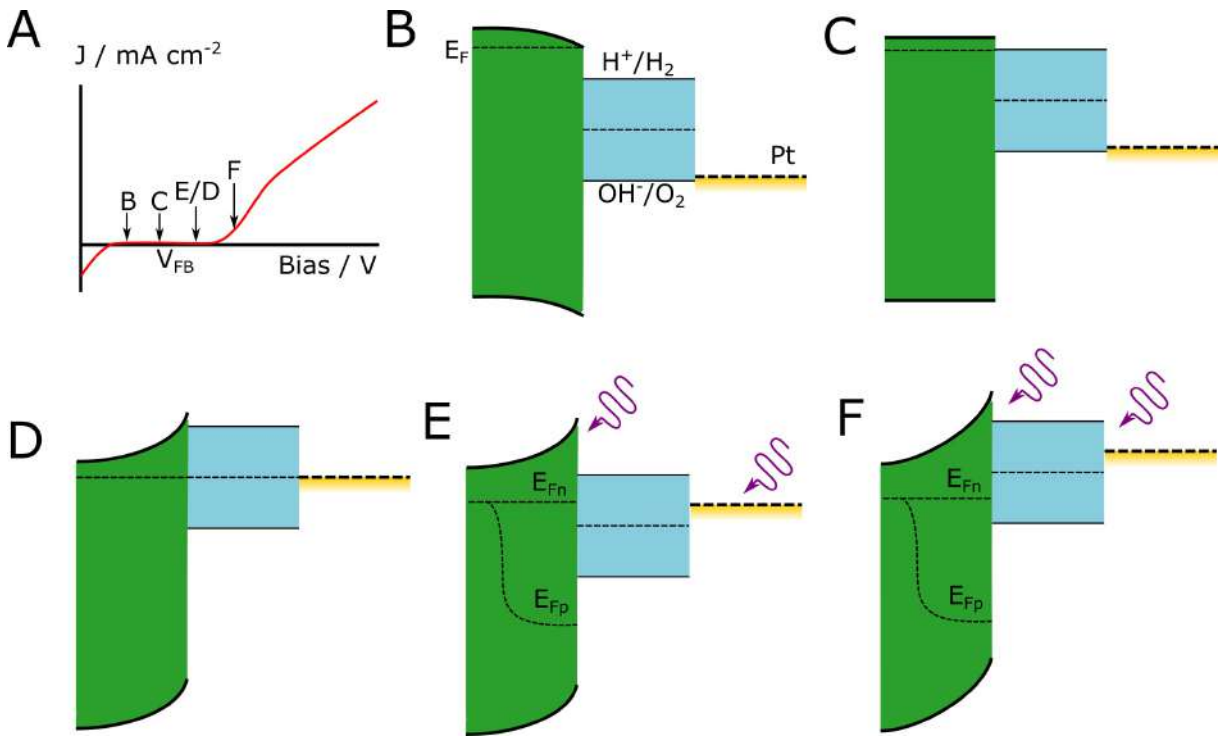


Figure 2.7: A typical water splitting LSV is displayed in A), with points on the curve describing different potentials B-F. In B), the potential vs counter electrode is negative, downwards band bending prevents charge transfer to the solution. In C) the flat band condition is achieved at a slightly less negative potential. In D) the potential is equal to zero with in the dark, whereas E) shares the same voltage with illumination. Finally F) shows a positive potential where its favourable for electron injection at the counter electrode, and oxidation at the photoanode.

the raising of this level is sufficient by illumination to favour electron injection at the cathode, or if the solution redox potentials are lowered by base, the reaction can begin unbiased. In this example, this is not the case, and further bias is required to begin the reaction yielding photocurrent Figure 2.7F. Photo generated holes are injected at the photoanode according to their quasi $E_F$, evolving oxygen; electrons are injected at the cathode reducing hydrogen.[275]

Other potentiostatic measurements include chronoamperometry and IPCE. In both cases the potential is fixed at 1.23 $V_{RHE}$ for watersplitting anodes and 0 V short circuit condition for PV cells. In chronoamperometry the output current is measured over time, measuring the degradation of the material. IPCE allows the measurement of the external quantum efficiency (EQE) of the anode or device.[119] Differing in set up from usual IV measurement, a monochromatic beam of photons is required, as well as a more powerful 300 W xenon lamp. This is due to the optical losses incurred through the monochromator, whilst still integrating to the calibrated total power of 100 $\mathrm{mW\,cm^{-1}}$ over all wavelengths. The optical power at each wavelength is measured with a silicon diode photodiode detector; allowing the calculation of photon number. The output current measures the flux of photogenerated electrons.[277]

$$EQE = \frac{\Phi_e}{\Phi_\gamma} = \frac{J/e}{I_\gamma/h\nu} \tag{2.13}$$

Where $\Phi_e$ and $\Phi_\gamma$ are the electron and photon flux respectively; $J$ is the generated photocurrent; $e$ is electron charge; $I_\gamma$ is the optical power and $h\nu$ is the photon energy at that wavelength. Due to the presence of dark current in the PEC setup, each measured photocurrent at particular wavelength is subtracted by the current when the light source is blocked.

### 2.4.2 Electrical Impedance Spectroscopy

Electrical Impedance Spectroscopy (EIS) is a powerful tool used to probe the interface between electrolytes and semiconductors. This technique utilises the properties of RC circuits by in-

troducing a sinusoidal AC potential perturbation imposed on a DC bias. Depending on the required information, this can involve varying the angular frequency of the sine wave $\omega$, yielding impedance information plotted as Nyquist. Alternately, fixing the frequency whilst altering the DC bias gives rise to Mott-Schottky plots of capacitance vs potential. These spectra rely on the capacitive and resistive nature of the junction interfaces. Such as the space / charge region in a semiconductor, the Helmholtz layer or the diffuse layer in electrolytes. These regions act as leaky capacitors: Storing charge on parallel plates, while Faradaic processes transfer electrons through the gap.[278]

Ohm's law applied to periodically varying potential gives rise to complex impedance; described either by magnitude and phase angle, or real and imaginary components. The relation between capacitance C and the magnitude of Impedance $|Z|$ is given by the equation

$$|Z| = \frac{1}{j\omega C} \tag{2.14}$$

where $\omega$ denotes the angular frequency of the oscillating circuit. Mapping the capacitance of the space charge region $C_{sc}$ vs DC potential yields Mott-Schottky plots which give information such as flat band potential, number density of donors and charge layer width.[223]

$$\frac{1}{C_{sc}^2} = \frac{2}{e\epsilon\epsilon_0 A^2(N_d - N_a)}\Delta\phi_{sc} \tag{2.15}$$

Where balanced number of holes and electrons would lead to a vertical undefined gradient indicating an undoped, intrinsic semiconductor. The inverse of the gradient can be used to quantitatively measure the extent or type of doping. This can be converted to the common summary value $N_D = N_d - N_a$ where $N_D$ is described as dopant density. Positive or negative gradients in the linear region indicate n or p type doping respectively. Note that the factor of $A^2$ in the denominator corresponds to the electrode surface area.[223,279]

The value of $\Delta\phi_{sc}$, the potential across the charge layer is defined by the following equation

$$\Delta\phi_{sc} = V_E - V_{FB} - \frac{kT}{e} \tag{2.16}$$

Where $kT/e$ is in the order of thermal energies ($\sim 0.025$ V) and it is therefore neglected. The $V_{FB}$ is the flat band potential; the potential at which there is no band bending due to charge depletion. $V_E$ is the potential bias cycled through in order to produce the Mott-Schottky plot and move the conduction and valence bands with respect to the counter electrode.[223]

Even more useful information is obtained by varying frequency at a fixed potential and plotting real vs imaginary resistance in a Nyquist plot. By fitting the plot with a lumped equivalent circuit, such as Randle's circuit Figure 2.8A, key physical values such as chemical capacitance, $C_\mu$, charge transfer resistance $R_{ct}$ and series resistance $R_s$ can be determined.[280] Features of this model are identified by their shape and the frequency at which they occur in the plot, right. The typical arc most commonly seen is due to $C_\mu$ in parallel with $R_{ct}$, defining the frequency range and the arc radius respectively. $R_s$ Simply transforms the spectrum along the real axis. Linear regions are either assigned as constant phase elements, or diffusion regions when the angle is similar to 45°. Such a feature in the low frequency end is assigned to the Waburg impedance $Z_W$, due to ionic diffusion in the electrolyte.

This feature in the high frequency zone can be assigned to solid state diffusion of electrons moving through a nanocrystalline solid.[281] Such a feature would lend itself to description using the transmission line model, Figure 2.8B. This allows the determination of key material parameters by decoupling transport and charge transfer properties. The model works by assuming a semi-infinite series of small transport resistances, $r_T$, representing the trap limited diffusion of electrons through a nanocrystal matrix. This is mirrored by parallel recombination elements occuring at the solid / liquid interface, $r_R$ reaction resistance, and chemical capacitance $c_\mu$, responsible for the typical arc in the Nyquist plot. When incorporating the geometric properties

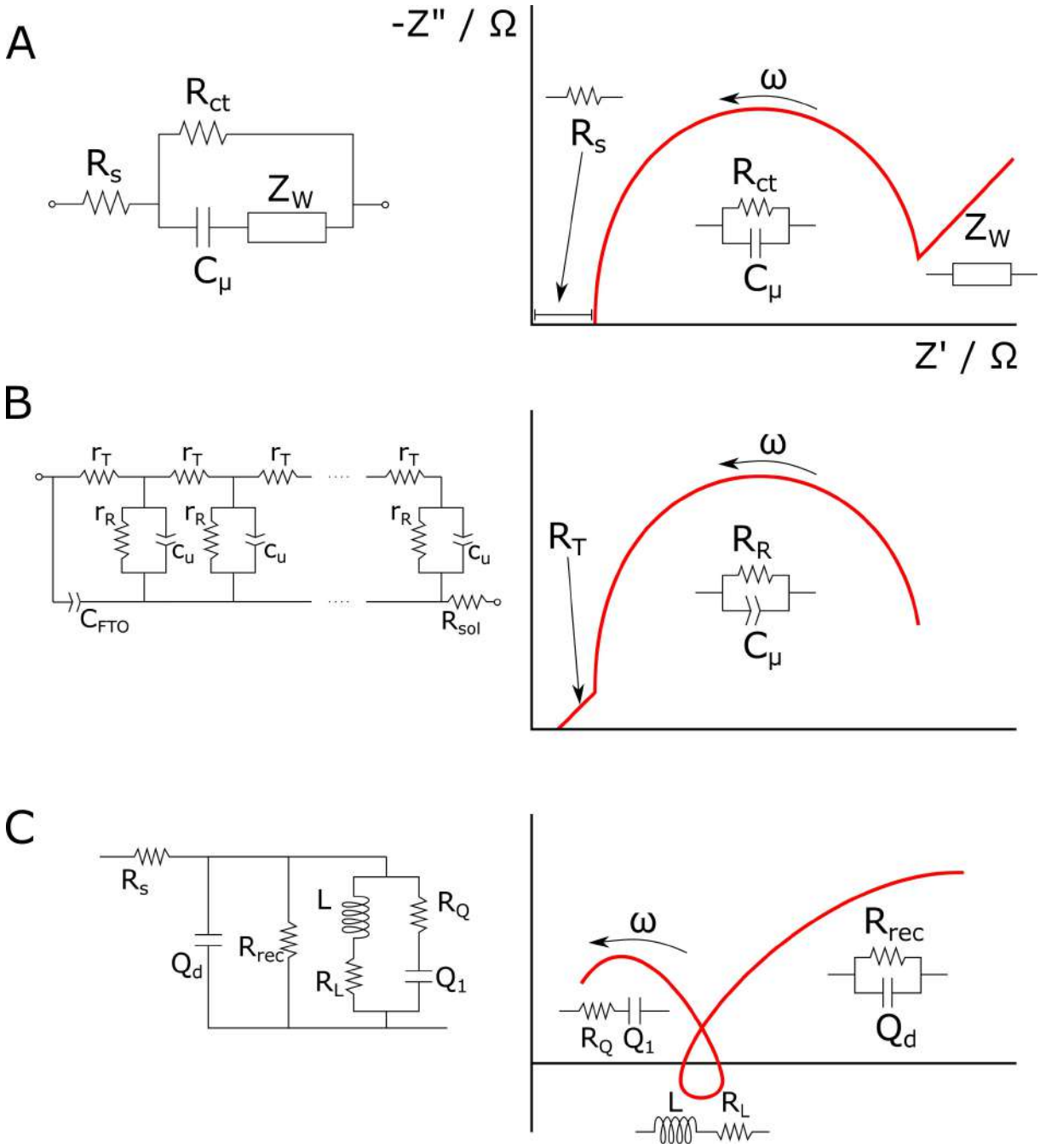


Figure 2.8: A) shows a typical Randle's equivalent circuit left, alongside the expected Nyquist plot right. B) shows the transmission line model alongside its expected spectrum. C) shows the surface polarisation model applied to perovskite solar cells.

of the structures determined by SEM, This series of elements follow the following equation.[282]

$$Z = \left[\frac{R_T R_R}{1 + (i\omega/\omega_R)^\beta}\right]^{1/2} coth((\omega_R/\omega_T)^{\beta/2}[1 + (i\omega/\omega_R)^\beta]^{1/2}) \tag{2.17}$$

The impedance $Z$ depends on the AC frequency $\omega$, constant phase element exponent $\beta$ and two more characteristic frequencies, transport $\omega_T$ and reaction $\omega_R$.

$$\omega_T = \frac{1}{(R_T C_\mu)^{1/\beta}} \tag{2.18}$$

Eq. 2.18 defines the former, and Eq. 2.19 the latter.

$$\omega_R = \frac{1}{(R_R C_\mu)^{1/\beta}} \tag{2.19}$$

The values $R_T = L \times r_T$ where $L$ is the nanorod length; $C_\mu = L \times c_\mu$ and $R_R = r_R/L$ define the two different regions of the Nyquist plot as labelled.

The connotations vary greatly whether the system is biased or illuminated. For example a forward biased dark solar cell would give a recombination resistance instead of a charge transfer resistance as the system is geared toward diodic electron injection. Such solid state perovskite systems can even give rise to exotic features such as negative capacitance and inductors.[283] The surface polarisation model effectively describes the unusual features, Figure 2.8C. These effects occur due to the migration of halide ions through the soft perovskite bulk, to the counter electrode as well as grain boundaries. Meanwhile immobile cation vacancies sit at their absences, also explaining the common current voltage hysteresis observed in the cells.[284] The inductance resistance series feature defined by $L$ and $R_L$ allow the calculation of a kinetic relaxation constant for the mobile ions; while recombination resistance $R_{rec}$ provides the recombination current. Such versatility and breadth of application is encountered through the course of this work.

# Chapter 3

# Defect-Rich ZnO Nanorod Arrays for Efficient Solar Water Splitting

## 3.1 Abstract

A novel ultra rapid synthetic method for the production of vertically aligned ZnO nanorod (NR) arrays has been demonstrated, using a microwave assisted chemical bath deposition method. High quality NR arrays with controllable film thickness were achieved with fine control of the growth conditions. A fast growth rate averaging 0.9 $\mu\mathrm{m\,h^{-1}}$ was achieved in comparison to 0.1 $\mu\mathrm{m\,h^{-1}}$ from the conventional chemical bath deposition. The MW synthesised NRs have a high level of n-type doping, which confers excellent photoelectrochemical performance. In comparison with the typical chemical bath deposition synthesised NRs, the ultra-fast MW synthesised NRs offer 3 times more efficient PEC water splitting. The population densities and electronic states of these defects were monitored using photoluminescence spectroscopy and electrical impedance spectroscopy. The dopant level was further controlled by thermal annealing in air and an optimised density of $1.68 \times 10^{19}\ \mathrm{cm^{-3}}$ was achieved after annealing at 500°C. This in turn led to a twofold increase in PEC efficiency to 0.31% with a photocurrent density of 0.705 $\mathrm{mA\,cm^{-1}}$ at 1.23 V vs RHE, which is one of the best performances from similar ZnO NR structures.

## 3.2 Introduction

The ambitious targets set in the landmark Paris Agreement in 2015 call for an increased push for renewable alternatives to fossil fuels in order to limit global warming to 2°C.[285] Recently, the 48th session of the Intergovernmental Panel on Climate Change (IPCC-48) recognised that it is still possible to achieve this target, although it requires unprecedented technology transitions within the next decade.[1] Photoelectrochemical (PEC) water splitting has been researched extensively for efficient harvesting of solar energy in $H_2$ gas.[24,32,241] A number of nanostructured metal oxide semiconductors, such as $TiO_2$ and ZnO, are suitable for this application, due to their wide band gap and stability in water.[286,287] A higher electron mobility of 205 $\mathrm{cm^2\,V^{-1}\,s}$ and longer minority carrier diffusion length give ZnO the advantage over $TiO_2$.[124] Much literature has been published employing a number of different strategies to enhance the photoconversion efficiency through doping,[100,145,288] sensitising,[141,289,290] and plasmonic enhancement.[291,292] For examples, Cu, V and N doped ZnO nanorods have shown significant enhancement in either UV or visible light sensitivity.[288,293,294] One of the most promising ZnO structures, vertically aligned nanorod arrays (NRs), offer large surface area and effective charge transport. However, ZnO NR arrays are synthesised slowly, at a typical growth rate of 0.1-0.5 $\mu\mathrm{m\,h^{-1}}$, through either chemical bath deposition CBD, hydrothermal method or chemical vapour deposition.[295–297] Both the CBD method used by Meng Wang *et al.*[294] and the hydrothermal synthesis by Chenglong Zhang *et al.*[293] and Li Cai *et al.*[288] take as long as 24 hours.

Metal oxide nanowires are highly effective materials for solar water splitting.[37] ZnO nanowires provide the basis for highly efficient photoanodes, especially those sensitised with visible light absorbing materials such as CdS and $ZnFe_2O_4$.[298] Therefore improving the pure ZnO properties, as achieved in this work, has the potential to impact a wide field of junction applications.

Here we report for the first time an Ultra Rapid Microwave Assisted Deposition (URMAD)

of vertically aligned ZnO NR arrays applied as a photoanode for the photolysis of water. This method uses the synergy of efficient microwave (MW) dipole heating and conductive heating of the system. Not only were NRs grown in a fraction of the time compared to conventional methods, the synthesis led to high density of surface defects with increased n-type doping. Consequently, the MW NRs showed a great increase in photoconversion efficiency for water splitting compared to the CBD sample.

Producing nanostructures using microwave (MW) heating has drawn recent attention in the literature due to rapid, efficient and uniform dipole heating in aqueous solution.[299–301] The challenge of this rapid method is to control the morphology and the uniformity of the NR crystals. Microwave assisted synthetic methods have been applied to a number of ZnO nanostructures.[302–306] Vertically aligned ZnO NR arrays have appeared recently in the literature with limited control of morphology. They were used as a photocatalyst or in a gas ionization sensor.[135,307] In both cases enhanced electronic properties were observed and this was attributed to increased oxygen vacancies from rapid crystallisation.

Oxygen vacancies ($V_O$) and zinc interstitials ($Zn_i$) are often suggested to be responsible for n-type doping in ZnO and its photocatalytic activity.[135,308] However, acceptor defects, such as zinc vacancies ($V_{Zn}$ ) contribute to p-type doping.[309,310] An appropriate n-type doping with very little p-type doping gives higher water splitting ability due to faster charge transfer to the electrolyte.[311] On the other hand, the p-type defects can have a significant negative impact due to a shift of the flat-band potential towards the valence band. In this work, the abundance of individual crystal defects are quantitatively analysed using photoluminescence (PL) spectroscopy and electrical impedance spectroscopy (EIS) measurements. This allowed greater control of the doping through annealing at a range of temperatures in air, yielding a significantly higher PEC efficiency at 500°C.

In this paper, a novel ultra rapid MW assisted chemical bath deposition method for the

growth of ZnO NR arrays is presented and their solar water splitting ability is compared to a conventional CBD method. The NR arrays show high density of native defects, which is responsible for the increase in PCE conversion efficiency over the conventional CBD NRs by a factor of 3. The populations of these defects were then controlled using thermal annealing in air at various temperatures to double the efficiency achieved. This yielded a photocurrent density of 0.893 $\mathrm{mA\,cm^{-2}}$ at 1 V potential bias vs KCl saturated Ag/AgCl reference electrode.

## 3.3 Experimental Method

### 3.3.1 Synthesis of Nanorods

All chemicals used were purchased from Sigma Aldrich with no further purification. Transparent conductive Fluorine-doped Tin Oxide (FTO) sheet glass was used as the substrate, cut into sample sizes of $1 \times 3\ \mathrm{cm^2}$. The substrate was cleaned by sonication successively in acetone, isopropanol then deionised (DI) water, for 20 minutes each, followed by drying in air. The seeding solution was prepared by dissolving 0.219 g zinc acetate and 0.6 g polyvinyl alcohol (PVA) for increased viscosity in 10 ml of DI water. The seeding solution was spin coated on the FTO glass for 3 minutes at 500 RPM. After this, the substrate was annealed in air for 20 minutes at 500°C to convert the zinc acetate into zinc oxide nano seeds.[99]

In the URMAD method, the seeded substrate was placed in a 35 ml microwave vessel with 20 ml growth solution, 1:1 hexamethylnetetramine (HMT) and zinc nitrate $Zn(NO_3)_2$ at a concentration of 40 mM. The microwave (Discover SP, CEM) was set to 100°C for 30 minutes at a power of 100 W, no stirring was used to avoid disturbing the crystal growth. The process was repeated four times (total 2 hours) for film thickness of around 2 $\mu\mathrm{m}$. Following growth, all samples were rinsed with DI water. Annealing in air was performed using a tube furnace for 30 minutes at 300°C, 400°C, 500°C and 550°C to optimise crystal defect concentration. For comparison, a previously developed CBD technique was also used.[99] To achieve similar 2 $\mu\mathrm{m}$

NRs in CBD, the seeded substrate was placed in a beaker with 100 ml growth solution at 90°C for 16 hours.

### 3.3.2 Structural and Physical Characterization

The cross sectional and surface morphologies were observed using scanning electron microscopy (SEM, JSM820M, Jeol). The nanorod length and diameters were measured from SEM images using Image J software (National Institutes of Health, USA). The crystallinity and structural orientation of the nanostructures were analysed by powder x-ray diffractometer (XRD, Siemens D500). The reaction temperatures were recorded by FLIR ONE thermal camera and processed via the corresponding Android application; an attenuator was fixed to the microwave allowing the direct imaging inside.

### 3.3.3 Water Splitting and Optoelectronic Measurement

PEC water splitting performances were measured using a standard 3 electrode set up. A KCl saturated Ag/AgCl electrode was used as the reference and platinum foil was used as the counter electrode. ZnO NR arrays grown on FTO-glass substrate were used as the photoanode. A potentiostat (EA163, eDAQ) was used to control the voltage bias and to measure the photocurrent. The voltage was scanned from -0.6 to 1.2 V and the electrolyte used in the PEC cell was 0.5 M $Na_2SO_4$. No additional scavenging chemical was added to the electrolyte. A calibrated 100 $\mathrm{mW\,cm^{-2}}$ solar simulator (Oriel LCS-100, Newport) with built-in AM 1.5 G filter used as the light source. The photoabsorption spectra used to calculate the band gap with Tauc plots were examined using a UV-Vis spectrophotometer (Thermospectronic UV 300) and the crystal defects were characterised using PL spectra recorded with a fluorescence spectrometer (Perkin Elmer LS 45). Finally EIS measurements were performed using an electrochemical controller (Palm Sens 3, PalmSens BV). Nyquist (illuminated) and Mott-Schottky (dark) plots were pro-

cessed using PSTrace 4.5 (PalmSens BV).

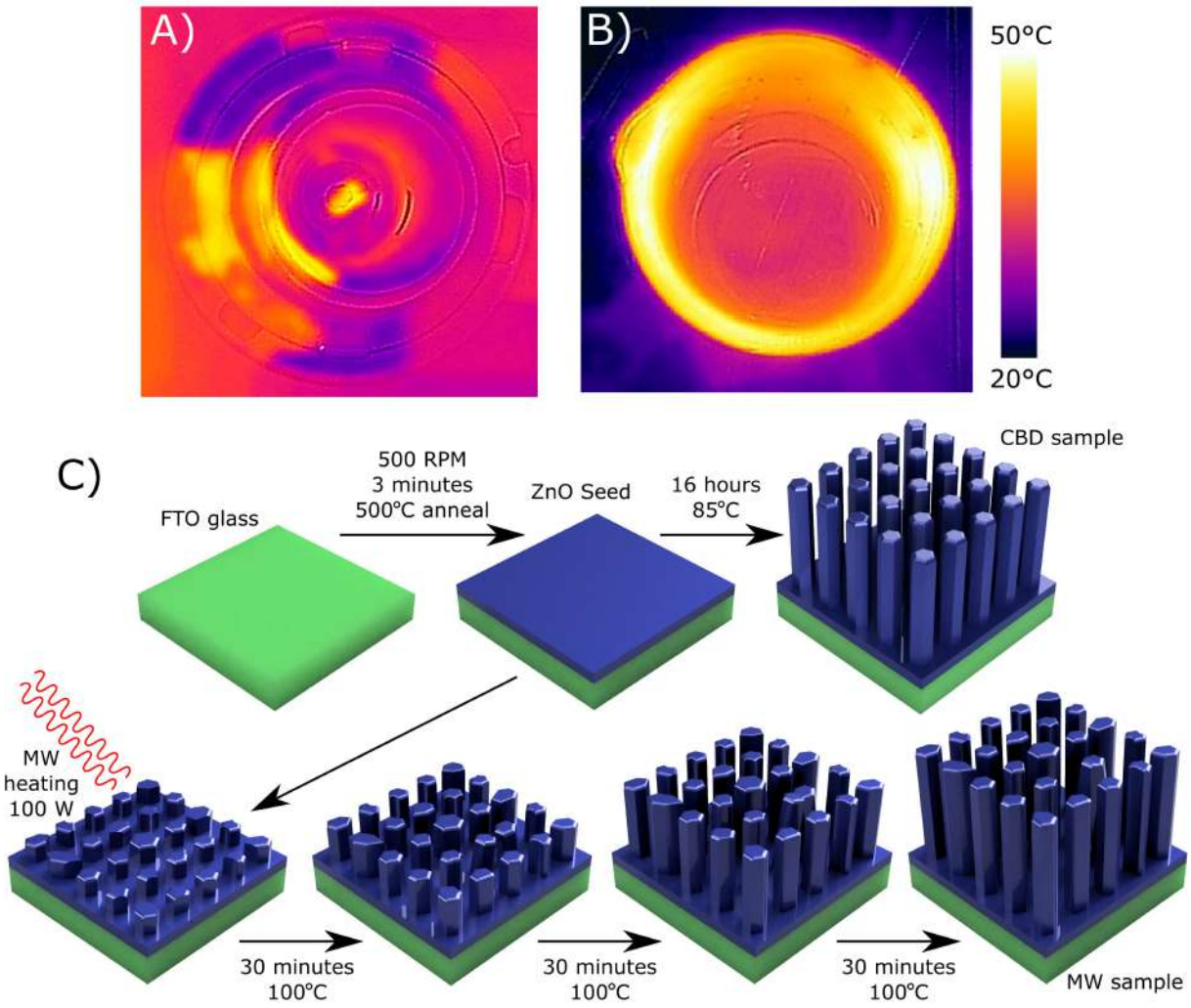


Figure 1

Figure 3.1: Thermal images of the solutions in A) the MW and B) the CBD processes with an FTO-glass inside. C) A schematic diagram shows both the CBD and URMAD methods.

## 3.4 Results and Discussion

### 3.4.1 Morphology and Crystal Structure of URMAD Synthesised Nanorods

A clear benefit from the novel MW synthetic method is the efficient delivery of heat into the growth solution. The thermal image in the MW heating process, Figure 3.1A, indicates the peak temperature is located in the aqueous solution near the FTO substrate. This suggests that the MW energy is delivered directly to the aqueous solution via dielectric heating, and the presence of conductive FTO glass also contributes by resistive heating, from physical movement of charge polarised by the MW. In contrast, with the conventionally heated CBD method, Figure 3.1B, heat was transferred through the glass vessel resulting in less effective heating of the reaction solution. If the difference between conventional CBD and our URMAD is only limited to the heat transfer rate, one would not expect significant difference in the growth kinetics as we observed here. This confirms that the FTO layer behaves as an antenna which focuses the MW energy, resulting in the rapid growth using the microwave.

A high surface area photoanode is important for highly efficient PEC water splitting, which allows faster Faradaic charge transfer from semiconductor to electrolyte. Figure 3.2 shows the uniform hexagonal wurtzite crystal morphology of the NRs synthesised from the URMAD method. The average diameter of the NRs was determined to be $138 \pm 22$ nm comparable to the NRs synthesised using conventional CBD method (Figure S3.1). A small fraction of the rods appears irregular in shape, occurring from the coalescing of rods due to their rapid growth rate. The vertical growth of the rods can be seen in the cross-section SEM image in Figure 3.2B with a thickness of 1.85 $\mu\mathrm{m}$ after total of 2 hours growth. The average growth rate is 0.93 $\mu\mathrm{m\,h^{-1}}$, which is about 9 times faster than the conventional CBD method.

The ability to grow long ZnO NRs in a fraction of the time while maintaining the good quality morphology of conventional growth is important to their future use in solar energy. The

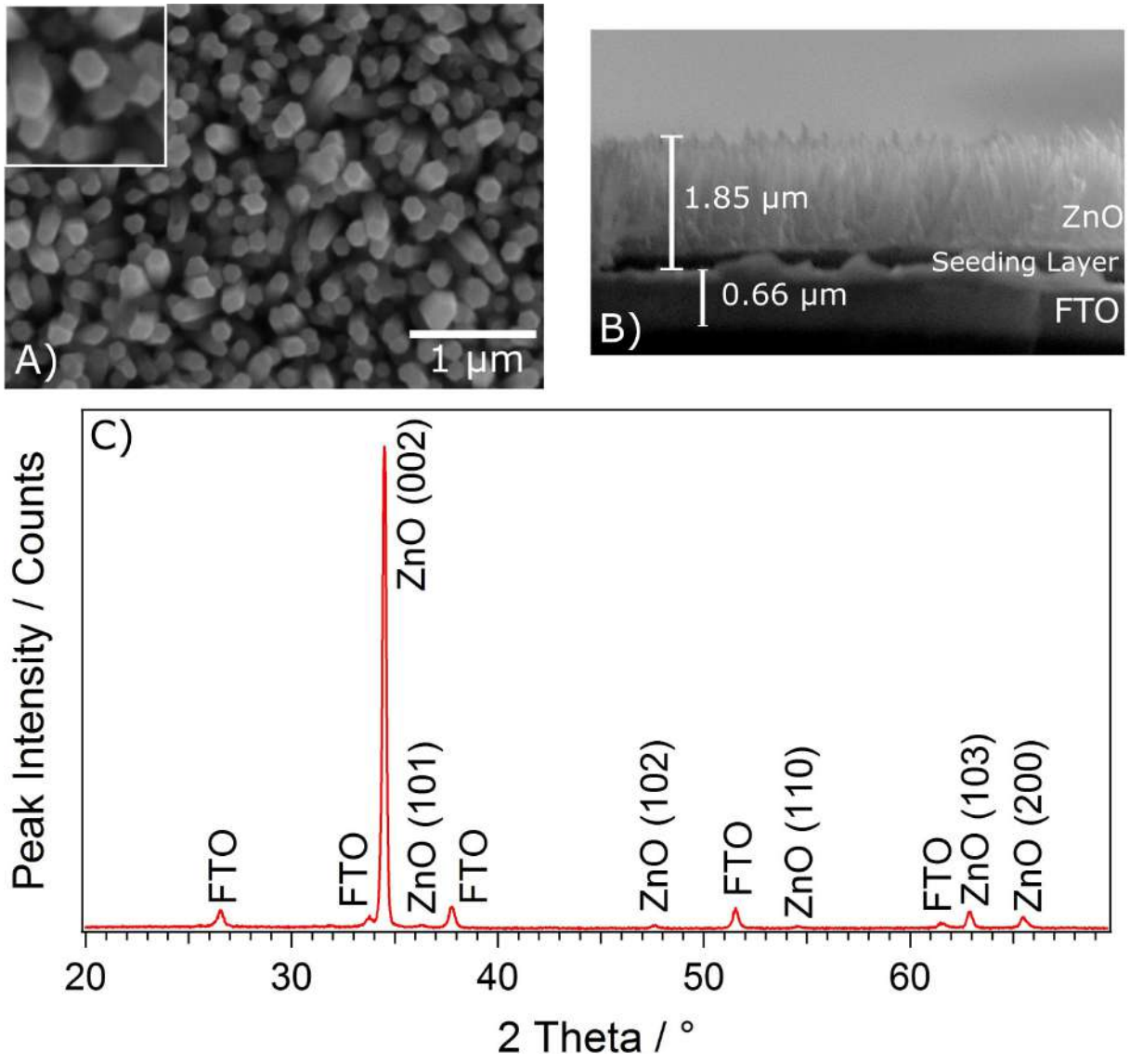


Figure 3.2: The top down and cross-sectional SEM images of the MW NRs can be seen in A) and B) respectively. The inset in A) shows the zoomed top view image. C) shows the XRD of the MW rods.

vertically aligned growth of the wurtzite crystal structure is also evidenced with XRD, shown in Figure 3.2C. The pattern was indexed according to the standard database crystal patterns for wurtzite ZnO (JCPDS 36-1451). The dominant (002) peak confirms that the majority of these crystal planes are parallel to the substrate with a strong vertical alignment in the $c$ axis.

### 3.4.2 PEC water splitting performance

The rapid growth rate in the URMAD process leads to high density of defects in the ZnO NRs and appropriate concentration of defects could enhance the PEC performance. Evidence for the high density defects of the MW NRs can be analysed from the full width half maxima (FWHM) of the main (002) X-ray diffraction peaks, which is inversely proportional to the crystal domain size following the Scherrer equation.[312]

The high resolution (002) XRD peaks are displayed in Figure S3.2. The measured peak widths from the CBD and URMAD NRs, as well as the samples annealed at different temperatures are presented in Figure 3.3A. The CBD sample has the smallest diffraction peak width of 0.18° and the synthesized MW sample has the largest peak width of 0.22° inferring either smallest crystal domain size or highest density of crystal defects. Thus, one could expect that the URMAD samples will have a relatively high density of defects in the form of oxygen vacancies ($V_O$) and zinc interstitials ($Zn_i$). Annealing the MW sample in air at different temperatures will affect the defect density of the NRs. A systematic reduction of peak width can be observed when the sample is thermally annealed at temperatures above 400°C. Under such conditions, both the densities of $V_O$ and $Zn_i$ at the NR surfaces were significantly reduced by the reaction with hot air.

Alongside peak width reduction there was also a systematic shift in peak position (Figure S3.2) corresponding to a decrease in crystal lattice spacing. The calculated c-axis lattice constants for different samples are also shown in Figure 3.3A. High density of defects can lead

to increased spacing as interstitial atoms and charged vacancies deform the lattice. The MW sample displays the largest c axis spacing at 5.206 Å, compared with 5.200 Å in the CBD sample likely due to this effect. This spacing is reduced with the temperature of annealing following a similar trend to FWHM, confirming the effect of defect population.

The direct electronic band gap energies, $E_g$, of the ZnO NR arrays are also correlated to the density of defects. Native defects acting as dopants introduce new states into the electronic band structure of materials, if these states lie within the band gap of semiconductors it can lead to an effective reduction in band gap energy.[313] The values of $E_g$ displayed in Figure 3.3B, were determined using UV-Vis absorption spectroscopy and Tauc plots (Figure S3.3).[261] For the MW sample, the band gap energy was 3.19 eV, which is a significant red shift from the 3.28 eV for the CBD sample in association with the high defect density. Such a decrease would allow the ZnO to absorb the leading edge of the visible spectrum which enhances its photocatalytic activity.[100] The effect of thermal annealing on the MW NRs is as expected, increasing the band gap energy approaching the $E_g$ of the CBD sample as $V_O$ and $Zn_i$ are reduced during the annealing process.[30]

The photocatalytic activity of the URMAD ZnO NRs with a high density of defects was investigated in PEC water splitting. In comparison with low defect density CBD NRs, a much higher PEC water splitting activity was observed from the URMAD NRs, shown in Figure 3.3C and D. At a potential bias of 1.23 $V_{RHE}$, the photocurrent of 0.420 $\mathrm{mA\,cm^{-1}}$ was achieved from the MW samples with respect to the 0.140 $\mathrm{mA\,cm^{-1}}$ from the CBD sample, although both have almost identical nanostructures. This was then further improved to 0.705 $\mathrm{mA\,cm^{-1}}$ by thermal annealing at 500°C. Careful analysis of the effects of annealing temperature reveals a monotonic increasing in the photocurrent from 300 to 500°C, at which the maximum photocurrent was achieved. Further increasing the annealing temperature to 550°C, the photocurrent decreased to 0.601 $\mathrm{mA\,cm^{-1}}$. This is likely due to the optimisation of conductivity from higher

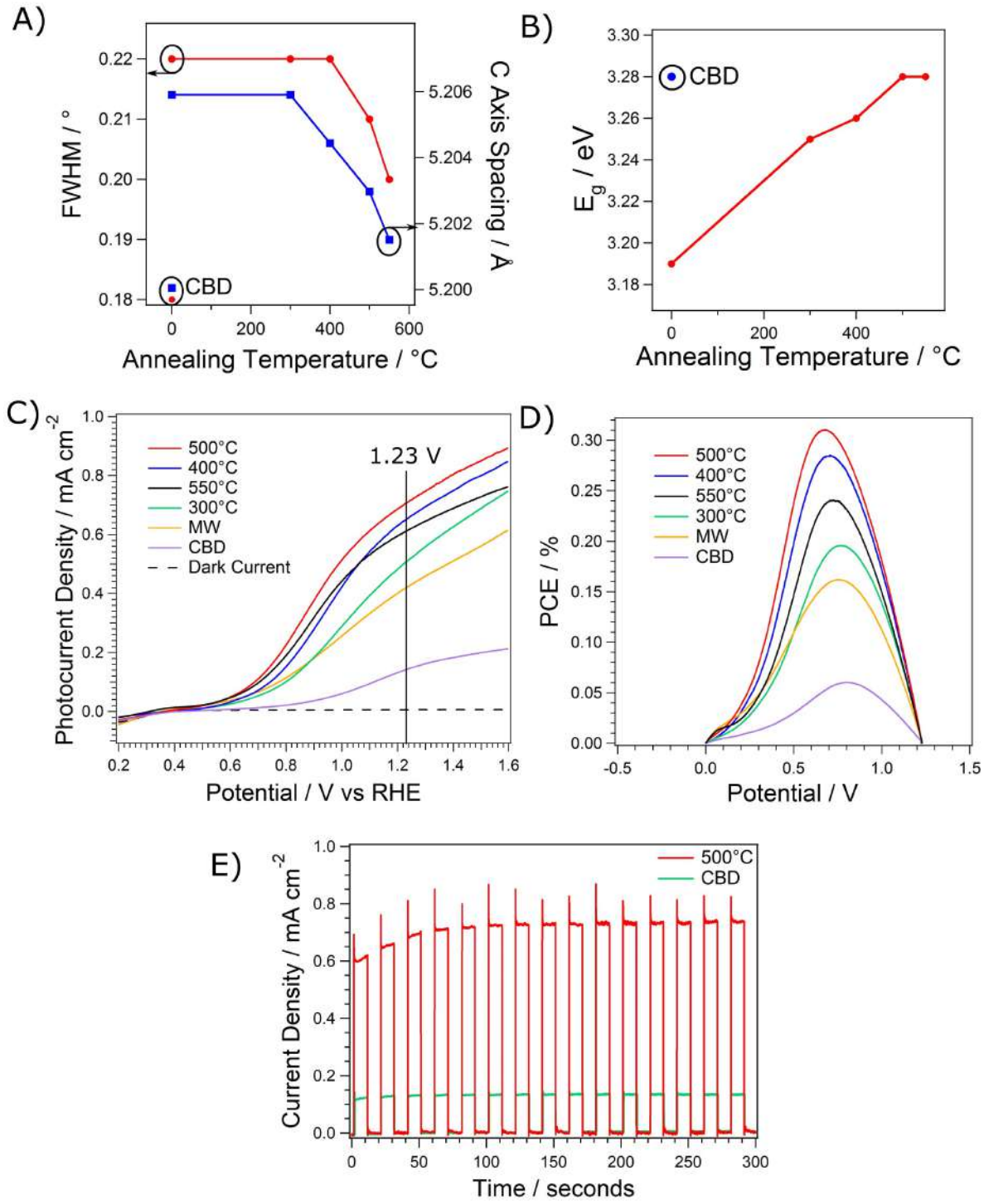


Figure 3.3: A) Displays the FWHM of (002) ZnO wurtzite peak of the samples against annealing temperature, along with lattice parameter c. B) Shows the evolution of band gap energy with annealing temperature. Water splitting data showing C) photocurrent densities and D) photoconversion efficiency curves. E) Shows the time dependent photocurrent for CBD and MW samples measured at 1.23 VRHE.

dopant density, versus the negative effect of high electron hole recombination, after annealing at 500°C transportation properties are still improved while recombination is possibly reduced in comparison to the unannealed sample. The achieved photocurrent from the MW NRs is also greater than the reported Na doped ZnO NRs of 0.480 $\mathrm{mA\,cm^{-1}}$ at 1.23 $V_{RHE}$.[100] Similar but lower photocurrent (0.600 $\mathrm{mA\,cm^{-1}}$ at 1.23 $V_{RHE}$) was achieved from the hydrothermal synthesised ZnO NRs by Baek *et al.*[113] Their synthetic process took 12 hours and their sample was annealed at 700°C under vacuum which could increase the defect density of the ZnO NRs significantly. To prove the current is contributed from the photoexcitation process, the light chopped I-V curves for the as synthesised MW sample, the annealed MW sample and the CBD sample are demonstrated in Figure S3.4.

The corresponding photoconversion efficiencies were plotted in Figure 3.3D. A similar trend can be found as the photocurrent and best photoconversion performance was achieved from the MW sample annealed at 500°C with maximum photoconversion efficiency of 0.31%, which is 5 times higher, with respect to the value from the CBD NRs (0.06%). Annealing at 550°C leads to a decrease as too many of the n-type impurities have been lost, which reduces the electron conductivity.[132]

The chemical stability and the lifetime of the photoanode are crucial in practical application. Shown in Figure 3.3E, time dependent photocurrent was recorded for the duration of 300 seconds at a fixed positive bias of 1.23 $V_{RHE}$. For clarity, the illumination light was chopped during measurement. For both CBD and MW samples, there is no observed photocurrent decrease. This confirms the stability of the MW photoanode.

In a wider review of pristine ZnO nanostructures found in Figure S3.5, photoanode performance, measured by photocurrent density at 1.23 $V_{RHE}$, was compared to the literature. This work was found to be one of the fastest processing times compared with the prior art, only slower than one hydrothermal method46 and glancing angle electron beam deposition thin

films.[286,314] However, the water splitting photocurrents of these samples were an order of magnitude lower than ours. In fact, the PEC performance of our optimised MW ZnO NRs is among the best reported in literature.[113,119,141] Vuong *et al.* achieved a slightly higher photocurrent of $\sim$0.9 $\mathrm{mA\,cm^{-1}}$ from their hydrothermal synthesised ZnO NRs, with a special rapid scan rate of 50 $\mathrm{mV\,s^{-1}}$ (relative to 10 $\mathrm{mV\,s^{-1}}$ commonly used).[141] Nevertheless, their synthetic method is much slower than our URMAD method.

### 3.4.3 Density of Defects and their Effects on PEC Performance

A high density of defects could affect the PEC efficiency in two opposite ways, depending on their concentration, location and function. Defects in semiconductors generate additional electronic states between the band gap which can increase the dopant density of the material. The surface defects form recombination centres which trap excited charges. High density of such defects could decrease the PEC performance. Secondly, the bulk defects help to improve the electron conductivity without significant increase in charge recombination, thus enhancing the PEC performance. With a high density of recombination centres, the excited electrons and holes recombine and emit photoluminence (PL) signal. Therefore, one can use the PL signal to study the samples' relative defect density. Figure 3.3A shows the thin film PL signals from different samples, excited at 320 nm. There are 5 major PL peaks located at the wavelengths of 397, 421, 446, 486 and 528 nm. The first peak found at 397 nm corresponds to the Near Band Edge (NBE) emission,[315] defined by the band gap energy of 3.18 eV. The intensity of this peak is proportional to the natural pathway of recombination of electron hole pairs. The peak at 421 nm can be attributed to the donor level associated with $Zn_i$,[316,317] while the two peaks centred at 446 and 486 nm arise from two different electronic states of $V_O$.[124,318] Finally, the 528 nm peak is reported to originate from $V_{Zn}$, an acceptor defect.[316,319,320]

Defect density of ZnO has been controlled by changing the reactant concentration or post

annealing. Cui *et al.* controlled the defects density by altering the concentration of HMT in the growth solution.[321] Post annealing was also used to reduce surface defects in the form of hydroxyl groups which achieved great enhancement in water splitting efficiency.[113]

Furthermore, Zeng *et al.* controlled the blue defect emission attributed to $Zn_i$ defects by annealing in both air and $N_2$ environments, reducing and increasing its abundance respectively.[322] Annealing in air was therefore selected to reduce the defect density in the defect rich microwave samples in this study.

The difference in the PL emission from URMAD to CBD sample confirms the rapidly grown samples contain a high density of defects, since the CBD sample has much lower PL intensity. The coexistence of $Zn_i$, $V_O$ and $V_{Zn}$ defects, suggests that both Frenkel and Schottky defects were formed during the URMAD process. The rapid decomposition of HMT in MW will cause the fast increase of the solution pH. This results in the fast conversion of $Zn(NO_3)_2$ into $Zn(OH)_2$ and the formation of ZnO with less time to remove the crystal defects. The PL intensity was gradually reduced with thermal annealing in air up to 500°C. This suggests that the defect densities of all types, including $Zn_i$, $V_O$ and $V_{Zn}$, are significantly reduced through the diffusion and reactions starting from NR surface.[316] In particular, the population of the Frenkel defects was decreased through the annihilation of $Zn_i$ and $V_{Zn}$, while the Schottky defects were reduced by the reaction between $V_O$ and $V_{Zn}$. However, with annealing temperature reaching 550°C, the PL signal at 528 nm, assigned to the $V_{Zn}$ species increases. This can be explained in that the corresponding thermal energy at 550°C exceeds the energy barrier for dissociating the Zn-O bonding within the ZnO lattice, allowing the displacement of $Zn^{2+}$, creating $V_{Zn}$.[319] The slight increase in the 486 nm peak suggests that paired $V_O$ also formed under these conditions. Therefore, additional Schottky defects were formed at high temperature. TEM images of the CBD and URMAD synthesised ZnO nanorods are shown in Figure S3.6, where some morphological abnormalities are observed from the URMAD sample while the CBD sample shows relatively

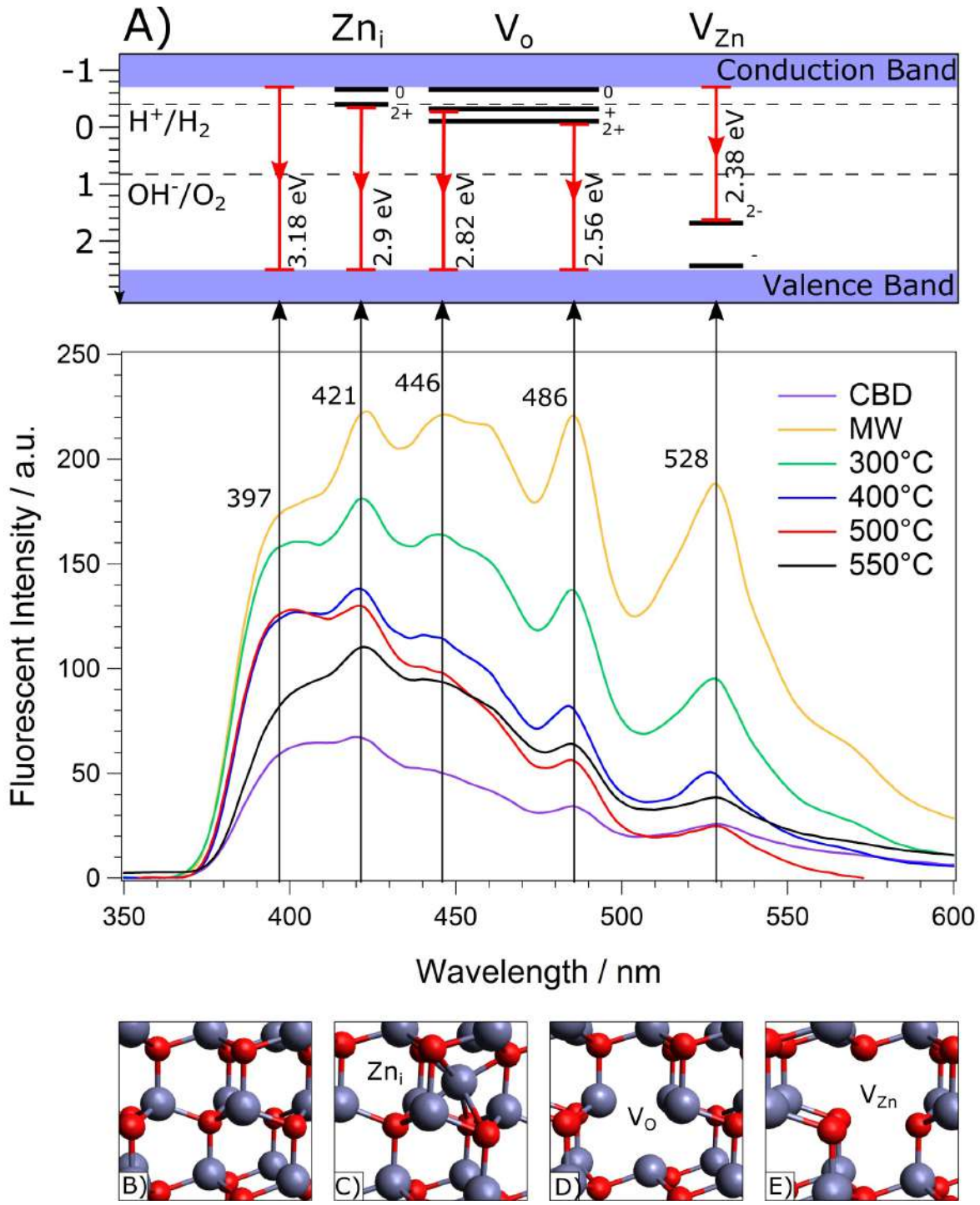


Figure 3.4: A) displays Forbidden zone band structure with electronic transitions indicated (top) and PL spectra of different samples (bottom) with peak positions in nm and C-F) diagrams of crystal defects. Transition energies have been applied as follows: 397 nm to Near Band Edge Emission;[315] 421 to $Zn_i$;[316,317] 446 and 486 to $V_O$;[124,318] and 528 to $V_{Zn}$.[316,319,320]

fewer.

EIS was recorded with a sinusoidal AC modulated (1 kHz, 10 mV) DC potential scanning from -0.6 to 0.6 V vs Ag/AgCl. The measured capacitance was used to produce Mott-Schottky (MS) plots in order to probe the flat band potential, and vitally, the density of dopants in the NR crystals. By plotting against DC bias, the key values of $N_D$, the dopant density, is determined from the inverse of the gradient of the linear section of the plot and $V_{FB}$, the flat band potential can be obtained from its intercept.[223,278] $N_D$ measures the excess concentration of n-type or p-type dopants in the sample. Greater populations of charge carriers lead to faster charge transfer and greater conductivity.

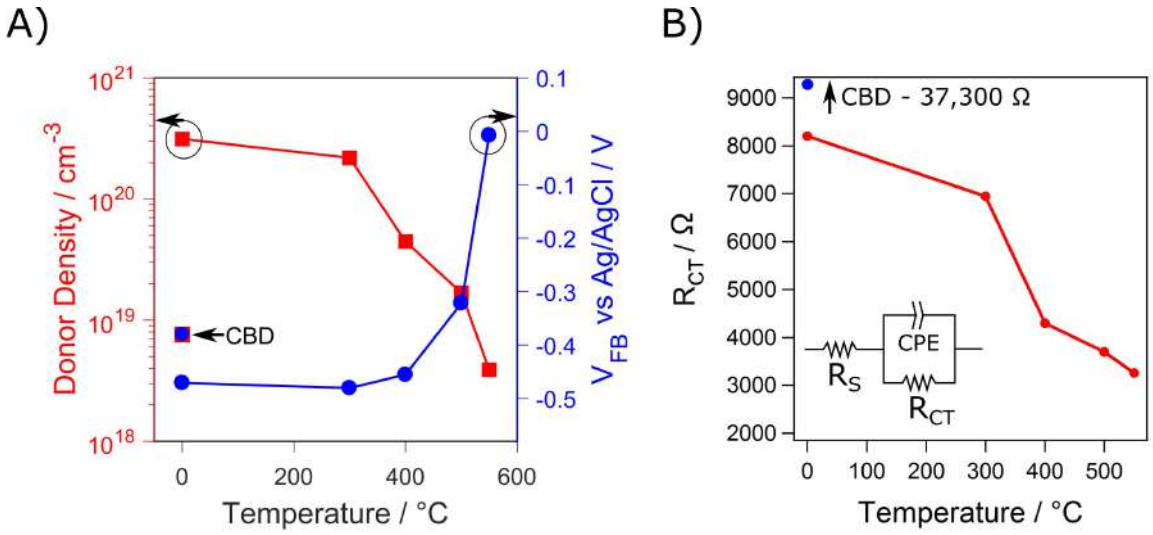


Figure 3.5: Donor density is shown on a logarithmic scale in A) with the flat band potential against annealing temperature. Charge transfer resistance, $R_{CT}$, vs annealing temperature is shown in B), inset shows Randles circuit with constant phase element (CPE), $R_{CT}$ and series resistance ($R_S$) elements.

The measured MS plots are shown in Fig. S7 and the obtained $N_D$ and $V_{FB}$ are plotted in Figure 3.5A. An increase of two orders of magnitude in n-type dopant density to 3.12 $\times$ $10^{20}$ $\mathrm{cm}^{-3}$ is observed in the MW sample compared to 7.61 $\times$ $10^{18}$ $\mathrm{cm}^{-3}$ for a CBD sample. This is directly related to the rapid synthesis of the URMAD. The associated defects are likely to be

$V_O$ and $Zn_i$, as identified in our PL measurements in Figure 3.5.

By annealing the sample from 300°C to 550°C, the dopant density of the URMAD sample is reduced monotonically, reflecting a significant reduction in n-type doping ($V_O$ and $Zn_i$) with temperature, as annealing with increased temperature in air would lead to the healing of crystal structure, also observed by PL spectroscopy. In the annealing process, the surface defects will be significantly reduced initially, since they are in direct contact with air. The reduction in the surface Frenkel defect density leads to a reduction in recombination rate, which results in improved water splitting performance up to 500°C. Annealing at 550°C led to a further reduction of net dopant density which is lower than the CBD sample; though this comparison is limited as this sample was unannealed. This could be the result of either the reduction of n-type dopant ($V_O$ and $Zn_i$), or the increase of p-type dopant ($V_{Zn}$). The PL observation confirms the later is the dominant effects for the sample annealed at 550°C. The increase in the p-type dopant ($V_{Zn}$) will trap the holes and create extra energy barriers for the transportation of surface holes to facilitate the oxidation of $H_2O$ and thus the decrease of the PEC performance.

The flat band potentials from the MS analysis are also plotted in Figure 3.5. The measured $V_{FB}$ are typical for ZnO materials, with values varying from -0.59 V to 0.03 V vs Ag/AgCl in identical electrolyte.[288,295,323] A dramatic increase in $V_{FB}$ is observed due to the reduction of n-type dopants in the ZnO NRs during the annealing process. With a reduction in n-type doping, the flat band potential descends towards the valence band.[223,237] Similar effects have been explained by the Moss-Burstein relation.[38,324,325] The significant shift of the $V_{FB}$ for the 550°C annealed sample is due to the population increase in $V_{Zn}$, an acceptor impurity, increasing the p-type doping in the sample. Such upper shift of the $V_{FB}$ will significantly reduce the reduction power of the photoexcited electrons in the conduction band, resulting in the limitation of the PEC performance.

The URMAD synthesised samples have a high density of donor defects, which are respon-

sible for charge trapping and electron-hole recombination. Annealing the samples at mild temperature reduces the donor concentration and improves the PEC performance. However, by annealing the sample at high temperature, the concentration of acceptor starts to increase. Such acceptors, in the form of $V_{Zn}$, can trap holes in the valence band and reduce the reduction potential of the excited electrons in the conduction band due to the increase in the $V_{FB}$. Our experiment shows that the optimum condition is to anneal the URMAD sample at 500°C yielding optimum dopant density of $1.68 \times 10^{19}$ $\mathrm{cm}^3$, retaining over double the value of the CBD sample. Furthermore, as the annealing was performed in a tube furnace at temperature with no sample ramping, followed by rapid cooling, there is an inherent surface bias to the healing of defects. This could protect defects in the bulk, retaining enhanced transport, while reducing electron hole recombination at the sample surface. It is clear, that any existence of accepters in the ZnO will significantly reduce the PEC performance.

Varying the AC frequency from 10 kHz to 0.1 Hz at a constant voltage bias of 0 V vs Ag/AgCl under illuminated conditions allowed the interface resistance and charge recombination rate of the samples to be analysed. The result is displayed in a Nyquist plot of imaginary vs real impedance Figure S3.8. In order to determine the critical value of charge transfer resistance, $R_{CT}$, the Nyquist plot is fitted with a standard Randles circuit model.[167] As there are no distinct frequency regions in the Nyquist plot, the values of $R_{CT}$ represent resistance at the liquid/solid interface as the resistance in the bulk semiconductor is far lower in comparison.[282] A lower $R_{CT}$ indicates less resistance for charge moving via faradaic charge transfer through this junction resulting a rapid charge transfer or lower recombination resistance at the junction.[326] In Figure 3.5B, $R_{CT}$ is plotted against annealing temperature with a stark difference from 37.3 $\mathrm{k}\Omega$ for the CBD sample to 8.2 $\mathrm{k}\Omega$ for the MW sample. This explains the PEC performance increase in the MW sample as charges are more efficiently transferred at the electrolyte-ZnO interface.

The $R_{CT}$ values decrease monotonically with annealing temperature. This is likely due to the

healing of surface defects, evidenced by PL measurement and MS analysis, despite a potential coincidence as the techniques requiring very different conditions. This would systematically reduce the recombination resistance at this junction as less charge is lost and more is transferred, further explaining the increase in solar water splitting efficiency. Despite the loss of $V_O$ and $Zn_i$ at the surface, many of the bulk defects remain providing good conductivity. At 550°C, despite the lowest $R_{CT}$, the addition of p-type Schottky doping becomes the dominant factor for the decreasing in PEC performance, as the flat band potential shifts towards the valence band.

## 3.5 Conclusion

We demonstrate a novel ultra rapid microwave assisted synthetic method for the production of ZnO NR arrays. For the first time MW ZnO NR arrays are applied to PEC water splitting with significantly high efficiency. The inclusion of a high population of crystal defects has led to an increase in n-type doping and a significant enhancement in water splitting. The most likely defects responsible are $Zn_i$ and $V_O$ determined by the PL measurements. The populations of defects were successfully controlled using thermal annealing in air. EIS measurements showed a dramatic reduction in the surface Frenkel defects of n-type dopant, with increasing annealing temperature. The dopant density was optimised from thermal annealing in air at 500°C. This led to a fivefold increase in photoconversion efficiency from the CBD sample. Further increasing the annealing temperature to 550°C led to a higher concentration of $V_{Zn}$, a p-type dopant, which behaves as a hole trap and shifts the flat band potential towards the valence band. This in turn led to a reduction in the PEC performance.

## 3.6 Supporting Information: Defect-Rich ZnO Nanorod Arrays for Efficient Solar Water Splitting

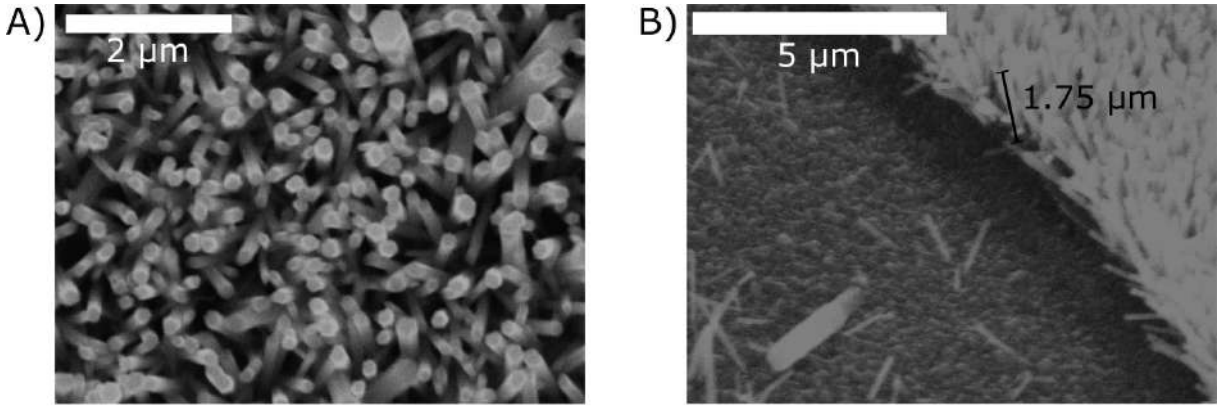


Figure S3.1: SEM images of CBD sample, A) top down view, B) cross sectional view.

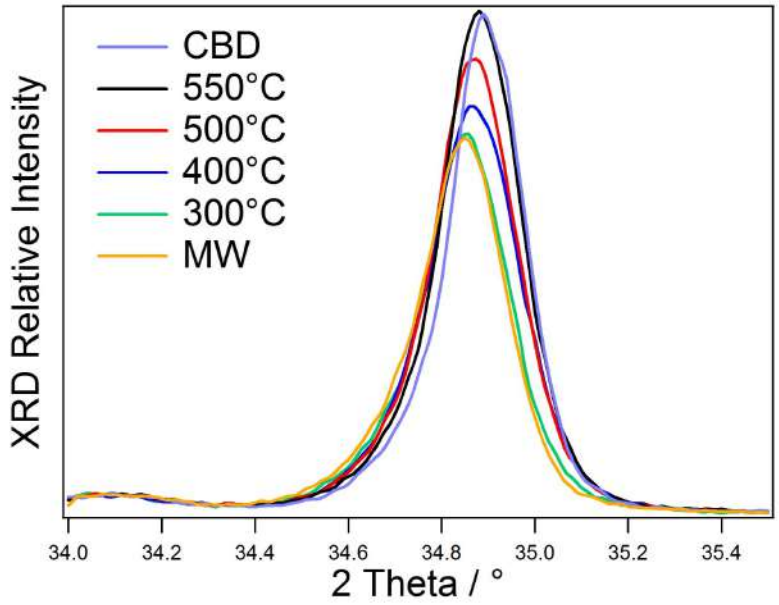


Figure S3.2: XRD 002 peaks of the different samples with various annealing temperatures.

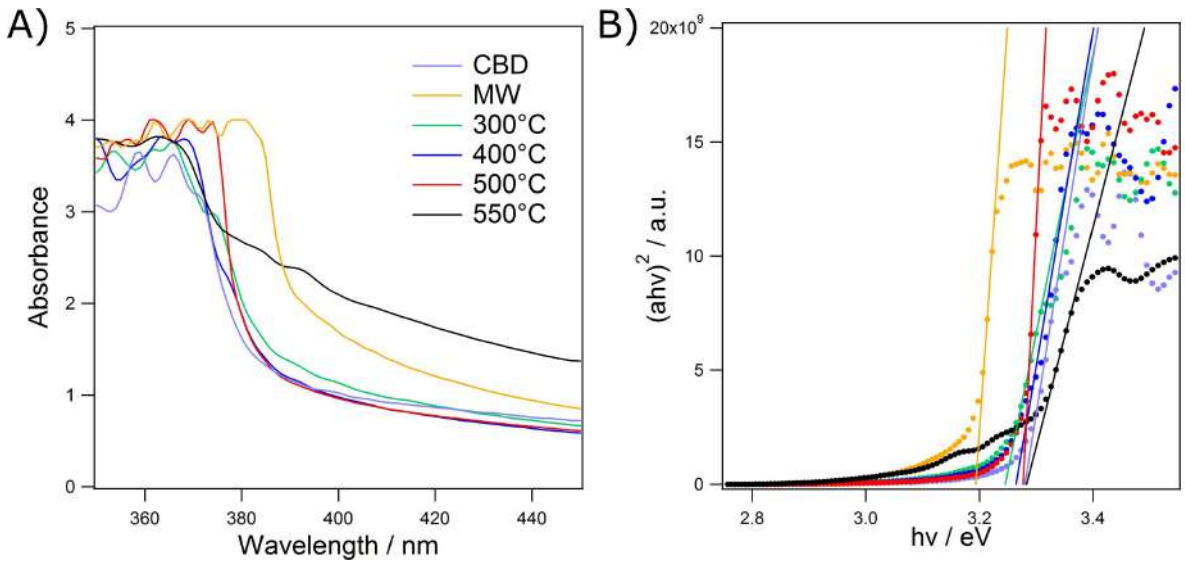


Figure S3.3: UV-Vis absorption spectra A) and Tauc plots B).

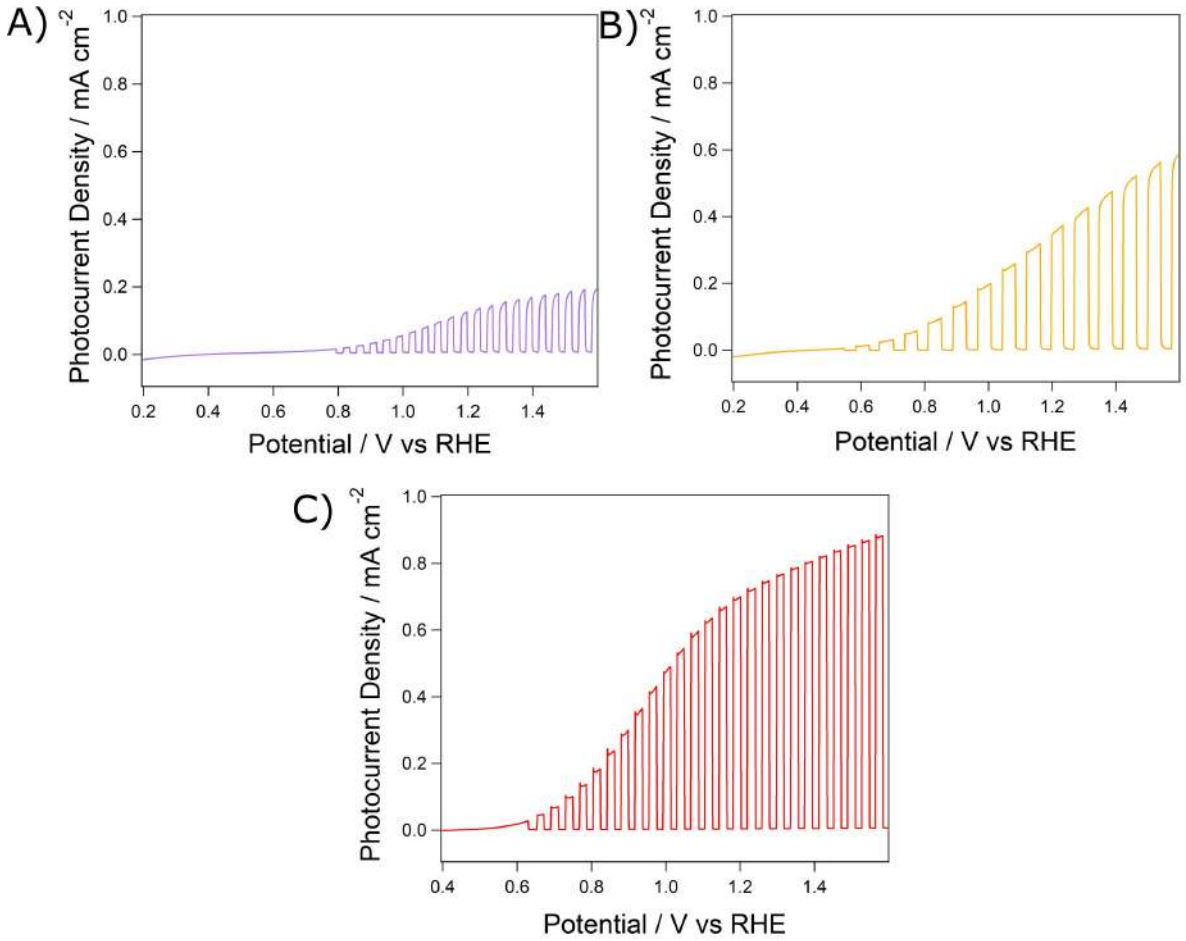


Figure S3.4: To prove the current is contributed from the photoexcitation process, the light chopped I-V curves for the as synthesised MW sample, the annealled MW sample and the CBD sample are demonstrated in Fig. S4.

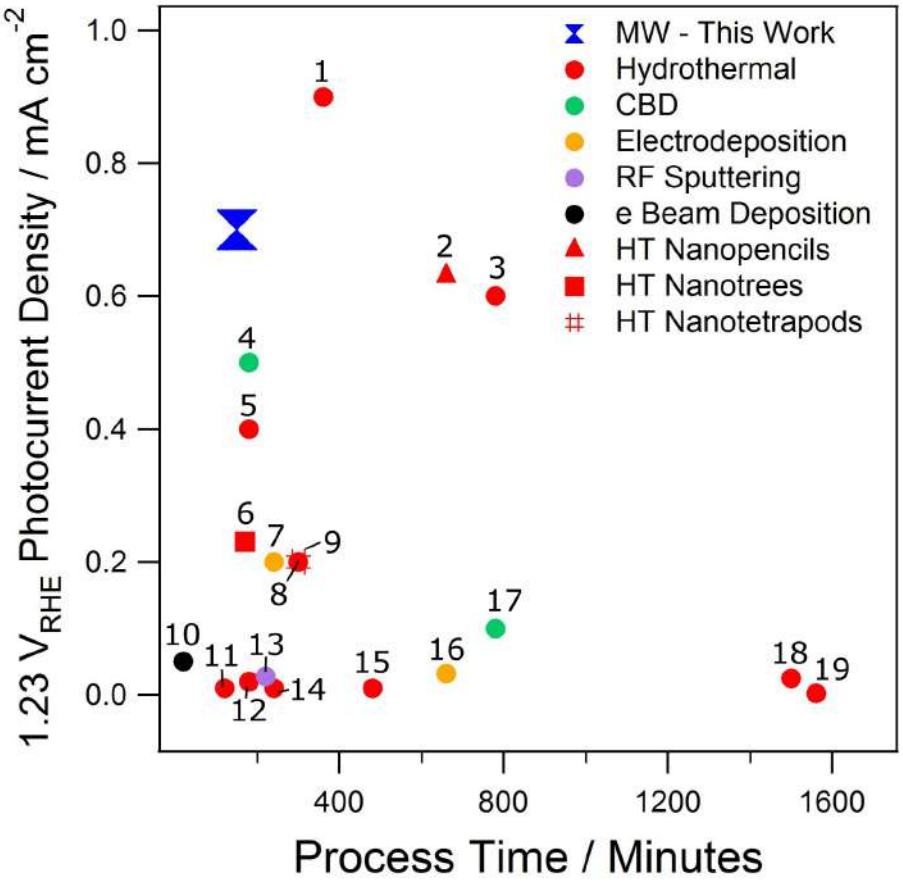


Figure S3.5: Review of Performance vs Processing Time

### 3.6.1 Literature Review

Literature search of pristine ZnO nanostructures, works were screened from any with extrinsic dopants or coatings. Process time excludes any seeding processes, and was the sum of growth time and post annealing time. Photocurrents were taken at 1.23 $V_{RHE}$ calculated from reference electrode and pH via the Nernst equation.[327] Only works using a solar simulator calibrated to one sun, or Xenon lamps calibrated to 100 $\mathrm{mW\,cm^{-2}}$ with AM 1.5 G filter were used in this study. A number guide to the references can be found below.

Table S3.1: Chart number with references.

| No. | Reference | No. | Reference |
|---|---|---|---|
| 1 | Vuong *et al.*[141] | 0 | Li *et al.*[314] |
| 2 | Ly *et al.*[119] | 12 | Li *et al.*[290] |
| 3 | Baek *et al.*[113] | 13 | Ahn *et al.*[328] |
| 4 | Wang *et al.*[329] | 14 | Yang *et al.*[143] |
| 5 | Hu *et al.*[98] | 15 | Jin *et al.*[330] |
| 6 | Ren *et al.*[117] | 16 | Shen *et al.*[331] |
| 7 | Xie *et al.*[332] | 17 | Lee *et al.*[100] |
| 8 | Majumder *et al.*[333] | 18 | Wang *et al.*[334] |
| 9 | Qiu *et al.*[335] | 19 | Cai *et al.*[288] |
| 10 | Wolcott *et al.*[286] | | |

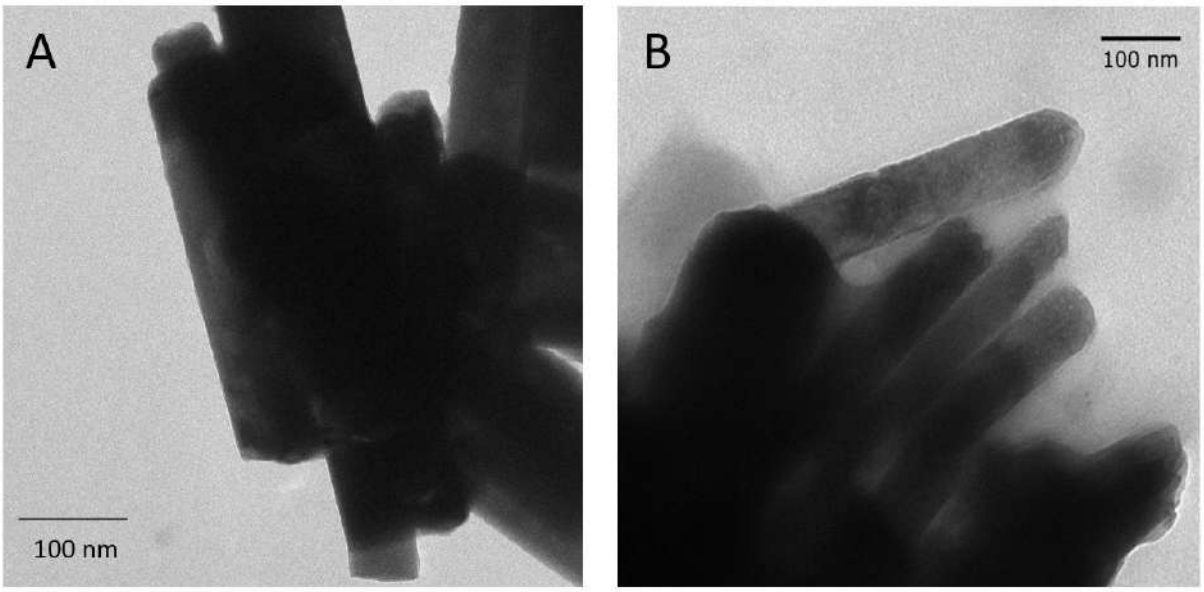


Figure S3.6: TEM images of A) CBD and B) URMAD synthesised ZnO nanorods.

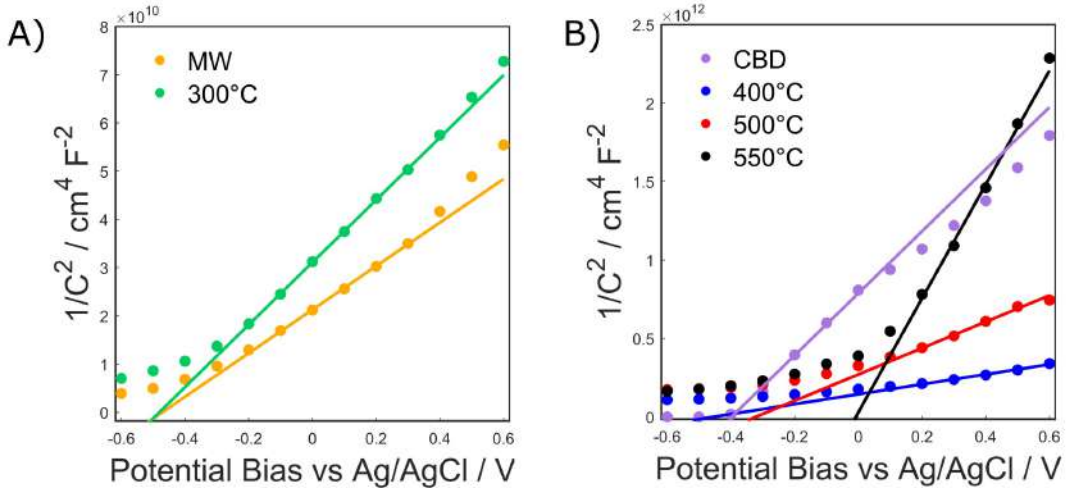


Figure S3.7: Mott Schottky Plots of the various samples, measured at 1 kHz 10 mV sinusoidal AC at various DC potentials.

### 3.6.2 Mott Schottky Relation

The MS relation is as follows:

$$\frac{1}{C_{sc}^2} = \frac{2}{e\epsilon\epsilon_0 A^2 (N_d - N_a)} \Delta\phi_{sc} \tag{S1}$$

The values $\epsilon$ and $\epsilon_0$ correspond to the relative permittivity of the material (taken as 10 for ZnO) and permittivity of free space respectively. The surface area contact with the electrolyte is given by $A$. The key values that can be determined from the gradient of the linear section of the plot are the $N_d$, donor density and $N_a$ the acceptor density. Often simplified as $N_D = N_d - N_a$ where $N_D$ is the dopant density, a majority p-type semiconductor will give a negative gradient and n-type, positive. The extent of doping is given by $N_D$.[278]

The value of $\Delta\phi_{sc}$, the potential across the space charge layer is defined by eq. (S2).

$$\Delta\phi_{sc} = E - E_{FB} - \frac{kT}{e} \tag{S2}$$

Yielding more useful physical values, $E$ is the measured DC potential and the final thermal term is often neglected. The flat band potential $E_{FB}$ is the required voltage to remove the

charge depletion layer at the interface and prevent band bending.

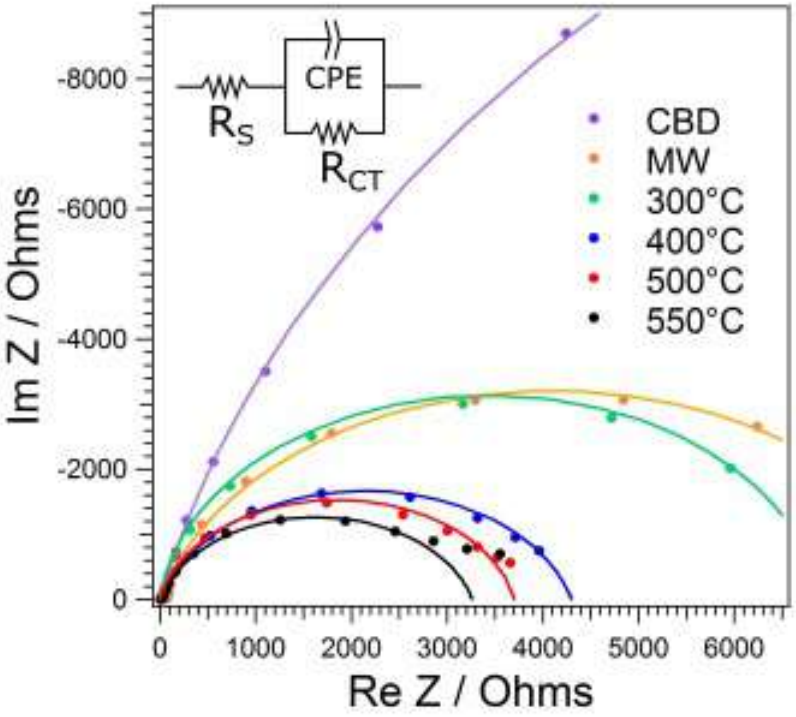


Figure S3.8: Nyquist Plots, varying 10 mV AC voltage frequency from 10 kHz to 0.1 Hz at 0 V vs Ag/AgCl DC bias in 0.5 M $NaSO_4$ under illumination.

# Chapter 4

# Yttrium Doped ZnO Nanorod Arrays for Increased Charge Mobility and Carrier Density for Enhanced Solar Water Splitting

## 4.1 Abstract

An innovative procedure is presented, when for the first time, yttrium doped ZnO vertically aligned nanorods have been synthesized using a unique rapid microwave assisted method. In comparison with pristine ZnO NRs, the Y-doped samples present more favourable morphology along with reduced crystallinity due to substitutional defects, $Y_{Zn}$. The Y acted as a shallow donor type defect, leading to an 80% increase in dopant density, to $1.36 \times 10^{18}$ $\mathrm{cm}^{-3}$ in the 0.15% Y sample. The transmission line model was used to analyse the transport properties. It was found that a 1000-fold increase in conductivity and electron mobility was achieved by doping 0.15% Y, resulting in a high density of donors which fill charge traps. Meanwhile, a significant improvement in conductivity was accompanied by greater electron hole recombination and band gap reduction. Analysis of photoluminescence spectra reveals the effect of Y doping on native point defects, initially reducing $Zn^{2+}$ vacancies by filling with $Y_{Zn}$, followed by the reduction of $O^{2-}$ vacancies with interstitial doping at higher Y concentration. With a fine bal-

ance of superior conductivity and charge recombination rate, the photocatalytic water splitting performance was optimised achieving photocurrent of 0.84 $\mathrm{mA\,cm^{-2}}$ at 1.23 $V_{RHE}$ with 0.1% Y doping. This corresponded to a 47% enhancement in photoconversion efficiency compared to the pristine sample.

## 4.2 Introduction

In order to meet the challenge of the energy crisis, the 'hydrogen economy' has the potential to play a significant role in the storage and renewable generation of energy.[17] Photoelectrochemical (PEC) water splitting is an emerging method of hydrogen production that has seen great advancement since its first demonstration by Fujishima and Honda.[24,32,241] In this rapidly advancing field various materials have been applied, such as highly oriented rutile $TiO_2$ nanorods,[336] along with flexible polymeric carbon nitride films.[337] Stability in water, wide electronic band gap and appropriate band edge position afford ZnO suitable properties for this process,[338] furthermore, high electron mobility and high charge carrier density give this material an edge over $TiO_2$.[339] Nanostructured photoanodes provide increased photoconversion efficiency (PCE) in systems reliant on Faradaic charge transfer,[340] leading to a plethora of ZnO morphologies such as nanoparticles,[136] nanotubes,[341] nanoflowers[323] and nanorods.[89,323] The electronic and optical properties of ZnO can be improved by extrinsic doping, allowing further light absorption in the visible spectrum through band gap narrowing,[100] or increased conductivity. By introducing shallow donors electron concentration can be raised, resulting in the reduction of transport resistance and increasing rate of photolysis.[342]

In this work, yttrium doped ZnO nanorods (NRs) have been applied to PEC water splitting for the first time, for a significant enhancement in PCE. Vertically aligned ZnO NRs were grown via rapid microwave assisted synthesis, with Y addition in the growth solution leading to reduced crystallinity and more favourable geometry. This also resulted in greater n-doping along

with dramatically increased electron mobility, improving the charge dynamics in the semiconductor bulk. This led to a significant increase in photocurrent density and therefore water splitting ability, when compared to the pristine sample, with potential application to photovoltaic technology in future.

Yttrium doped ZnO is well known for its conductivity in the strongly n-type semiconductor,[315,343–346] leading to applications as a transparent conducting oxide,[127,347] gas ionization and humidity sensor.[133,348] Favourable optical properties of Y doped ZnO have led to applications as photoanode in organic light emitting diodes,[349] displaying enhanced UV emission.[350] These attractive prospects have led to the exploration of Y doped ZnO powder as a photocatalyst for dye degradation,[116,351] and for hydrogen generation in the water-lactic acid system.[352] Y doped ZnO NRs were applied to solar water splitting coated with carbon nitride achieving a photocurrent of 0.4 $\mathrm{mA\,cm^{-2}}$ at 1.23 $V_{RHE}$.[337] In all cases, the Y doping led to a remarkable improvement in catalytic rates.

This study aimed to better understand and quantify the effects of Y doping on the charge transport and interfacial transfer in the ZnO NR / electrolyte system. Therefore, electrochemical impedance spectroscopy (EIS) was performed and analyzed with the transmission line model, determining electron mobility, conductivity, recombination resistance and chemical capacitance. This method has been applied to many nanocrystalline systems including mesoporous $TiO_2$,[282] mesoporous $Fe_2O_3$, and organic heterojunction films.[353,354] Furthermore, it has become a common characterisation technique in dye sensitised and perovskite solar cells,[355–358] as well as ZnO nanotube and nanorod arrays.[120,341] Here, we used the transmission line model to analyse the effects of Y doping on ZnO, revealing dramatically improved electron mobility.

In this paper yttrium doping is presented to be an effective method of increasing the efficiency of ZnO NR water splitting photoanodes. Incorporation of Y into the ZnO lattice led to reduced crystallinity and improved morphology by reducing NR diameter from 111 to 92 nm

at 0.15% Y doping. The extrinsic atomic addition was confirmed as a shallow donor, increasing n-type doping by 80%, which also led to a significant enhancement in trap limited electron mobility reflected by several orders of magnitude gain in conductivity. Such an improvement would not be possible without the effect of Y on the native point defects of ZnO, where PL spectroscopy displayed a reduction in $V_O$ and $V_{Zn}$ densities, lowering electron scattering through the bulk. Furthermore, UV-Vis spectroscopy revealed the reduction in band gap of the doped ZnO, allowing greater visible light absorption. However, further increasing the doping level also led to faster electron hole recombination and therefore energy loss. Ultimately yttrium content was optimised at 0.1% leading to a 47% enhancement in photoconversion efficiency.

## 4.3 Experimental Method

### 4.3.1 Synthesis of Nanorods

All chemicals used were purchased from Sigma Aldrich with no further purification. Transparent conducting glass substrates (flourine-doped tin oxide FTO) were cleaned by sonication in acetone, isopropanol and DI water for 15 minutes in each solvent. Each 12 $\times$ 20 mm FTO glass was seeded using a 0.1 M zinc acetate solution in DI water with added 0.6 wt% polyvinyl alcohol for added viscosity. The solution was spin coated using a two stage program, 800 RPM for 90 seconds followed by 30 seconds at 2000 RPM in order to remove beads of solution from the edge. This was followed by annealing in air at $500\,^{\circ}\mathrm{C}$ for 20 minutes in order to form the zinc oxide seeding layer.[263]

The vertically aligned NRs were synthesised using a microwave chemical bath deposition. The details were published separately.[114] Each cycle was heated at 100 W to 100°C for a 30 minute holding time. A total of 4 cycles were used for each ZnO sample, substrates were placed face down in 20 ml aqueous solution of 40 mM zinc nitrate and hexamethylenetetramine (HMT) in 1:1 molar ratio. Cycles took 3 minutes to reach temperature and 5 minutes to cool,

the microwave reactor used was the CEM Discover.

Samples were subsequently annealed in air at 500°C for 30 minutes. Yttrium doped samples were produced by 0.5, 1, and 2% molar addition of yttrium nitrate (with respect to zinc nitrate) to the growth solution.

### 4.3.2 Materials Characterisation

The real concentration of yttrium dopants was measured by inductively coupled plasma mass spectrometry (ICP-MS, Agilent 7500ce). Samples were prepared for ICP-MS by dissolving in 2 ml, 1.5 wt% nitric acid, followed by dilution to 50 ml volume by DI water addition. Scanning electron microscopy (SEM, JSM820 M, Jeol) was used to analyse the morphology of the samples. The crystallinity and structure orientation of the nanostructures were analysed by powder x-ray diffractometer (XRD, Siemens D500). The dimensions of the nanorods were measured from SEM images using Image J software (National Institutes of Health, USA). A standard 3-electrode set up, with Ag/AgCl reference and platinum counter electrodes was used for both water splitting photocurrent and electrical impedance spectroscopy (EIS). ZnO NR arrays were grown on FTO-glass substrate (Sigma-Aldrich UK) forming the photoanode. Using a 0.5 M $Na_2SO_4$ electrolyte and a linear potential scan from 0.2 to 1.6 $V_{RHE}$ photocurrents were determined. A solar simulator (Oriel LCS-100, Newport) with an AM 1.5 G filter at a distance calibrated to 100 $\mathrm{mW\,cm^{-2}}$ was used as the light source. PL spectra were characterised using a fluorescence spectrometer (Perkin Elmer LS 45) and UV-Vis diffuse reflectance spectra used to determine optical band gap were acquired using Ocean Optics ISP-REF integrating sphere equipped with an inbuilt tungsten-halogen illumination source 300 nm $\leq \lambda \leq$ 1000 nm, with MgO reference. EIS was performed in the dark using a Palm Sens 3 (PalmSens BV) electrochemical sensor, processed using PS Trace 4.8 (PalmSens BV) and Elchemea Analytical (DTU Energy, Technical University of Denmark).

## 4.4 Results and Discussion

### 4.4.1 Morphology and Crystallinity

High surface area, fast charge transport and efficient photo-absorption are beneficial to the rate of water photolysis.[359,360] The presence of dopant ions in the growth solution often affects the morphology and crystallinity of zinc oxide NRs, due to the surface charging of the wurtzite structure in a basic solution..[100] $Y^{3+}$ ions have been previously reported to form a negatively charged complex, stifling the lateral growth of ZnO due to the partial positive charge of the NR walls.[133] The effect of Y doping on the morphology was observed by SEM, shown in Figure 4.1. Cross sectional SEM used to measure NR length and diameter distributions can be found in Figure S4.1. The averaged ZnO NRs diameters and lengths are plotted in as shown in Figure S4.2. With increase in Y concentration, the diameter of ZnO NRs decreases from 111 to 92 nm. This effect is also conversely seen in the length of the nanowires, from 1650 to 2000 nm. This is likely due to the opposed charging of the top 002 face, leading to increased growth in the c axis.[133] This could be beneficial to PEC performance as larger aspect ratios lead to greater interfacial area for charge transfer.

ICP-MS was used to give accurate concentrations of Y. To assess the averaged dopant concentration, the ZnO NRs were dissolved in acid first. with growth solutions containing 0, 0.5, 1 and 2% molar addition of yttrium nitrate, dopant concentrations of 0, 0.04, 0.10 and 0.15% Y were achieved in the ZnO NRs.

Powder XRD was used to analyse the crystal properties of the samples, shown in Figure 4.2A. Both the wurtzite ZnO (JCPDS 36-1451) and FTO (JCPDS 71-0652) structures were identified. No new peaks were observed from the presence of yttrium oxide due to low abundance and homogenous incorporation into the zinc oxide. This is consistent with literature.[133,361] The feature dominating the pattern is the c-axis ZnO (002) peak at 34.5°. This is typical of NR

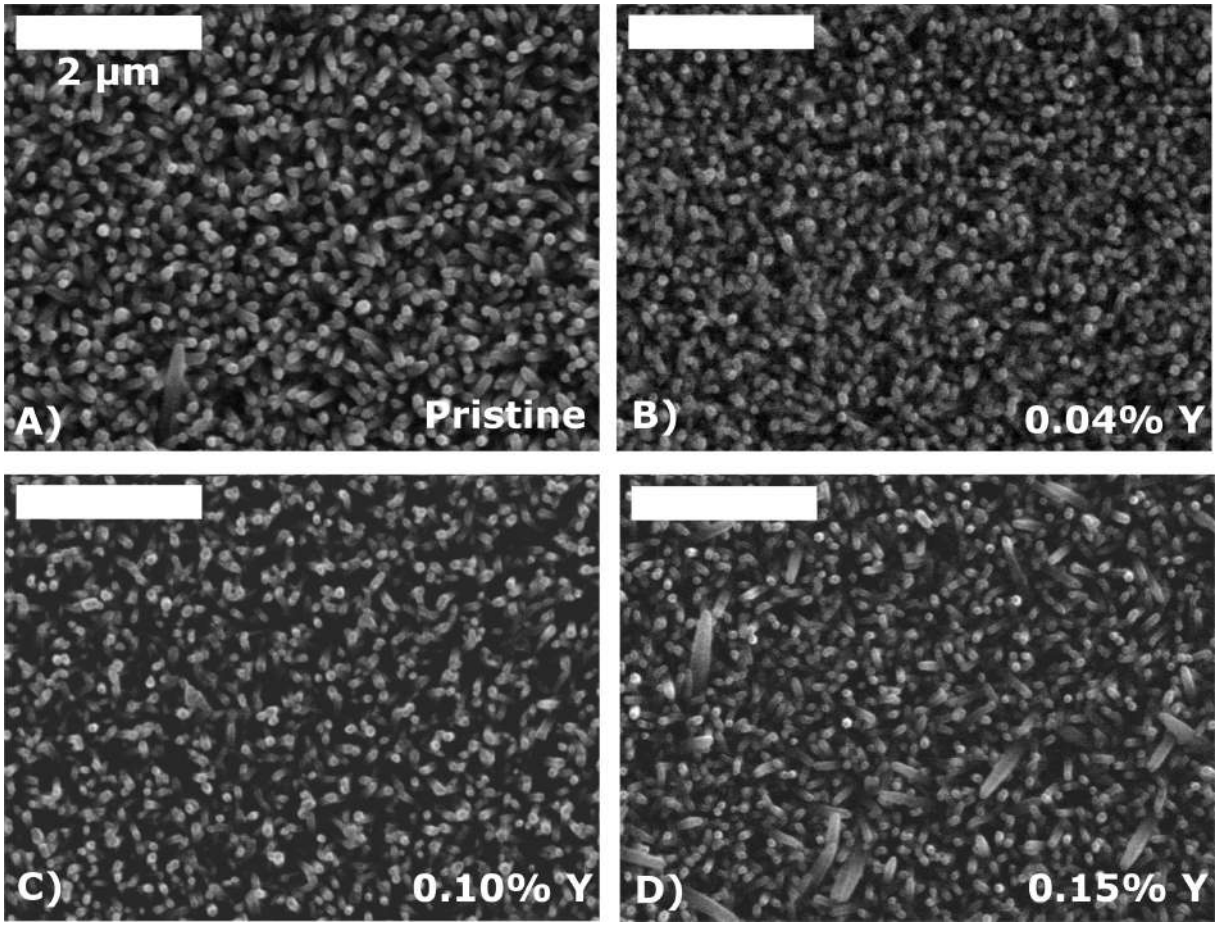


Figure 4.1: SEM images A), B), C) and D) corresponding to Y molar doping of 0, 0.04%, 0.10% and 0.15% respectively. The scale bars correspond to 2 µm.

arrays due to the strong vertical alignment of the structures, which has the (002) plane parallel to the substrate. The other ZnO signals were dwarfed in comparison due to this unique crystal alignment.

Values of peak position and full width half maximum (FWHM) provide information about the lattice spacing and crystal domain size respectively. The most significant trend from increased doping is seen in the FWHM increase for the (002) peak, seen in Figure 4.22B with the expanded (002) peak shown in Figure S4.3. This corresponds to a reduction in crystallinity due to the Y ions incorporated into the ZnO lattice, giving a decrease in grain size $D$ given by the Scherrer formula.[312]

$$D = \frac{0.9\lambda}{\beta \cos \theta_{hkl}} \tag{4.1}$$

Where $\lambda$ is the x-ray wavelength, $\beta$ and $\theta$ are the FWHM and the angle of diffraction, respectively. The crystal grain size decreases from 42.8 nm (0% Y) to 41.6 nm (0.15% Y) due to the lattice addition. This trend closely follows the aspect ratio change with yttrium doping, confirming the linked morphological and crystallographic effects. This change in FWHM could have also been caused by increased crystal defect population. A reduction in diffraction angle is seen for 0.15% doping due to the larger ionic radius of $Y^{3+}$, $0.92$ Å, compared to $Zn^{2+}$, $0.74$ Å.[362] This stretches the crystal wurtzite structure leading to a larger lattice constant, from $5.201$ Å to $5.204$ Å for pristine and 0.15% Y respectively.[133] As the dopant concentration increases, the diffraction peak width increases as well as the peak height, Figure 4.2A. Hence, the overall diffraction intensity from the (002) increases. Such increase can be explained by the longer NWs in the c axis, leading to greater abundance of (002) crystal planes.

### 4.4.2 Optical and Electronic Properties

Electrical Impedance Spectroscopy (EIS) is a powerful tool for understanding charge transfer in the semiconductor-electrolyte system. The Mott-Schottky plot of $1/C^2$ vs potential bias yields

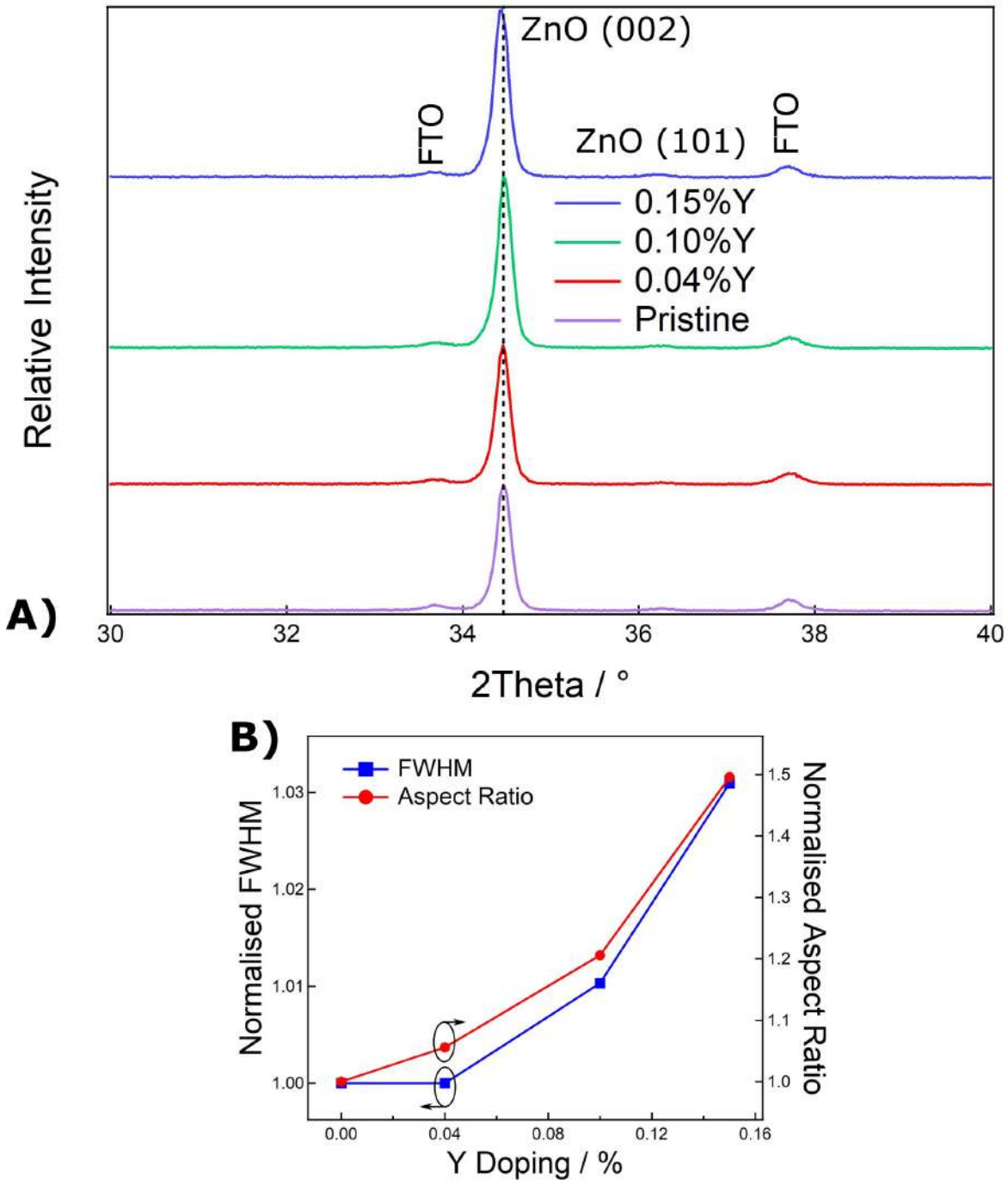


Figure 4.2: A) a segment of wide scan XRD of the different samples. B) the normalised FWHM compared to the normalised NW aspect ratio as a function of dopant concentrations.

the valuable parameters of dopant density $N_D$, and flatband potential $V_{FB}$. Both values are generally determined by the gradient and extrapolated intercept of the linear region. However, Mora-Seró *et al.* developed a more accurate model reflecting ZnO NR cylindrical geometry.[363] The depletion region in an array of vertically aligned NRs was calculated by solving the Poisson equation using cylindrical polar coordinates. With this geometry correction, the potential bias, V, is related to the capacitance per unit area, $C_s$ , following 4.2.

$$V - V_{FB} = -\frac{N_D e}{2\epsilon}\left[R^2 - \frac{C_s R^3}{2\epsilon + C_s R} + R^2 \ln \frac{C_s R}{2\epsilon + C_s R}\right] \tag{4.2}$$

Where $e$ is the electron charge, $\epsilon$ is the product of the permittivity of free space and dielectric constant of ZnO, valued at 10. $R$ is the NR radius in cm as measured by SEM. The derivation of 4.2 along with the calculation of $C_s$ from raw values of $C$ can be found in the supplementary information (section S2.1). 4.2 is significantly different from the planar Mott-Schottky model in which the $1/C^2$ is linearly proportional to $V - V_{FB}$, and inversely proportional to the donor density. The experimental data (points) and model fits (lines) are shown in Figure 4.3A. Despite some divergence seen at higher potentials, the fit is accurate over a far greater potential window than the typical linear model. This implies the cylindrical morphology has significant effects on the impedance properties of the NR material and the non-planar model could improve the accuracy of $N_D$ and $V_{FB}$ in comparison to the typical Mott-Schottky analysis for planar electrodes.

As expected, increased doping leads to a higher dopant density in the NR samples, due to $Y^{3+}$ ions acting as shallow n-type donors to the conduction band.[344] This leads to lower transport resistance and higher conductivity, suitable for rapid charge collection.[364] Figure 4.3B shows the obtained $N_D$ and $V_FB$ values as a function of doping level. The value of ND monotonically increases from $7.53 \times 10^{17}$ $\mathrm{cm}^{-3}$ for pristine, to $1.36 \times 10^{18}$ $\mathrm{cm}^{-3}$ of 0.15% doping. At low level doping, the modest increase in $N_D$ is possibly due to reduction in oxygen vacancies, $V_O$ and Fermi level pinning within the conduction band.[365] However, high level doping fills more

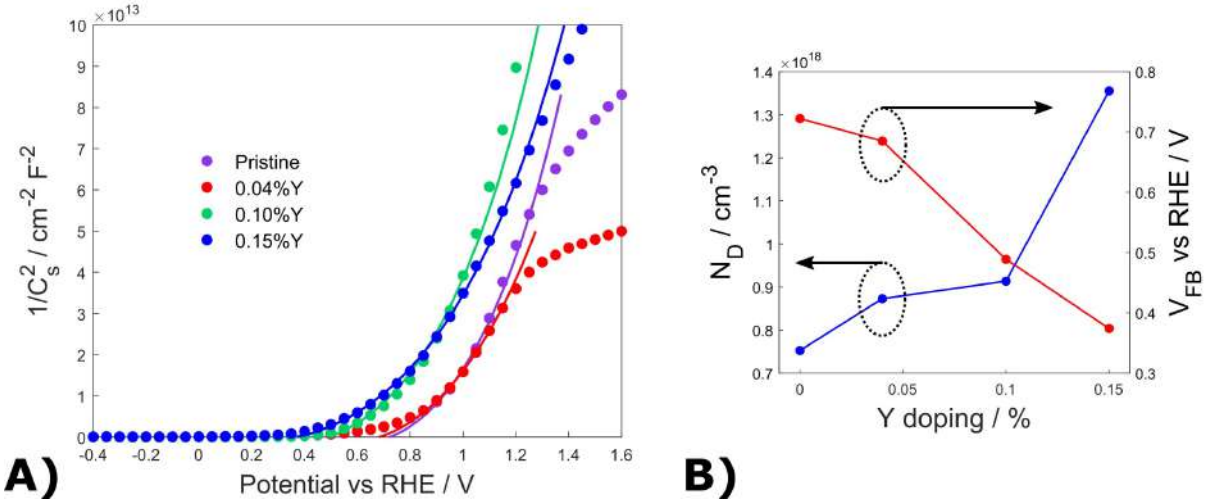


Figure 4.3: A) shows the sample capacitance, $1/C_s^2$ vs potential bias, dots denote experimentally measured data and lines show model fits. B) shows $N_D$ and $V_{FB}$ against doping.

states in the band, leading to a higher energy Fermi level which in turn, increases the formation energy of n-type native defects such as $V_O$.[319] This is confirmed by the negative shift in flat band potential with increasing Y doping. This effect was also observed by Kelley et al., using low levels of yttrium doping in CdO films.[366]

In order to investigate the fundamental material parameters of conductivity and electron mobility along with recombination resistance at the solid liquid interface, the transmission line model with reflecting boundary condition, Figure 4.4B) inset, was applied to impedance data across a range of potentials.[281] Originally used to decouple transport and transfer properties of $TiO_2$ by Fabregat-Santiago *et al.*, this model has been applied widely to mesoporous $TiO_2$[282,358] and ZnO NRs,[367,368] in electrolyte and dye sensitised solar cells.

Raw Nyquist plots along with their model fits can be found for sample 0.4% Y in Figure 4.4. In the potential region $< 0.2$ $V_{RHE}$, the ZnO is conductive and can be fit by a simple RQ circuit shown in Figure 4.4A (inset) as it displayed a single arc, yielding the chemical capacitance, $C_\mu$, and recombination resistance, $R_R$. However, from 0.3 to 0.8 V, shown in Figure 4.4B, the

Nyquist plots displayed a visible upward bend which is clearly visible in the magnified plots in Figure 4.4C. This is a typical transmission line behaviour. The bend separates two distinct regions. The high frequency region is dominated by the electron transport resistance, $R_T$, while the low frequency region determined by the recombination resistance at the interface, $R_R$ at the interface. To fit the data that includes both the transport resistance and the recombination resistance, the transmission line model was used as an equivalent circuit, displayed in the inset of Figure 4.4B. Each resistance is constituted of equally incremented smaller resistive components, $R_T$ is the product of NR length $L$ and $r_T$, whereas $R_R$ is defined as $r_R/L$.

Often, when analysing this high frequency region it is challenging to obtain reliable values of transport resistance $R_T$ with highly doped conductive ZnO,[368] although, in this study a noticeable high frequency feature can be distinguished in all the samples. However, in the high frequency region, the constant phase angles of all samples are significantly larger than 45°. Similar behaviour was reported and is likely due to the added capacitance from the FTO.[120,282,369] The experimental data and simulated fits for the remaining samples are shown in Figure S4.4-Figure S4.6.

Once transport resistance $R_T$ is determined, electron conductivity $\sigma_n$ can be calculated from a cylindrical model for the vertically aligned hexagonal nanorods.[281]

$$\sigma_n = \frac{L}{AR_T} = \frac{L}{R_T \pi r^2 \rho} \tag{4.3}$$

Where $L$ is the nanowire length, $r$ the radius and $\rho$ the number of NRs per unit area, all determined by SEM. $\sigma_n$ is a bulk material parameter which describes the emergent electron transport properties regardless of geometry. Typically this value depends on the product of electron mobility, $\mu_n$, and free carrier concentration related to $N_D$. Electron mobility describes the ease of electron drift in the presence of an electric field. It can be calculated via transmission line

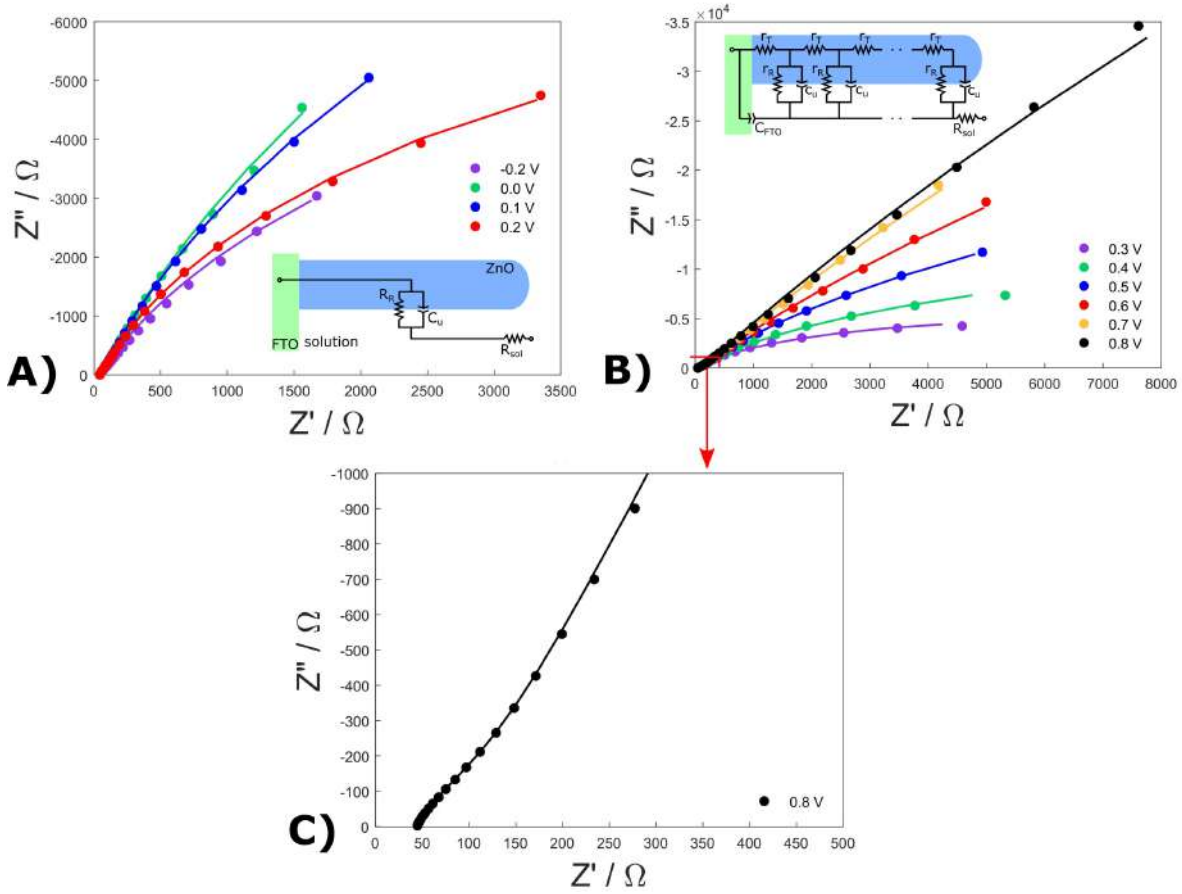


Figure 4.4: A) and B) raw experimental Nyquist data (points) and simulated model fits (lines) from 0.04% Y sample. The models used are shown in the insets for the potential ranges 0.3 to 0.8 and -0.2 to 0.2 $V_{RHE}$ respectively. C) expanded view of the plot indicating the high frequency diffusion region below the 'knee'.

parameters $R_T$, $C_\mu$ and constant phase element exponent $\gamma$ with 4.4.[282]

$$\mu_n = \frac{eL^2}{kT(R_T C_\mu)^{1/\gamma}} \tag{4.4}$$

The mobilities calculated by this technique often display different character to those determined by Hall conductivity measurements due to the nature of trap limited diffusion.[370]

The transport properties of the NRs, including conductivity, charge mobility and charge recombination resistance, determined by transmission line model as a function of potential for samples at different dopant concentrations are shown in Figure 4.5A-C. The conductivities for all samples decreases as the potential increases, due to the positive potential pushing the Fermi level below the conduction band minimum, causing a significant drop in electron concentration.[341]

A clear increase in conductivity is observed in the doped samples, at 0.3 and 0.8 V, 0.15% Y sample showed 1000 and 10,000 fold increase in conductivity over the pristine sample, respectively. This is too large to be explained by an 80% gain in dopant density (Fig. 3B), but an accompanying enhancement in electron mobility.

The electron mobility of the samples has been calculated using 4.4 and shown in Figure 4.5B. The variation of electron mobility as a function of dopant concentration, suggests trap-limited diffusion, where electrons from defect states are injected into the conduction band.[370] Higher electron concentration associated with defect states leads to increased mobility in ZnO NRs by neutralising charge traps.[339] The highest values of mobility from the 0.15% samples are the same order of magnitude as the value determined by Hall effect measurement (200 $\mathrm{cm^2\,V^{-1}\,s^{-1}}$).[124] The rest of the values fall far short of this quantity due to the nanocrystalline, trap mediated transport in the films, rather than in-plane transport across solid thin films. The transmission line model gives a more practical window into the electron motion of the nanostructures, more useful for understanding charge dynamics in the water splitting system.

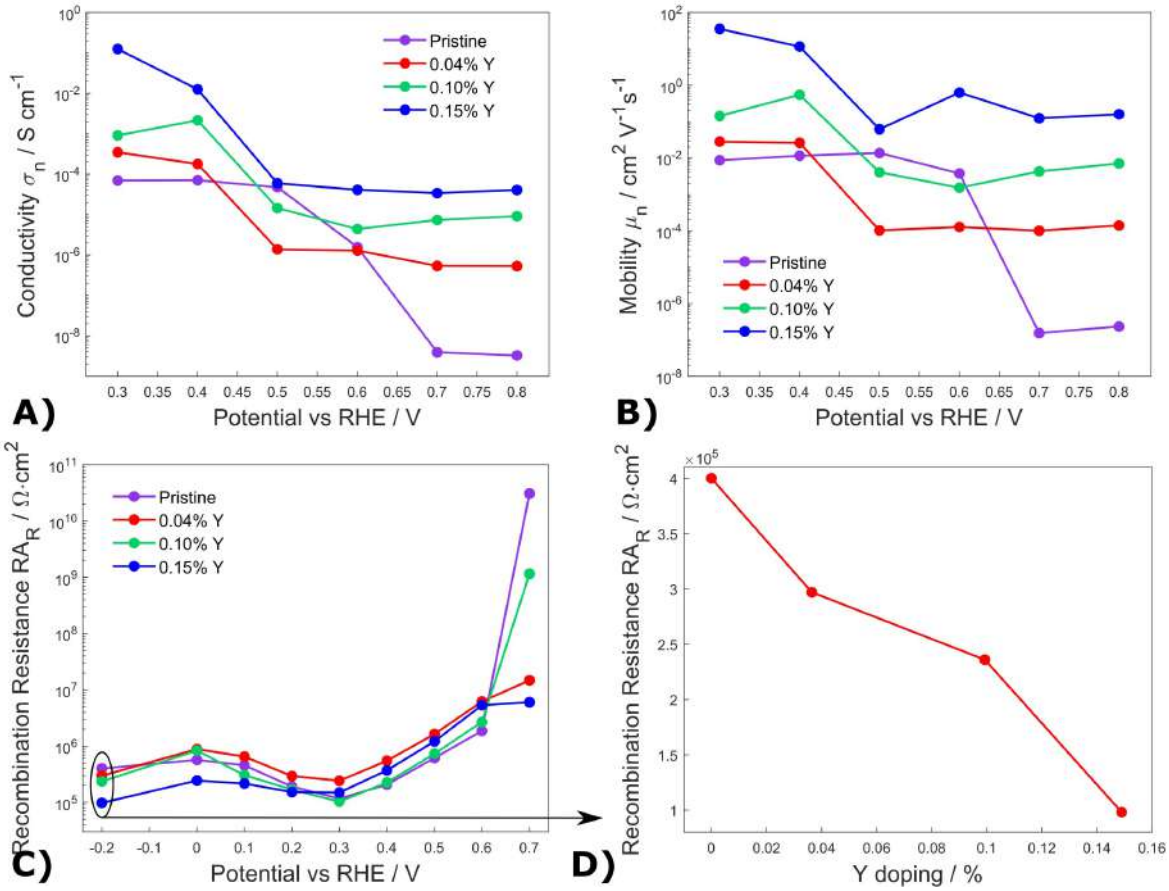


Figure 4.5: A) shows the conductivity of the samples. B) electron mobility through the transmission line potential region, and C) area normalised recombination resistance, $RA_R$. The potential range is wider as it could be determined using both equivalent circuits over the entire voltage window. D) normalised recombination resistance of the samples measured at -0.2 $V_{RHE}$.

The recombination resistance $R_R$, inversely proportional to recombination current flux,[206] is normalised by multiplication by the sample surface area, $RA_R$,[371] and displayed in Figure 4.5D. A similar trend can be observed for all the samples, beginning low, negative of $V_{FB}$ and rising rapidly up to 0.7 $V_{RHE}$. At -0.2 $V_{RHE}$ when the ZnO yields a metallic response, a monotonic decrease in $R_R$ is observed with doping, Figure 4.5D. Higher doping of yttrium causes greater recombination of electron hole pairs due to the dopant ions acting as recombination centres in the bulk and at the surface.[372] As expected the pristine sample shows a dramatic rise in $R_R$ towards higher potentials past the onset, and 0.15% retains the fastest recombination. Somewhat unexpected is the reversal of recombination rates of 0.10% and 0.04% samples at 0.7 $V_{RHE}$. This is perhaps due to the more negative position of $V_{FB}$ for the 0.10% samples, promoting charge transfer across the junction and restricting recombination current.

The effect of yttrium doping on light absorption was measured using UV-Vis reflectance spectroscopy. Band gaps were calculated using the Kubelka-Munk function $F(R)$, detailed in section S2.2 in the appendix.[262] This was followed by the use of Tauc plots for the n-type semiconductors, shown in Figure 4.6A, with B presenting a decreased band gap with yttrium doping.[261]

The band gap behaviour is in good agreement with our previous measurements made on hydrothermal bath deposited Y doped ZnO NRs.[133] The decrease in the band gap energy as the dopant concentration increases is due to additional donor states formed close to the conduction band minimum within the band gap of ZnO.[373] This requires lower energy photons to promote valence band electrons to these states resulting in greater visible light absorption. Though small, this band gap reduction is advantageous to the photoelectrochemical water splitting performance of the samples, accessing a greater portion of the visible light in the solar spectrum.

PL spectroscopy was performed to confirm recombination rates and the electronic defect structure of the samples. An excitation of 320 nm was used, and the spectra were normalised

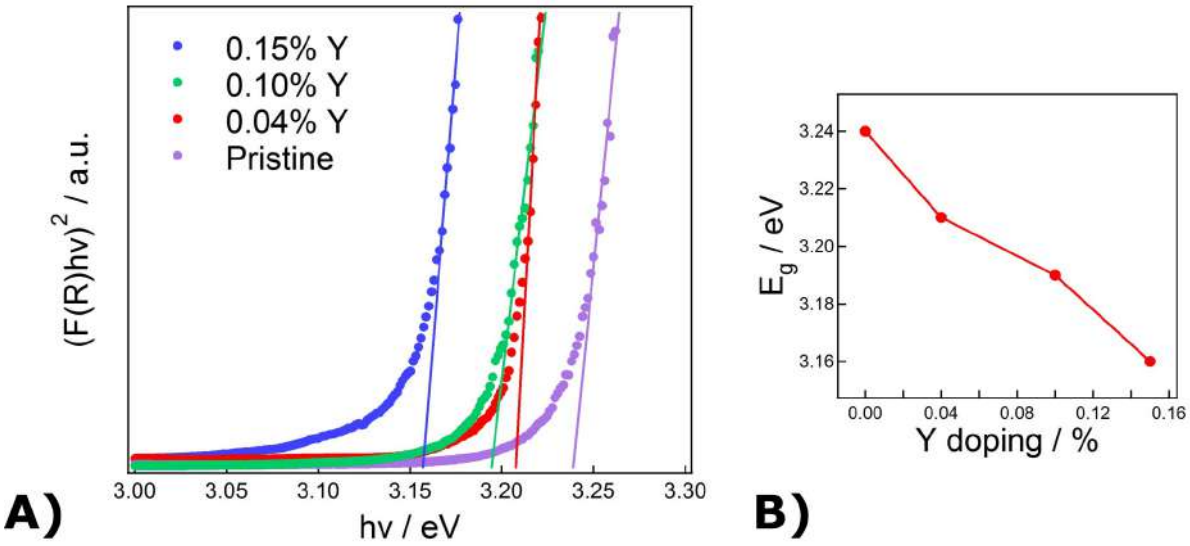


Figure 4.6: A) Tauc plot of the samples along with extrapolated linear regions for determination of band gap. B) band gap energy against doping, determined by Tauc plot.

using the absorbance of each sample at this wavelength. Greater intensity across the entire spectra was observed with higher yttrium concentration, confirming the trend in recombination resistance $R_R$ determined by EIS. Faster electron hole recombination yields more intense near-band-edge (NBE) emission as a result of the interaction of excitons with substitutional yttrium, $Y_{Zn}$, provided that recombination is radiative. No new distinct peaks can be seen from $Y_{Zn}$ doping, confirming that it is a shallow donor. However, interstitial yttrium $Y_i$ may be responsible for larger peaks across the spectra due to its interaction with native point defects. The integrated spectra, Figure 4.7, reveals the increase in PL intensities as doping levels increases, negatively impacting water splitting rate.

Six distinct peaks are observed forming the PL spectra, centred at 398, 419, 441, 462, 485 and 528 nm, labelled a-f) in Figure 4.7A. The spectra were analysed with non-linear least square fitting to resolve the PL emission intensity of each peak which is related to the corresponding defect concentration. The assignment of the emission peaks is shown in Figure 4.7B. The leading emission peak at 398 nm, peak a, is assigned to the NBE. Peak b is associated with

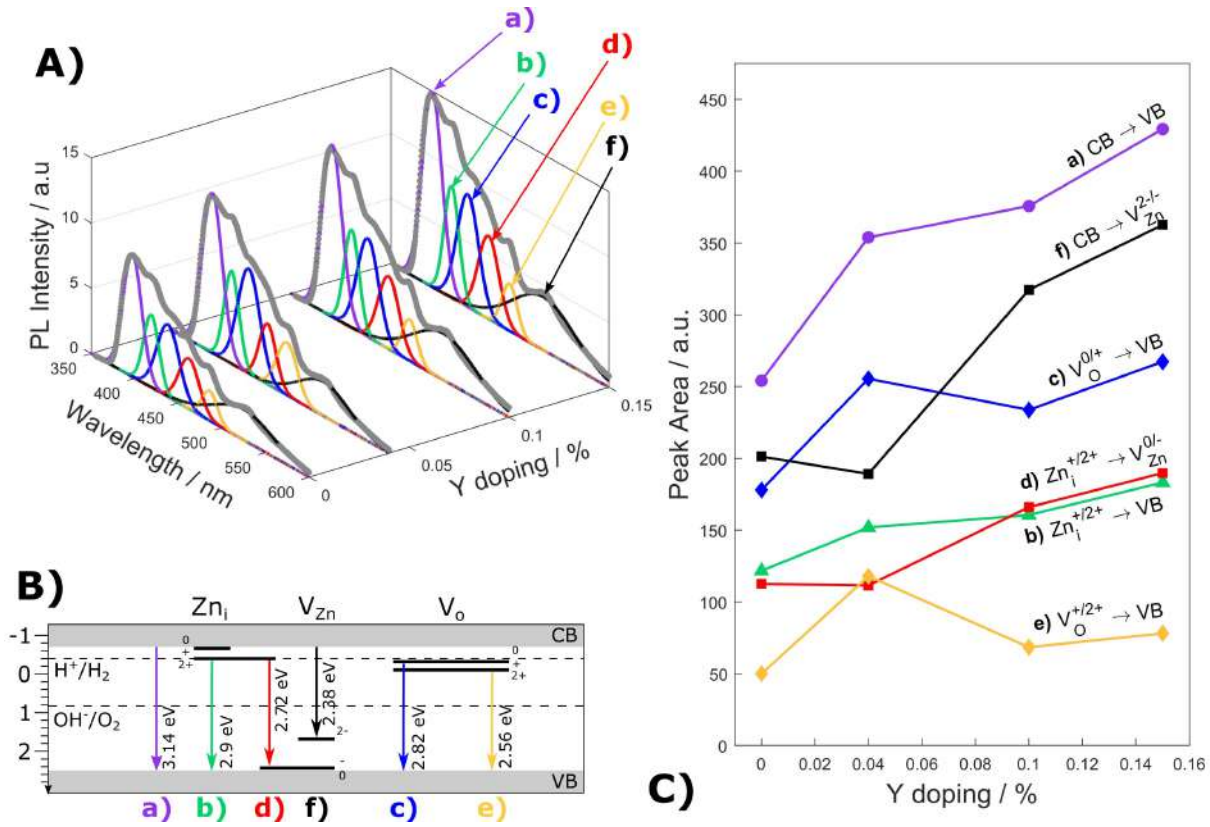


Figure 4.7: A) expanded view of PL spectra, allowing the changes in peaks a-f to be observed. B) transitions assigned to each peak, and finally C) integrated peak intensity for each of the transitions at different Y concentrations.

donor level introduced by $Zn_i$.[316,318] Peaks c and e occur from the two charge state transitions of $V_O$.[318,319] Peak d is due to an inter-defect transition from $Zn_i$ to the $V_{Zn}^{-/0}$ state, 0.18 eV above the valence band,[319] and finally f originates from the $Zn^{2+}$ vacancies $V_{Zn}$.[316,319,320]

The intensity of NBE peak is seen to increase from pristine to 0.15% sample, following the trend seen in the total PL integrals due to faster exciton recombination rate.[370] A subtle rise in intensity for peak b is also observed, however it is unlikely due to a higher concentration of $Zn_i$ with increased Y doping in the NRs. Rather, this defect is probably being fed by a more populous conduction band. More prominent effects are seen in peaks c-f. An initial drop in peak f is observed, followed by substantial increase in intensity due to increasing population of $V_{Zn}$ as a result of Y doping. The initial decrease in $V_{Zn}$ concentration at low level doping (from pristine to 0.04% Y) is due to the filling of $V_{Zn}$ with $Y_{Zn}$ substituting a deep acceptor state with a shallow donor. Further increase in the Y doping will lead to the increase of interstitial $Y^{3+}$ which decreases the $R_R$ with enhanced electron mobility (Figure 4.5D).[366] Consequently, this effect increases the formation energy of $V_O$, leading to a decline in peak c and e for Y doping of 0.1%.[319] It is important to note in the interpretation of the PL spectra that the penetration depth of the absorbed and emitted photons is low, giving the results a strong surface bias.[305] Furthermore, the peaks observed only yield data on deep electronic states causing radiative transitions. Shallow states with energies close to or inside the conduction band, such as those likely caused by yttrium dopants, introduce vibrational states, with energies too small to be detected by this technique.[374]

### 4.4.3 Water Splitting Performance

The measured photocurrent densities of the pristine and yttrium doped samples display their photoelectrochemical water splitting abilities, found in Figure 4.8A. Photocurrent density uniformly increased across all samples with positive bias to a maximum of 0.84 $\mathrm{mA\,cm^{-2}}$ for

the optimised 0.1% Y sample at 1.23 $V_{RHE}$. This represents a 23% enhancement from the undoped sample, due to improved charge transportation from higher conductivity. This value is greater than those achieved by doping ZnO NRs with N,[143] Na and Al,[100,342] which achieved photocurrent of 0.3, 0.5 and 0.3 $\mathrm{mA\,cm^{-2}}$, respectively, at the same bias. Furthermore the rapid microwave synthesis used in this work,[114] displays over double the photocurrent achieved by carbon nitride coated YZnO (0.4 $\mathrm{mA\,cm^{-2}}$ at 1.23 $V_{RHE}$).[375] Although, the photolysis in this work falls short of doped and coated core-shell structured photoanodes, which have much improved visible light absorption. With hydrogen doping or hematite coating,[141,178] photocurrents of 1.00 or 1.27 $\mathrm{mA\,cm^{-2}}$ were achieved, respectively. In order to utilise ZnO in higher performing photolysis, its major shortcoming of low visible light absorption must be overcome. One solution is the decoration with noble metal plasmonic nanoparticles, such as the gold tipped match-like structures produced by Wu et al.[89] Alternately low band gap, CdS and CdSe quantum dots have been used in conjunction with ZnO for enhanced solar performance.[154,155] Hence, visible light sensitisation offers potential for further enhancing the YZnO as a photoanode in future.

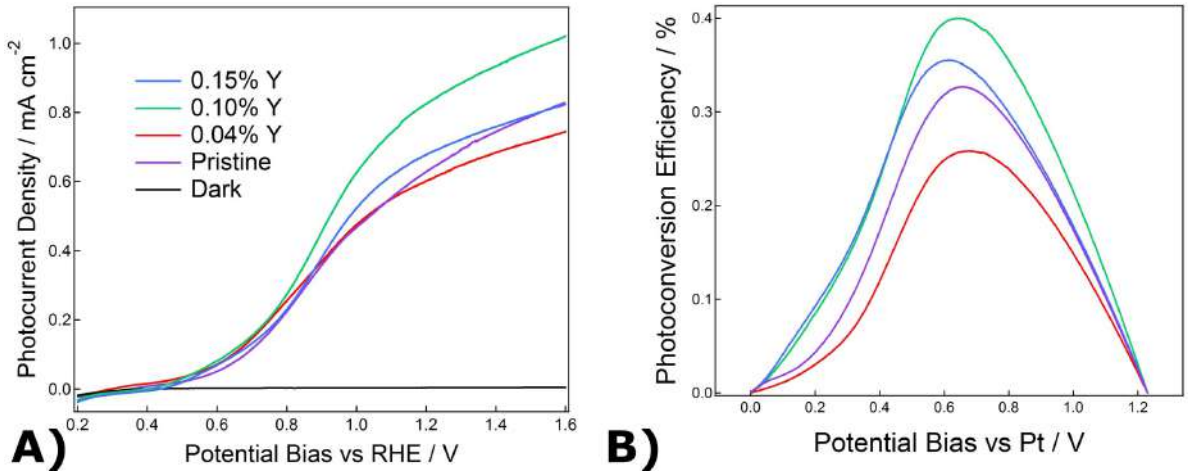


Figure 4.8: A) shows the photocurrent density curves against potential bias V vs RHE, and B) the photoconversion efficiency.

Calculated photoconversion efficiency, $\eta$, curves are displayed in Figure 4.8B, The equation used is the ratio of output electrochemical power to input solar power densities, $P$, in 4.5.[376]

$$\eta = \frac{J(1.23 - V)}{P} \tag{4.5}$$

Where $J$ is the photocurrent density and $V$ is the applied bias vs the platinum electrode. As expected the $0.1\%$ Y sample achieved the highest efficiency of $0.4\%$, giving a $47\%$ enhancement over the pristine NRs. Further increases to the doping level leads to a high density of defects on the NR surface which effectively forms recombination centres. Hence, it is important to optimise the appropriate defects level while maintaining the electron transportation benefits. The stability of the photoanode is shown in Figure S4.6. The photocurrent was monitored at constant potential of 1.23 $V_{RHE}$. There is no degradation after 5 minutes of stepped illumination.

The microwave synthesis also performs favourably in comparison to yttrium doped zinc oxide nanorods synthesised by conventional hydrothermal method. Solar water splitting data of hydrothermal NRs can be seen in Figure S4.7, where yttrium doping once again leads to more favourable performance. The results are comparable to the microwave synthesis as both contained the same atomic concentration of yttrium, as seen in Table S3.1, which varied little between the methods. The microwave samples had the advantage of more rapid growth time, 2.5 hours compared with 4 hours hydrothermal for similar NR lengths. This difference is amplified as microwave heating typically requires lower power consumption, in this experiment microwave power was set to 300 W, whereas low temperature oven heating is usually $>$ 1000 W.[377]

Yttrium doping led to a $33\%$ increase in photocurrent at 1.23 $V_{RHE}$, from $\sim$0.15 to $\sim$0.20 $\mathrm{mA\,cm^{-2}}$. The MW samples significantly outperform these values due to native point defect states that contribute to both light absorption and dopant density as outlined in our previous work.[114] Furthermore, hydrothermal ZnO NRs are crippled by surface hydroxide groups acting

as recombination centres due to the high pH synthesis. To overcome this Baek et al. vacuum annealed samples produced by this method in a vacuum at 700°C for restored performance.[113]

Not only did the improved conductivity lead to higher photocurrent from the 0.1% Y sample, but greater resistance to photocorrosion. Beyond the 5 minute on-off cycles shown in Figure S4.6, the NRs were subjected to continuous illumination for 40 minutes held at 1.23 $V_{RHE}$, shown in Figure S4.7. The pristine sample decayed to half performance after 12 minutes where as this took 3 times longer for the 0.1%Y sample. The mechanism for this is unclear and beyond the scope of this study, perhaps a thin layer of $Y_2O_3$ formed on the surface of the NRs, slowing the light induced corrosive reaction. This further advantage cements yttrium as a stand out dopant for ZnO in solar applications going forward.

The mechanism for the high efficiency of Y doped ZnO are explained in terms of morphological and electronic effects in Y doping. Firstly, the Y doping results in the reduction of NR diameter with increased NR length. Hence, the effective surface area is increased, Figure 4.9A. Longer NRs also provide greater optical depth for light absorption. Secondly, the great increase in electron mobility provides improved electron transport. This is especially important for nanomaterials with vertically aligned morphology. As the optical depth increases with the increased NR length, photoexcited electrons also need to travel a significantly longer distance. The improved electron transportation reduces the energy cost for electrons travelling from the NR surface to the FTO conductive layer. Although increasing Y doping leads to significantly improved $\sigma_n$, reduced $R_R$ is the cost as the ZnO NR crystals become too defective. This has been confirmed with both EIS and PL measurements. The highest doped sample, 0.15% Y, presents a reduction in efficiency from 0.1% Y as the anode is stifled by the high rate of recombination. Hence, the doping level must be controlled in order to balance increased $\sigma_n$ against increased recombination rate.

Thirdly, a reduction in electronic band gap caused by Y doping would allow the ZnO to ab-

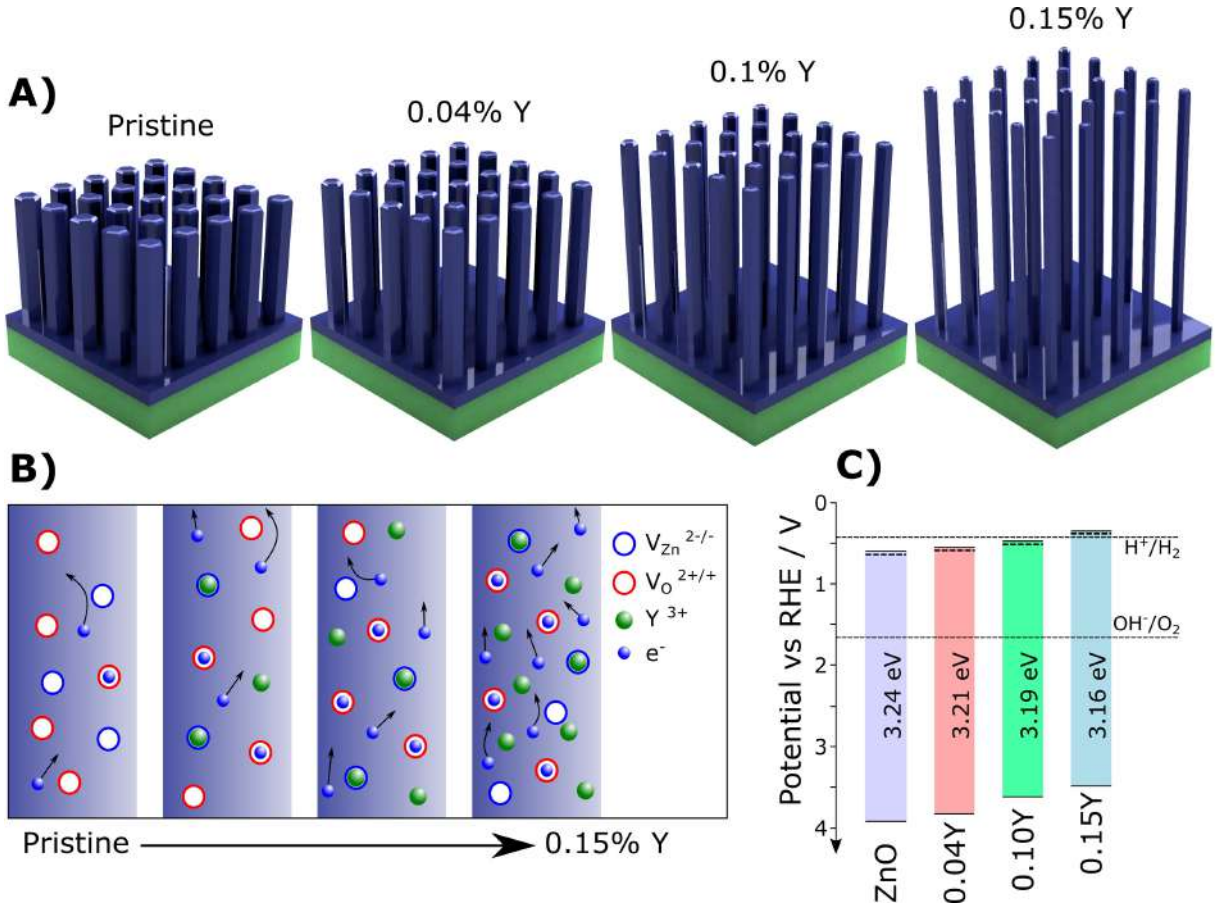


Figure 4.9: A) morphological benefits of Y doping allowing greater NR number density and therefore increased surface area, B) schematic explaining increased electron mobility from trap filling, and C) measured band edge and $E_F$ positions typical of ZnO,[378] with redox potentials at standard hydrogen potential, equivalent to pH 0.

sorb more visible light. The reduction of band gap energy was identified by UV-Vis reflection spectroscopy as a result of trap filling, illustrated in Figure 4.9B. This is particularly important when utilising solar energy with ZnO, since solar irradiance becomes much more intense with shifting wavelength from UV to blue visible. Fourthly, the negative shift in flat band potential provides an earlier onset potential for solar water splitting. This was observed from a morphology-corrected Mott-Schottky analysis, shown in Figure 4.3. The effects of doping on the band alignment for water splitting is shown in Figure 4.3C.[379] The 0.04% Y sample shows the lowest performance. This is possibly due to its greater recombination rate without significant enhancement of electron transport.

## 4.5 Conclusion

In conclusion, bare yttrium doped zinc oxide NRs have been synthesised for application to solar water splitting. Samples were prepared with 0, 0.04, 0.1 and 0.15% yttrium incorporation into the structures. The microwave synthesised NRs displayed more favourable morphology with a reduction in radius, along with enlarged crystal domain size implying the penetration of yttrium into the lattice. The Y acted as a shallow n-type donor, increasing the donor density in the ZnO NRs leading to increased conductivity determined by transmission line model. There was also a significant gain in electron mobility due to the filling of trap states, leading to a 1000 fold improvement from pristine ZnO. The electronic effects of higher Y concentration were confirmed by UV-Vis reflectance spectroscopy, reducing the band gap due to new states at the edge of the conduction band. PL spectroscopy displayed accompanying recombination rate increase along with the reduction in some crystal defects by deconvoluting the transition peaks. Yttrium addition, overall, led to higher concentrations of $V_{Zn}$ and less $V_O$ by altering their respective formation energies, further impacting mobility and increasing hole concentration. The superior transport properties of YZnO resulted in a 47% enhancement of photoconversion efficiency,

indicating their promise as electron transport materials in solar cells and coated photoanodes.

## 4.6 Supporting Information: Yttrium Doped ZnO Nanorod Arrays for Increased Charge Mobility and Carrier Density for Enhanced Solar Water Splitting

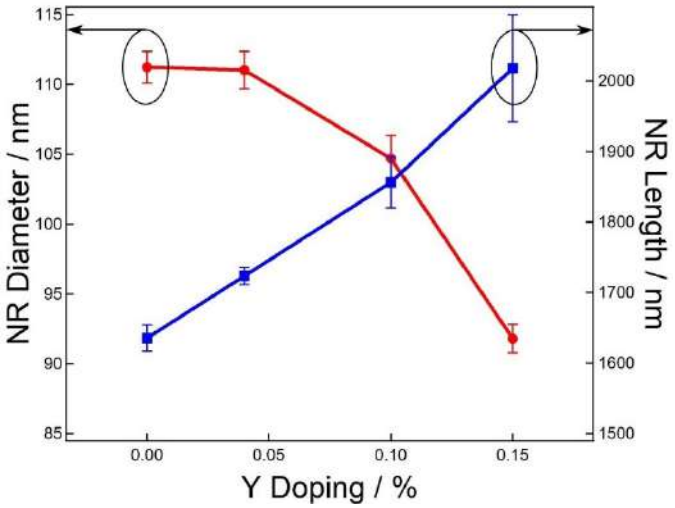


Figure S4.1: Shows the Y doping effect on nanorod length and diameter.

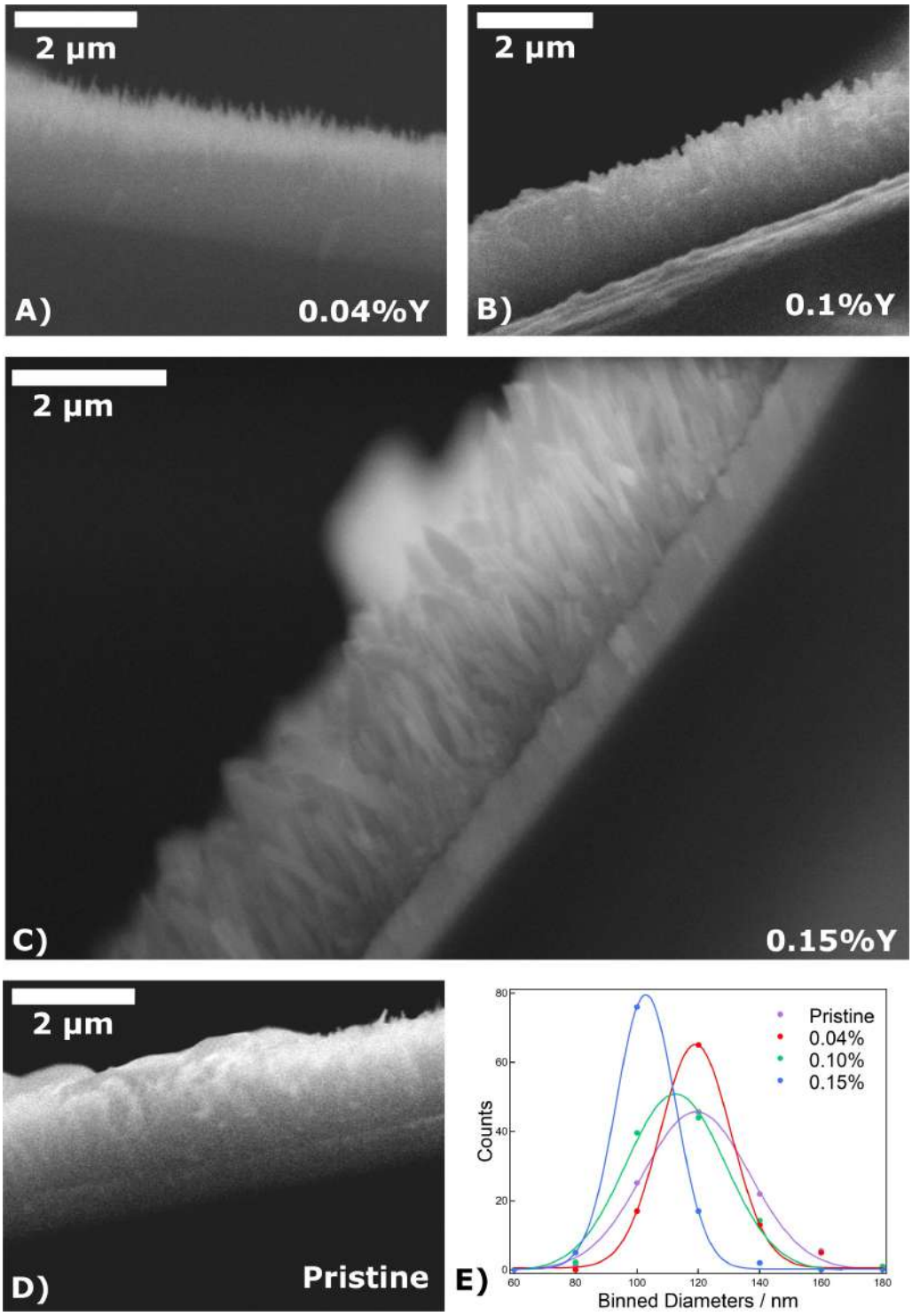


Figure S4.2: A-D) show Cross sectional SEM to determine the film thicknesses of the samples, E) shows diameter histograms.

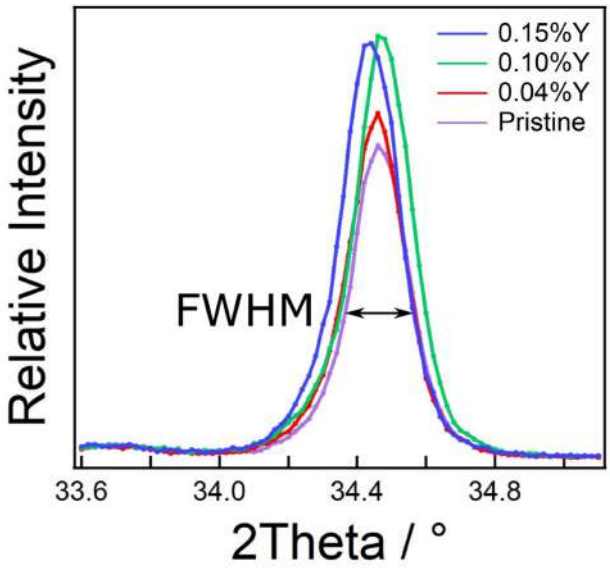


Figure S4.3: Displays a close up of 002 XRD peak of different doped samples.

### 4.6.1 Derivation of Equation (2)

The starting point of the equation used to derive the relation between potential $V$ and $C_s$ can be found in the work by Mora-Seró et al. Using their final relations determined as follows.

$$V_{sc} = -\frac{N_D e}{2\epsilon}\left[\frac{1}{2}(R^2 - x^2) + R^2 \ln\frac{x}{R}\right] \tag{S1}$$

Where $V_{sc}$ is the voltage drop across the space charge region and $e$ is electron charge. The permittivity constant is defined by $\epsilon = \epsilon_r \epsilon_0$ where $\epsilon_r$ is the dielectric constant of ZnO equal to 10,[114] and $\epsilon_0$ is the permittivity of free space; $R$ is the NR radius and $x$ is a central neutral region where $n = N_D$. Along with the capacitance per unit area, $C_s$ given by S2.[363]

$$C_s = \frac{2\epsilon x^2}{R(R^2 - x^2)} \tag{S2}$$

Which was rearranged to obtain $x^2$ for substitution.

$$x^2 = \frac{C_s R^3}{2\epsilon + C_s R} \tag{S3}$$

Leading to the final equation along with incorporating the definition $V_{sc} = V - V_{FB} - \frac{kT}{e}$ and neglecting the thermal term as follows,[278] picking up a factor of $\frac{1}{2}$ outside the square brackets.

$$V - V_{FB} = -\frac{N_D e}{4\epsilon}\left[R^2 - \frac{C_s R^3}{2\epsilon + C_s R} + R^2 \ln \frac{C_s R}{2\epsilon + C_s R}\right] \tag{S4}$$

Where $V$ is the raw value of the potential. Furthermore in order to use the raw capacitance, $C$ determined by PS Trace 4.8, the total geometric area of the rods was taken into account using the area calculation.

$$C_s = \frac{C}{(2\pi RL + \pi R^2)D} \tag{S5}$$

The term $L$ is the length of the rods in $\mathrm{cm}$ and $D$ is the total number of vertical nanowires, determined by measuring number density from SEM and extrapolating over the 1 $\mathrm{cm}^2$ exposed area.

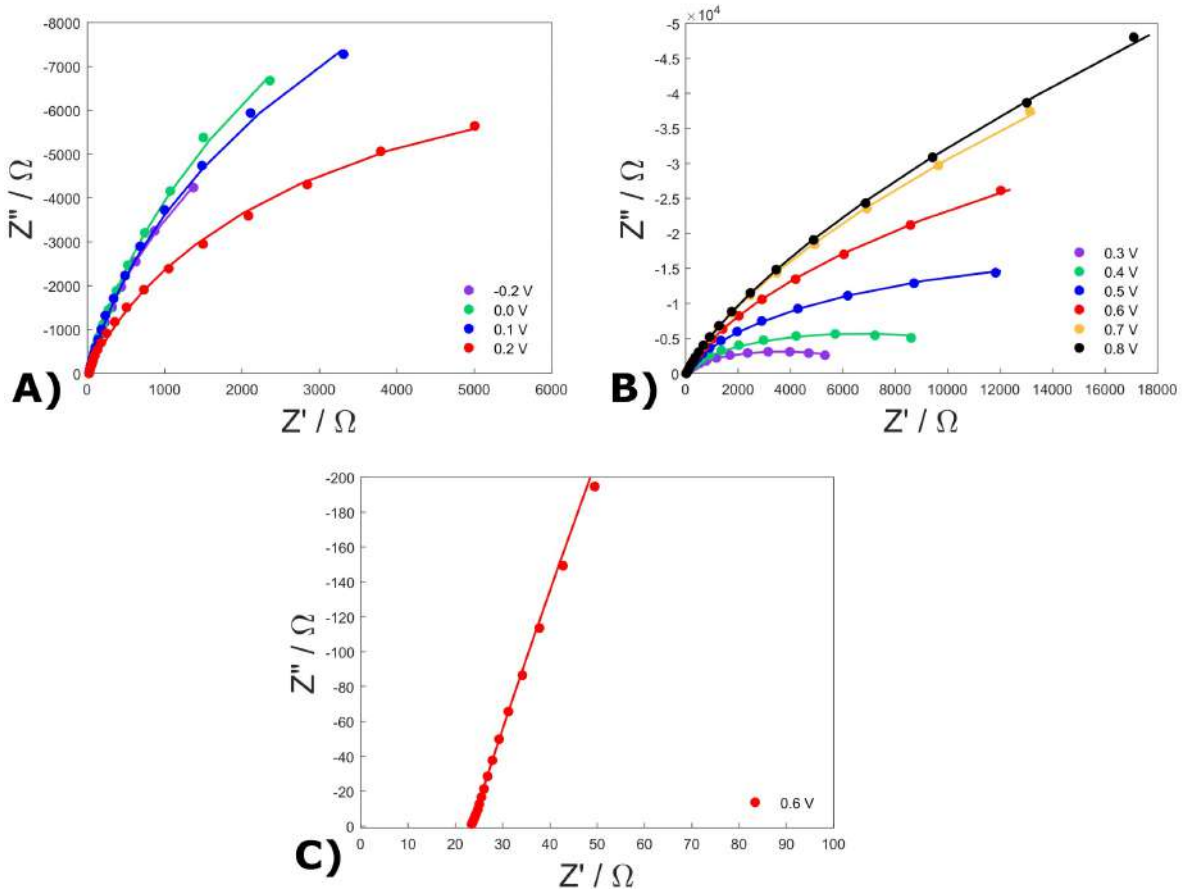


Figure S4.4: Displays the raw Nyquist plots of the pristine sample with experimental data (dots) and fitted models (lines) for the pristine sample. Expanded axes of spectra taken from -0.3 to 0 V can be found in C)

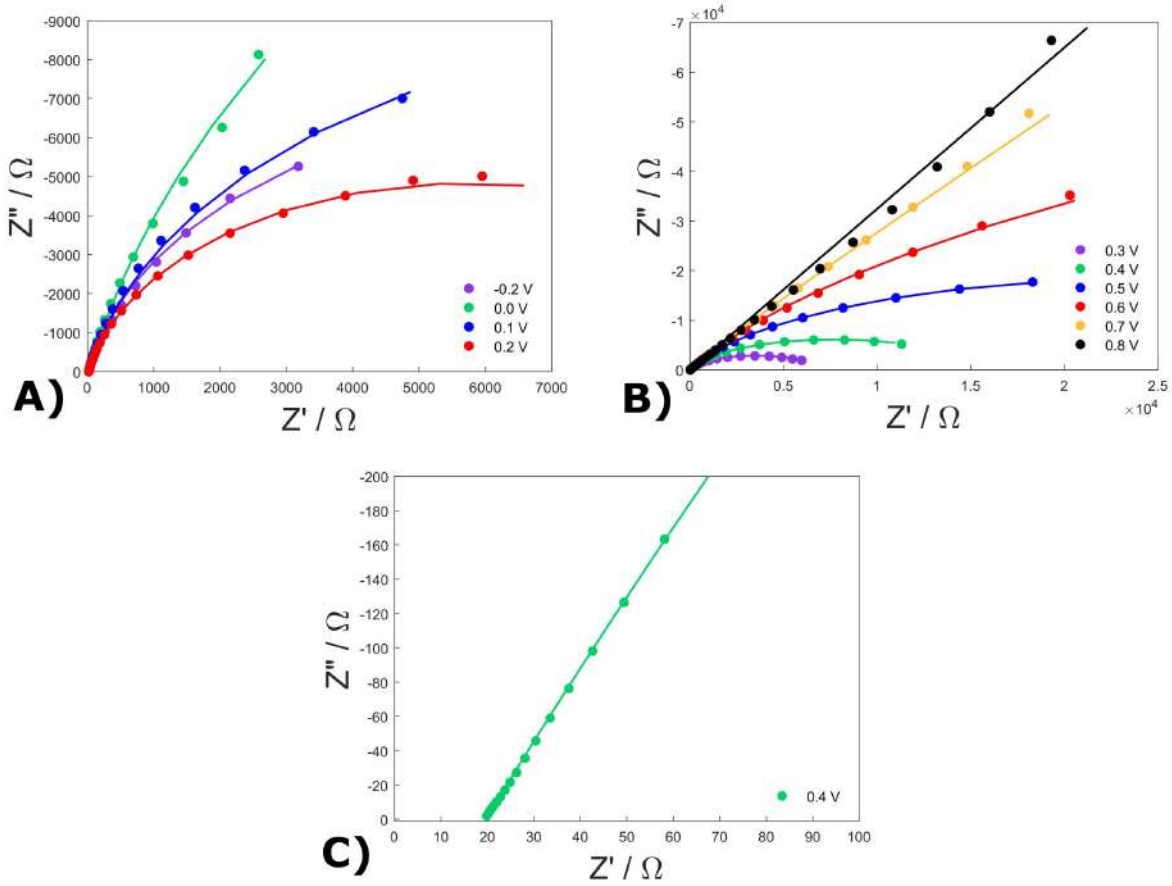


Figure S4.5: Raw Nyquist plots of the 0.1% Y sample with experimental data (dots) and fitted models (lines). Expanded axes of spectra taken from -0.3 to 0 V can be found in C)

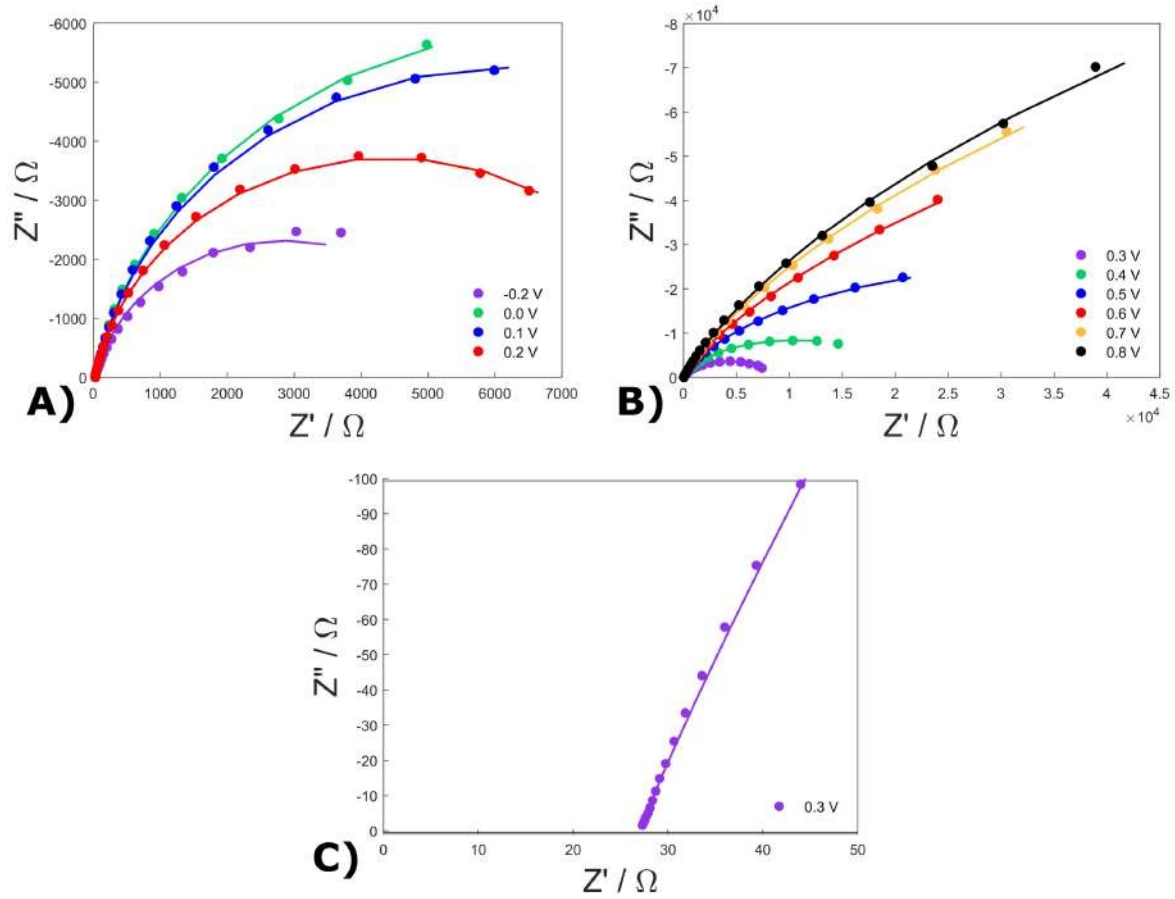


Figure S4.6: Raw Nyquist plots of the 0.15% sample with experimental data (dots) and fitted models (lines). Expanded axes of spectra taken from -0.3 to 0 V can be found in C).

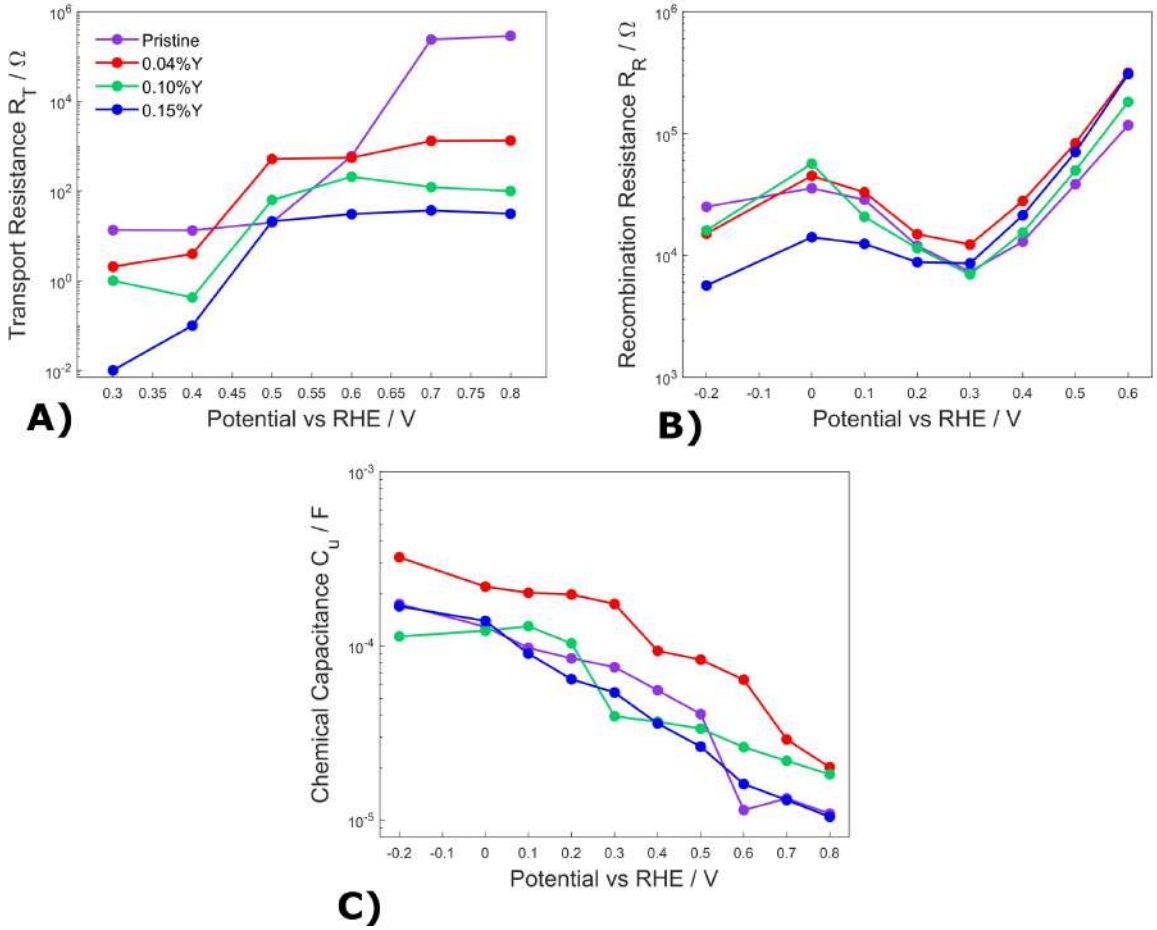


Figure S4.7: Displays raw model parameters of the transmission line determined from experimental Nyquist plots, A) shows transport resistance for the samples vs potential VRHE, B) shows recombination resistance and C) the chemical capacitance.

### 4.6.2 Kubelka-Munk Function

Proportional to optical extinction coefficient, $F(R)$, of the samples was calculated using the Kubelka-Munk function.[262]

$$F(R) = \frac{(1-R)^2}{2R} \tag{S6}$$

Where $R$ is the diffuse reflectance of the sample as a fraction.

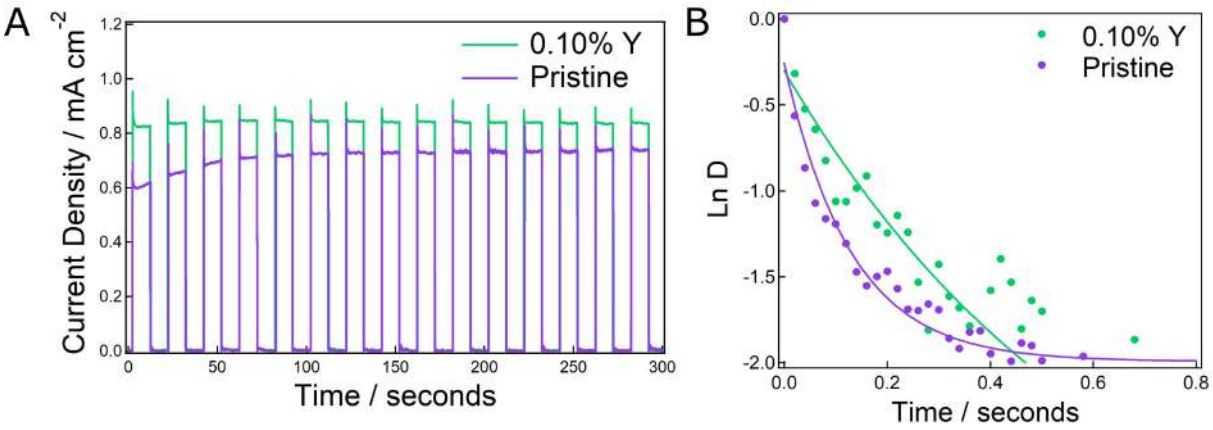


Figure S4.8: A) shows chronoamperometry data showing the stability of the anode performance. B) shows the normalised current decays from the chronoamperometry data.

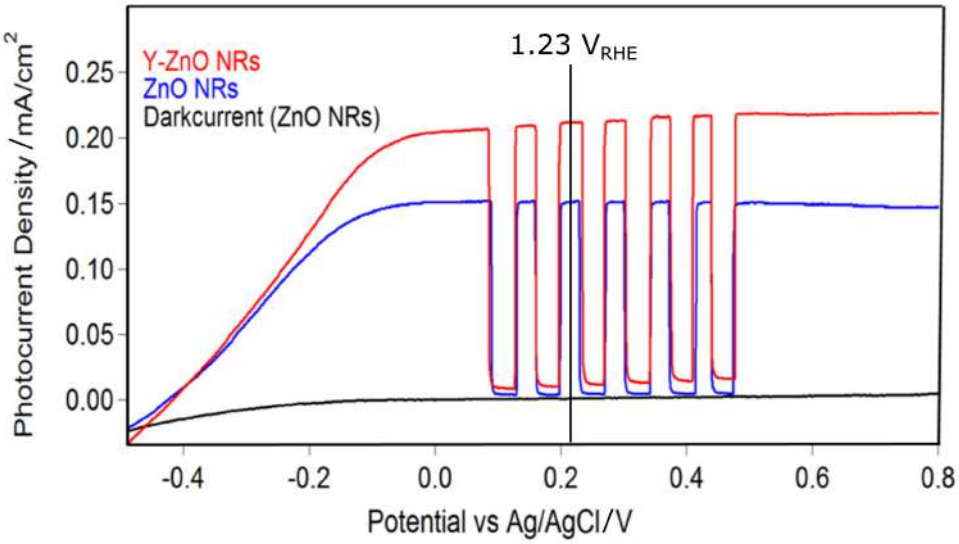


Figure S4.9: Hydrothermally synthesised nanowire photoelectrochemical water splitting results, performed in pH 13.6, 1 M KOH, with identical illumination to the microwave samples.

Table S4.1: A comparison of synthetic methods and quantities of yttrium atoms incorporated into the nanorods as measured by ICP-MS, as a % of zinc atoms. MeOHthermal data taken from Lee *et al.*[133]

| Solution Atomic Concentration / % | Microwave Synthesised ZnO / % | Hydrothermal Synthesised ZnO / % |
|---|---|---|
| 0 | 0 | 0 |
| 0.5 | 0.04 | 0.05 |
| 1 | 0.10 | 0.10 |
| 2 | 0.15 | 0.13 |

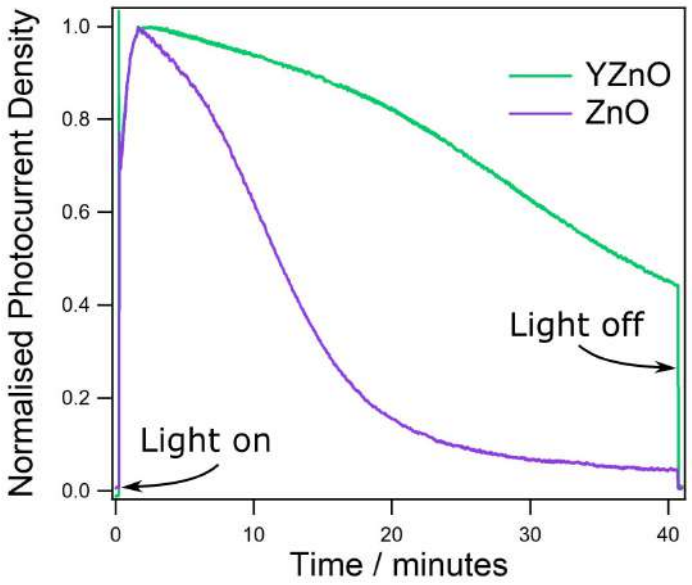


Figure S4.10: Photocorrosion data was measured after chronoamperometry of the same samples, with constant potential of 1.23 $V_{RHE}$ with constant illumination.

# Chapter 5

# Designing 3D Hematite Nanostructures for High Efficiency Solar Water Splitting

## 5.1 Abstract

Hematite ($\alpha$-$Fe_2O_3$) crystals were electrochemically deposited over vertically aligned conductive zinc oxide nanorods (NR) to form a specially designed 3D heterostructure with a unique triple layer structure. The structure formed with a thin layer of $ZnFe_2O_4$ sandwiched between the hematite and the ZnO, which forms a barrier to reduce the back migration of holes. Hence, the charge separation is significantly improved. The small unequal band gaps of $\alpha$-$Fe_2O_3$ and $ZnFe_2O_4$ help to enhance and broaden visible light absorption. The electron transportation was further improved by yttrium doping in the ZnO (YZnO) NRs, resulting in increased conductivity. This allowed the vertically aligned NRs to perform as electron highways, which also behave as effective optical waveguides for improved light trapping and absorption, since ZnO absorbs little visible light. All these benefits made the unique structures suitable for high performance photoelectrochemical (PEC) water splitting. Optimisation of $\alpha$-$Fe_2O_3$ thickness led to a photocurrent density improvement from 0.66 to 0.95 $\mathrm{mA\,cm^{-2}}$ at 1.23 $V_{RHE}$. This was further improved to 1.59 $\mathrm{mA\,cm^{-2}}$ by annealing at 550$^{\circ}$C for 3 hours, representing a record-breaking photocurrent for $\alpha$-$Fe_2O_3$/ZnO systems. Finally IPCE confirmed the successful generation and

transfer of photoelectrons under visible light excitation in the specifically designed heterostructure photoanode, with 5% efficiency for blue light, and 15% for violet light.

## 5.2 Introduction

Great innovation and radical new solutions are required to meet the threat posed by climate change.[380] Although great progress has been achieved in renewable energy generation, one of the key factors restricting electrification is energy storage.[285] PEC water splitting provides an elegant solution, harvesting and storing solar energy in chemical $H_2$ bonds.[21,24,32] Requiring aqueous insolubility and band edge positions suitable to surmount the over potentials for water redox, metal oxides such as $TiO_2$ and ZnO have been the focus of much literature for this application.[294,381] Boasting superior electronic properties and the simple solution growth of nanostructures, ZnO has yet to reach its full potential for solar water splitting.[124] The main restriction is its large band gap, 3.2 eV, rendering this material unable to absorb most sunlight, although this factor can be negated through the use of doping and coating.[141]

This has led to the investigation of many small band gap semiconductors for visible light sensitisation, including CdS,[382] $MoS_2$,[383] $WO_3$,[384] $Ta_3N_5$,[385] $BiVO_4$,[386] g-$C_3N_{415}$ and $\alpha$-$Fe_2O_3$.[171] Hematite $\alpha$-$Fe_2O_3$ is an excellent candidate to facilitate the photocatalytic water splitting reaction. It absorbs a greater portion of the solar spectrum with a narrow band gap of 2.1 eV. However, it suffers from poor charge transportation. The room temperature charge mobility for hematite is of the order of $10^{-2}\ \mathrm{cm\,V^{-1}\,s}$,[387,388] compared to 166 $\mathrm{cm\,V^{-1}\,s}$ for ZnO NRs.[389] Hence, its diffusion length of minor charge carriers (holes) is extremely short (2-4 nm) and so is the lifetime of charge carriers (6 ps, $\sim$1000 times shorter than $TiO_2$), resulting in the high probability of electron-hole recombination.[173,390,391] Meanwhile, hematite also has a relatively low optical absorption coefficient, due to its indirect band gap.[392] A minimum film thickness of 400 nm is needed to absorb 95% of the light at 550 nm.[230]

In fact, limited charge mobility and high recombination rate are the common problems for many semiconductors due to partial hybridisation of electronic structures. For hematite, several approaches have been taken to overcome the mobility problem. Firstly, dopants were introduced to modify various aspects of hematite properties selectively.[392] Adding tetravalent cations, such as $Si^{4+}$ and $Ti^{4+}$, has helped achieve the highest photocatalytic water splitting performances so far.[171,392] Alternatively, innovations in the design of morphologies also show promise. For example nanostructured hematite, like NRs,[393] nanowires,[180] cauliflowers,[234] or highly porous films could also address poor minority carrier diffusion.[175] With specific anisotropic nanoscale morphologies, charge recombination can be effectively reduced, resulting in significantly improved photocatalytic performance.[164] However, such unsupported nanostructures with material thickness of 4-5 nm could significantly weaken the mechanical and chemical stability of hematite. Hence, a new composite nanostructure design has been developed to achieve both improved charge mobility as well as short charge diffusion pathways, without sacrificing the stability of the hematite materials. For example, hematite nanocrystals were deposited on conductive nanowires made of Au and Si,[179,394] obtaining structures with conductive cores and hematite shells. However, due to the opaque nature of Au and Si, the light scattering within the nanostructures and light absorption by hematite is highly restricted. This in turn, could limit the photocatalytic performance.[179]

Although doping tetravalent cations can improve the overall photocatalytic performance, the approach is specifically effective for hematite.[171,395] Hence, it is important to develop a universal design that can be applied to any photocatalyst suffering from limited charge mobility and weak light absorption. In this paper, we present a 3D electrode platform based on vertically aligned transparent conductive oxide (TCO) nanorods. The TCO structure is formed with YZnO nanorods (NR) synthesised by rapid microwave assisted chemical deposition.[114] Hematite nanocrystals were deposited on the TCO NRs to test the enhancement of photocat-

alytic water splitting performance. In our previous work, Y doping has shown favourable effects due to high conductivity and increased NR aspect ratio.[396] The high conductance of the NRs minimises the energy cost with rapid photoelectron transport. ZnO is transparent in the visible light region, hence the vertically aligned NRs behave as optical waveguides for visible light. The photonic advantages are made clear in Figure S5.1, where simple Fresnel calculations show total internal reflectance above 40° of incident angle from ZnO to aqueous electrolyte. Conversely, light trapped within the ZnO has a finite probability of transmitting into the iron oxide at all incident angles, implying effective light trapping and delivery. With side-emitted light scattered between $\alpha$-$Fe_2O_3$ thin films, light illumination and absorption can be significantly improved. As such, only a very thin layer of hematite (8-16 nm) was required to coat the YZnO NRs, allowing a short diffusion distance for minority charge carriers to the electrolyte. By combining $\alpha$-$Fe_2O_3$ with TCO, YZnO NRs, the weaknesses of $\alpha$-$Fe_2O_3$, including: Limited charge mobility; short hole diffusion length; poor light absorption and the mechanical stability of the nanostructured hematite can be effectively overcome. More importantly, this novel design can be generally applied to any semiconductor materials with similar weaknesses.

Furthermore, upon annealing of the sample at 550°C, a $ZnFe_2O_4$ layer was formed at the interface between YZnO and $\alpha$-$Fe_2O_3$. This material has a favourable band structure with smaller band gap energy relative to YZnO and $\alpha$-$Fe_2O_3$. Therefore, a wider range of solar spectrum can be harvested.

In this work we demonstrate the benefits of doping ZnO with yttrium, and the electrochemical deposition and formation of $Fe_2O_3$ nanoparticles, which increase effective surface area to facilitate rapid evolution of oxygen under visible light excitation. Furthermore, the triple junction of YZnO/$ZnFe_2O_4$/$Fe_2O_3$ structure allows efficient charge separation evidenced by electrical impedance spectroscopy. The structure of the 3D photoanode design, light scattering and absorption, short hole diffusion pathways as well as fast charge transportation are summarised

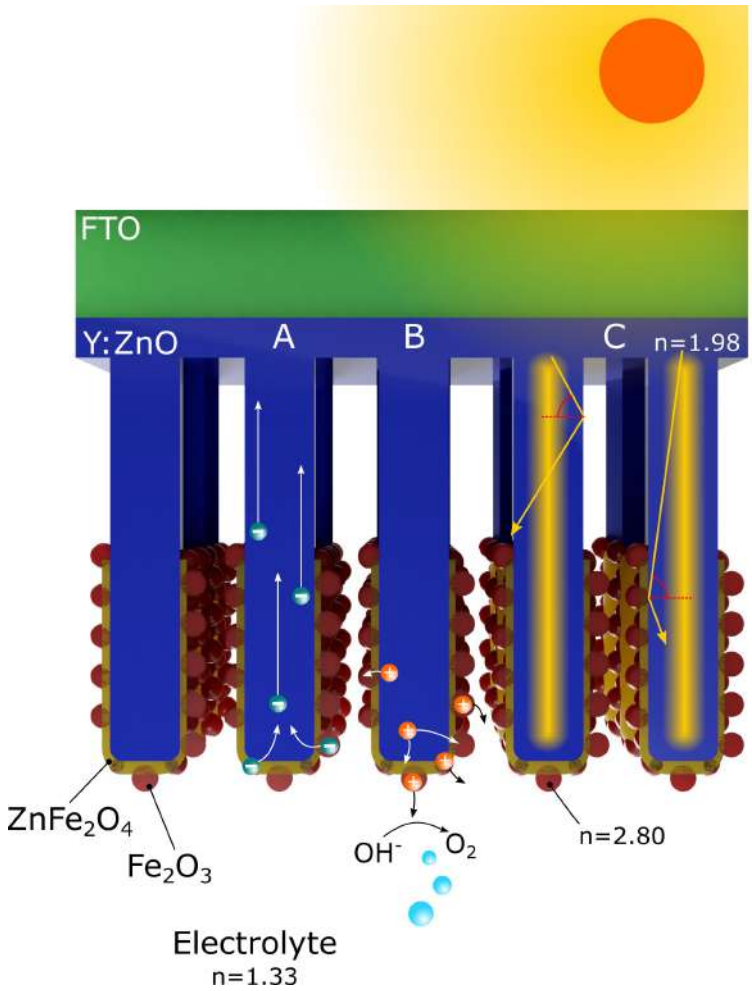


Figure 5.1: The YZnO/$ZnFe_2O_4$/$Fe_2O_3$ triple junction architecture of designed 3D photoanode with key mechanisms affecting the solar water splitting. The mechanisms include A), rapid electron transportation using conductive Y doped ZnO; B), short hole diffusion pathways to electrolyte and C), the visible light waveguiding through light scattering and side emission through ZnO NRs.

in Figure 5.1. Under optimised conditions, a top performance of 1.59 $\mathrm{mA\,cm^{-2}}$ at 1.23 $V_{RHE}$ was achieved, launching the novel nanostructured photoanodes to one of the highest performances in literature. The success of the junction is down to the suppression of electron hole recombination in the iron oxide species, alongside the effective electron transportation and light illumination through the TCO, YZnO NRs.

## 5.3 Experimental Methods

### 5.3.1 Y doped ZnO Synthesis

Transparent conducting glass substrates (fluorine doped tin oxide, FTO) of 12 × 20 $\mathrm{mm}$ were cleaned by sonication in a sequence of acetone, isopropanol and DI water for 20 minutes each. The substrate was seeded using a 0.1 M zinc acetate solution in DI water with added 0.6 wt% polyvinyl alcohol for viscosity. The solution was spin coated using a two stage program, 800 RPM for 90 seconds followed by 30 seconds at 2000 RPM. This was followed by annealing in air at 500°C for 20 minutes to form the zinc oxide seeding layer.[99] The vertically aligned NRs were synthesised using a rapid microwave assisted deposition described in previous work.[114] Briefly, the substrate was placed face down in 20 ml aqueous solution of 40 mM zinc nitrate and hexamethyltetramine (HMT) in 1:1 molar ratio. The sample was heated at microwave power of 100 W to 100°C for a 30 minute holding time.[114] A total of 4 heating cycles were used for each sample. Samples were subsequently annealed in air at 500°C for 30 minutes. Yttrium doped samples were produced using 1% molar addition of yttrium nitrate (with respect to zinc nitrate) to the growth solution. The achieved dopant concentration was previously measured to be 0.10 at% by ICP-MS.[396]

### 5.3.2 Electrochemical deposition of $Fe_2O_3$

All chemicals were purchased from Sigma Aldrich without further purification. Layers of iron oxide of various thicknesses were formed on the surface of the YZnO NRs by electrochemical deposition. Firstly an aqueous solution of 0.1 mM $FeCl_3$ was prepared and transferred to a 100 ml round bottom flask. The YZnO NR on FTO glass sample and a counter electrode of stainless steel foil were inserted into the $FeCl_3$ solution. The sealed system was then sonicated under vacuum condition to draw out the air between the NRs, shown in Figure S5.2A. In order to control the deposition rate and film thickness, constant electrochemical potentials were applied at -1.08, -1.15, -1.56 and -1.89 V respectively, which offers steady deposition current density of 20, 40, 80 and 120 $\mu A\,cm^{-2}$. The typical transient current density behaviour is shown in Figure S5.2C. The deposition time was fixed for 1 hour for all samples. Therefore, the film quality and thickness is controlled by the deposition rate, which is reflected by the deposition current.

After deposition, the samples were dipped in DI water in order to remove any excess solution, followed by annealing at 550°C for either 30 minutes, 3 hours or 5 hours to convert into hematite phase.[178] The substrate post deposition, followed by annealing shows a visible orange colour, shown in Figure S5.2B. The range of voltages used was significantly higher than found in literature due to the low concentration $FeCl_3$ solution required to protect the YZnO.[397]

### 5.3.3 Structural and Physical Characterization

Scanning electron microscopy (SEM, Leica Stereoscan 420) was used to characterise the morphology of the ZnO NRs and their various coatings, INCA software (Oxford Instruments) was used to measure the EDX spectra of the samples. To view the heterojunctions on a nanometre scale transmission electron microscopy (TEM, JEOL, JEM1400-Plus) was used. Microscopy images were processed using Image J software (National Institutes of Health, USA). And finally

available crystal phases on the sample were identified using powder x-ray diffraction (XRD, Siemens D500).

### 5.3.4 Photoelectrochemical and Optoelectronic Measurement

For the band gap energy measurement, a UV-Vis absorption spectroscopy was used (Lambda 265, PerkinElmer). Photoluminescence (PL) spectroscopy, used to infer recombination rate, was performed with a fluorescence spectrometer (PerkinElmer LS 45). Electrical Impedance Spectroscopy (EIS) was performed using a three electrode setup, with applied bias across the working photoanode and platinum counter electrode, and a KCl saturated Ag/AgCl reference electrode in a 1 M KOH aqueous electrolyte (pH 13.6). Nyquist plots were measured under illumination at a fixed DC potential (1 $V_{RHE}$) with a 10 mV AC sinusoidal modulation, at frequencies from 0.1 to 10,000 Hz. A calibrated solar simulator (Oriel LCS-100, Newport) including a built-in AM 1.5G filter with output power of 100 $\mathrm{mW\,cm^{-2}}$ was used as the light source. The electrochemical controller used for EIS measurement was Palm Sens 3 (Palm Sens BV) and the results were processed in PSTrace 4.5 (Palm Sens BV). The same system under dark conditions was used to measure Mott-Schottky plots at a fixed AC frequency of 1000 Hz, with a DC potential varied from 0 to 1.6 $V_{RHE}$. Surface valence band measurements were performed using x-ray photoelectron spectroscopy (XPS, Thermo Scientific K-alpha using Al K$\alpha$source). PEC water splitting was tested using linear sweep voltammetry (LSV). Standard three electrode set up was used with a potentiostat (EA163, eDAQ) scanning in a range from 0 to 1.8 $V_{RHE}$. Incident photon to current conversion efficiency (IPCE) was measured at 1.23 $V_{RHE}$ with a 300 W xenon lamp coupled with a monochromator. The incident light power was calibrated with a Newport optical power meter and silicon photodiode detector.

## 5.4 Results and Discussion

### 5.4.1 Structural and Physical Properties

When a cathodic current is applied, $Fe^{3+}$(aq) is reduced and deposited at the surface of the ZnO. The substrate changes colour from milky YZnO to a slight yellow tint with a dark grey tone, shown in Figure S5.2B. Once the sample is annealed at 550°C, the Fe deposition is oxidised to α-$Fe_2O_3$ and the sample colour became more typical light brown. The schematic of the electrodeposition atop the NRs followed by post annealing is shown in Figure 5.2

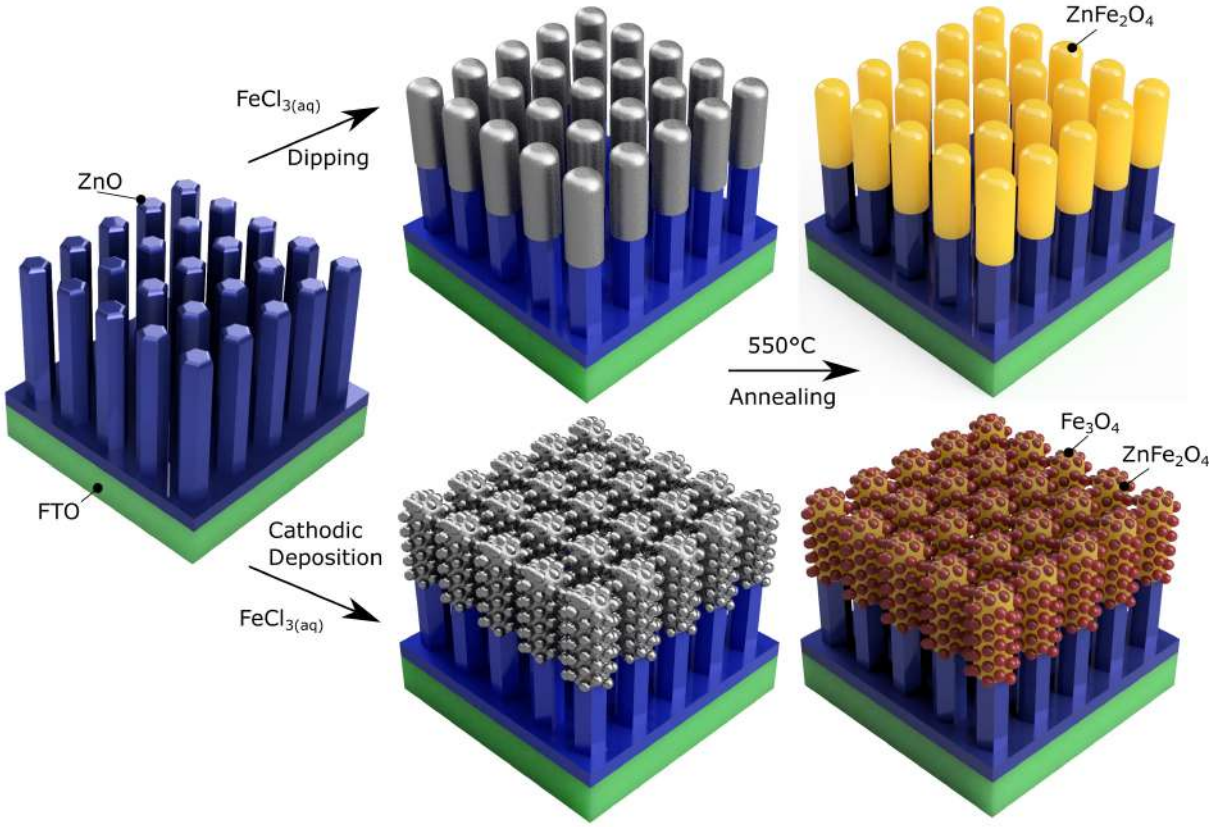


Figure 5.2: Schematic diagram of the deposition process, beginning with ZnO NW array (top left) and followed by the $ZnFe_2O_4$ layer build up from the unbiased reaction with $FeCl_3$(aq) (top right). With an applied bias, the reduction of $Fe^{3+}$ occurs, depositing $Fe_s$ on the surface (bottom right), this is then converted to α-$Fe_2O_3$ when thermally annealed in air at 550°C (bottom left).

The morphology of the hematite coated TCO YZnO array was studied by SEM, with a cross

sectional image in Figure 5.3A and top down images in Figure S5.3. The hexagonal wurtzite ZnO NRs cross section is still visible after deposition at a low current density of 20 $\mu A\,cm^{-2}$, shown in Figure S5.3A. The light deposition, confirmed to be surface $Fe_2O_3$ by EDX (Figure S5.4), was also observed on the surface. The density of the $Fe_2O_3$ coating was increased with greater deposition current density. At 80 $\mu A\,cm^{-2}$, Figure S5.3C, the nanorod structure is overwhelmed, and the channels between the YZnO are filled by cross linked $Fe_2O_3$, leading to suppression of surface area. At 120 $\mu A\,cm^{-2}$, Figure S5.3D, the surface is completely covered by a connected film of hematite. This film will restrict the infiltration of electrolyte within the NRs and have negative effects on the photocatalytic performance. Thus, it is important to avoid such films while achieving optimum film thickness of the hematite on the NRs. Under our experimental conditions, the optimal hematite morphology was observed at 40 $\mu A\,cm^{-2}$, shown in Figure S5.3B. Nanocrystals of $\alpha$-$Fe_2O_3$ are formed which increase surface roughness, beneficial to Faradic charge transfer to the electrolyte. The coated YZnO NRs show some brightened edges which can be associated to the formation of $ZnFe_2O_4$ at the interface between YZnO and $Fe_2O_3$. The top view SEM image in Figure S5.3A reveals bright rings on the edge of YZnO NRs. The formation of $ZnFe_2O_4$ and its effect on morphology was previously observed by Xu et al.[342] The edge brightening is likely due to the ferrimagnetic properties of $ZnFe_2O_4$ affecting the incoming electron beam.[398] The depth of the coating the overall surface morphology is better viewed in the angled cross sectional SEM of the 40 $\mu A\,cm^{-2}$ sample, Figure 5.3A. The aggregates of $\alpha$-$Fe_2O_3$ nanocrystals are visible toward the tips of the wires. The $ZnFe_2O_4$ could be indicated by the bright sleeves coating the YZnO side walls.

Powder XRD was used to confirm the presence of ZnO, $ZnFe_2O_4$ and $\alpha$-$Fe_2O_3$ on the surface, Figure 5.3B. XRD of pure $Fe_2O_3$ film without ZnO is also displayed as reference. The peaks observed confirm the presence of hematite, $\alpha$-$Fe_2O_3$, with dominant peaks occurring at 24.5°, 33.4°, 36.1°, 40.2° and 49.9° corresponding to crystal planes (012), (104), (110), (113)

and (024) respectively (ICDD 01-075-5065). On the Y doped ZnO samples, the strongest (104) peak is seen increased intensity with greater deposition current, from just a shoulder at 20 μA $\mathrm{cm}^{-2}$, to an obvious broad peak for 120 μA $\mathrm{cm}^{-2}$. This is the only peak visible from α-$Fe_2O_3$ on the coated ZnO NRs due to the relative thin film coating and significant peak overlap with the ZnO and FTO. Meanwhile, ZnO peaks are clearly visible, dominated by the diffraction from the (002) plane at 34.8°, typical for vertically aligned ZnO NRs. Finally, only appearing in samples with both iron and ZnO depositions, a small peak at 43.0° is visible, matching the $ZnFe_2O_4$ (400) peak (ICDD 22-1012). The peak is visible in all the coated samples, but is most intense for 20 μA $\mathrm{cm}^{-2}$, likely due to the majority of deposited Fe reacts with Zn to form $ZnFe_2O_4$ with the least formation of α-$Fe_2O_3$.

In order to accurately determine the structure of the triple junction at a nanometre scale, TEM was used to study the coated samples, shown in Figure 5.3C. A thin layer structure along with nanoparticles is observed coated on the NRs. The 8 nm thickness film directly attached to the ZnO NRs is likely to be the $ZnFe_2O_4$. Such a thin layer explains the low intensity of the XRD peak. Connected nanoparticles forming a mesoporous network (right) are likely to associated with the α-$Fe_2O_3$ phase. The particles have an average diameter of 16 nm. This information sheds light on the advantages of electrochemical deposition, firstly there is a good electrical contact between the YZnO/$ZnFe_2O_4$ and YZnO/α-$Fe_2O_3$ interfaces, allowing smooth charge transfer. Secondly the iron phases with typically small minority carrier path length, have small enough domains that charge can reach the surface reaction centres before recombination.[399] Finally the nanoparticle network of α-$Fe_2O_3$ allows increased roughness and therefore surface area, than the smooth NRs, promoting high hole transfer rate to the electrolyte.

The structure of the triple junction was more clearly visible under HRTEM, as shown in Figure 5.4. In this case, atomic resolution was obtained for the NRs, nanoparticles and the thin film coating that encased the NRs. Such distinctive morphological features are clearly identified

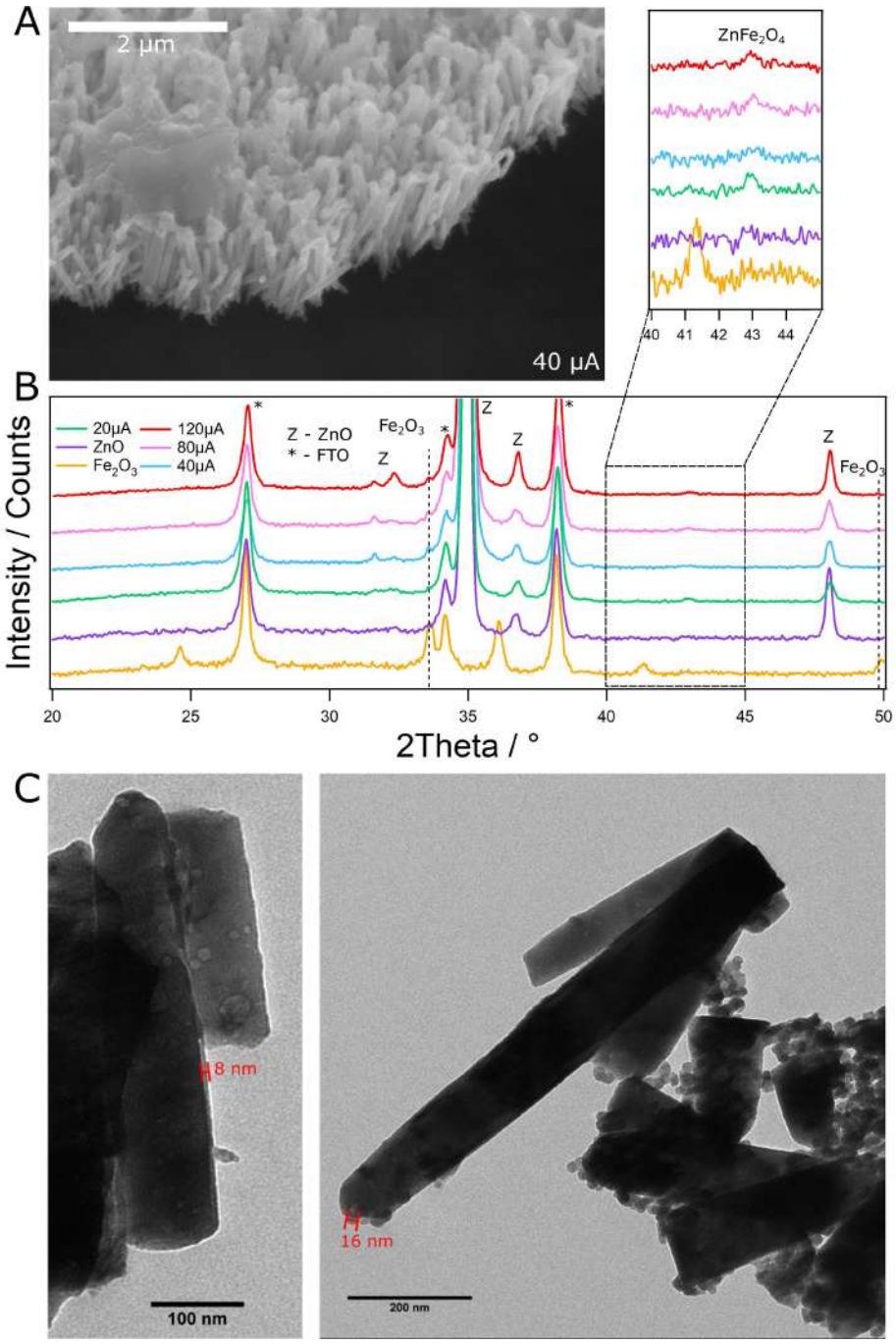


Figure 5.3: A) SEM image shows an angled cross sectional image of the 40 µA $\mathrm{cm}^{-2}$ deposited sample after annealing. B) powder XRD curves of various $Fe_2O_3$ coating thickness, along with pure ZnO and $Fe_2O_3$ samples, with expanded view of the $ZnFe_2O_4$ peak occurring at 43°. C) shows TEM images of hematite coated ZnO NRs deposited at 40 µA $\mathrm{cm}^{-2}$.

in the zoomed out view of Figure 5.4A, while Figure 5.4B, C and D respectively corresponds to their higher resolution images reviewing lattice constants of each phase. Unsurprisingly, the NR was confirmed as wurtzite zinc oxide with an atomic spacing of 2.45 Å, the (101) plane spacing, as well as displaying a (002) spot in the FFT of the image in Figure 5.4B. Figure 5.4C shows the atomic spacing of a spherical nanoparticle, showing high crystal orientation with 4.62 Å spacing, assigned as 2× (006) planar spacing of hematite. Though this is a high index for this structure, its high prevalence has been previously observed in the ZnO / $Fe_2O_3$ system by Zhang *et al*.[400] This could be due to the compatibility of this plane with the atomic spacing of $ZnFe_2O_4$, leading to high abundance near the interphase boundary. Finally, Figure 5.4C shows wide spacing of 4.88 Å in the lighter region that forms the full coating around the NR. This is likely to be the 311 plane of $ZnFe_2O_4$ matching the dominant phase observed by Xu et al.[401]

In summary hematite nano crystals were formed together with a thin layer of $ZnFe_2O_4$ at the interface between YZnO and α-$Fe_2O_3$. This novel layered structure formed with three materials utilises the suitability of band edges allowing much improved charge separation and greatly increased visible sunlight water splitting. While highly conductive Y doped ZnO provides rapid transport, α-$Fe_2O_3$ yields photoexcited electrons and $ZnFe_2O_4$ offers an effective electronic barrier blocking the return of electrons from ZnO to the α-$Fe_2O_3$. The hybrid structure in this work shows a great deal of inhomogeneity as evidenced by the SEM and TEM images, therefore accurate geometric models cannot reasonably be calculated. This is largely due to the simple wet chemistry utilised to grow the hybrid structures, rather than alternative methods such as chemical vapour deposition which yield more uniform NRs and coatings.[402] The advantage of the methods used here are high scalability and low cost,[403] with potential for higher water splitting performance due to the novel hybrid structure.

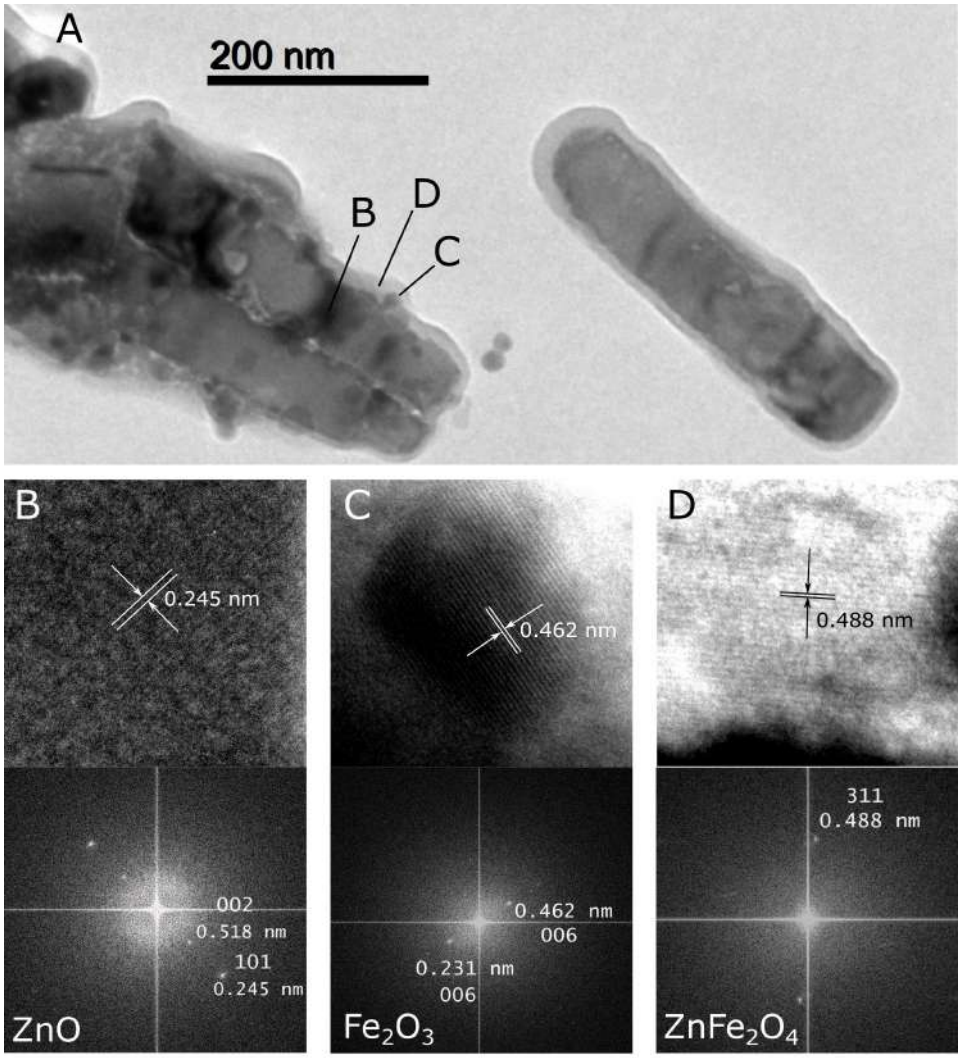


Figure 5.4: A) HRTEM micrograph of the sample at low magnification with specific sites labelled. B) the magnified image of the NR showing (top) atomic real space and (bottom) the FFT of the image, C). The nanoparticle magnified image with atomic spacing (top) and FFT (bottom), D). The thin film coating of the NR magnified, atomic spacing (top) and FFT (bottom).

### 5.4.2 Band Structure and Water Splitting Performance

With a composite layered semiconductor structure, an internal electrical field can be formed due to the alignment of their valance and conduction bands. This field could improve the charge separation and hence improve the photocatalytic charge efficiency. For PEC water splitting, they must form a junction with suitable band alignment to allow electron transfer away from the solution, and the converse for holes.[21]

To determine the band gap energies, $E_g$, of the junction, UV-Vis absorption measurements were applied to pure $Fe_2O_3$, YZnO and $Fe_2O_3$ coated YZnO samples (coated at 40 $\mu A\,cm^{-2}$). Tauc plots are shown in Figure 5.5A.[179] The UV-vis absorption spectra of all coated samples are displayed in the supplemental information in Figure S5.5A and B. Assuredly, the pure $Fe_2O_3$ sample and the YZnO yielded $E_g$ values of 2.11 and 3.18 eV respectively, typical of these metal oxides. It is worth noting that the Y doped sample displayed a red shift compared to the pristine ZnO prepared by the same method, due to the doping forming new electronic states, outlined in greater detail in our previous work.[404] These results also show that the iron deposition has successfully sensitised the YZnO to visible light, allowing the generation of photoexcited electrons using a far greater portion of the solar spectrum. Electronic transitions from both ZnO and hematite are visible for the $\alpha$-$Fe_2O_3$ coated YZnO NRs, but significantly shifted. The 2.11 eV gap associated with $\alpha$-$Fe_2O_3$ gained a blue shift to 2.34 eV, and the YZnO experienced a red shift to 3.05 eV. This is likely due to two simultaneous doping effects caused by mobile zinc and iron ion migration from sustained 550$^{\circ}$C heating. Firstly, $Fe^{3+}$ introduced into the zinc oxide lattice has been previously shown to decrease the electronic band gap.[399] Secondly, $Zn^{2+}$ is a known p-type dopant for hematite,[404] this could impart new impurity states below the Fe2O3 valence band causing the blue shift. Finally, no discernible band gap could be determined for $ZnFe_2O_4$ therefore the value was taken from literature as 2.1 eV.[405]

In order to determine electronic properties, electrochemical impedance spectroscopy was

used to determine key parameters. The electronic band configuration can be determined using the Mott-Schottky relation applied to EIS data taken in dark conditions, displayed in Figure 5.5B. Measurements were taken at a fixed frequency of 1 kHz and a voltage scanned from -0.4 to 1.6 $V_{RHE}$ at 0.05 V intervals. The capacitance is modelled with a simple Randle's circuit, and the results are plotted $1/C^2$ against potential vs RHE. These plots in Figure 5.5B provide useful physical information such as dopant density $N_D$, and flat band potential, $V_{FB}$, corresponding to the Fermi level of the material. The M-S plot of pristine ZnO can be found in Figure S5.5C.

The determined M-S values can be found in Table S1 alongside their detailed calculation in the supporting information. Y doping leads to a significant increase in dopant density and a 0.2 V negative shift in $V_{FB}$, confirming the conductivity increase from doping. The carrier density of ZnO is nearly doubled with Y doping from $7.5 \times 10^{19}$ $\mathrm{cm}^{-3}$ (ZnO) to $1.35 \times 10^{20}$ $\mathrm{cm}^{-3}$ (YZnO), in agreement with our previous work.[396] This confirms the electron highway function of the conductive YZnO NRs which can efficiently transport charge to the FTO. The pure α-$Fe_2O_3$, conversely has a more positive value of VFB alongside a lower n-type doping of $5.08 \times 10^{19}$ $\mathrm{cm}^{-3}$.

As no pure $ZnFe_2O_4$ sample was synthesised in this work, the precise band positions could not be determined. However, it was reported to have a $V_{FB}$ of 0.83 $V_{RHE}$ with an accompanying ND value of $3.63 \times 10^{16}$ $\mathrm{cm}^{-3}$.[406] These values are crucial as they determine the nature of the n-n junction. At the interface, the higher n-type doped sample will donate electrons forming a space charge region, equalising $E_F$ across the junction.[407] Therefore, in this case, YZnO will donate electrons to the contacting layer of $ZnFe_2O_4$ causing a positive potential shift in $E_F$ in the former, and negative in the latter. By extension, the same effect will occur from $Fe_2O_3$ to $ZnFe_2O_4$, shifting $E_F$ to be more positive within hematite.

XPS was also used to determine valence band (VB) position by scanning for the valence

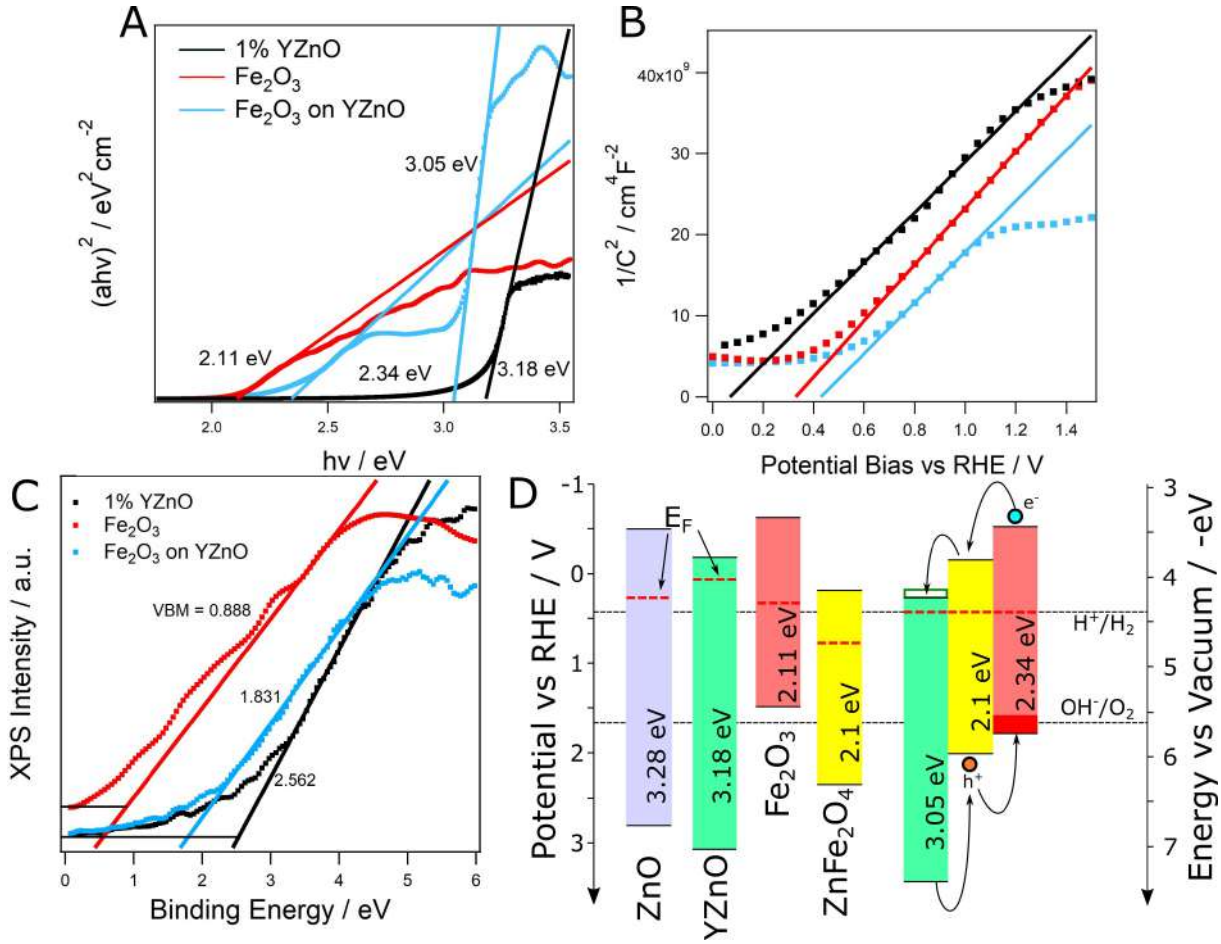


Figure 5.5: A) shows the Tauc plots calculated from UV-Vis absorbance data used to calculate the direct band gaps of the samples. Mott-Schottky plots of the uncoated Y doped sample, the pure $Fe_2O_3$ sample and the optimised 40 µA coated sample are displayed in B). C) shows the XPS valence band maxima survey of the samples. The calculated Fermi level, conduction band and valence band positions of the semiconductors found in this study are shown with respect to the redox potentials of water in D). Valence band positions with respect to the vacuum level were calculated by summing the binding energy with the vacuum energy (+4.44 eV).[237,375] The right hand portion of D) displays the junction at equilibrium.

edge from 0 to 10 eV binding energy, followed by extrapolating linear regions to the base line intercept. Once the VB is determined, the conduction band edge was calculated using the corresponding $E_g$. The results for YZnO, $Fe_2O_3$ and the composite material can be found in Figure 5.5C, whereas the VB of undoped ZnO sample is displayed in Figure S5.5D. The VB of ZnO and YZnO were measured to be 2.182 and 2.562 eV respectively, in good agreement with literature.[375] The value for pristine $Fe_2O_3$ was determined to be more positive, at 0.888 eV, similar to the value of 1.4 eV determined by Li et al.[408] Finally the hematite coated YZnO NRs yielded a value of 1.831 eV. As a technique XPS is only surface sensitive, as the path length of electrons excited within the bulk is typically around a few nm due to rapid reabsorption.[409] Therefore, based on the HRTEM micrographs indicating homogenous coverage of $ZnFe_2O_4$, it can be assumed that the junction valence band maximum is due to this material, bolstered by its close match with previously reported values.[405] Using this information, the full electronic structure of the triple heterojunction can be mapped out, displayed in Figure 5.5D. By aligning the Fermi levels, it becomes clear that the triple junction has significant improved charge separation, which could enhance the efficiency for solar water splitting. Firstly, due to their significantly difference in $E_g$ values, both UV and visible light will be utilised to generate holes. Secondly, the VB positions of the triple junction gives suitable alignment for rapid hole transfer from the core YZnO NRs through the $ZnFe_2O_4$ thin film to the surface particulate $Fe_2O_3$. Thirdly, the conduction band positions allow the electrons to cascade into the YZnO cores, which, in turn, shuttle electrons quickly to the counter electrode with high conductivity. This is essential for removing charge before recombination with holes and consequentially enable high rate evolution of hydrogen at the platinum surface. This mechanism is confirmed by $E_F$/band shifts predicted by dopant density values, anticipating high performance solar water splitting.

The impact of the designed novel NR structure can be seen clearly in the dramatic enhancement in PEC water splitting, Figure 5.6. Firstly, the effects of $Fe_2O_3$ coating and the Y-doping

in ZnO on photocurrent density are presented in Figure 5.6A. With the 40 $\mu A\,cm^{-2}$ Fe deposition rate, the photocurrent increased by 44% over the uncoated, undoped ZnO, from 0.66 to 0.83 $mA\,cm^{-2}$ at 1.23 $V_{RHE}$. This is due to the benefits of the n-n triple junction previously described, alongside the absorption of visible light photons due to the low band gap of $Fe_2O_3$ and $ZnFe_2O_4$. Using the additional beneficial transport properties of Y doping alongside coating, the performance increases further to 0.95 $mA\,cm^{-2}$. Despite high natural donor defect density in the microwave synthesised sample,[114] the conductivity gains by yttrium doping allow the same 40 $\mu A\,cm^{-2}$ coating to yield 14% higher photocurrent at 1.23 $V_{RHE}$.[396] This is due to more efficient transportation of charge carriers from the solid/electrolyte interface by YZnO. The pure $Fe_2O_3$ sample shows critically low water splitting due to the high recombination and likely higher charge transfer resistance $R_{CT}$, managing 13 $\mu A\,cm^{-2}$ at 1.23 $V_{RHE}$.

The performance is highly sensitive to the deposition current density as shown in Figure 5.6B, with the lightest coating, 20 $\mu A\,cm^{-2}$, only slightly outperforming the uncoated YZnO NRs. This is due to the lack of extra light absorption with such a thin layer of $Fe_2O_3$. Conversely the 120 $\mu A\,cm^{-2}$ sample sees a large performance drop, achieving a lower photocurrent than the uncoated sample. The reasons for this are twofold, firstly the unfavourable morphology measured by SEM indicates a loss in surface area, restricting the access to electrolyte. Secondly, electron-hole recombination stifles the performance of thick $Fe_2O_3$ film, due to the short minority carrier path length in $\alpha$-$Fe_2O_3$.[410] This is evidenced by the largest charge transfer resistance, $R_{CT}$, indicated by the greatest arc radius in its Nyquist plot, Figure S5.6A and B. The values of $R_{CT}$ were calculated using a simple Randle's circuit and plotted against deposition current in Figure S5.6C. A large $R_{CT}$ is due to a greater resistive barrier for charge to overcome to enter the electrolyte, caused by the poor charge transportation of $Fe_2O_3$. The photoluminescence spectra in Figure S5.6D, directly measure the outgoing photons when recombination occurs. Once the photoabsorbing layer becomes sufficiently thick, the photoexcited electrons are un-

able to reach the YZnO resulting in increased charge recombination. Therefore an increase in PL intensity is seen with deposition current.

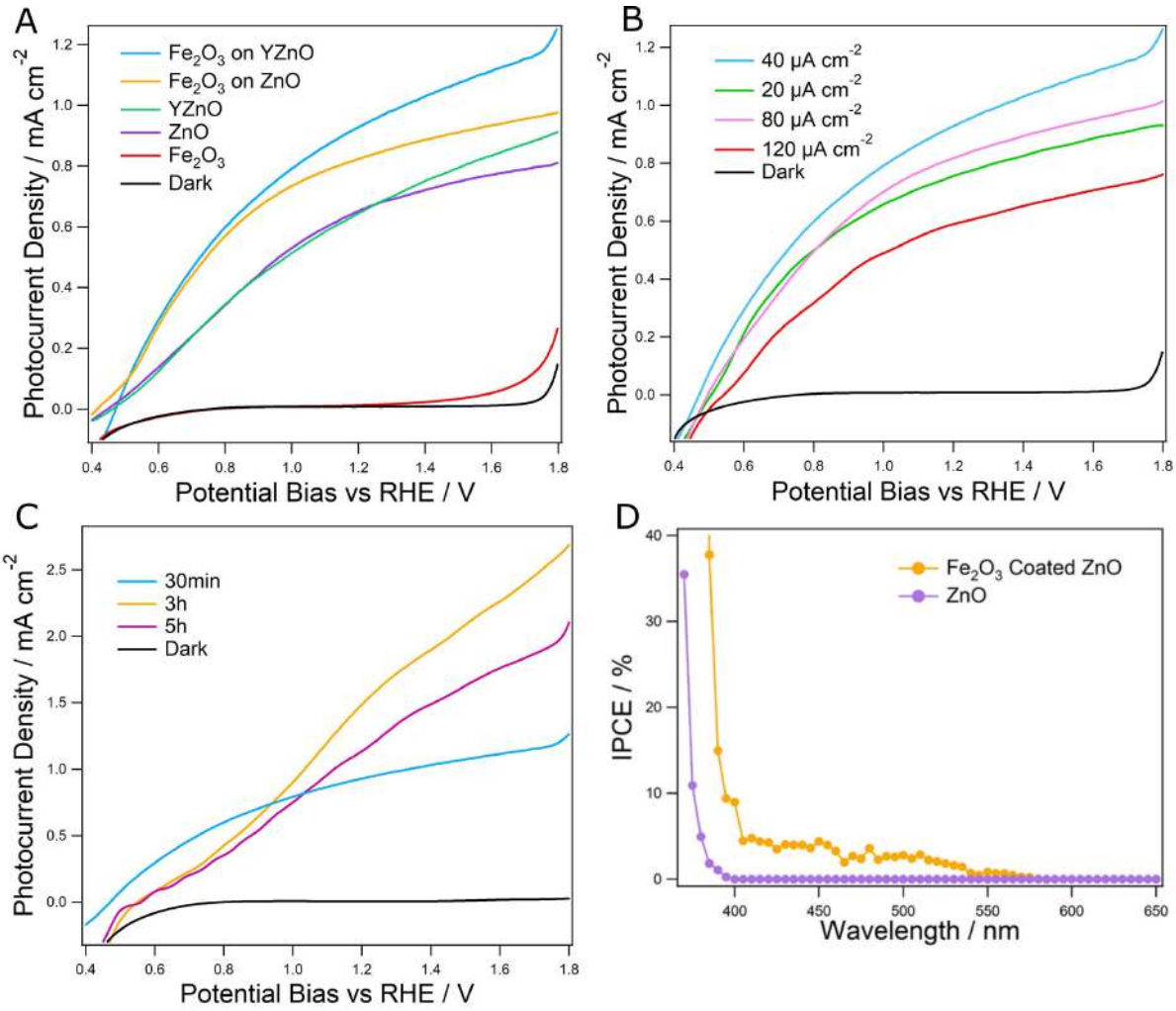


Figure 5.6: A) shows the general comparison of doped vs undoped samples, with and without coating, the performance optimisation from the various electrodeposition currents is shown in B). C) Shows the annealing duration optimisation, showing further enhancement, and finally D) shows the incident photon to current efficiency.

The 40 µA $\mathrm{cm}^{-2}$ samples were further optimised by different durations of annealing. Longer periods of air annealing can be used to greatly improve the crystal quality of hematite,[164] reducing the electron hole recombination rates. The results are displayed in Figure 5.6C, displaying

a dramatic further enhancement in photocurrent density for the optimised duration of 3 hours at 550°C, up to 1.59 $\mathrm{mA\,cm^{-2}}$ at 1.23 $V_{RHE}$. This 67% enhancement over the sample annealed for 30 minutes represents a significant improvement, and a 2.4 times increase over the uncoated nanorods. Stepped light/dark LSV was also performed, Figure S5.77A and B, which shows negligible dark currents. Furthermore, the optimised anode performances were stable in solution at a fixed potential of 1.23 $V_{RHE}$, shown in Figure S5.7C. There is no significant decay of photocurrent over time.

The optimised performance catapults this work to the frontier of solar water splitting, achieving nearly the highest photocurrent ZnO/iron oxide photoanode in literature. To the authors knowledge this is the most efficient solar water splitting device utilising a ZnO/$Fe_2O_3$ junction at 1.23 $V_{RHE}$. Typically these devices achieve negligible photocurrent in this potential region, requiring larger potential bias to promote water oxidation.[400,411,412] The most successful device constructed by Hsu *et al.* generated 1.25 $\mathrm{mA\,cm^{-2}}$ at 1.23 $V_{RHE}$ through spin coating $Fe_2O_3$ on pristine ZnO NRs.[178] More success has been achieved by the coating of $ZnFe_2O_4$ on ZnO surfaces, with typical photocurrents ranging from 0.05 to 0.57 $\mathrm{mA\,cm^{-2}}$.[413,414] The great achievement of 1.72 $\mathrm{mA\,cm^{-2}}$ by Xu *et al.* was achieved through coating Al doped ZnO, on NRs.[342] This implies further optimising the ZnO NRs with doping may improve our samples further.

Finally, incident photon to current conversion efficiency can be found in Figure 5.6D elegantly displaying the visible light sensitisation of the final sample. This data shows a significant efficiency increase at photon energies higher than 529 nm (2.34 eV) due to the $Fe_2O_3$ absorption onset, increasing to $\sim$5% from 450 - 500 nm. Optical power density vs wavelength is displayed in Figure S5.8. Some photocurrent is generated at wavelengths as long as 575 nm, likely due to the presence of the 8 nm layer of $ZnFe_2O_4$ on the rods, injecting electrons at even lower energies. This is in contrast to the uncoated ZnO sample which remained flat ($\sim$ 0 %)

at wavelengths longer than 400 nm. At this wavelength the coated sample experiences a stark increase in efficiency again, due to the effective band gap reduction of ZnO, rising to 10% at 395 nm. All this confirms the success of the triple junction, able to absorb visible light photons and transfer photoexcited electrons to yttrium doped ZnO NR highways, for greatly improved solar water splitting.

## 5.5 Conclusion

In conclusion a novel electrodeposition method was developed and used to build a ZnO / $Fe_2O_3$/ $ZnFe_2O_4$ triple junction photoanode, based on yttrium doped ZnO NRs. The new coating method allowed fine control the morphology of hematite grown on the surface of the nanorods, as evidenced by SEM, XRD and TEM. Meanwhile the presence of $ZnFe_2O_4$ was also confirmed, forming a thin layer coating on the NRs. This had the effect of sensitising the ZnO to visible light, as evidenced through UV-Vis absorption spectroscopy and IPCE, utilising a favourable junction cascade for electron transfer to the ZnO and hole transfer to the solution. This effectively reduced the charge recombination effects in $\alpha$-$Fe_2O_3$ as measured by EIS and PL spectroscopy, leading to an optimised coating thickness at a current density of 40 $\mu A\,cm^{-2}$. The yttrium doping of the NRs yielded a 14% enhancement over the pristine ZnO NRs, confirming the effects of conductive ZnO in addition to its photon trapping and light waveguiding effects. Optimising hematite crystallinity by control the annealing process led to a champion photocurrent of 1.59 $mA\,cm^{-2}$ at 1.23 $V_{RHE}$, representing a 2.4 times enhancement over the uncoated ZnO NRs. This work represents an important advancement in the application of nanostructured junctions to PEC water splitting.

## 5.6 Supporting Information: Designing 3D Hematite Nanostructures for High Efficiency Solar Water Splitting

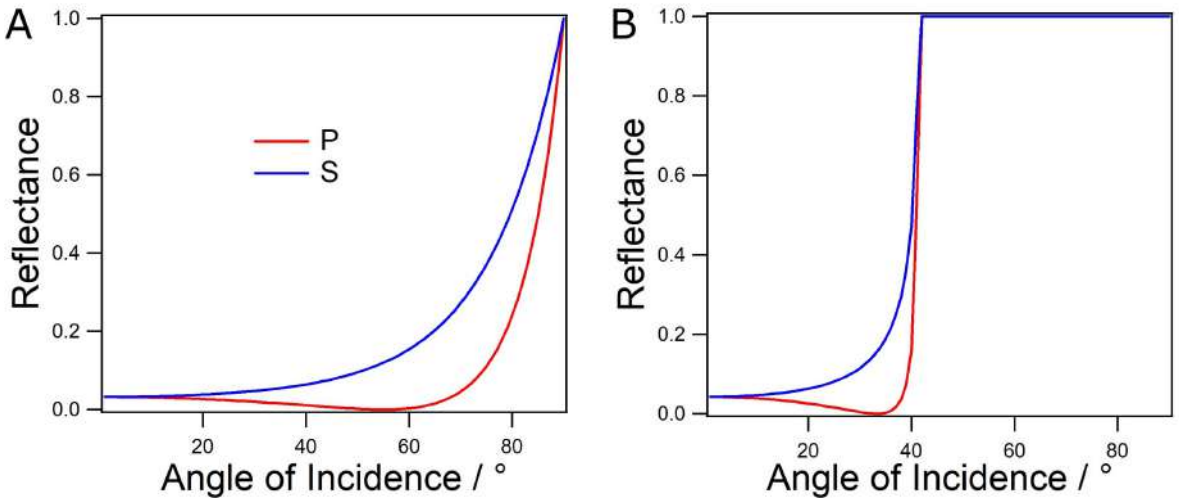


Figure S5.1: A) shows a simple calculation of the reflectance at the ZnO/$Fe_2O_3$ interface, showing some transmission even at high angle, for S and P polarisations. B) shows the reflectance from ZnO to aqueous electrolyte, yielding total internal reflection beyond the critical angle of 40°.

### 5.6.1 Reflectance Calculation

The reflectance calculations displayed in Figure S5.1 were performed using simple Fresnel equations for P and S polarisation respectively. The refractive indices of the doped ZnO, α-$Fe_2O_3$ and water were found to be 1.98,[415] 2.80 and 1.33 respectively for 590 nm wavelength visible light.[416,417] The equation for S polarisation reflectance, $R_S$, is as follows.[418]

$$R_S = \left[ \frac{n_1 cos\theta_i - n_2 \sqrt{1 - \left(\frac{n_1}{n_2} sin\theta_i\right)^2}}{n_1 cos\theta_i + n_2 \sqrt{1 - \left(\frac{n_1}{n_2} sin\theta_i\right)^2}} \right]^2 \quad \text{(S1)}$$

The corresponding equation for P polarisation reflectance, $R_P$ is as follows.

$$R_P = \left[ \frac{n_1 \sqrt{1 - \left(\frac{n_1}{n_2} sin\theta_i\right)^2} - n_2 cos\theta_i}{n_1 \sqrt{1 - \left(\frac{n_1}{n_2} sin\theta_i\right)^2} + n_2 cos\theta_i} \right]^2 \quad \text{(S2)}$$

Where incident angle is given by $\theta_i$, $n_1$ is the initial medium refractive index and $n_2$ is the secondary material refractive index.

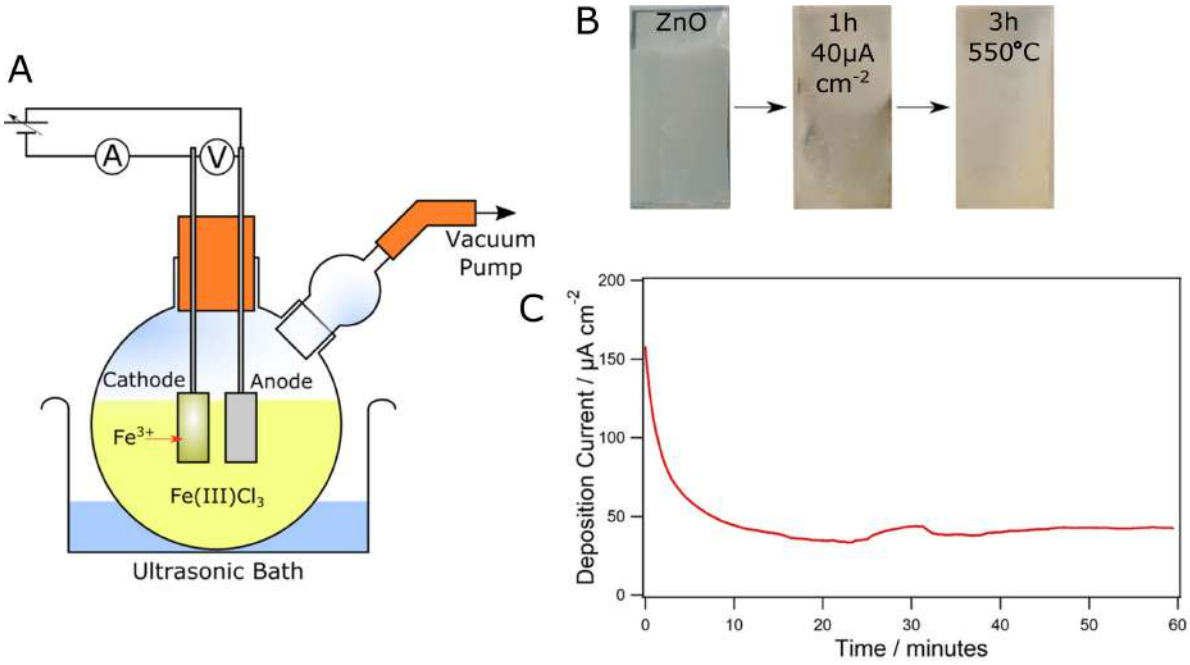


Figure S5.2: Schematic diagram of the deposition process, A), showing the setup including ultrasonic bath, and electrode positions. B) shows photographs of the sample before and after deposition, followed by post annealing. C) shows the typical fixed potential current density of the deposition over time for the 40 $\mu\mathrm{A\,cm^{-2}}$ sample.

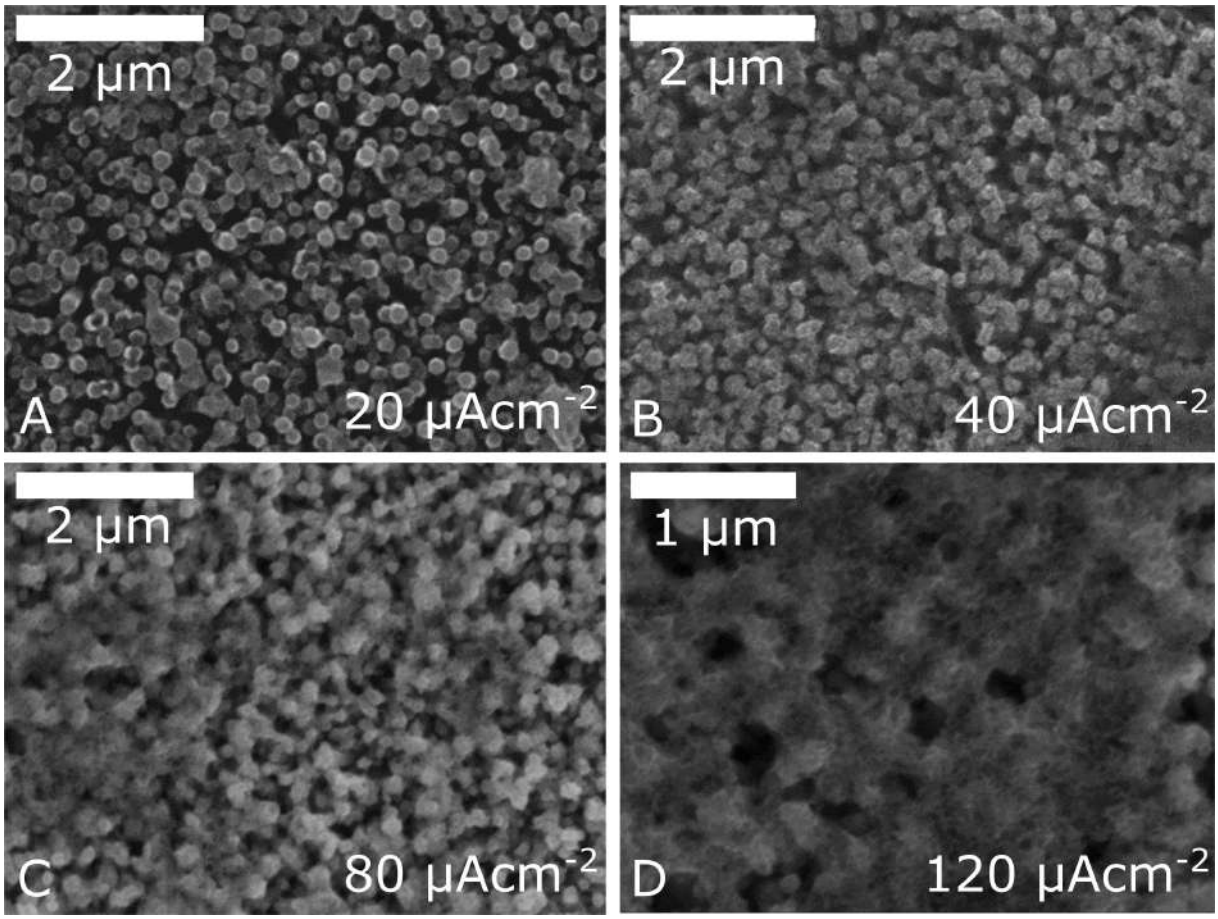


Figure S5.3: Top view SEM images of samples deposited at A) 20, B) 40, C) 80 and D)120 µA $\mathrm{cm}^{-2}$.

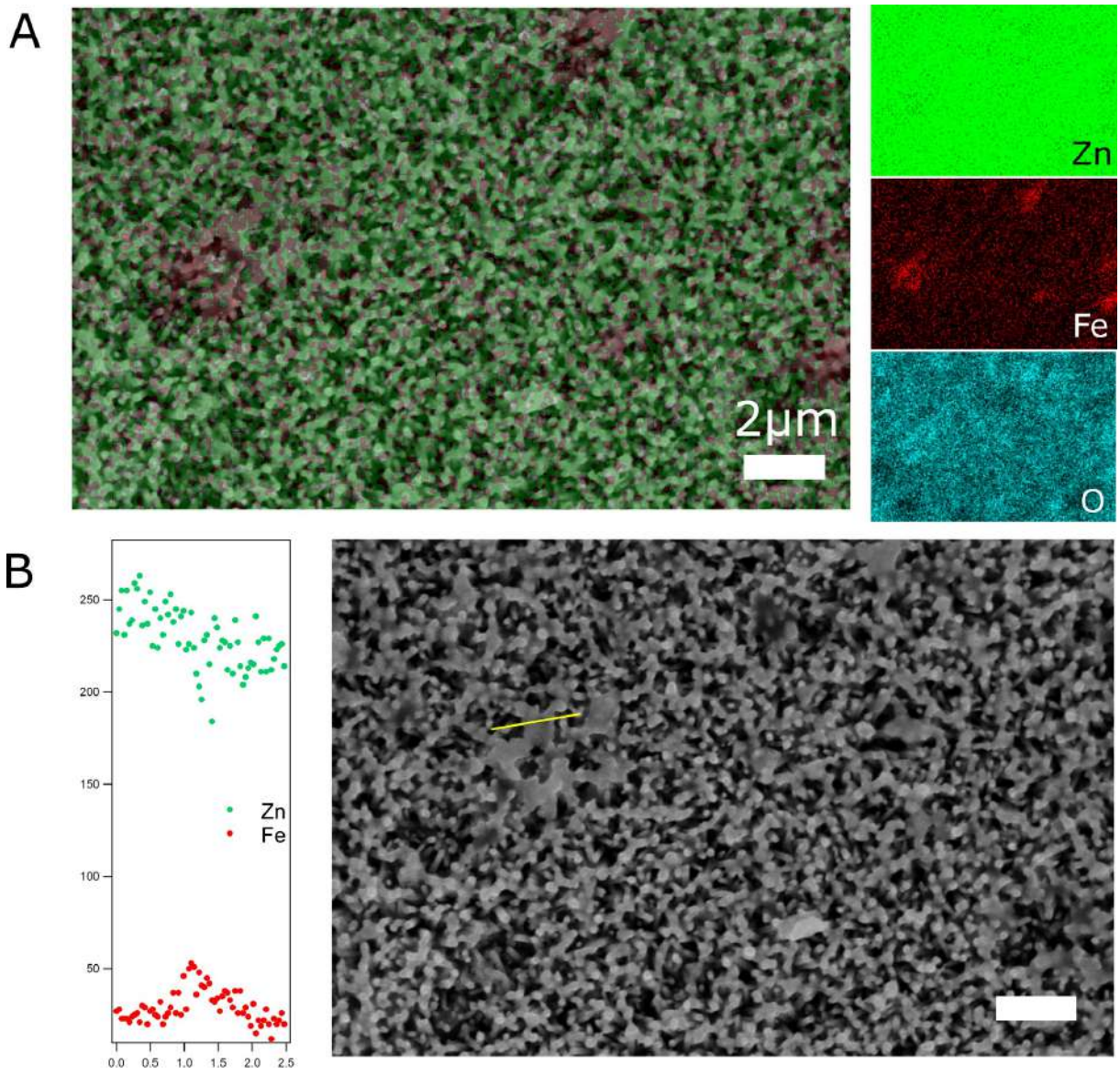


Figure S5.4: A) shows EDX maping of the sample area of a typical 40µA, with composite image of Zn and Fe (left) and component elements (right). B) Shows an EDX line scan of an $Fe_2O_3$ aggregate on the surface.

### 5.6.2 Calculation of Band Positions

The following details how Fermi level, dopant density $N_D$ and conduction band position were calculated for this study.

$$\frac{1}{C_{sc}^2} = \frac{2}{e\epsilon\epsilon_0 A^2(N_d - N_a)}\Delta\phi_{sc} \tag{S3}$$

The values $\epsilon$ and $\epsilon_0$ correspond to the relative permittivity of the material (taken as 10 for ZnO and 80 for $Fe_2O_3$)[143,237] and permittivity of free space respectively. The surface area contact with the electrolyte is given by $A$. The key values that can be determined from the gradient of the linear region of the plot is the $N_d$, donor density and $N_a$ the acceptor density. Often simplified as $N_D = N_d - N_a$ where $N_D$ is the dopant density, a majority p-type semiconductor will give a negative gradient and n-type, positive. The extent of doping is given by $N_D$.[278] The value of $\Delta\phi_{sc}$, the potential across the space charge layer is defined by S4.

$$\Delta\phi_{sc} = V_E - V_{FB} - \frac{kT}{e} \tag{S4}$$

Yielding more useful physical values, $V_E$ is the measured DC potential and the final thermal term is often neglected. The flat band potential $V_{FB}$ is the required voltage to remove the charge depletion layer at the interface and prevent band bending, corresponding to the Fermi level of the material. This can be obtained from the intercept of the extrapolated linear region with the x axis.[223]

Table S5.1: Displays values determined from Tauc plots, MS plots and XPS.*[405]**[406]

| Semiconductor | $E_g$ / eV | $N_D$ / $m^{-3}$ | $V_{FB}$ vs RHE / V | VB / eV |
|---|---|---|---|---|
| ZnO | 3.28 | $7.5 \times 10^{25}$ | 0.27 | 2.547 |
| YZnO | 3.18 | $1.35 \times 10^{26}$ | 0.07 | 2.562 |
| $Fe_2O_3$ | 2.11 | $5.08 \times 10^{25}$ | 0.33 | 1.151 |
| $ZnFe_2O_4$ on YZnO | 2.1* | $3.63 \times 10^{22}$** | 0.83** | 1.831 |
| Full Junction | n/a | n/a | 0.43 | n/a |

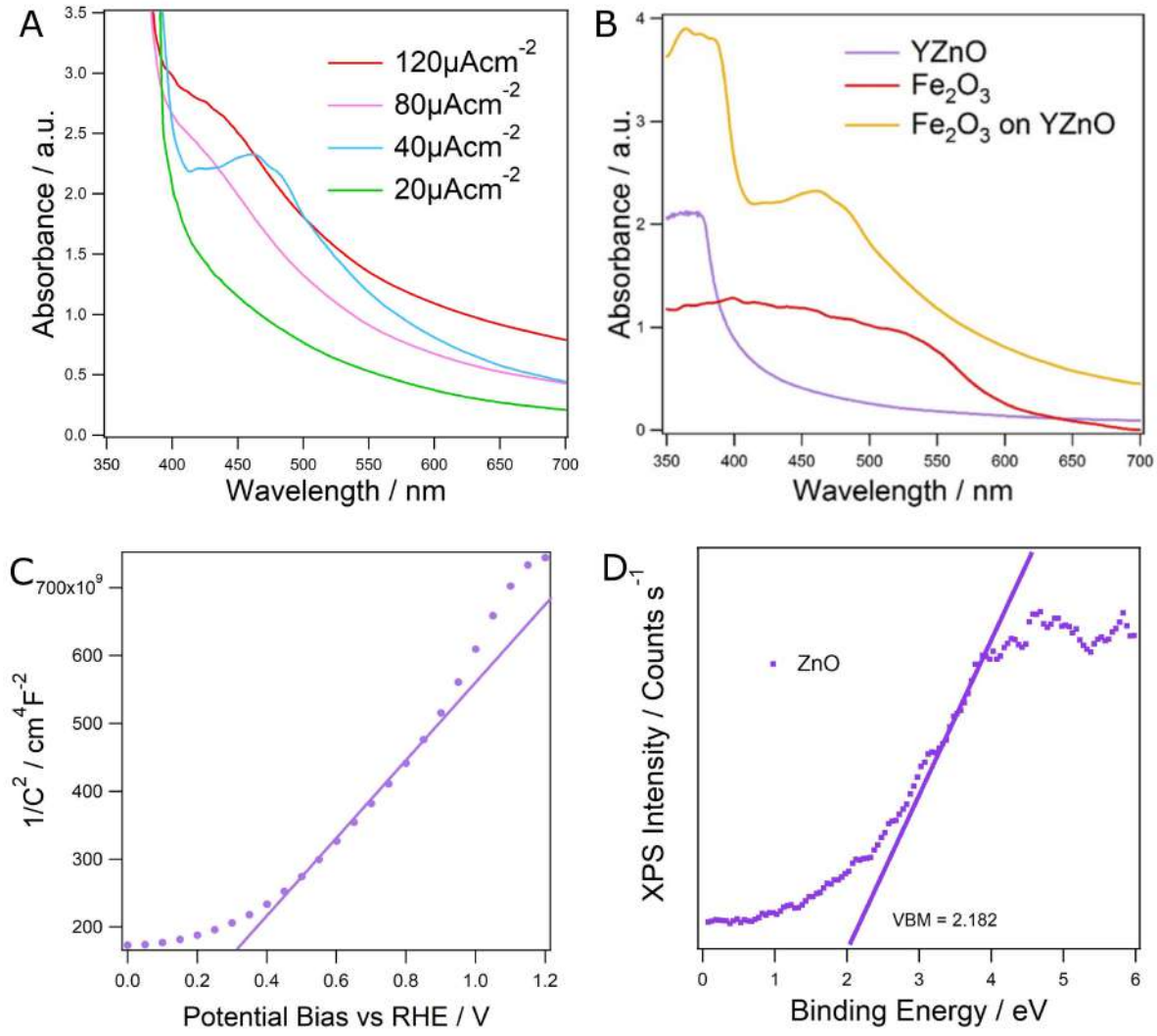


Figure S5.5: A) shows the UV-Vis absorption spectra of the various coating current densities, and B) shows the spectra for the uncoated YZnO, pure $Fe_2O_3$ and the optimised sample. C) shows the Mott-Schottky plot of the undoped ZnO sample for comparison. D) shows the XPS valence band determination for undoped ZnO.

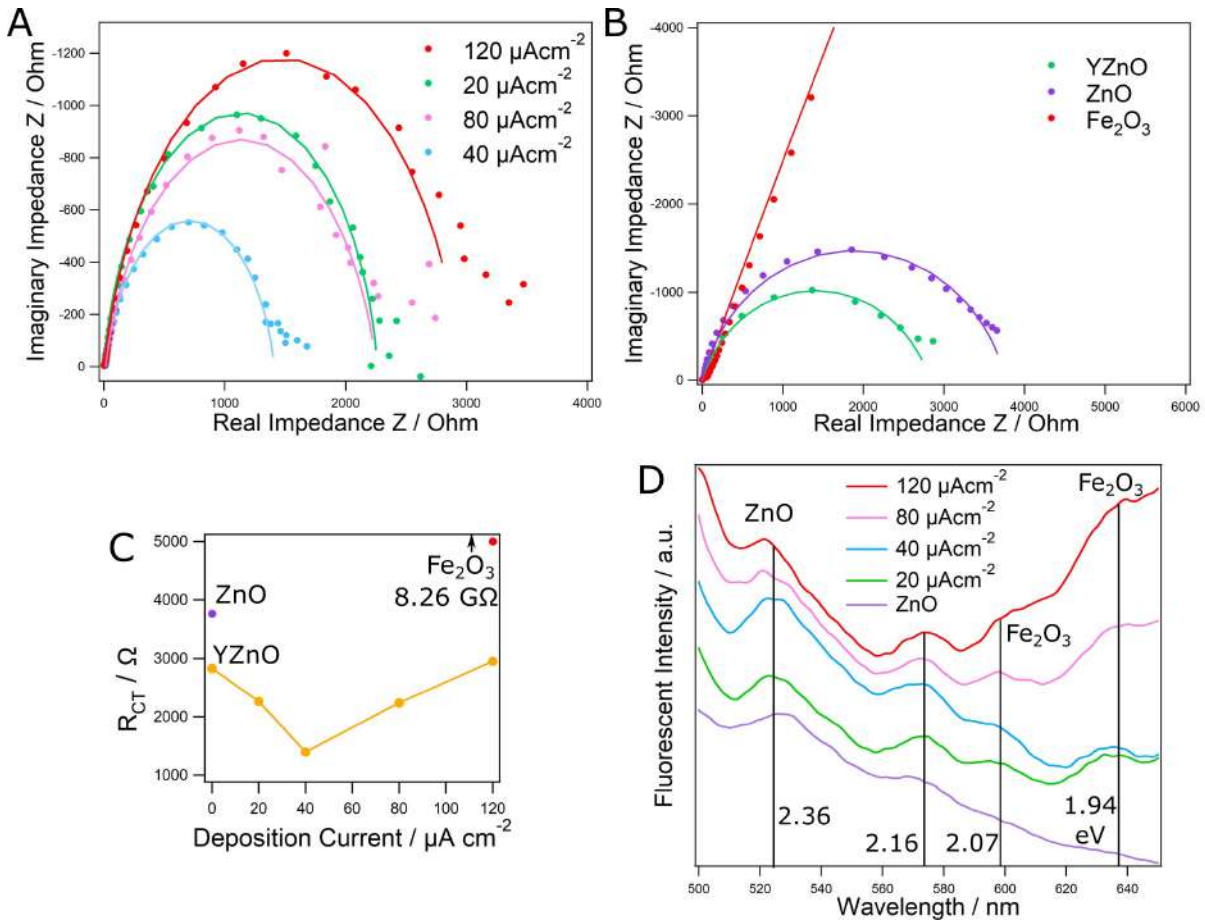


Figure S5.6: A) shows the raw Nyquist plots and fits of the coated samples at different coating rate. B) shows the Nyquist plots of undoped ZnO, Y doped ZnO and pure $Fe_2O_3$, C) shows the charge transfer resistance $R_{CT}$ against coating thickness as well as for pure ZnO and $Fe_2O_3$. D) shows the PL data for the various sample coatings, along with the pristine ZnO sample.

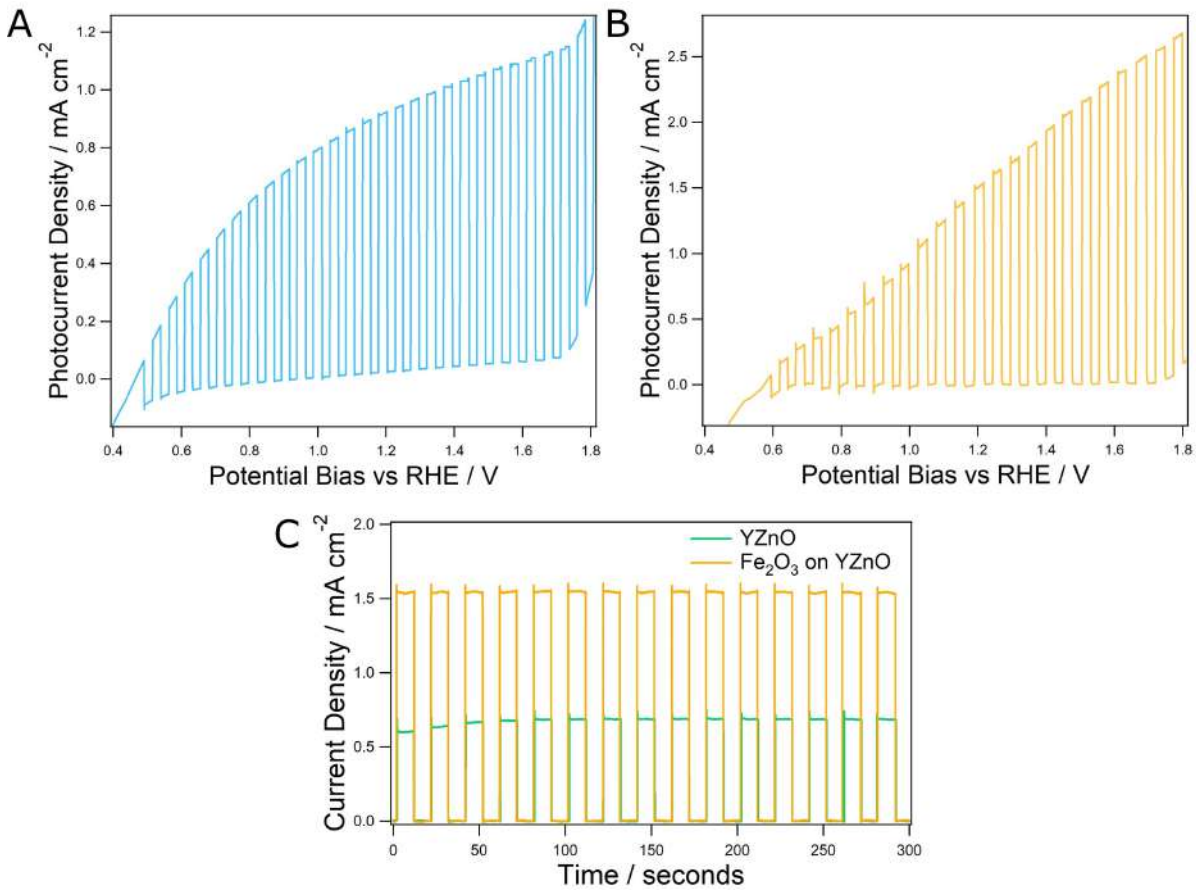


Figure S5.7: Shows the light/dark stepped linear sweep voltammetry of the top performing photoanodes, with 30 minutes of annealing A), and 3 hours annealing B). C) Shows the stability of the nanostructures at 1.23 $V_{RHE}$, through photocurrent vs time.

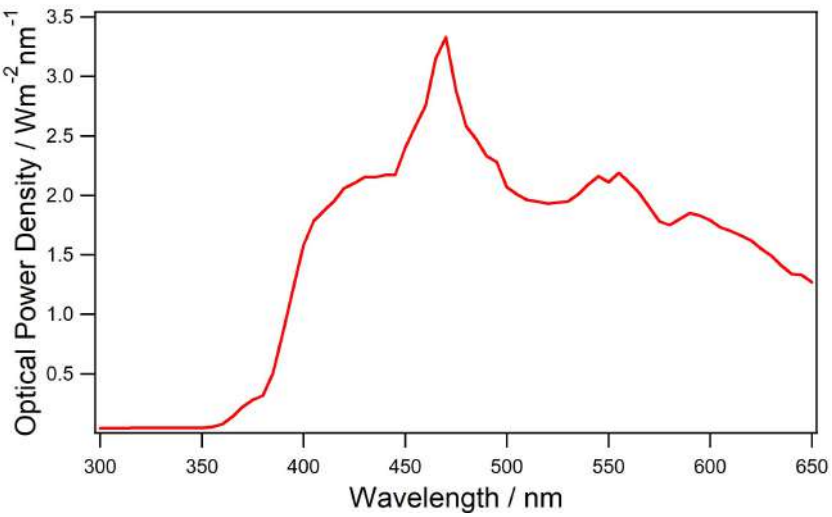


Figure S5.8: Shows the photon flux vs wavelength of light in nm for the Xenon light source used for IPCE, calibrated to 100 $\mathrm{mW\,cm^{-2}}$ using a silicon photodiode detector.

# Chapter 6

# In Situ Decoration of Doped ZnO Nanowires with $\alpha$-$Fe_2O_3$ Nanosheets for Solar Water Splitting

## 6.1 Abstract

Hybrid metal oxide nanostructures have drawn much attention recently in their ability to overcome disadvantages in any specific material to achieve high performance solar water splitting. Using anodic electrochemical deposition, yttrium doped ZnO nanowires (NWs) were decorated with $\alpha$-$Fe_2O_3$ nanosheets (NSs) which led to more favourable morphology as measured by SEM. The high surface area hybrid was optimised by well controlled geometry, altered by varying the duration of deposition. The materials synthesised were confirmed to be ZnO, $\alpha$-FeOOH and $\alpha$-$Fe_2O_3$ via powder xrd and their elemental confinement to particular structures confirmed by EDX. The samples showed much improved visible light absorption as measured by UV-Vis spectroscopy, along with greatly reduced charge transfer resistance as measured by EIS. This was due to suitable band alignment as evidenced by improved photocurrent density and IPCE showing good visible light sensitisation. This resulted in a two times increase in water splitting ability as measured by photocurrent at 1.23 $V_{RHE}$ from pristine to Y doped NWs to 0.57 $\mathrm{mA\,cm^{-2}}$, followed by a 60% further enhancement with the new heterojunction yielding 0.92

$\mathrm{mA\,cm^{-2}}$. This represents a highly competitive strategy to improving the ability of ZnO for water splitting. Furthermore, this work presents anodic deposition atop ZnO NRs as a strong route for making these junctions as the highest performance anodic $Fe_2O_3$ deposited sample so far.

## 6.2 Introduction

Photoelectrochemical (PEC) water splitting proposes the ability to directly capture sunlight in the simple-to-contain form of $H_2$, establishing a key technology for tackling the energy crisis.[24] The specific material requirements for this purpose include rapid charge transport, suitable band edge alignment and stability in water. Several metal oxides present promising candidates.[32] A noteworthy example is hematite ($\alpha$-$Fe_2O_3$) which has a comparitively low band gap of 2.1 eV and outstanding chemical stability.[172,231] For this reason a plethora of research into this semiconductor over the last two decades has been published, particularly for the application of water photolysis.[171,419,420] Primarily this interest has focussed on surmounting the material shortcomings, such as poor charge transport properties. This is due to the short life time of photoexcited charge carriers and slow polaron charge transport in the bulk.[421] Furthermore, in many cases synthesised hematite has a non-ideal conduction band position requiring large overpotentials to begin the reaction.[422] The nanostructuring of $\alpha$-$Fe_2O_3$ has been a key method to overcome short minority carrier path lengths giving rise to a number of morphologies yielding high water splitting performances.[164,167,393]

In this study, novel vertically aligned $\alpha$-$Fe_2O_3$ nanosheets (NSs) were synthesised using an anodic electrochemical deposition method, and were applied for the first time to decorate ZnO nanowire arrays (NRs). The NSs show wide growth in plane whilst maintaining nanoscale thickness, yielding high contact area for the solid / electrolyte interface. This enables rapid charge transfer to the solution for the evolution of oxygen at the anode surface. The dimensions of

the nanosheet widths were highly tunable by varying the duration of electrochemical deposition growing linearly with time. Remarkably the sheet thickness remained the same, 35 nm, with the different times maintaining low path lengths for minority carrier transfer. This led to the optimisation of the nanostructure to 5 minutes deposition time. Furthermore, by coupling the structures with vertically aligned ZnO NWs the slow transportation of photo generated charge was overcome by superior conductivity in the NWs. This was further improved by yttrium doping of the ZnO NWs for greatly enhanced solar water splitting.

The variety of different nanostructured forms of $Fe_2O_3$ such as thin films,[167,423] nanowires,[393,424,425] and mesoporous films have improved the surface area of photoanodes by orders of magnitude.[164,175,176] Hou *et al.* prepared mesoporous $\alpha$-$Fe_2O_3$ through microwave annealing of $\beta$-FeOOH for an impressive photocurrent of 3.9 $\mathrm{mA\,cm^{-2}}$ at 1.23 $V_{RHE}$. These films have been produced using a number of methods, none more versatile than anodic electrochemical deposition, yielding structures such as nanoparticles,[426–428] nanowires,[429,430] nanotubes,[170,431,432] and nanoporous films.[433,434] Such diversity is achieved by altering the substrate material, deposition electrolyte, reaction solution and electrode potential. So far the highest performing anodic deposited sample produced a photocurrent of 0.8 $\mathrm{mA\,cm^{-2}}$ at 1.4 $V_{RHE}$.[422] High performing solar water splitting hematite nano structures can be further improved by doping the material or creating hybrid junctions with complementary materials.[171,435]

Such strategies have also been applied to zinc oxide, a material with favourable band alignment to the redox potentials, along with charge mobility.[124] The primary aim of doping and coating ZnO is to sensitise the wide band gap structure (3.2 eV) to absorb visible light.[100] This has proven to be an effective method, for example hydrogen doping combined with CdS coating managed photocurrents greater than 5 $\mathrm{mA\,cm^{-2}}$.[141] Forming n-n junctions with ZnO and $Fe_2O_3$ has been investigated with mixed success, in several cases the raised onset potentials yielded negligible photocurrents at 1.23 $V_{RHE}$.[236,400,411,412] Despite this both Qin *et al.* and Hsu

*et al.* succeeded in enhancing photocurrent offered by the junction to 0.85 and 1.25 $\mathrm{mA\,cm^{-2}}$ at this potential respectively.[178,436] In both cases the use of $FeCl_3$ likely causes the formation of $ZnFe_2O_4$, a lower band gap material with a far more positive conduction band, likely aiding the junction.[342,436]

The deposition method described herein achieved great enhancement in PEC water splitting photocurrent, where 5 minutes of deposition time on yttrium doped ZnO gave 0.91 $\mathrm{mA\,cm^{-2}}$ at 1.23 $V_{RHE}$. This presents the highest performance of an anodic deposition of $Fe_2O_3$ applied to water splitting due the advantages incurred from unique hybrid morphology of $Fe_2O_3$ NSs with ZnO NRs. Overall this represented a 4.1 times improvement over pristine ZnO samples due to more favourable charge transport properties as measured by electrical impedance spectroscopy, and visible light sensitisation as measured by UV-Vis absorption spectroscopy. The successful transfer of photogenerated charge in the $Fe_2O_3$ to the YZnO NW electron highways led to improved incident photon to current conversion efficiency in the visible spectrum range. Overall the marriage of these two material nanostructures is able to overcome the disadvantages of each semiconductor to achieve greater efficiency water photolysis.

## 6.3 Experimental Methods

### 6.3.1 ZnO NW Synthesis

Zinc oxide nanowires were prepared by a two step chemical bath deposition method outlined in our previous work.[114] Briefly, FTO glass substrates were cut and cleaned via sonication, followed by seeding with spin coating, 0.1 M zinc acetate solution, at 800 RPM for 2 minutes followed by 2000 RPM for 30 seconds. Following oxidation via thermal annealing at 500°C, samples were then placed face down in aqueous growth solution containing 40 mM concentration 1:1 $Zn(NO_3)_2$ : hexamethylenetetramine, for 16 hours at 85°C. After this the samples were again annealed at 500°C for 30 minutes. Yttrium doping took place at the growth stage with

1% molar addition of $Y(NO_3)_3$ to the solution, determined by ICP-MS to yield 0.1% doping in the final YZnO.[396]

### 6.3.2 $Fe_2O_3$ NS Growth

The hematite, $\alpha$-$Fe_2O_3$ film coating was added to the ZnO NRs by performing an anodic electrochemical deposition on the NWs in an Fe II solution. The solution was prepared by dissolving 10 mM $Fe(NH_3)_2(SO_4)_2$ and 0.4 M NaCl electrolyte into 250 ml DI water. The pH of the Fe II solution (pH = 6.0) was adjusted to 8.0 by adding 0.14 g NaOH and 23 drops 1.0 M NaOH (pH = 13.0) to the solution. The ZnO/FTO substrates were submerged into the Fe II solution in a round bottom flask with a two-electrode electrochemical deposition setup with stainless steel counter electrode. The system is displayed in Figure S6.1A, along with current time curves for the deposition, B, the flask was evacuated using a a vacuum pump and sonicated to remove air bubbles between the wires. In order to produce pure $\alpha$-FeOOH cyclic voltammetry was performed in three electrode set up with saturated KCl, Ag/AgCl reference and platinum counter, oxidation peaks were assigned to particular reactions and the potential for goethite production was translated to be 0.56 V in the two electrode setup, Figure S6.1. The potential was kept fixed for the deposition duration, which was varied to 2, 5, 10, 30 and 60 minutes to optimise the samples. Having grown $\alpha$-FeOOH on the surface, samples were then annealed at 550°C for 3 hours in order to form $\alpha$-$Fe_2O_3$ nanosheets (NSs).

### 6.3.3 Structural and Physical Characterization

The morphological and crystallographic characterisation of the pure $Fe_2O_3$, ZnO, YZnO and anodic coated samples was performed by scanning electron microscopy (SEM, Leica Stereoscan 420) and powder x-ray diffraction (XRD, Siemens D500). SEM images were measured using Image J software (National Institutes of Health, USA), and energy dispersive x-ray spectroscopy

was used for elemental mapping with INCA software (Oxford instruments). In order to identify high magnification morphology as well as atomic spacing high resolution transmission electron microscopy was used (HRTEM, JEOL-3010 at 300 kV).

### 6.3.4 Photoelectrochemical and Optoelectronic Measurement

A spectrophotometer (PerkinElmer, Lambda 265) was used to measure UV-Vis absorption spectroscopy and used to calculate band gap energies. Photoelectrochemical water splitting and electrical impedance spectroscopy (EIS) was performed using a the same 3 electrode set up to cyclic voltammetry previously described but with a 1 M KOH aqueous electrolyte (pH 13.6). The completed samples made the photoanode. PEC water splitting used a potentiostat (EA163, eDAQ) varied from 0.4 to 1.8 $V_{RHE}$, with a solar simulator as the illumination source (Oriel LCS-100, Newport, $100\,\mathrm{mW\,cm^{-2}}$ with built-in AM 1.5G filter). Samples were masked at 0.15 $\mathrm{cm^2}$ for photocurrent measurements. EIS Nyquist plots used to determine charge transfer resistance, were performed under identical illumination, with fixed DC potential at 1 $V_{RHE}$ and a sinusoidal modulated AC potential of 10 mV with frequency varied from 0.1 to 10,000 Hz using an electrochemical controller (Palm Sens 3, Palm Sens BV). Mott-Schottky plots were performed in the dark with the same controller, fixed frequency at 1000 Hz, and varied potential from 0 to 2 $V_{RHE}$. Data was processed using PSTrace 4.5 (Palm Sens BV) and equivalent circuit models were applied using Elchemea Analytical (DTU Energy). X-ray photoelectron spectroscopy (XPS, Thermo Scientific K-alpha using Al K$\alpha$source) allowed the elucidation of valence band position. Incident photon-current conversion efficiency was determined using a 300 W xenon lamp with monochromator calibrated to $100\,\mathrm{mW\,cm^{-2}}$ using an optical power meter and silicon photodiode detector (Newport), at 1.23 $V_{RHE}$.

## 6.4 Results and Discussion

### 6.4.1 Structural and Physical Properties

Proposed schematic representation of the novel structures can be found in Figure 6.1A along with optical photographs of the colour changes involved, B. The intended structural design likely offers great advantages to the photolysis of water, as it dramatically increases surface area. Furthermore by combining $Fe_2O_3$ nanosheets with ZnO nanorods, it could overcome the disadvantages associated with either material in isolation, sensitising ZnO to visible light and quickly separating and transporting charge from $Fe_2O_3$. The mechanism for the deposition is also outlined, as using a low potential of -0.14 V vs Ag/AgCl for oxidation of the $Fe^{2+}$, this closely follows the -0.13 V used by Martinez *et al.* to grow goethite (α-FeOOH) on titanium substrates using a similar solution.[437] The open circuit voltage occurred at -0.70 V vs Ag/AgCl with three electrodes and ∼0.00 V vs stainless steel in the two electrode set up, therefore 0.56 V was chosen to selectively grow α-FeOOH. Cyclic voltammetry of the reaction can be found in Figure S6.1C, showing clear oxidation events associated with magnetite, goethite and lepidocroautocite. α-FeOOH was grown on the surface via the following reaction.[420]

$$\mathrm{Fe^{2+} + 2\,H_2O \longrightarrow \alpha\text{-}FeOOH + 3\,H^+ + e^-} \tag{6.1}$$

This is confirmed by the noticeable colour change in the samples, from white ZnO to a light yellow brown colour on the surface, Figure 6.1B. This is accompanied by a surprising green colour, likely due to the chlorination of the rust species from the electrolyte. After thermal annealing in air the α-FeOOH is further oxidised to form α-$Fe_2O_3$, as indicated by the colour change from yellow to deeper orange and red.

The morphology of the nanostructures was observed using scanning electron microscopy (SEM), with the resulting top down images displayed in Figure 6.2A-E. Two distinctive features are clear, the wurtzite structure of the ZnO NWs with their hexagonal faces, and $Fe_2O_3$

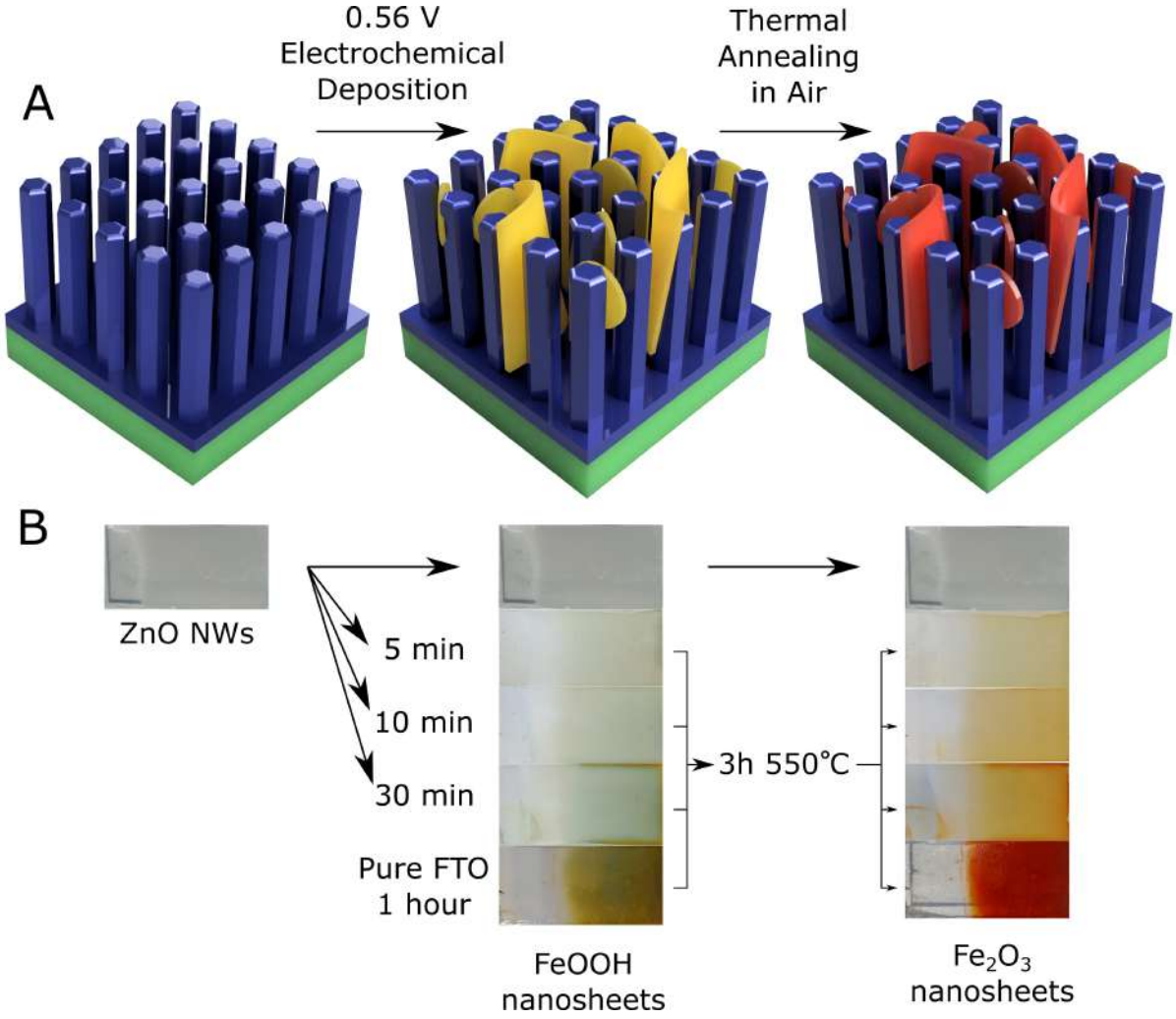


Figure 6.1: The schematic for the deposition process A), along with sample photographs B). On the left it shows the pristine ZnO NRs, with no coating, in the centre, the NRs with FeOOH nanosheet coating falling between the NRs after electrodeposition. Finally on the right, the conversion of FeOOH to $Fe_2O_3$ by thermal annealing in air.

nanosheets (NS) vertically aligned parallel to the wires with bright edges. The NSs are a direct result of the electrodeposition in $Fe^{2+}$ ion containing solution, as the pure ZnO showed no signs of this feature. The prevalence of the NSs increases with deposition duration, confirming electrodeposition as the cause of their growth. Enhancement in surface contact, beneficial to solar water splitting, is clear when analysing the geometries of the features. The NW diameter remains fixed across the samples, 141 $\pm$ 6 nm, the thickness of the NSs is also constant at 35 $\pm$ 3 nm, providing far greater area due to their vertical alignment (histograms of binned measurements, Figure S6.2A and B). Furthermore, longer duration yields greater NS width, showing remarkable linearity, Figure S6.2C and D. This allows the hybrid morphology to be highly tunable to find the optimised geometry. It is clear in the solution that the favoured growth direction of the $\alpha$-FeOOH sheets is along the plane perpendicular to the side walls of the NWs, explaining the formation of nanosheet structures. Larger width yields greater contact with the electrolyte, but longer distances for charge to travel before reaching the ZnO. Also, after 10 and 30 minutes they become large enough to begin obscuring the NWs and filling in the channels between, leading to reduced surface area. The strengths of the hybrid system begin to emerge, not only do the NSs likely offer greater light absorption and surface area, they are effectively plugged into the ZnO NWs. This could reduce the path length for holes to reach solution and by extension their chance of recombination.[178]

The morphology in this chapter differs substantially from the NP embedded NWs occuring from cathodic deposition; with key advantages and disadvantages. The advantage of NSs is their vertical alignment allowing greater optical depth for absorption, in order to overcome the indirect band gap of $Fe_2O_3$;[423] with isolated NPs light has a greater chance of transmission and loss. The disadvantage of this morphology over the previous chapter is poorer junction contact where photogenerated charge in the sheet is unable to reach the ZnO before recombination. However, the sluggish transport properties of $Fe_2O_3$ can be substantially improved by doping

with $Ti^{4+}$, enabling the electrons to reach the ZnO junction.[174]

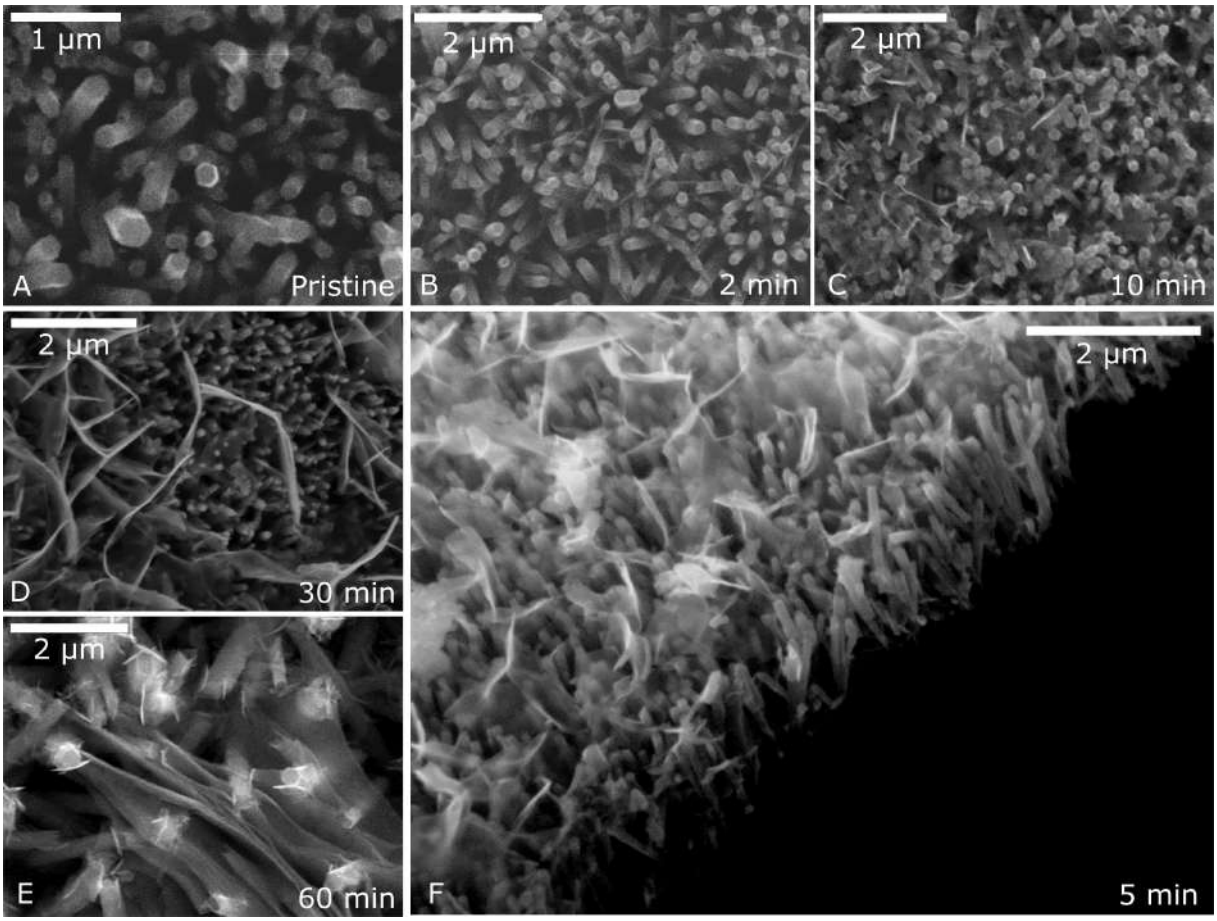


Figure 6.2: This shows the top down SEM images of the pristine and coated samples after annealing, A-E), the morphology shows increased $Fe_2O_3$ nanosheets with greater deposition duration. The angled cross section image of the 5 minute deposition sample is visible in F).

The nanostructure morphology was further analysed by angled cross sectional SEM of the 5 minute deposition, displayed in Figure 6.2F. This once again shows the favourable alignment of the $Fe_2O_3$ sheets, reaching outward toward the solution. This also evidences the formation of $Fe_2O_3$ deeper between the wires towards the FTO substrate, as some cross-linking is seen near the NW base. The ZnO / $Fe_2O_3$ junction appears well connected throughout the geometry, with the smaller NSs wrapping around the NR. This would allow unrestricted charge transfer between the materials, provided the appropriate band edge alignment. This also confirms the

success of the sonication and vacuum removal of air pockets between the wires without which, aggregation at the surface can occur. Elemental mapping of this sample is found in Figure S6.3, using EDX to confirm the presence of Zn, Fe and O on the surface. This shows concentrated areas of Fe in the regions with saturated nanosheets, and higher Zn over the exposed NWs, evidencing the $Fe_2O_3$ NS and ZnO NR structure separation.

Powder X-ray diffraction data, Figure 6.3A, confirms both the reaction and the final species on the NW surface. Firstly, pure samples of $Fe_2O_3$ and ZnO were prepared in order to confirm their presence on the surface of the sample, details of the pure $Fe_2O_3$ synthesis can be found in the experimental methods section. The ZnO NW sample gave its predictable high intensity 002 peak at 34.8°, because of strong vertical alignment due to stifled growth in the lateral planes.[396] The presence of $Fe_2O_3$ was confirmed by typical peaks matching its reference spectrum, (ICDD 01-075-5065). At lower deposition times of 5 minutes and shorter, no noticeable hematite peaks occur, but with increased deposition time features of iron oxide coating become obvious. They reach their highest intensity for the 30 minute sample, where two different Fe phases are present, goethite (α-FeOOH) and hematite. Peaks occuring at 25.8° and 31.8° are attributed to goethite with high intensity, where the initial deposition is not yet fully oxidised to hematite (ICDD 29-713).[437] The prominence of this phase could be beneficial to the oxygen evolution reaction, and further absorption of visible light.[438] This represents the first time these three materials have been used together as a photoelectrochemical water splitting anode. In the annealed samples the second iron phase displays a strong peak emerging at 33.4°, corresponding to the (104) plane of hematite. This is likely the favoured plane growth direction of the nanosheet morphology. This is due to the partial surface charging of lattice planes within the basic deposition media, stifling growth in the (010) direction. The full XRD of the polycrystalline iron oxide precursor film prior to annealing is displayed in Figure S6.4A. The dominating phase is unsurprisingly goethite, confirming the proposed reaction scheme, though other phases present

include magnetite and lepidicrocite.

In order to confidently assign crystal phases to particular morphological features, high resolution transmission electron microscopy (HRTEM) was used, displayed in Figure 6.3B. In the low magnification image of the 5 minute deposited sample both nanosheets and nanorods are clearly visible. Upon magnification to atomic resolution the NR portion of the sample, i), spacing of 0.261 nm is visible, corresponding to the 002 lattice plane of ZnO as the preferred growth orientation. This is bolstered by the evidence displayed in the FFT (inset), where the orthonormal 100 plane is also measured. The NS region, ii), showed the clear crystalline lattice of hematite, 0.273 and 0.461 nm spacings follow closely the known values of the 104 and 006 planes respectively. A full radius of spots is visible in FFT, highly characteristic of the material showing high phase purity. This also confirms the strong 104 directional alignment of the nano sheet growth reflecting its XRD pattern prominence. No evidence for goethite planar spacing was observed, likely due to the low duration of coating. The quantity of goethite deposited after 5 minutes is likely fully oxidised to hematite after 550°C heating, whereas higher deposition may take more time. This would be an interesting avenue for further study, outside the scope of the current work.

### 6.4.2 Optoelectronic and Photoelectrochemical Properties

A highly effective strategy of ZnO water splitting enhancement is sensitisation, UV-Vis absorption spectroscopy was used to measure the junctions ability to harvest visible light.[89] The resulting spectra can be found in Figure 6.4A, where the various coating durations are compared to pristine $Fe_2O_3$, ZnO and YZnO. These latter three samples each display one clear absorption onset, corresponding to their band gap energies. Pristine $Fe_2O_3$ shows good visible light absorption, a significant increase at wavelengths shorter than 600 nm. This is in contrast to ZnO and Y doped ZnO, which show low values down to wavelengths shorter than 400 nm towards

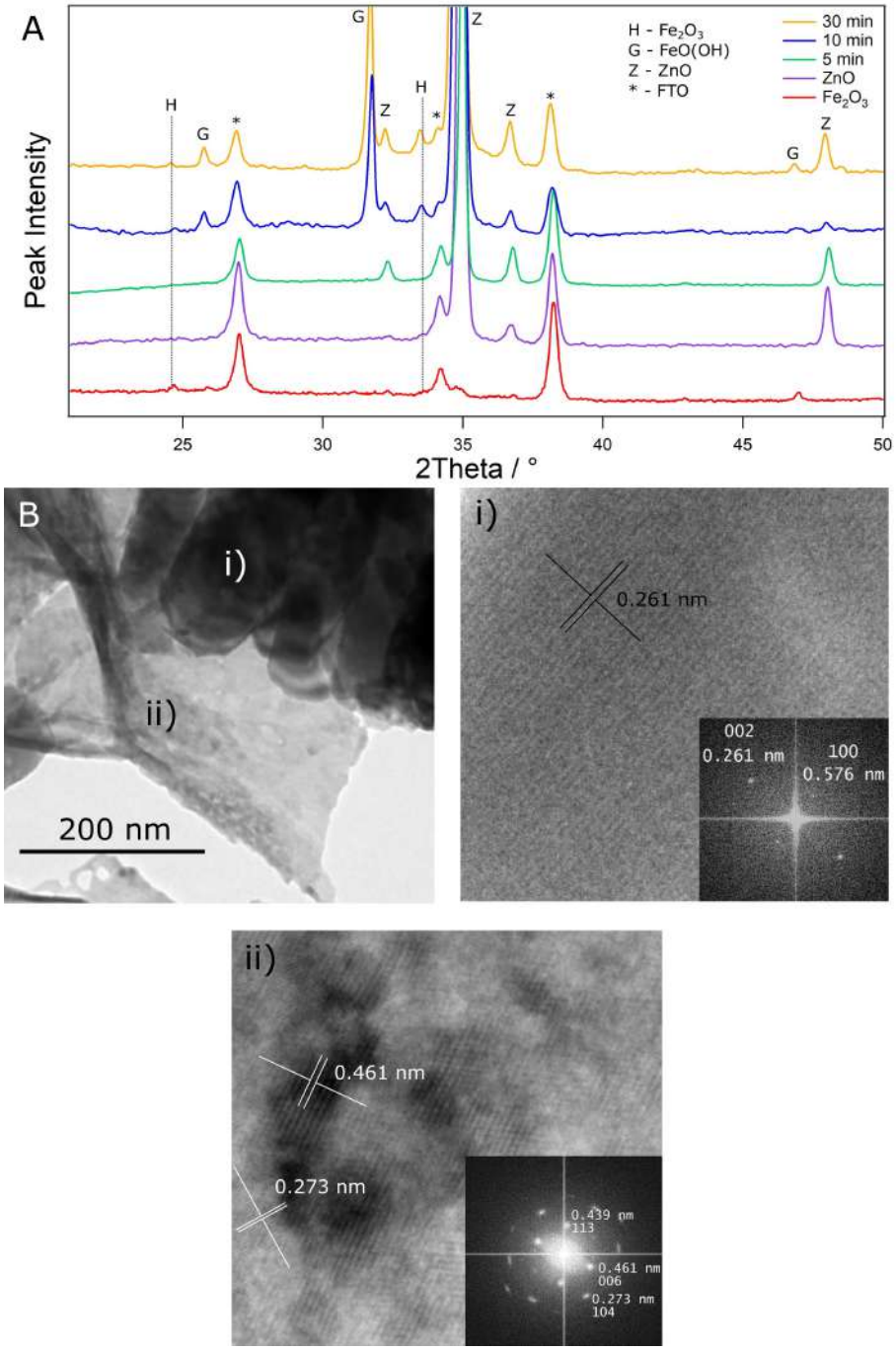


Figure 6.3: A) Shows powder XRD graphs of the samples with increasing deposition thickness, alongside pure ZnO and pure $Fe_2O_3$ on FTO glass. B) Shows HRTEM microscopy of the NS and NR structure, with magnified images of i) the NR and ii) the NS with respective insets of FFT.

UV energies as expected. Despite the values dramatically rising over the $Fe_2O_3$ the majority of solar photons fall in the region greater than 400 nm, giving $Fe_2O_3$ the advantage in solar applications.[180] The coated samples share this feature, with each showing higher absorbance through the visible range, greater coating duration yields higher values across the 450-550 nm range. Despite this, clearly distinct ZnO and $Fe_2O_3$ absorption onsets only become visible after 5 minutes of deposition, lower than this the 2 minute sample appears to have too little $Fe_2O_3$ to use the full absorption potential. When looking in more detail at the onset for ZnO in the samples, this appears to be first red shifted in the Y doped sample, then even further red shifted in the coated samples. This first effect is due to the introduction of new electronic states near the conduction band minimum due to the effect of yttrium as an n-type dopant in ZnO, as described in more detail in our previous work.[396] These shallow states allow the donation of conduction band electrons at thermal energies, yielding higher conductivity. The more dramatic red shift due to the $Fe_2O_3$ coating is more subtle, and is likely due to the nature of the n-n junction between the materials.

In order to quantify the shifts in band gap energies, $E_g$, the Tauc relation was used for direct transitions calculated by extrapolating the linear regions to the x axis in Figure 6.4B.[261] The first two plots displayed direct band gaps of 3.28 and 3.23 for ZnO and YZnO samples respectively. This corresponds to the expected value for NRs grown by chemical bath deposition,[100] while yttrium doping led to a 0.05 eV red shift. This is due to interstitial yttrium atoms introducing states within the electronic band gap, reducing direct transition energy.[396] Linear extrapolation was selected for the lower energy region of the $Fe_2O_3$ sample, shown in the inset, as it corresponds to the first absorption onset clearly visible in the absorbance graph, A. This gave a value of 2.13 eV, typical for hematite.[393] The 30 minute $Fe_2O_3$ coating upon YZnO gave band gaps at 3.04 and 2.28 $\mathrm{eV}$ for its dual absorptions. This represents a significant red shift for the ZnO band energy of 0.19 eV, coupled with a blue shift of 0.15 eV for the $Fe_2O_3$. This is accompanied

by an apparent 0.25 eV blue shift in band gap for the $Fe_2O_3$ species. This is most likely due to the mobility of transition metal ions during the extended high temperature annealing step. At 550°C, Fe ions from the hematite are able to invade the ZnO lattice, causing a known band gap reduction as a dopant.[399] Furthermore, the same process occurring from Zn ions in the $Fe_2O_3$ causes p type doping,[404] possibly introducing electronic states below the valence band.

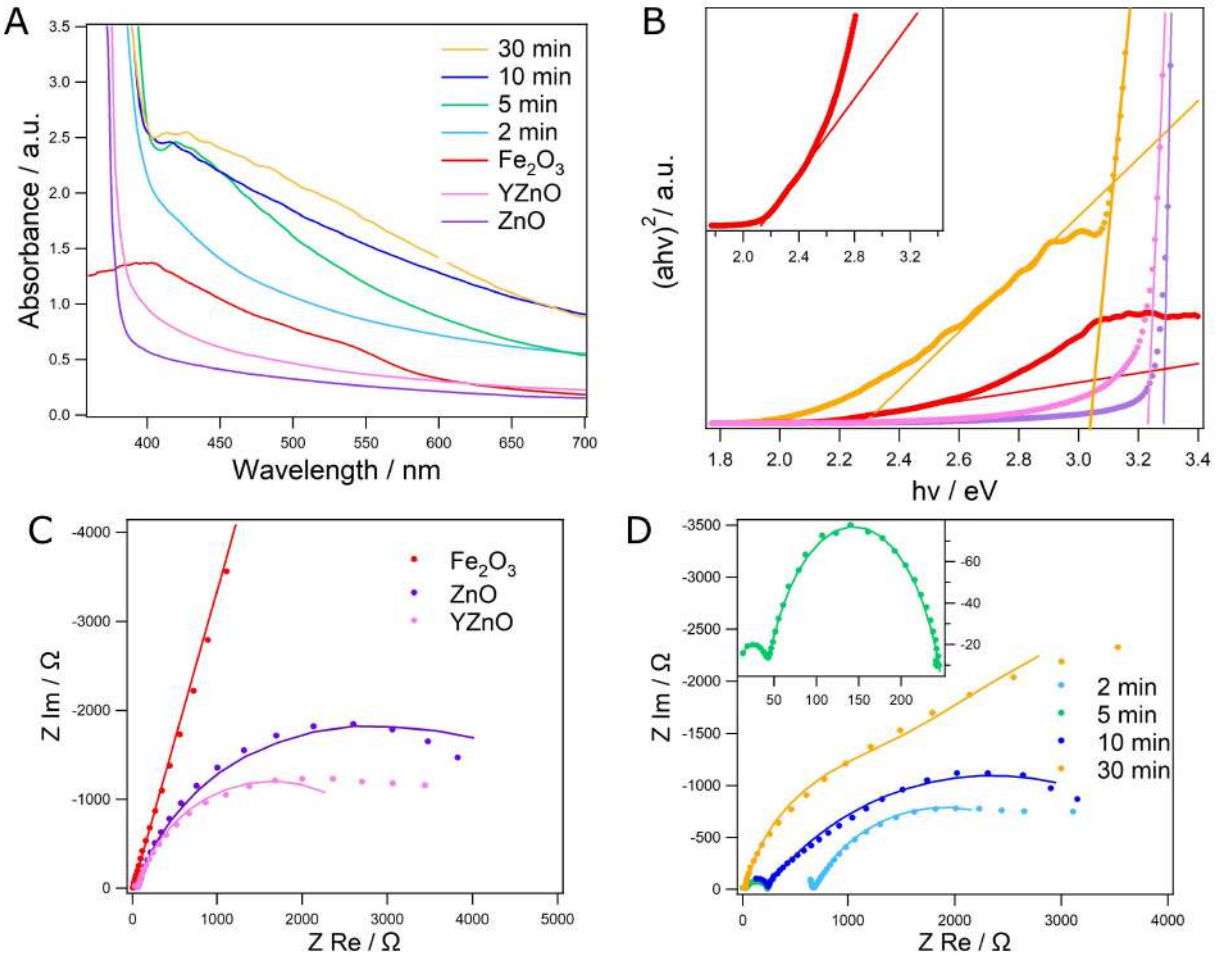


Figure 6.4: The UV-Vis absorption data of the various sample coatings, along with pure ZnO, $Fe_2O_3$ and YZnO can be found in A). The Tauc plots of the selected samples for band gap measurements are displayed in B). Graphs C) and D) display Nyquist plots of the illuminated samples, with C) showing pure $Fe_2O_3$, ZnO and YZnO and D showing the various coating durations with 5 min inset.

The electronic properties of the samples were analysed using electrical impedance spectroscopy (EIS), at a fixed DC potential of 1 $V_{RHE}$, sinusoidal AC of 10 mV at frequency varied from 10,000 to 0.1 Hz, Figure 6.4C,D. This method was used to determine the charge transfer resistance of the samples, using the equivalent circuit found in Figure S6.4B where dual arcs were visible, and a simple Randles circuit when there was only one arc measured (pure $Fe_2O_3$ sample). Typically, the arc radius is proportional to the charge transfer resistance, $R_{CT}$, an indication of recombinative energy losses.[439] In nearly all the samples two arcs are observed, a small arc at high frequencies associated with charge transportation through the materials, $R_{ct1}$, and a large low frequency arc associated with the large resistance at the solid liquid interface, $R_{ct2}$. The Y doped sample shows a significant reduction in $R_{ct2}$ as a negative shift in flat-band potential allows for lower friction Faradaic charge transfer, aided by significantly reduced electronic resistance through the material bulk.[396] The pure $Fe_2O_3$ sample meanwhile shows orders of magnitude higher $R_{CT}$ due to its sluggish charge dynamics and high recombination rate. This summarises the main disadvantage of $Fe_2O_3$ as a water splitting photoanode, surmounted by the coated samples in Figure S6.4C,[164] where the values of $R_{CT}$ are plotted.

A dramatic reduction in arc radius is observed with 5 minutes coating (inset) showing the smallest values of both $R_{ct1}$ and $R_{ct2}$, 33 and 208 $\Omega$ respectively. A decrease in $R_{ct1}$ means lower transport resistance, which occurs due to greater numbers of photogenerated charge carriers from visible light absorption from $Fe_2O_3$. Not only will this contribute larger quantities of photoelectrons, it will also increase the electron mobility in the materials as charge transportation is trap mediated.[169] The filling of surface and bulk traps with excited electrons means their neutralisation for the passage of further charge. The reduction in $R_{ct2}$ confirms that there is good electron transfer from $Fe_2O_3$ to YZnO, reducing recombination due to traps at the solid / liquid interface by shuttling the electrons into the YZnO electron highways.[178] Effective movement of charge across the $Fe_2O_3$ / YZnO junction means better electron hole separation, indicating

good band alignment. Furthermore, larger surface area would also reduce $R_{ct2}$, as it provides a wider door for charge transfer from enlarging the physical contact space between electrode and electrolyte. Greater deposition thickness sees the values of both charge transfer resistances monotonically increase above 5 minutes, due to larger $Fe_2O_3$ sheets overwhelming the transport properties of the NRs, causing greater recombination at the solid liquid interface.

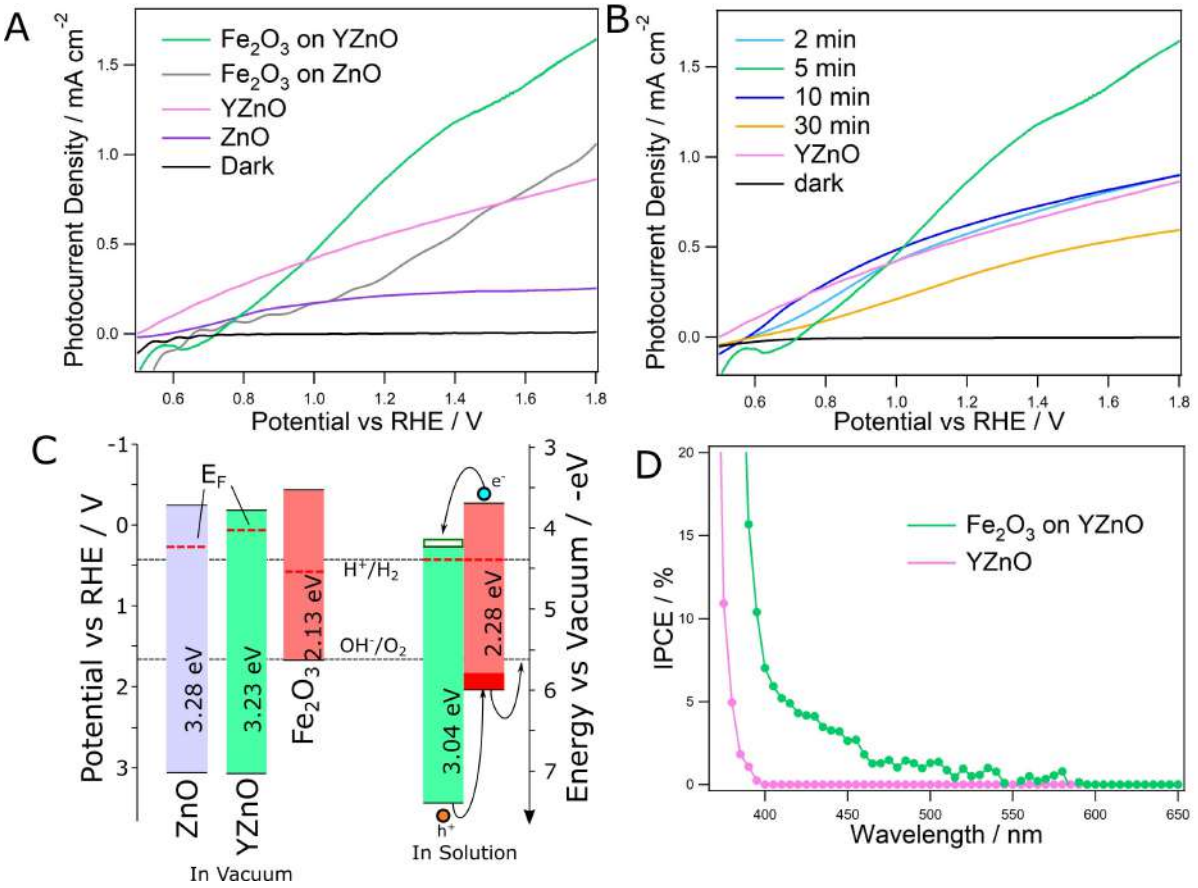


Figure 6.5: Photoelectrochemical water splitting performance is shown in A) and B), with overall enhancement in A) optimisation of deposition in B). C) Shows the electronic band structure diagram, and D shows the IPCE for the same samples.

Reduced $R_{CT}$, increased visible light absorption and favourable morphology with greater surface area are all factors that have a vital impact on solar water splitting performance. The photocurrent densities measured under simulated solar illumination can be found in Figure 6.5.

In Figure 6.5A the overall enhancement due to the synergy of Y doping and $Fe_2O_3$ coating is displayed. The undoped chemical bath deposition ZnO measured a photocurrent of 0.22 $\mathrm{mA\,cm^{-2}}$ at 1.23 $V_{RHE}$, typical of this pristine nanostructured material. The 5 minute coating applied to the undoped ZnO NWs, yields an enhanced photocurrent of 0.36 $\mathrm{mA\,cm^{-2}}$, a remarkable 60% improvement. Improving the charge transport properties of the ZnO alone, with Y doping, gave a 2.6 fold boost. The two strategies together incurred $> 4$ times enhancement in comparison with the unaltered sample, yielding 0.91 $\mathrm{mA\,cm^{-2}}$ at 1.23 $V_{RHE}$. This promising result for the hybrid nanostructured photoanode, is amongst the highest in ZnO and $Fe_2O_3$ water splitting literature. Typically pristine ZnO nanostructures achieve photocurrents of around 0.20 $\mathrm{mA\,cm^{-2}}$,[113,290,328,329,440] however novel synthetic methods, such as microwave heating, lead to values as high as 0.70 $\mathrm{mA\,cm^{-2}}$.[114] In comparison with ZnO / iron oxide heterostructures the anodes reported here perform favourably, often ZnO / $Fe_2O_3$ junctions yield negligible photocurrent at 1.23 $V_{RHE}$.[400,411,412] They also outperform the $Fe_2O_3$ coated ZnO NRs synthesised by Qin *et al.*[436] which achieved 0.85 $\mathrm{mA\,cm^{-2}}$ at 1.23 $V_{RHE}$, prior to $Fe_2PO_4$ encapsulation. They fell short of the work by Hsu *et al.* who achieved 1.27 $\mathrm{mA\,cm^{-2}}$ likely due to their superior ZnO morphology.[178] The chopped illumination performances of the key samples can be found in Figure S6.5A-C.

The optimisation of deposition duration is shown in Figure 6.5B, the highest performance occurs at 5 minutes deposition time. This represents once again a 60% increase over the uncoated Y doped sample, achieving 0.57 $\mathrm{mA\,cm^{-2}}$ at 1.23 $V_{RHE}$. Photoelectrons are generated by visible light photons in the hematite layer, which are then delivered rapidly to the YZnO electron highway reducing recombination with holes. This is evidenced by the photocurrent decay curves in Figure S6.5D, where the lifetime of current in the hybrid is longer due to extended electron lifetime from effective charge separation. This leaves holes in the hematite able to evolve oxygen at the solid / liquid interface. Clearly, the performance is highly sensitive to the

deposition time, with 2 minutes of coating only slightly improving the photocurrent as there is little visible light absorption. At depositions over 5 minutes, a critical decline in water splitting is observed with the 30 minute sample measuring lower than no coating at all, 0.36 $\mathrm{mA\,cm^{-2}}$. This can be explained by the $Fe_2O_3$ nano sheets growing large enough that energy loss due to electron hole recombination cripples the cell, as evidenced by very large $R_{CT}$. Thicker $Fe_2O_3$ layers lengthen the path required for photogenerated charge to travel before reaching the junction so that much is lost to recombination beforehand. The behaviour of the onset potential also describes the junction, with uncoated YZnO and thick $Fe_2O_3$ having lower values. This is due to the materials behaving in isolation, reflecting the flat band potentials of each material respectively. In order to reach even greater performance, extrinsic doping of hematite could be employed in future work. For example, introducing silicon into the lattice led to a high photocurrent of 2.2 $\mathrm{mA\,cm^{-2}}$ at 1.23 $V_{RHE}$.[171] An advantage of the hybrid presented in this work is that by using undoped $Fe_2O_3$ the anode has fertile prospects for improvement using this tactic.

The proposed electronic band structure diagram is displayed in Figure 6.5C. This is based upon Fermi level determination using the flat-band potential calculated from the Mott-Schottky plot of impedance for the hematite sample found in Figure S6.6A. The valence band position of the hybrid junction was determined using x-ray photoelectron spectroscopy (XPS) observing the low energy region in a survey scan, Figure S6.6B. Other values of the Fermi level used in the diagram of ZnO and YZnO along with their respective valence band positions are taken from our other work currently under review. This information combined with the previously measured optical band gap yields the conduction band position. The two materials together form a type two heterojunction, where conduction band electrons from the hematite are able to flow into the conduction band of the zinc oxide. Conversely holes generated in the $Fe_2O_3$ are blocked by the high energy of the ZnO valence band, confining them to the outer material to reach the solid / liquid interface. The n-n junction causes a depletion region to form at the YZnO/$Fe_2O_3$

interface and causes a higher concentration of electrons in the $Fe_2O_3$ and holes in the ZnO. This explains the shifts in Fermi levels allowing the equilibrium to form. The proposed band structure, evidenced by XPS, EIS and UV-Vis explains the successful enhancement of solar water splitting efficiency.

Furthermore, the photoanodes showed good stability, showing no decline under chopped illumination at a fixed 1.23 $V_{RHE}$ potential, Figure S6.6C. Finally, the incident photon to current conversion efficiencies are found in Figure 6.5D, displaying a clear absorption and utilisation of visible light at wavelengths shorter than 550 nm in the hybrid sample. This is in clear contrast to the YZnO, which has a sharp onset corresponding to the previously measured direct band gap on the material, with 0 % efficiency at wavelengths shorter than 400 nm. From 550 to 410 the top performing sample trends from 1 to 5% efficiency, before rising past 10% at 395 nm accessing significant proportions of visible light. This explains the 4 fold enhancement in photoelectrochemical water splitting, observed from photocurrent density. This is due to more favourable morphology leading to greater contact area, a suitable electronic junction for charge transfer and visible light absorption in $Fe_2O_3$ coupled with Y doped ZnO rapid transport.

## 6.5 Conclusion

In summary novel hybrid metal oxide nanostructures were constructed using anodic FeOOH electrochemical deposition to grow $\alpha$-$Fe_2O_3$ NSs on ZnO NWs. This process gave a high degree of control, allowing nanosheets of variable width to grow with time, optimised at 5 minutes duration. The mechanism of deposition was confirmed by matching the potential to produce goethite, $\alpha$-FeOOH, which was confirmed by xrd to form hematite, $\alpha$-$Fe_2O_3$, after annealing at 550 °C. The advantages of such a hybrid became clear as the NSs sensitised ZnO to absorb visible light, as confirmed by UV-Vis spectroscopy. Also, the novel samples showed greatly reduced charge transfer resistance from both pure $Fe_2O_3$ and ZnO, which was further reduced

by yttrium doping in the ZnO layer. This progress was combined to make an efficient system for the generation of photo excited charge, whilst maintaining desirable transportation properties. This is due to the relatively low band gap of $Fe_2O_3$ (2.13 eV) absorbing more abundant lower energy solar photons, and the rapid charge transport associated with ZnO and high conductivity Y doping. Overall the novel structures achieved a dramatic 4 times enhancement in water splitting photocurrent, 0.20 pure ZnO, compared to 0.91 $\mathrm{mA\,cm^{-2}}$ at 1.23 $V_{RHE}$ for the YZnO with optimised coating duration. The success of the junction shows good band alignment, with promising IPCE performance of 5% at 410 nm, compared with no current response from the YZnO at this wavelength. This work paves the way for further exploration into the ZnO/$Fe_2O_3$ junction such as through the doping of the $Fe_2O_3$ layer.

In comparison to the previous chapter the photocurrent densities achieved by the NS decorated YZnO NRs were less than those from the alternative cathodic deposition. This is most likely due to the morphology of the wide sheets in comparison to embedded nanoparticles, leading to the less efficient transportation of photogenerated electrons. The dimensions of the $Fe_2O_3$ allowed the charge to meet the junction after a maximum domain size equal to the diameter of the NP (16 nm, Figure 5.3C), whereas NS electrons had to traverse a $\sim$ 400 nm sheet without recombination (Figure S6.2). This greatly exceeds their expected path length, and therefore electron hole recombination is responsible for the lower photocurrent density and by extension, the lower IPCE values. It is worth noting however, the values of optical absorbance for the optimised sample was greater in the NS samples, 2.2 at 450 nm (Figure 6.4A), than the value of 2.1 in the NP sample (Figure S5.5). This indicates the NS ability to generate greater populations of photogenerated particles, if they could be harvested more efficiently. One other advantage is that the optimised sample only required 5 minutes of deposition time, far shorter than the 1 hour needed for cathodic deposition.

## 6.6 Supporting Information: In Situ Decoration of Doped ZnO Nanowires with $\alpha$-$Fe_2O_3$ Nanosheets for Solar Water Splitting

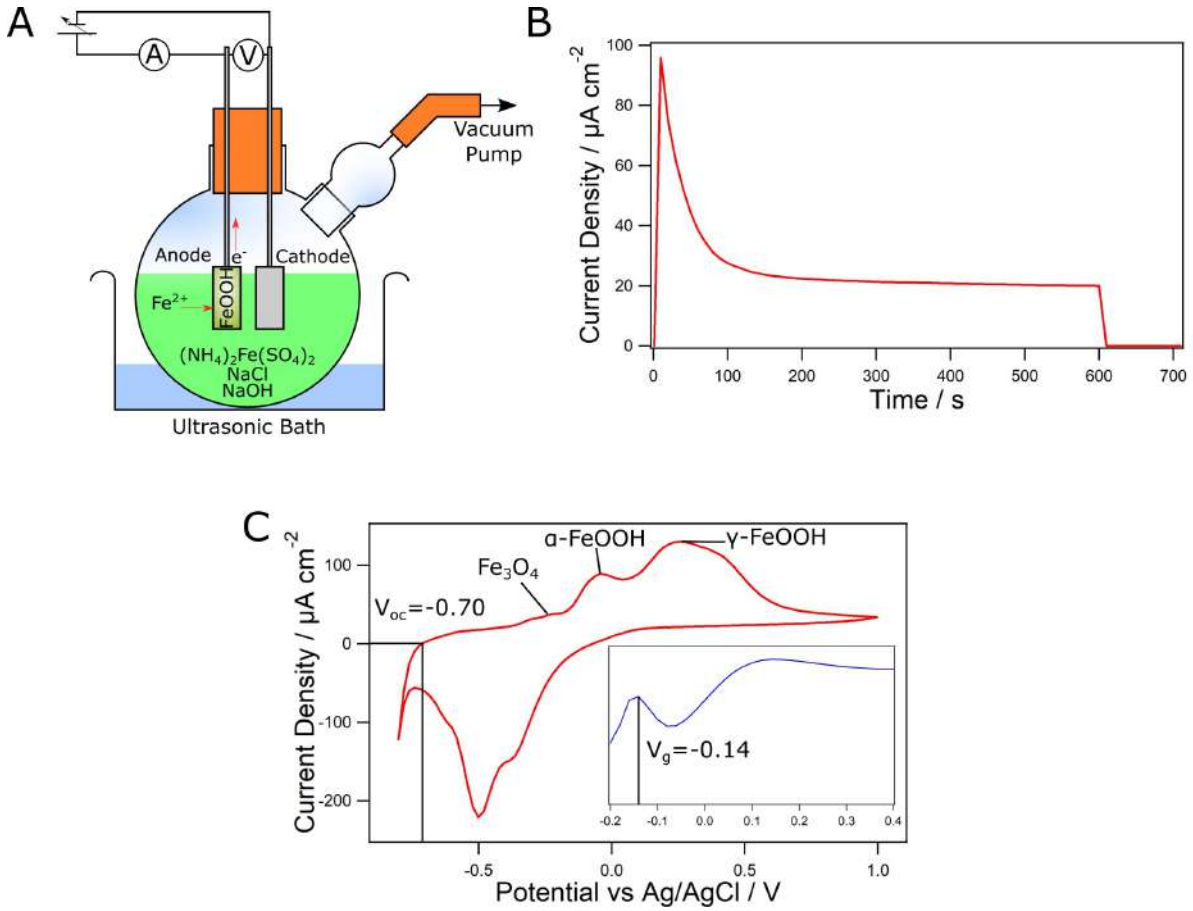


Figure S6.1: Schematic diagram of the deposition process, A), showing the setup including ultrasonic bath, and electrode positions. B) shows typical deposition current current over time, integrated to calculate charge density. C) shows the cyclic voltammetry with three electrode setup, used to determine the goethite potential, inset shows a slower scan speed linear sweep for greater accuracy.[437] 2 Electrode deposition potential was determined by the difference between $V_{oc}$ (-0.70) and goethite deposition potential (-0.14) as 0.56 V.

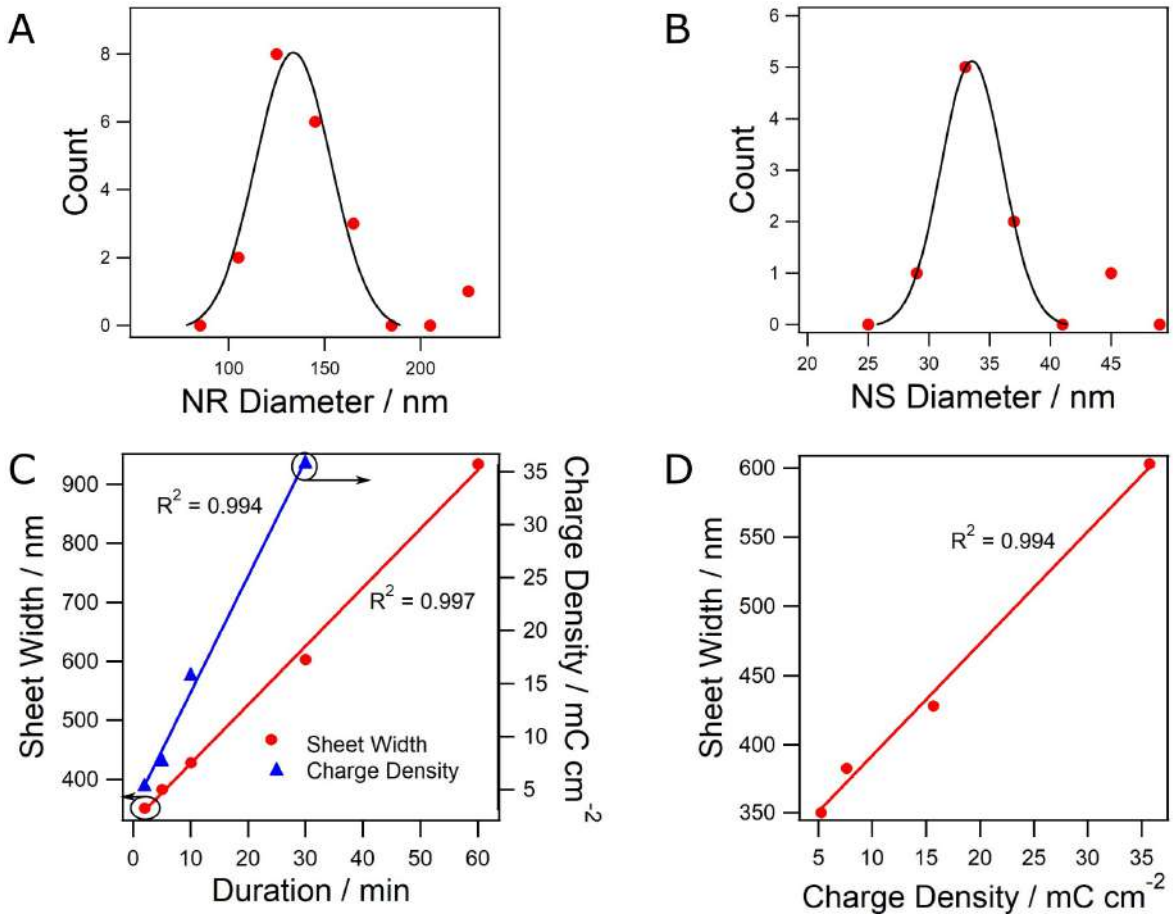


Figure S6.2: A) shows the histogram of a survey count of the nanorod diameter measured from SEM images, B) shows the nanosheet diameter survey result. C) shows the integrated total charge density deposited and the nanosheet width against the duration of deposition. D) shows the charge density plotted against nanosheet width.

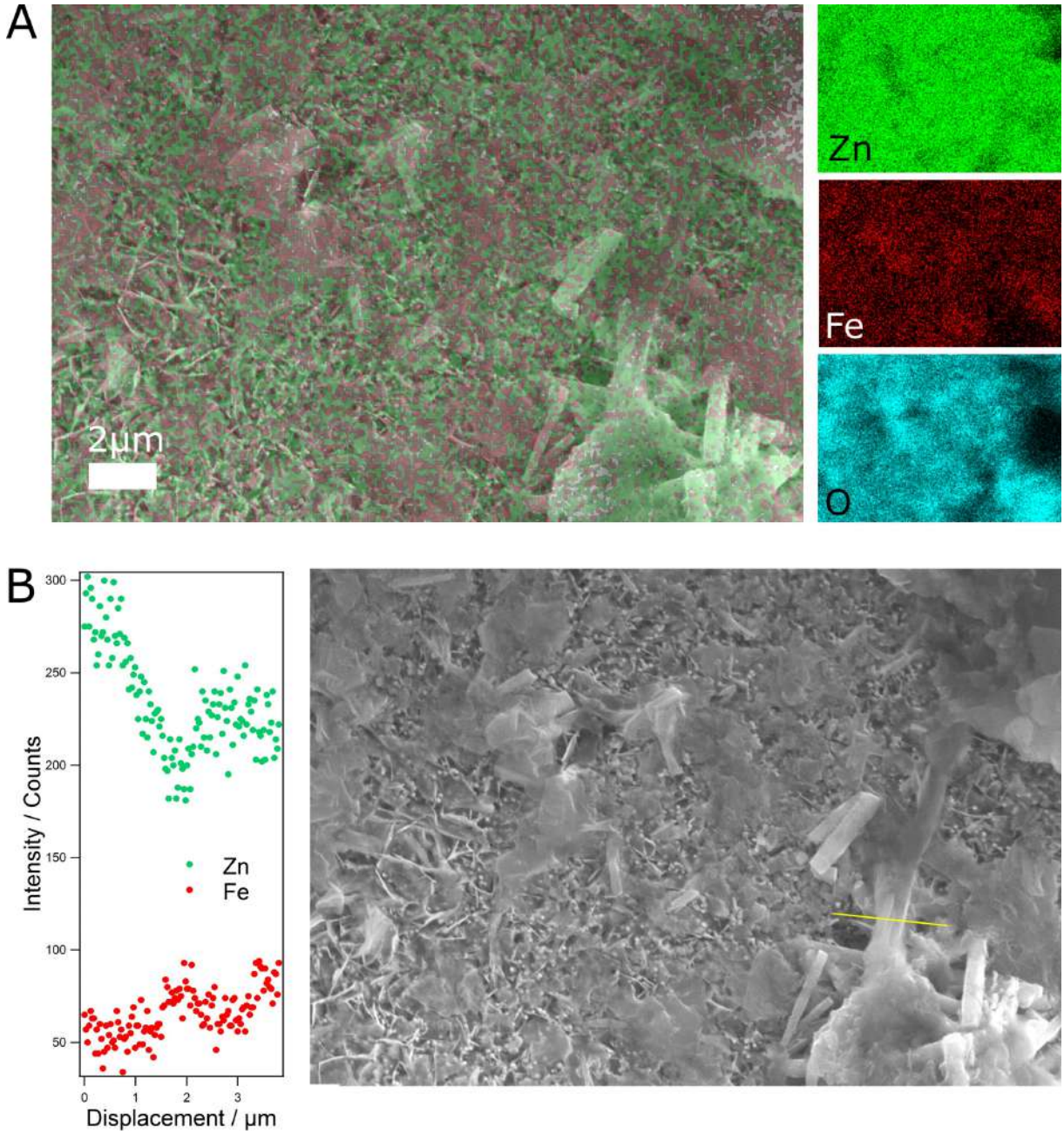


Figure S6.3: A) shows EDX maping of the sample area of a typical 40µA, with composite image of Zn and Fe (left) and component elements (right). B) shows an EDX line scan of an $Fe_2O_3$ aggregates on the surface.

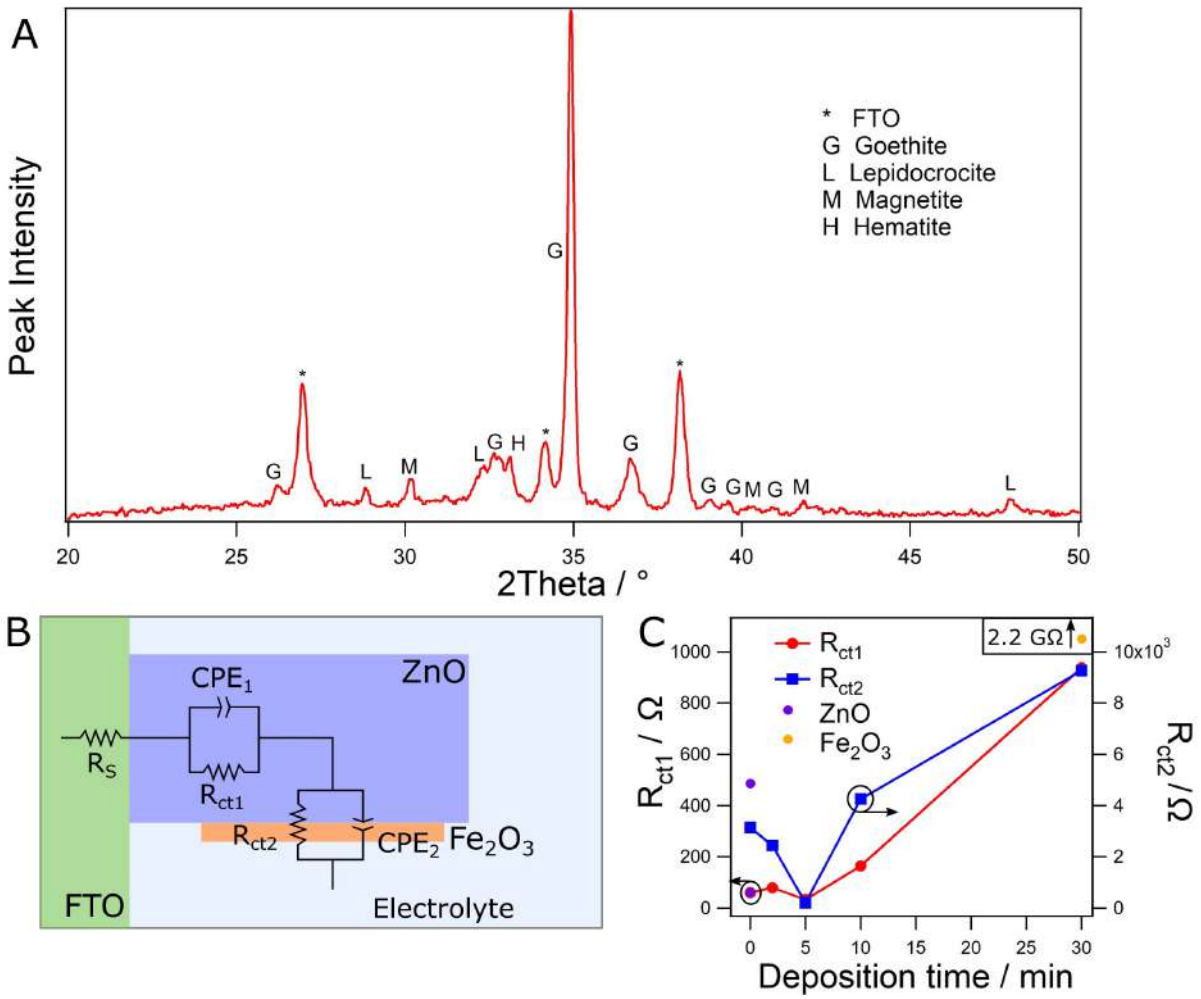


Figure S6.4: The unannealed XRD pattern of the optimised sample deposition is displayed in A). B) shows the equivalent circuit used to fit the Nyquist plots, and C) shows the different $R_{CT}$ values plotted against deposition duration, along with pure samples.

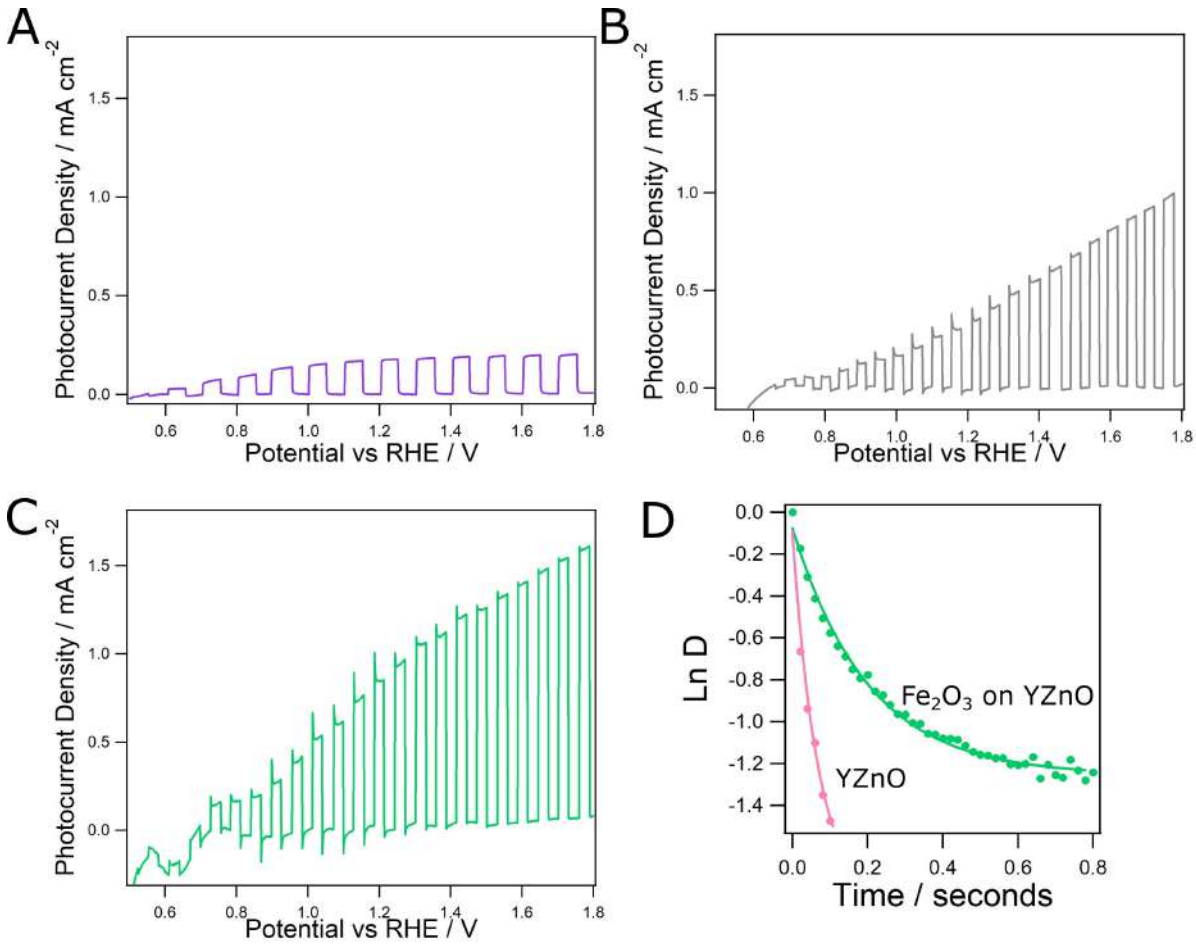


Figure S6.5: Shows the light/dark stepped linear sweep voltammetry of a comparative selection of anodes, with pristine ZnO A), and 5 minutes electrodeposition on pure ZnO B). C) shows the top performing sample, 5 minutes deposition on Y doped nanowires. Finally D) shows the normalised logarithm of current decay from the chronoamperometry measurements.

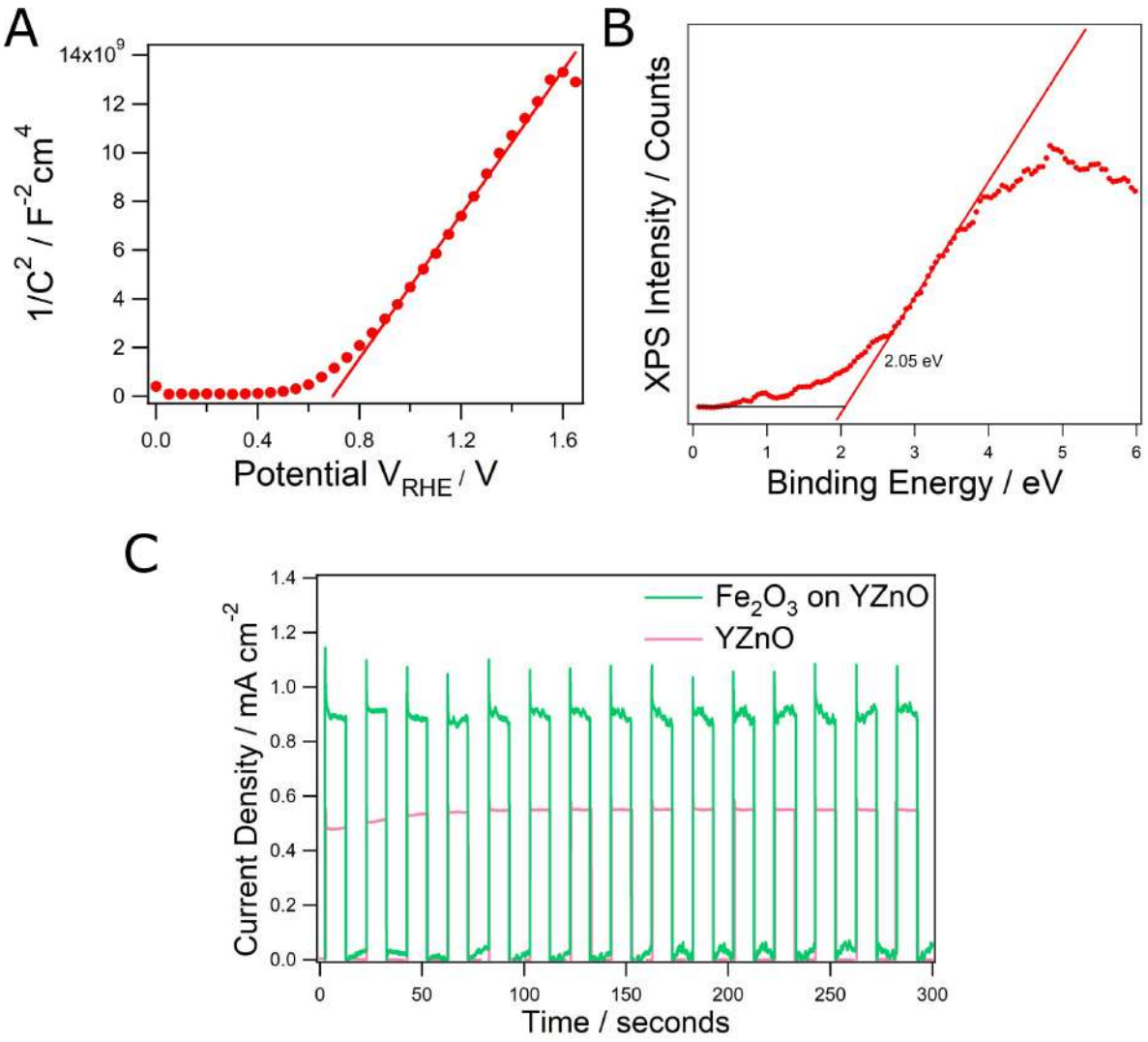


Figure S6.6: A) shows the Mott-Schottky plot of the anodic deposition of $Fe_2O_3$, yielding $V_{FB}$ value of 0.69 $V_{RHE}$ and dopant density of $1.19 \times 10^{26} \mathrm{m}^{-3}$. B) shows the XPS survey scan of the hybrid junction and valence band determination, finally C) shows the chopped illumination chronoamperometry test over a five minute period.

# Chapter 7

# All Inorganic, $CsPbBr_3$ Perovskite Solar Cells Using Modified ZnO Nanorods for Record Short Circuit Current

## 7.1 Abstract

3-D all-inorganic perovskite solar cells have been built using vertically aligned conductive zinc oxide nanorods as the electron transport layer and optical waveguide. Yttrium doping improved the conductivity and hence the electron transportation of the ZnO achieving a threefold improvement of the solar cell efficiency. The vertically aligned nanorods act as optical waveguides, which improve photoabsorption of the perovskite semiconductor. Our novel device structure was completed with an exfoliated multilayer graphite back contact for effective hole-extraction. The ZnO was further modified by nanometre scale coatings of $TiO_2$ in order to passivate the surface and reduce charge recombination. This novel strategy led to an overall nine times enhancement in the solar cell efficiency, yielding a highly competitive top value of 5.83%. More importantly, the all-inorganic solar cells demonstrated excellent stability, showing no decline in initial performance after 1000 hour storage in ambient conditions. This work presents yttrium doped ZnO as a suitable replacement for mesoporous $TiO_2$ achieving a record breaking short circuit current of $10.5\,\mathrm{mA\,cm^{-2}}$ for $CsPbBr_3$ perovskite devices.

## 7.2 Introduction

Over the last decade a tremendous rise in efficiency has brought organic-inorganic hybrid perovskite solar cells (PSCs) to the frontier of renewable energy research.[67,68,71] However, the poor stability of the material under hot and humid conditions has led to the burgeoning field of inorganic perovskite cells, replacing various organic cations with cesium.[441] In the three years since conception,[78] efficiency in such devices has risen to 13.4% using $CsPbI_3$,[163] and passed 10.1% using wide band gap, $CsPbBr_3$.[77] Crucially, these devices display superior long term stability in high humidity and temperature testing. Thus far, nearly all these devices have used mesoporous (mp) $TiO_2$ as electron transport material (ETM) with some notable exceptions, such as ETM free and interfacial quantum dot devices.[442,443] High charge mobility and tuneable morphology makes ZnO a promising alternative, leading to its wide application to hybrid PSCs.[444–446] So far, the performance of this material has been significantly enhanced using dopants.[159] Surface recombination has been overcome with coatings such as MgO.[447] For inorganic PSCs, ZnO thin films have been employed as ETM in a limited capacity,[162,163] leaving more exotic morphology unexplored.

In a typical hybrid PSC, doped 2,2',7,7'-tetrakis (N,N'-di-p-methoxyphenylamine)-9,9'-spirobifluorene (spiro-MeOTAD), and noble metal contacts are used as hole transport materials (HTMs). These materials are not only expensive ($\sim$ \$350/g and $\sim$ \$50/g respectively),[448] but contribute significantly to device degradation.[449] For this reason, many HTM-free PSCs have been designed, including amorphous carbon contacts.[229,450,451]

In this work, vertically aligned, conductive zinc oxide nanorods (NRs) have been applied for the first time to inorganic PSCs with $CsPbBr_3$. Using a two step deposition method the photoactive layer showed good infiltration into the NRs, yielding layers with very high photoabsorption. Modification of ZnO with yttrium doping and $TiO_2$ coating gave record short circuit currents for

$CsPbBr_3$ of $> 10\,\mathrm{mA\,cm^{-2}}$, in an efficient optical wave-guide and charge transfer system. This allowed the device to be highly competitive with the widely used mp-$TiO_2$, with a champion efficiency of 5.83%. These devices benefit further still, from a highly simplified liquid phase exfoliated (LPE) multilayer graphite, synthesised by one-step probe sonication and drop cast directly onto the perovskite. Highly stable and conductive graphite represents one high quality back contact material for PSCs.

## 7.3 Experimental Method

### 7.3.1 ZnO NR Synthesis

All chemicals used were purchased from Sigma Aldrich with no further purification. Fluorine-doped Tin Oxide (FTO) coated, conductive glass was cut into 12 by 25 mm substrates, and etched 8 mm from the edge using $2\,\mathrm{M}$ HCl and Zn powder. This was followed by cleaning via sonication in acetone, isopropanol and DI water for 15 minutes in each solvent and subsequent drying in air. ZnO nanorod arrays (NRs) were grown by a typical chemical bath deposition method.[100] The substrates were first seeded with spin coating using a two stage program, (800 RPM for 90 seconds followed by 30 seconds at 2000 RPM) with 0.1 M zinc acetate solution in DI water and 0.6 wt% polyvinyl alcohol. The seeding layer was completed by annealing in air at $500\,^{\circ}\mathrm{C}$ for 20 minutes to form zinc oxide seeds.[99] NR growth was achieved by chemical bath deposition, using a $20\,\mathrm{mM}$ equimolar solution of zinc nitrate, hexamethylenetetramine. Doping of yttrium was introduced to the growth solution with yttrium nitrate solution ($0.2\,\mathrm{mM}$). Substrates were placed face down in the solution and left for 16 hours at $85\,^{\circ}\mathrm{C}$ to achieve $\sim 1\,\mu\mathrm{m}$ NR length. The sample was rinsed with DI water, dried and annealed at $500\,^{\circ}\mathrm{C}$ for 30 minutes. The length of the NRs was finely controlled with mild acid treatment($0.1\,\mathrm{M}$ HCl), followed by quenching in DI water after the specified duration had passed. To expose the FTO contact, ZnO was removed from an area of $4 \times 12\,\mathrm{mm^2}$ with $2\,\mathrm{M}$ HCl.

### 7.3.2 $TiO_2$ Coating

Layers of amorphous $TiO_2$ were deposited on the substrate via a successive layer adsorption and reaction technique (SLAR). A $10\,\mathrm{mM}$ Titanium (IV) isopropoxide (TTIP) solution was first prepared in isopropyl alcohol, (IPA). The NR arrays were submerged in this solution and soaked for 15 minutes. This allowed TTIP in the solution to be adsorbed onto the surface of the rods, which were then dipped for 30 seconds in IPA to remove any excess, followed by dipping in DI water to convert the TTIP into $TiO_2$ via the following reaction.

$$\mathrm{Ti(OCH(CH_3)_2)_4 + 2\,H_2O \longrightarrow TiO_2 + 4\,(CH_3)_2CHOH} \tag{7.1}$$

This deposition sequence is referred to as one dip cycle. The thickness of the $TiO_2$ shell was controlled by the number of cycles applied. Finally, the substrates were annealed at $500\,^{\circ}\mathrm{C}$ for 30 minutes in order to convert amorphous $TiO_2$ into anatase phase, forming a core-shell NR structure with $TiO_2$ shell on ZnO NRs. The aim of depositing this layer was to passivate the surface of the conductive YZnO NRs, to reduce electron-hole recombination

### 7.3.3 $CsPbBr_3$ Deposition

The inorganic perovskite was deposited on and between the $TiO_2$-ZnO core-shell NRs by a two step method. Firstly, $PbBr_2$ was spin coated upon the rods using a $1\,\mathrm{M}$ solution in DMF, heated to $100\,^{\circ}\mathrm{C}$ for one hour prior to coating, while the substrates were maintained at $90^{\circ}\mathrm{C}$. The use of hot solution and sample is to prevent the formation of large crystals and ensuring they were dry. Spin coating was performed with a 2500 RPM cycle for 30s. The samples were dried at $90\,^{\circ}\mathrm{C}$ for one hour, and then submerged in $0.07\,\mathrm{M}$ CsBr methanol solution, for 40 minutes at $50\,^{\circ}\mathrm{C}$, reacting to form crystallised $CsPbBr_3$.[450] The substrates were then soaked in IPA for 5 minutes to remove any excess CsBr and dried in air.

### 7.3.4 Multilayer Graphite Ink Synthesis and Casting

Graphite ink was produced by liquid phase exfoliation (LPE) through sonication of graphite powder. The dried graphite powder is dispersed in chlorobenzene at a concentration of 10 $\mathrm{mg\,ml^{-1}}$ using a 300 W sonic probe for 40 minutes at 80% power. Residual particles were removed by centrifuge method. The dispersion remained stable for weeks. Glass templates with fixed area were used to pattern back contacts, after drop casting of graphite, resulting in an effective solar cell area of $\sim 0.1\ \mathrm{cm^2}$. The graphite coated glass was used as the cathode of the solar cell. The assembled solar cells were annealed at 250°C for five minutes to remove residual solvent and to improve the adhesion of graphite. The full experimental procedure for cell construction is summarised in Scheme 7.1.

### 7.3.5 Structural and Physical Characterization

ZnO NR, $TiO_2$ coating, $CsPbBr_3$, and graphite morphologies were determined using scanning electron microscopy (SEM, Leica Stereoscan 420) along with EDX measurements using INCA software (Oxford Instruments) in order to analyse elemental composition. Film thickness and surface morphology were analysed using Image J software (National Institutes of Health, USA) with SEM images of the cross section and surface respectively. Transmission electron microscopy (JEOL JEM1400-Plus) was used to confirm the multilayer structure of graphite and measure $TiO_2$ layer thickness. The crystallographic properties of each layer, and full device were characterised by powder x-ray diffractometer (XRD, Siemens D500).

### 7.3.6 Efficiency and Optoelectronic Measurement

Solar cell performance was analysed under illuminated conditions using a calibrated $100\,\mathrm{mW\,cm^{-2}}$ solar simulator (Oriel LCS-100, Newport) with built-in AM 1.5G filter, along with Palm Sens 3 (Palm Sens BV) electrochemical controller at a typical scan rate of $20\,\mathrm{mV\,s^{-1}}$. The same light

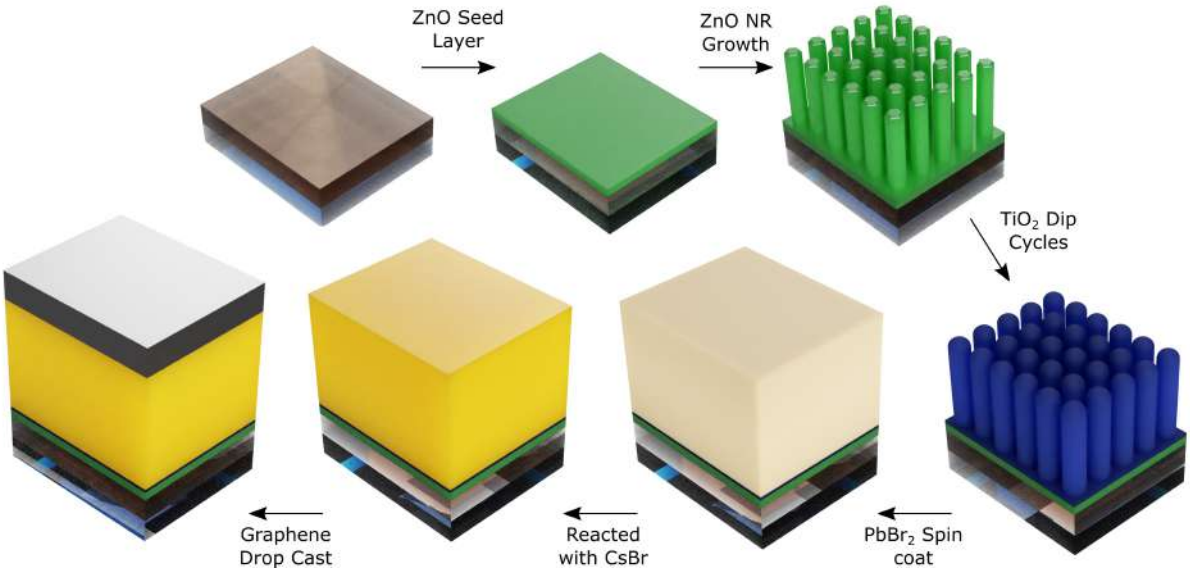


Scheme 7.1: The experimental procedure for the all inorganic perovskite solar cell construction including ZnO NR synthesis and $TiO_2$ coating followed by $CsPbBr_3$ and graphite deposition.

source and controller were used for illuminated Electrical Impedance Spectroscopy (EIS) under short circuit conditions (0 V) and sinusoidal AC at 10 mV at frequencies varying from 50,000 to 0.1 Hz. The results were processed with PSTrace 4.5 (Palm Sens BV). X-ray photoelectron spectroscopy (XPS, Thermo Scientific K-alpha using Al Kαsource) ) was used to determine valence band position and surface composition. UV-Vis absorption spectroscopy was performed using a spectrophotometer (Thermospectronic UV 300) to determine the optical band gaps of the materials. The incident photon-to-current conversion efficiency (IPCE) was measured using a 300 W xenon lamp with a monochromator and multimeter (GW Instek GDM-8341). The light intensity was characterised using a silicon photodiode sensor and optical power meter (Newport). Photoluminescence spectroscopy was used to confirm the presence of $CsPbBr_3$ along with its passivation effect at the ZnO/$CsPbBr_3$ interface, with a fluorescence spectrometer (Perkin Elmer LS 45). Finally, bandgap energy was measured using an Ocean Optics USB UV-Vis spectrometer and an ISP-REF integrating sphere and a powder MgO reference, equipped with

an inbuilt 300 nm $\leq \lambda \leq$ 1000 nm tungsten-halogen lamp.

## 7.4 Results and Discussion

The novel device design which combines ZnO NRs with $CsPbBr_3$ for the first time can be seen in schematic, Figure 7.1A, alongside a typical cross sectional SEM image of the solar cell. The layers of different materials are visible in the image, orthorhombic $CsPbBr_3$ crystal texture can be seen, penetrated by ZnO NRs with sheet like layers of graphite on the surface. The perovskite phase shows good infiltration into the ZnO layer, indicating good contact at the interface which likely facilitates rapid charge transfer. The thickness of ZnO/$CsPbBr_3$ together is $\sim$1.7 µm providing a strongly light absorbing layer, far thicker than typical planar, and mesoporous $CsPbBr_3$ solar cells.[229,442] Here, the thickness of the $CsPbBr_3$ has to be larger than the length of the ZnO NRs, otherwise, a short circuit between anode and cathode will formed. ZnO NRs have shown evidence of acting as optical waveguides, trapping the light in the geometry and feeding it into the photoactive layer,[452] a further advantage over mp-$TiO_2$.[453] The sheets of multilayer graphite back contact acts as a hole extraction layer, which was drop cast to a thickness of $\sim$50 µm. Most reports use a commercial carbon paint consisting of graphite and carbon black with other stabilising agents, applied typically by doctor blading.[443,454–457] By annealing post deposition at 250 °C the sheets become embedded in the surface of $CsPbBr_3$, providing channels for hole transport in an analogous way to the ZnO NRs for electrons.

Additional features to the device architecture, not directly seen in the SEM are the Y doping and $TiO_2$ coating of the ZnO NRs. Y doping was used to increase the conductivity of the NRs as an n-type dopant, increasing the electron conductivity.[133] The electronic structures of the solar cell is shown in Figure 7.1B. The conduction and valence band positions of ZnO and $TiO_2$ were determined by x-ray photoelectron spectroscopy (XPS) displayed in Figure S7.1 combined with UV-Vis absorption spectroscopy. The other values were found in literature as expanded in Ta-

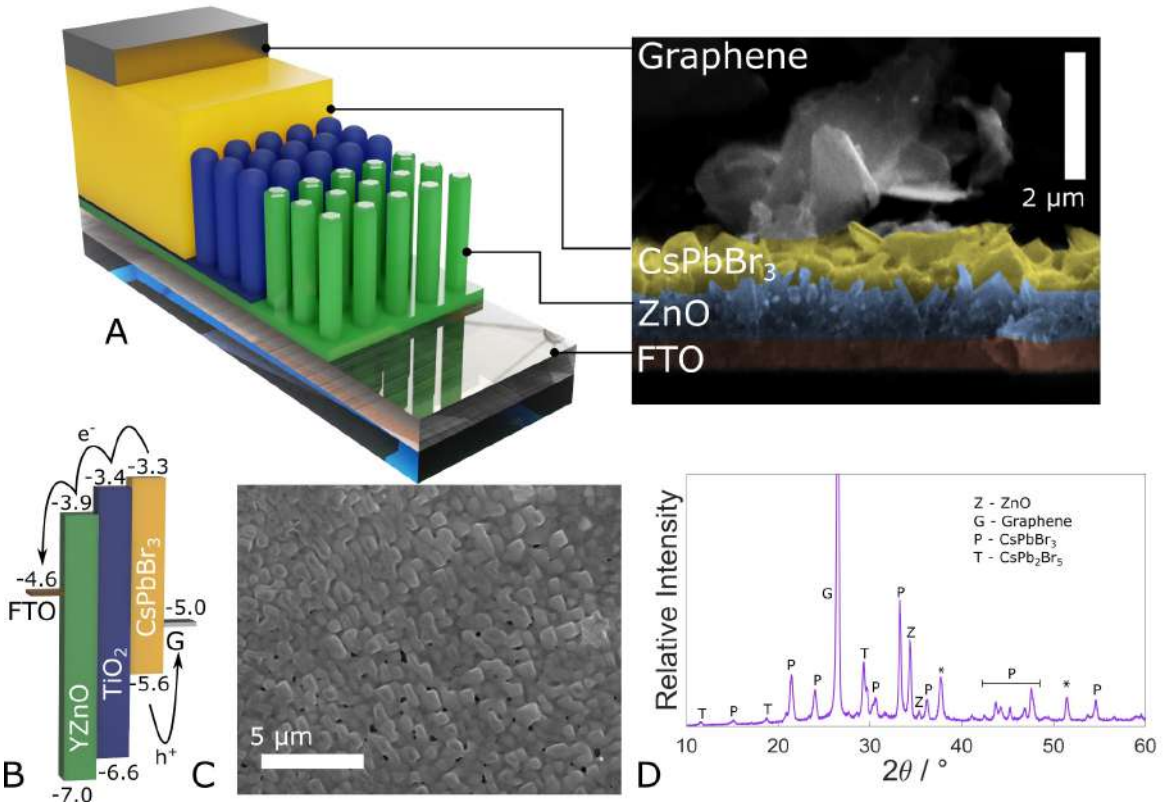


Figure 7.1: A) the solar cell schematic alongside a cross sectional SEM image of the cell, B). The energy level diagram of the layered device. C) a top down SEM of typical perovskite film quality and finally D). The powder XRD of the device.

ble S7.1. By employing the coating strategy electron transfer from $CsPbBr_3$ to ZnO conduction band becomes more favourable via the better aligned band of the $TiO_2$ shell.[229,446] Meanwhile, the valence band alignment also leads to significant hole blocking. The suitable work function allowing the graphite to select and transport holes effectively, blocking electrons via a Schottky barrier.[458] The top-down SEM image of the $CsPbBr_3$ layer in Figure 7.1C, shows reasonably large perovskite grains ($0.85\,\mu m$), vital for good performance due to recombination at grain boundaries.[457] The $CsPbBr_3$ was confirmed as the orthorhombic phase (PDF # 18-0364) by XRD (Figure 7.1D) with nearly all peaks indexed by this pattern. Small peaks occurring at $\sim$ 12, 18 and 29° are contributed from the tetragonal $CsPb_2Br_5$ (PDF # 25-0211) due to the incomplete formation of $CsPbBr_3$. The presence of this structure is common in two step depositions.[76,455,458] It can help reduce photoluminescent energy loss due to its indirect band gap.[459] Other observed peaks confirm the overall structure of the solar cell, corresponding to graphite, FTO and ZnO NRs with growth in the favourable 002 direction (PDF # 36–1451). The $TiO_2$ coating is too thin to be observed by XRD.

The graphite based dispersions employed to complete the structure of the solar cell, are elegant in their simplicity. Its compatibility with hole-transport materials and perovskite makes dispersed graphite an ideal back contact material.[460] In Figure 7.2A the stability of the colloid is observed over time showing lack of aggregation even after a month. Chlorobenzene was used as a suitable solvent for $C_{60}$ and graphite,[461,462] due to better matching Hansen solubility parameters it is able to hold a higher concentration of carbon allotrope in stable dispersion.[463,464] It is for this reason, chlorobenzene was selected in this work for liquid phase exfoliation of graphite. The most common alternative for this process is N-methyl-2-pyrrolidone (NMP), however this solvent was found to dissolve the perovskite phase.[465] Alternately, greener solvents such as water could not be used as it requires a surfactant for stable dispersion,[466] affecting the conductivity; besides this would also destroy the $CsPbBr_3$ layer.[467] Furthermore, basing the ink purely

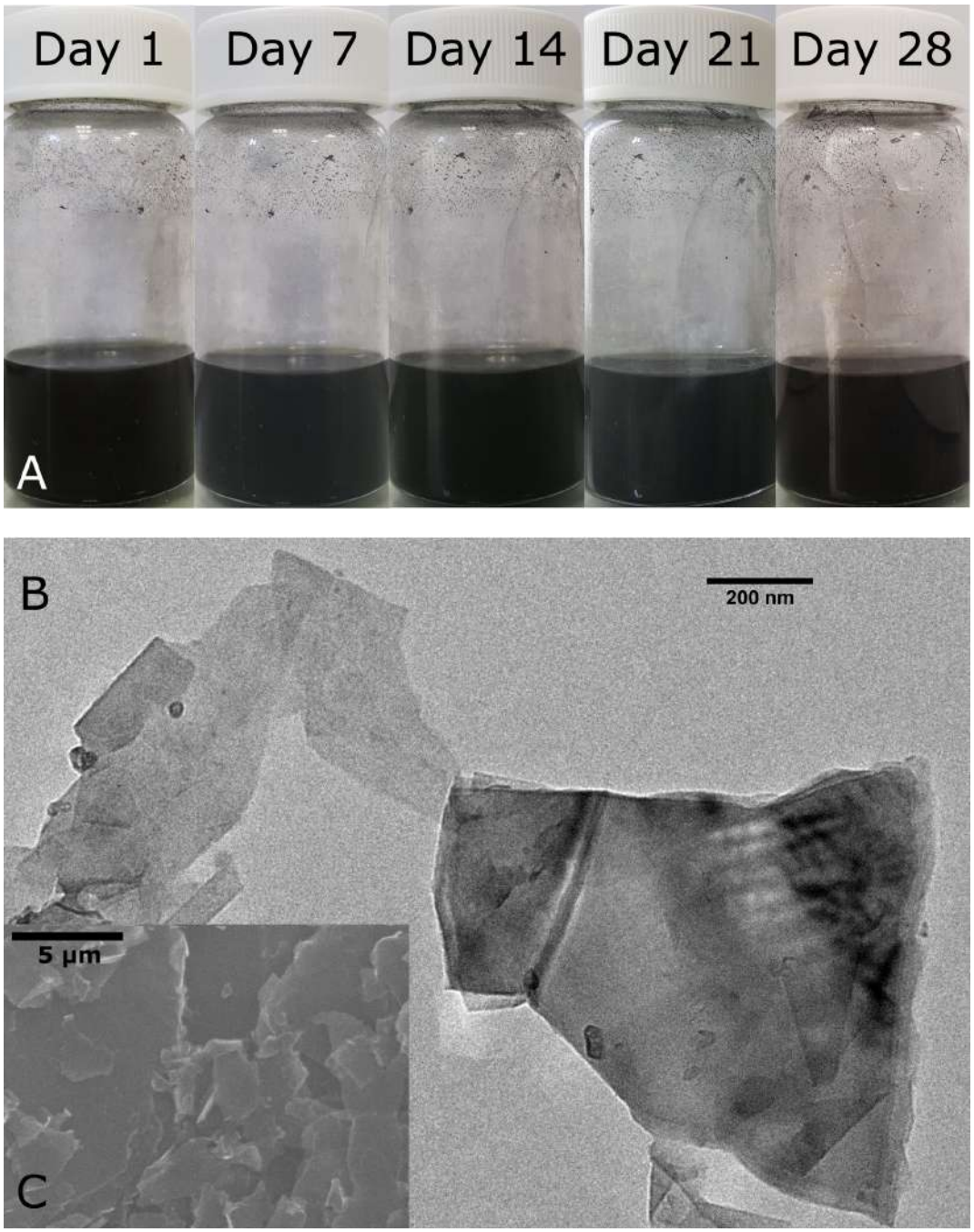


Figure 7.2: A) shows the stability of the exfoliated ink over time, up to 28 days. B) shows a TEM image of few-layer graphite and multilayer graphite along with inset C), showing a typical SEM of the drop cast material.

on graphite flakes leads to an environmental advantage over carbon black containing inks, which is a known pollutant.[468] Evidence that the ultrasonication of graphite leads to the exfoliation of few-layer graphite in the ink can be found in the TEM and SEM images (Figure 7.2B and C, respectively). Flakes of various thickness are observed, with faded few-layer graphite observable in the top left, and a thicker multilayer sheet on the right.

Despite the thickness of the flakes, the layers are clearly offset and folded from each other indicating strong exfoliation under the ultrasonic treatment, without using complicated graphite oxidation and reduction processes.[465,469,470] The graphite flakes vary in size from 180 - 1500 nm, with an average of 500 nm taken from a survey of flakes found in figure S2, typical of the exfoliated graphite.[471] The SEM image, shown in Figure 7.2C, confirms smooth morphology of drop cast graphite. This is reflected in the low sheet resistance of the films, measured to be $1.64\,\Omega\,\square^{-1}$ with a resistivity of $0.014\,\Omega\,\mathrm{cm}$, using a four point probe. This resistance is lower than the commercial FTO glass used ($\sim 7\,\Omega\,\square^{-1}$). As far as the authors are aware, this is the first reported time a ultrasonicated LPE ink has been applied as cathode back contact in a perovskite solar cell. Although, it has been used to enhance the electron transportation on the $TiO_2$ anode in perovskite cells.[472,473]

In this work, the electron transport layer was enhanced by yttrium doping, which had both a morphological and electronic effect on the ZnO NRs. The 1% molar addition of $Y^{3+}$ in the growth stage has been found to be optimal for solar application in previous work,[396] leading to increased conductivity and more favourable geometry with higher aspect ratio.[133] The true molar concentration of Y in the NRs was determined by inductively coupled plasma mass spectroscopy, to be 0.1% with respect to Zn.[396] The cross sectional SEMs of solar cells based on pristine (C), and Y doped (A,B,D) NRs based are shown in Figure 7.3. In samples A, B and D NR length was controlled by acid washing for 0, 10 and 30s with achieved layer thickness of 1195, 917 and 625 nm, respectively. The samples are named as Y1195, Y917 and Y625

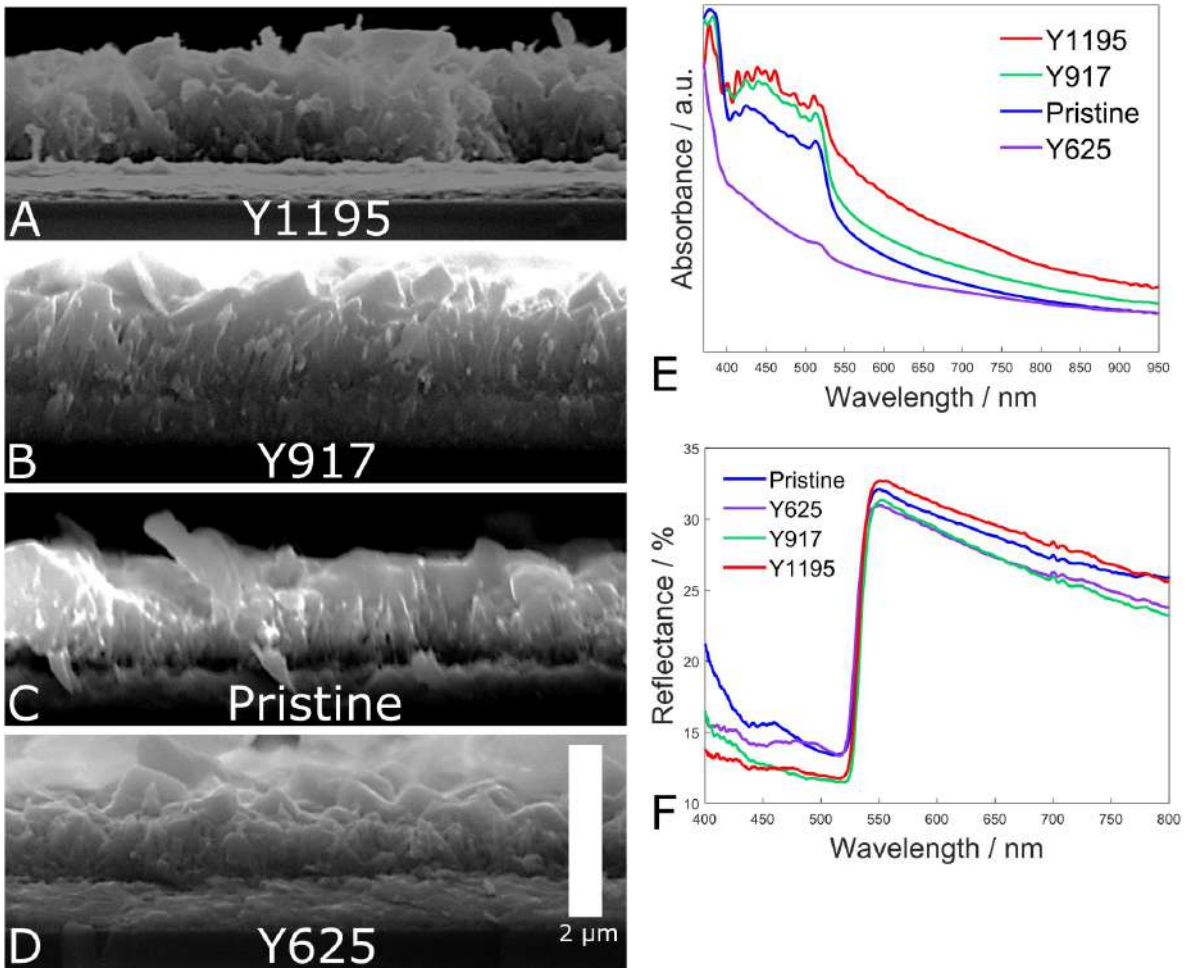


Figure 7.3: A-D) show SEM cross sectional images of the samples, A), B) and D) were the yttrium doped samples, labelled after the NR length. Y917 and Y625 had their length controlled by acid washing, the length of the pristine sample was found to be 808 nm. E) shows the UV-Vis absorption spectra of the samples and F the UV-Vis reflectance.

respectively. The ZnO NR length is confirmed by powder XRD of the devices, corresponding to the intensity of 34.5° 002 ZnO peak, found in Figure S7.3.

The unwashed Y doped NRs (1195 nm) grew $\sim 400\,\mathrm{nm}$ longer than the pristine sample (808 nm) due to the opposing partial charge of the NR sidewall planes in basic solution, to the complex formed by dopant ions.[133] This in turn led to a significant increase in light absorption, Figure 7.3E, above the band edge of $CsPbBr_3$ (<540 nm) due to a thicker supporting scaffold for the absorbing layer. This would lead to a higher population of photogenerated charge carriers in the photoactive layer. This effect can be seen in Figure 7.3A, and is also clear from the top down SEM images in Figure S7.4. Reducing the thickness of the ZnO layer, predictably, led to reduced absorption, reaching a minimum with 30s acid treatment as the NRs were significantly shorter than the pristine sample. However, increased film thickness can result in a higher charge recombination, which is the main limit of most thin film solar cell. Through embedding the perovskite in conductive ZnO NRs, such limitation can be effectively overcome. On the other hand, the perovskite coating has to be thicker than the length of the ZnO NRs to avoid short circuit.

The optoelectronic effect of dopant ions on the ZnO NRs can be seen in Figure S7.5, where the direct band gaps of the materials were measured using Tauc plots.[261] The reproducible value of 2.29 $\mathrm{eV}$ for $CsPbBr_3$ was obtained in agreement with literature,[457] along with a small red shift in band gap energy with Y doping in the absorption onset of ZnO at 3.14 eV. This shift is due to the effect of interstitial yttrium atoms, introducing electronic states in the band gap.[396] Though a minor optical effect, the n-type doping has a strong influence on the NR conductivity as indicated by Table 7.1, with samples Y917 and Y625 showing a four and two times reduction in series resistance, $R_s$, in comparison to the pristine sample respectively. This in turn leads to higher short circuit current, $J_{sc}$. Furthermore, the new $E_F$ position in the ZnO, raises the $E_F^n$ in the intrinsic perovskite phase yielding greater energy difference between the quasi levels.[474] This

led to larger open circuit voltage, $V_{oc}$, in these samples. Due to the synergistic improvement of $V_{oc}$ and $J_{sc}$ the efficiency of Y917 showed a greater than three-fold enhancement over the pristine sample. Also apparent is the sensitivity of the ZnO film thickness, the longest Y1195 sample showed only a slight increase over pristine due to the high $R_s$ value, low FF and low $V_{oc}$, possibly due to direct contact of the NRs with the graphite counter electrode. This will cause a significant back current and reduction of shunt resistance, crippling the cell. Almost as destructive to performance is the over shortening of the NRs, where photocurrent is significantly stifled due to the poor light absorption found in Figure 7.3E.

The UV-Vis reflectance spectra of the solar cells were also measured, with the results displayed in Figure 7.3F. The step at 530 nm indicates the onset of reflection from the $CsPbBr_3$ as it stops effectively absorbing at energies below its optical band gap. The reflectance at wavelengths below 530 nm show evidence of light trapping, as the sample with greatest absorption, Y1195, reflects the least light. This is likely due to the optical wave guiding properties of these nanostructures.[125,452] The longer the waveguide, the more reflections off side walls occur, with greater opportunity for light to be absorbed by $CsPbBr_3$. This is provided that there is no added space between the NRs, and population density increases with radius reduction as found in our previous work.[452] Conversely, in the short rods there is less chance of side wall reflections and emission, hence the device behaves more like planar cell with increased reflectance.[94] This side wall reflection could be further improved due to the increase of refractive index by doping in ZnO. Normal values of 2.0 for $CsPbBr_3$ 1.9 for ZnO and 2.0 for Al doped ZnO, doping would reduce optical impedance, and increase the intensity of side emission.[475–477] Secondly, the fractional power loss for guided modes is strongly dependant on the nanowire radius, with thinner wires causing greater loss in field intensity.[478] The effect of yttrium on the growth of the NWs has been previously reported to stifle lateral growth, reducing the radius to 40 nm would mean greater losses allowing light to better leak out into the cell.[133] Conversely, undoped wires with

radii of 100 nm would lead to >90% power retention, confining the light in the wire to reflect back out again.[478] Greater light trapping and delivery to the perovskite is another reason for the higher $J_{sc}$ in the doped samples.

Table 7.1: Solar cell performance and IV curve parameters, along with series resistance $R_s$. All parameters were derived from forward scans, full scans can be found in Figure S7.5

| Sample | $\eta$ / % | $J_{sc}$ / $\mathrm{mA\,cm^{-2}}$ | $V_{oc}$ / V | FF | $R_s$ / Ω |
|---|---|---|---|---|---|
| Pristine | 0.63 ±0.04 | 1.92 ±0.08 | 0.83 ±0.01 | 0.39 ±0.01 | 178 ±8 |
| Y1195 | 0.83 ±0.05 | 3.56 ±0.16 | 0.75 ±0.01 | 0.31 ±0.01 | 193 ±9 |
| Y917 | 2.10 ±0.13 | 4.02 ±0.18 | 0.90 ±0.01 | 0.58 ±0.02 | 36 ±2 |
| Y625 | 1.22 ±0.08 | 2.54 ±0.11 | 0.95 ±0.01 | 0.51 ±0.01 | 81 ±4 |

The Y doped ZnO NRs were further modified by coating with $TiO_2$ via a simple dipping method in order to improve the PCE of the solar cell structure further by reducing charge recombination at the ZnO surface. The morphological effect of the $TiO_2$ begins to be visible under SEM after three dip cycles (Figure 7.6A-D) leading to the presence of some surface roughness and bumps. This becomes more prevalent with further cycles up to 10 dips, where the rods themselves begin to be masked by surface coating and a significant amount of cross linking can be seen. In order to confirm the presence of coating, TEM was used in Figure 7.6E, on the sample with 3 dip coatings where a clear, lighter, outer layer is observed. Unfortunately this layer could not be distinguished from Fresnel fringes and therefore could not be used to measure the thickness. The presence of titanium was evidenced by EDX measurements, Figure S7.7. Though $TiO_2$ coating is a common strategy to improve ZnO NR performance, to the authors' knowledge this is the first time the thickness of said coating has been controlled at the nanoscale to optimise the performance of perovskite solar cells.[158,228,251,479]

In order to further confirm the presence of $TiO_2$ on the NR surface XPS was used to analyse the surface composition. The survey scan displayed in Figure 7.4F clearly shows the presence

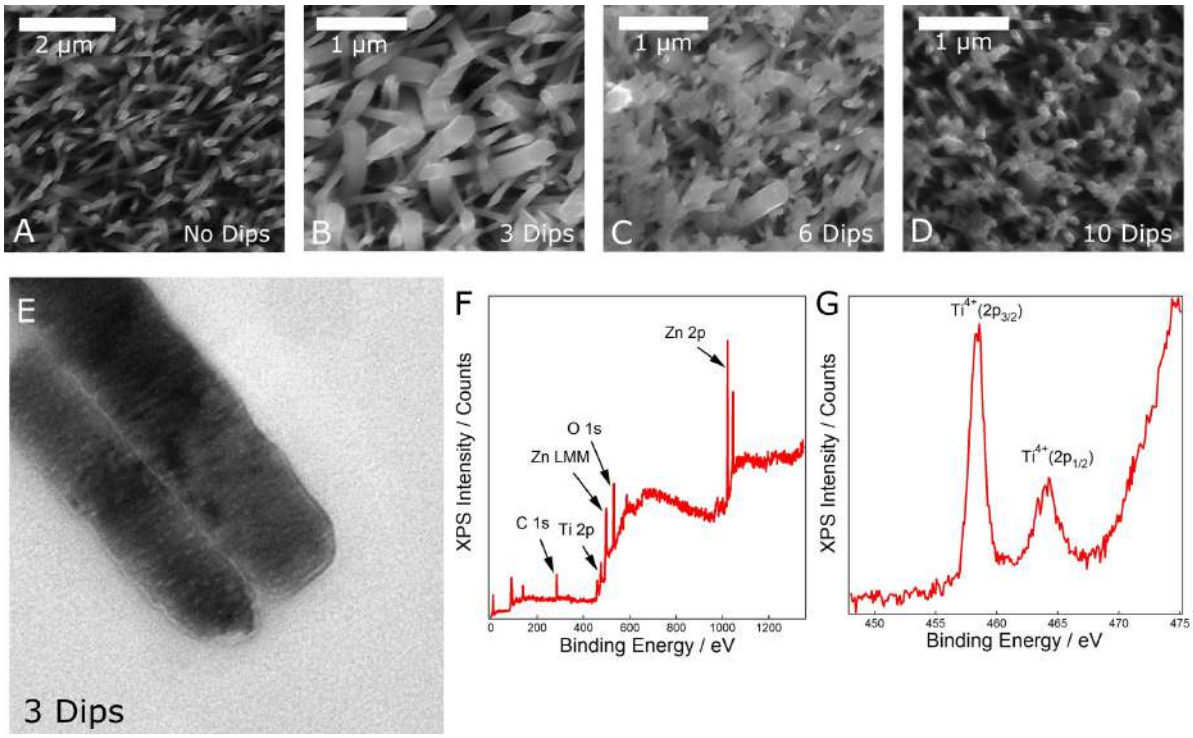


Figure 7.4: A-D) the top down SEM images of the ZnO NRs post $TiO_2$ coating, before perovskite deposition, with increasing dip cycles from 0, A) to 10, D) E). The TEM of the 3 dip cycle coated ZnO NRs, with the measured thickness of the $TiO_2$ layer.

of Zn, Ti and O on the substrate surface. In order to investigate the oxidation state of Ti, a high resolution scan was performed on the 2p region, from 445 to 475 eV. Unsurprisingly the titanium was confirmed to be in $Ti^{4+}$ state, with no obvious peak doubling or widening due to the presence of $Ti^{3+}$.[39] This confirms the presence of $TiO_2$.

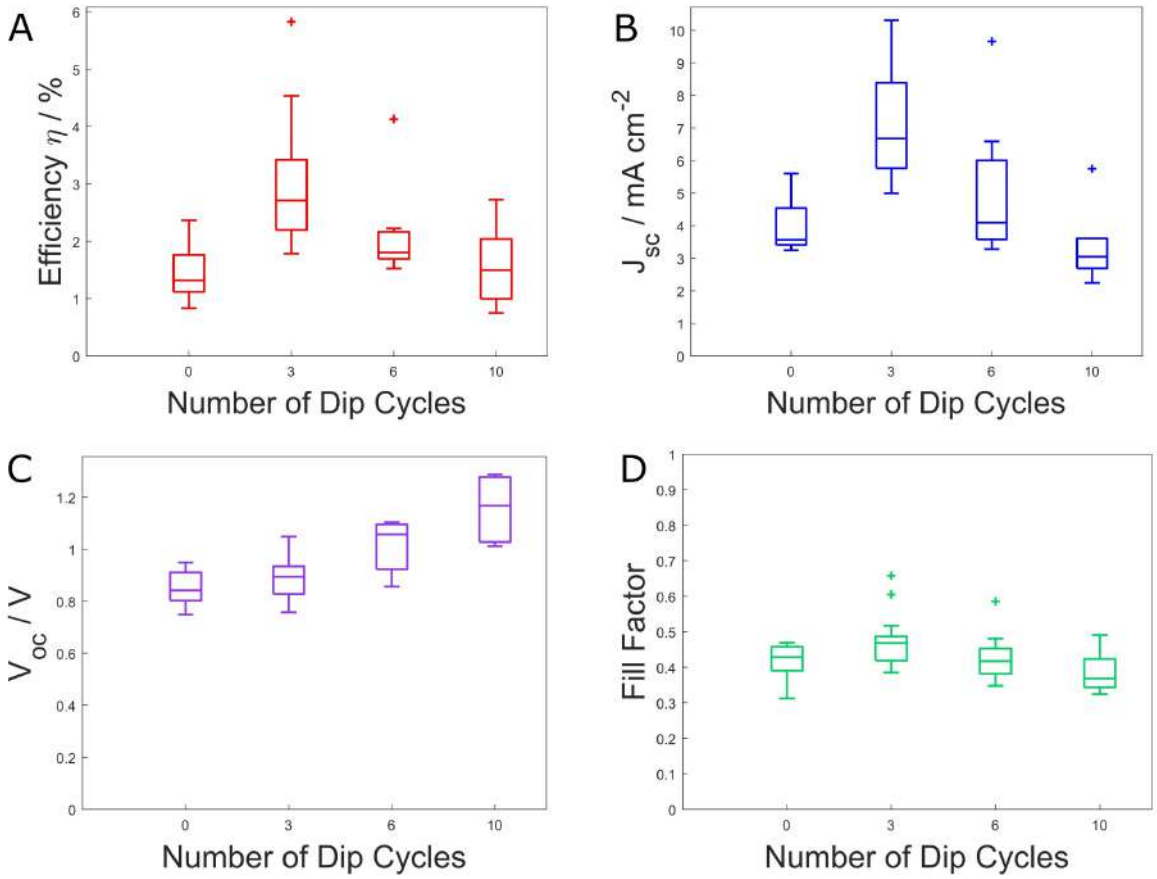


Figure 7.5: A-D) show the solar cell parameters with varying thickness of $TiO_2$ coating.

Box plots of the solar cell parameters are shown in Figure 7.5A-D, each point represents 5 or more different cells measured with varying $TiO_2$ coatings. The best performing 3 dip cycle NRs were confirmed with 27 cells in order to confidently reproduce data. The median value of efficiency (Figure 7.5A) increases dramatically for the lightest coating of 5.1 nm thickness, by a factor of over two. The mean average value of this coating is $2.93 \pm 0.2$ %, giving consistent

efficiency over various samples. This increase corresponds strongly with a leap in $J_{sc}$ due to passivation and hole-blocking effects at the YZnO/$CsPbBr_3$ interface.[158] One disadvantage of ZnO as the ETM is high recombination rate at the aforementioned interface, as electrons are free to combine with $CsPbBr_3$ valence band holes. A thin layer of $TiO_2$ significantly reduces this process, acting as a hole blocking layer. Furthermore, this layer causes better contact between the ZnO and perovskite, passivating traps on the NR surface. This tactic is vital for the function of ZnO in such devices, with the record breaking performance of this material in a perovskite solar cell achieved by Cao *et al.* using MgO for passivation.[447] $TiO_2$ coating also led to a monotonic increase in $V_{oc}$, Figure 7.5C, due to the more positive position of the $TiO_2$ conduction band and $E_F$. However, for 6 and 10 dip cycles this effect was accompanied by reduced $J_{sc}$ due to the added series ($R_s$) and charge transfer resistance ($R_{CT}$) measured by EIS, Table 7.2.

Table 7.2: EIS results of the equivalent circuit parameters, the raw data, equivalent circuit and simulated fits are found in Figure S7.8.

| Sample | $R_s$ / Ω | $R^z_{CT}$ / Ω | $C^z$ / nF | $R^p_{CT}$ / Ω | $C^p$ / μF |
|---|---|---|---|---|---|
| Pristine | 1339 ±44 | 2909 ±96 | 0.721 ±0.024 | 9585 ±316 | 110 ±4 |
| Y Doped | 398 ±12 | 2190 ±65 | 15.6 ±0.5 | 2231 ±67 | 142 ±4 |
| 3 dips | 0.782 ±0.026 | 1682 ±56 | 9.42 ±0.31 | 2212 ±74 | 186 ±6 |
| 6 dips | 135 ±5 | 1730 ±65 | 8.40 ±0.32 | 2473 ±93 | 951 ±36 |
| 10 dips | 249 ±8 | 3542 ±109 | 59.7 ±1.8 | 4498 ±139 | 356 ±11 |

The full impedance spectra can be found in Figure S7.8, displaying two distinct semicircle regions, the high frequency region is typically assigned to charge selective contacts, and the low frequency to the recombination and capacitance of the perovskite material.[480] Combining this with the equivalent circuit Figure S7.8B, the high frequency arc parameters were assigned to the ZnO/$CsPbBr_3$ interface, $R^z_{CT}$, $C^z$. The low frequency parameters were assigned to the perovskite material itself, $R^p_{CT}$, $C^p$. Both Y doping and $TiO_2$ coating have a dramatic effect on

the cell $R_s$, due to the optimisation of ZnO. As previously described the increased conductivity of the NRs from doping firstly leads to a reduction, then the passivation of surface traps with 3 dip cycles leads to a reduction below $1\,\Omega$. The difference in $R_s$ determined by EIS to the value from IV curve gradient is due to the differing potentials of testing. At low potential (0 V for EIS) the diodic character of the cell leads to increased resistance compared with IV values taken at the $V_{oc}$. This dual strategy leads to an accompanying drop in $R^z_{CT}$, promoting the transition of electrons across this boundary by reduced recombination, followed by their rapid transport from the surface.[481,482] The charge transfer and capacitive properties of the perovskite layer, correspond closely to this trend likely due to efficient charge extraction from the intrinsic material.

The benefits of the dual enhancement can be seen clearly in the champion IV curve along with the external quantum efficiency plots, Figure 7.6A and B respectively. The samples show a three times increase in efficiency with Y doping, and a 9 times enhancement when both strategies are employed, yielding PCE of 0.63, 2.10 and 5.83% for Pristine, Y doped and $TiO_2$ coated Y doped NRs respectively. This is reflected by dramatic increases in IPCE at 515 nm wavelength, leading to a doubling of value from $\sim$15 to 30% with Y doping, and $TiO_2$ coating leading to nearly 70%. For the champion cell, at 400 nm wavelength the EQE approaches 80% which is of similar value to this wavelength for the record holding ZnO based perovskite solar cell produced by Cao *et al.*[447] Photoluminescence spectroscopy measurements (Figure 7.6C) track the band edge emission of the perovskite. This confirms the passivation mechanism previously indicated by $R_{CT}$, with the 3 dip coating showing a dramatic fall in PL intensity, and therefore electron-hole recombination. Further coating thickness predictably reverses the trend, with greater surface roughness and cross linking seen in the SEM images in Figure 7.4.

The proposed mechanism leading to the reduction in PL emission, alongside the possible improvement of PCE by $TiO_2$ coating is shown in Figure 7.6D. On the left of the diagram,

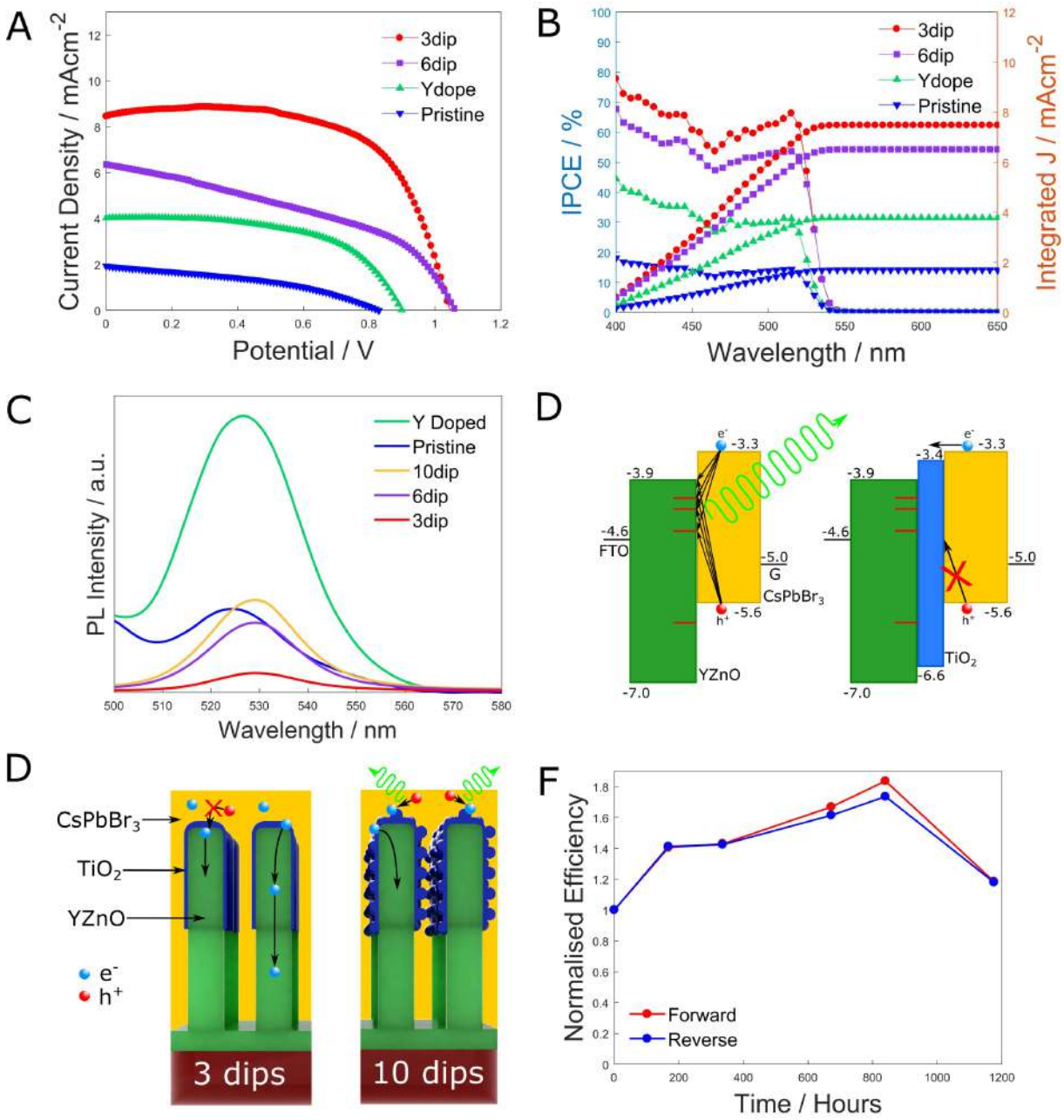


Figure 7.6: A) typical IV curves (forward scan) of various preparation conditions. B) the IPCE of the samples along with the integrated photocurrents. C) the photoluminescence spectra of the samples, with a 400 nm exciting wavelength. D) the proposed mechanism of holes blocking and surface passivation through $TiO_2$ coating. E) the explanation of rising photoluminescent intensity with thicker layers of $TiO_2$. F) the stability of the performance of the solar cell over time.

naked Y doped ZnO NRs are in contact with the $CsPbBr_3$ layer, including their measured band edge positions as well as established deep defect states found in ZnO.[452] At this interface both electrons and holes are able to transfer to the ETM, trapped in the available surface states, leading to high recombination rate and therefore high PL emission at the near band edge of $CsPbBr_3$. This is exacerbated by both non-ideal conduction band edge alignment, and high n-type doping. The introduction of the thin layer of $TiO_2$ allows effective blocking of holes, passivating the surface states acting as recombination centres.[483] This is due to a better aligned conduction band and lower n-type doping. Conduction band electrons in the perovskite are therefore more likely to transfer to the ZnO conduction band via the intermediate $TiO_2$ step. This is coupled with a greater energy barrier for the backflow of electrons into the $CsPbBr_3$ conduction band, or valence band to combine with holes. Equally a far greater energy barrier is imposed on the holes, combined with lower donor density, insulating their passage to the ZnO.[240] Although $TiO_2$ also contains surface defect states the thin layer will likely be well crystallised by annealing, and has been shown to fill in morphological defects such as pits and holes in the NR surface.[239]

The process by which thicker layers of TiO2 can lead to higher PL intensity (Figure 7.6C) is explained in Figure 7.6E. Once the layer becomes thick and fluffy as observed in the top down SEM (Figure 7.4) it becomes resistive to the transit of electrons.[251] Once trapped in this high surface area phase the electrons can begin to recombine with holes in the perovskite, rather than follow the YZnO electron highways.

The histograms of device performance parameters for the 27 solar cells produced with identical conditions are displayed in Figure S7.9A, showing reasonable reproduction of efficiency. Though the bins have a wide range the majority fall from 2 to 4% efficiency, the likely cause for the wide range is the control of NR geometry. Growth by CBD inevitably leads to some variation in the NR length, and more reproducible methods, such as chemical vapour and mi-

crowave assisted deposition could be further investigated.[295] The other parameters of the 27 cells can be found in Figure S7.9B-D. Finally the efficiency was measured over time, showing no decline under initial value in dark storage under ambient conditions after 1000 hours, shown in Figure 7.6F. This indicates excellent stability, a weakness for most perovskite solar cells. The unusual feature is the dramatic increase in solar cell efficiency seen for the first 5 weeks of storage, which is as of yet unexplained. More subtle increases in solar cells built on ZnO NRs have been previously reported, and explained by perovskite relaxation improving the contact with the rods.[252] Alternately thermal aging of $CsPbBr_3$ solar cells at $45\,^{\circ}\mathrm{C}$ for 300 hours reportedly led to a significant improvement, attributed to a self doping mechanism at the perovskite crystal grain boundaries.[484] The root cause of this phenomenon will be assessed in future work.

The performance of the novel structure reported in this work compares very favourably with existing $TiO_2$ based $CsPbBr_3$ solar cells. As the first application of ZnO to $CsPbBr_3$ cells, the record has been broken for short circuit current, surpassing $10\,\mathrm{mA\,cm^{-1}}$ (Figure 7.4G), outstanding for a band gap of $2.3\,\mathrm{eV}$. Thus far all focus to improve these cells in literature has been achieved by modifying the $CsPbBr_3$ itself,[77,93,459,474,485–487] or the hole transport layer interface.[76,443,451,454–456,458] And so there is great potential for improvement by applying the strategies reported in this work. As for the wider application of these structures to other perovskites, this is the first time both coating and doping have been applied, leading to greater PCE than several $MAPbI_3$ cell structures.[157,488–493] The dramatic enhancement seen in this work brings ZnO NRs closer than ever before to surpassing the performance of mesoporous $TiO_2$.

## 7.5 Conclusion

In summary ZnO NRs have been shown to be a highly competitive alternative to mesoporous $TiO_2$ as ETM for all-inorganic PSCs. From UV-Vis absorption and reflection data it is clear that the NRs are effective optical waveguides, delivering light to the $CsPbBr_3$. Y doping of

the NRs increased the efficiency of electron transfer from the perovskite by reducing overall series resistance of the solar cell. This optimisation strategy gave a three fold enhancement in the PCE of the solar cell. By then coating the ZnO with $TiO_2$, surface traps were passivated, leading to reduced recombination and a further increase in efficiency to a champion value of 5.83%. Due to the strengths of ZnO and the optimisation strategy, a record $J_{sc}$ of $10.5\,\mathrm{mA\,cm^{-2}}$ for $CsPbBr_3$ was achieved. Finally, a novel back contact material, multilayer graphite exfoliated by sonication was applied, to the devices. This provides a step forward in further reducing the production cost of PSCs, leading them closer to commercialisation.

## 7.6 Supporting Information: All Inorganic, $CsPbBr_3$ Perovskite Solar Cells Using Modified ZnO Nanorods for Record Short Circuit Current

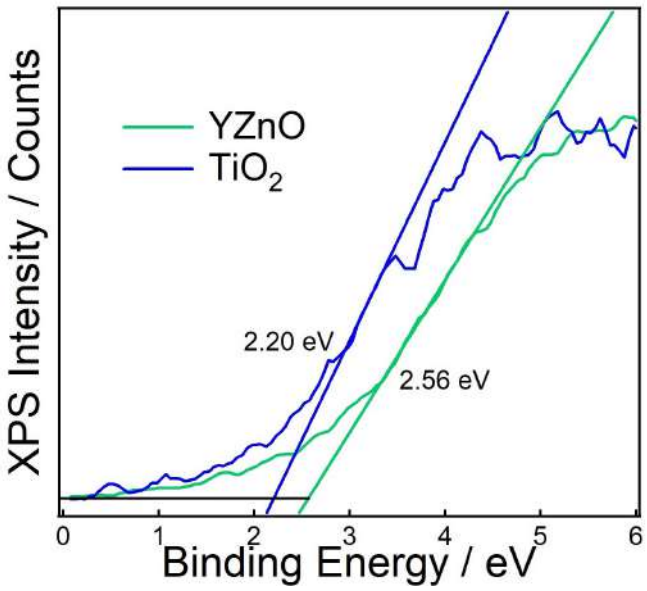


Figure S7.1: XPS survey scan of yttrium doped ZnO ($YZnO^{452}$) and $TiO_2$ coated ZnO ($TiO_2$).

Table S7.1: The electronic band structure parameters used to construct Figure 1b, including valence band, VB, band gap, $E_g$, conduction band, CB, and work function, $\Phi$.

| Sample | VB / eV | $E_g$ / eV | CB / eV | $\Phi$/ eV |
|---|---|---|---|---|
| YZnO | $-7.0^{452}$ | 3.1 | $-3.9^{452}$ | n/a |
| $TiO_2$ | -6.6 | 3.2 | -3.4 | n/a |
| $CsPbBr_3$ | $-5.6^{448}$ | 2.3 | $-3.3^{448}$ | n/a |
| FTO | n/a | n/a | n/a | $-4.6^{448}$ |
| Graphene | n/a | n/a | n/a | $-5.0^{494}$ |

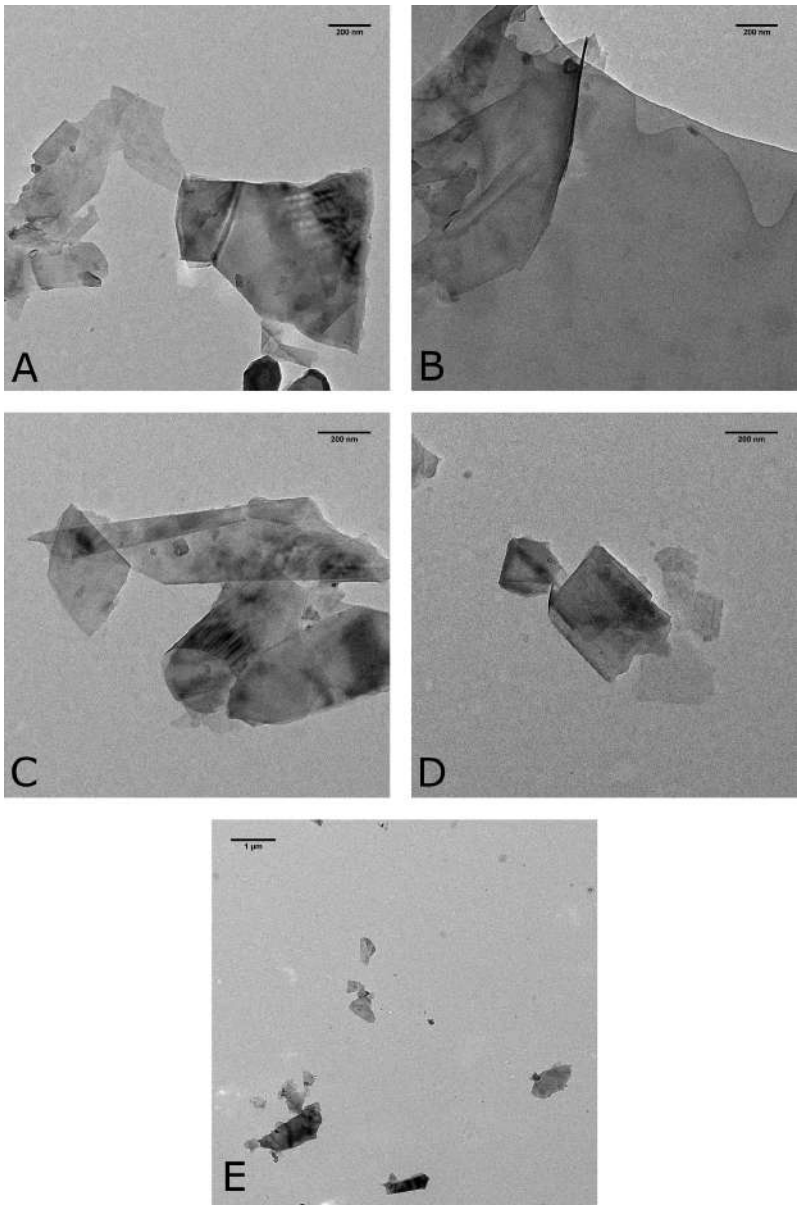


Figure S7.2: TEM images of multilayer and few-layer graphite flakes used for flake size investigation.

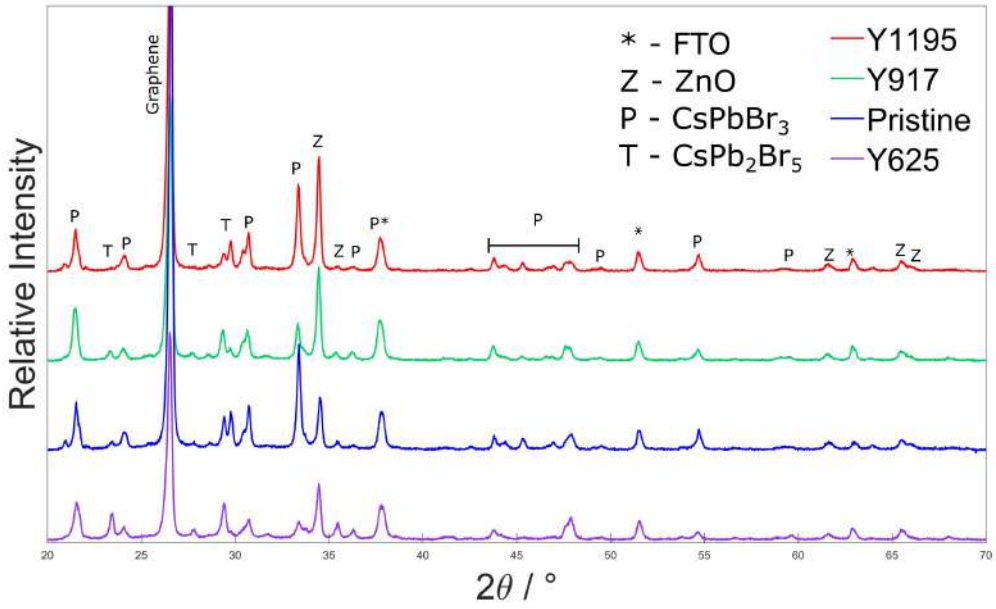


Figure S7.3: Powder XRD of the length optimisation along with undoped sample.

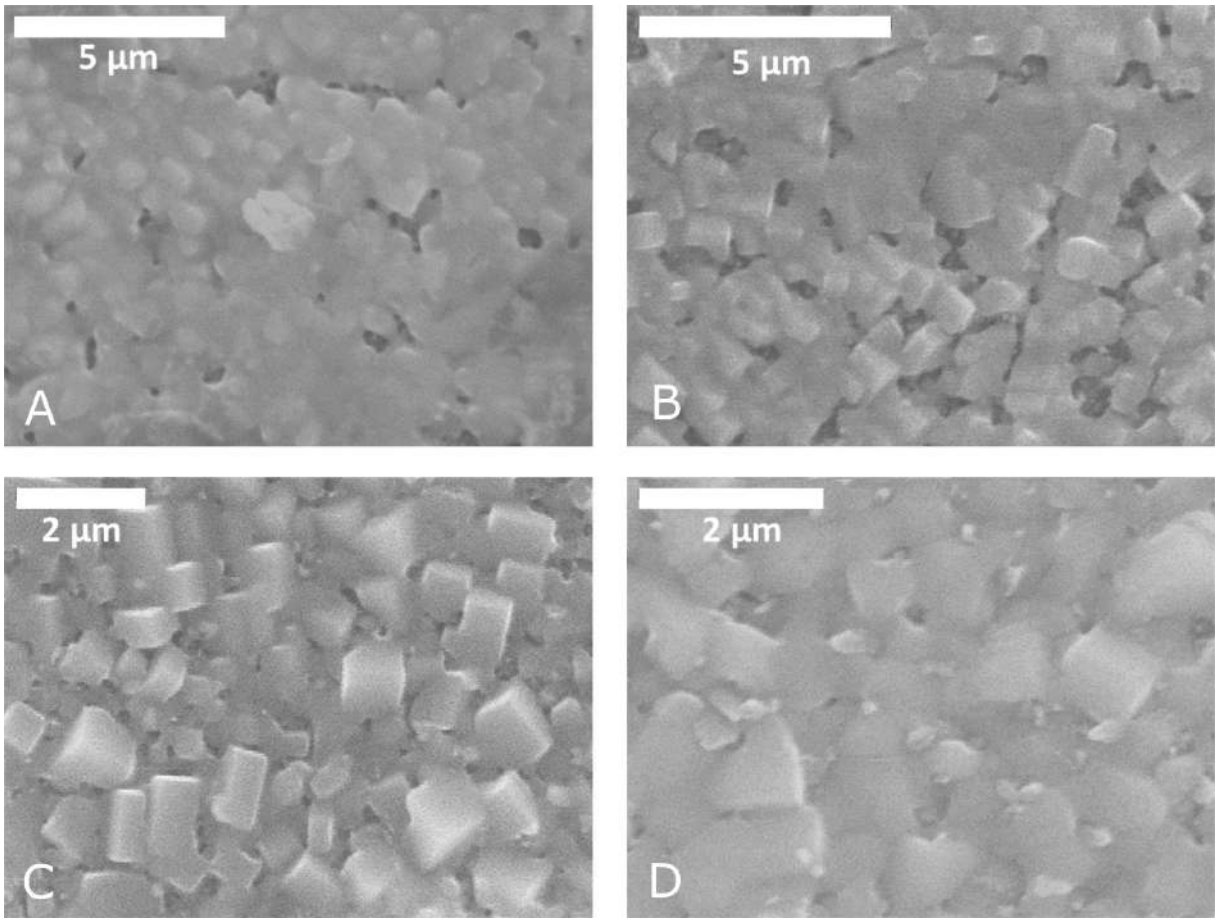


Figure S7.4: Top down SEM images of A) Y625, B) Pristine, C) Y917 and D)Y1195 samples.

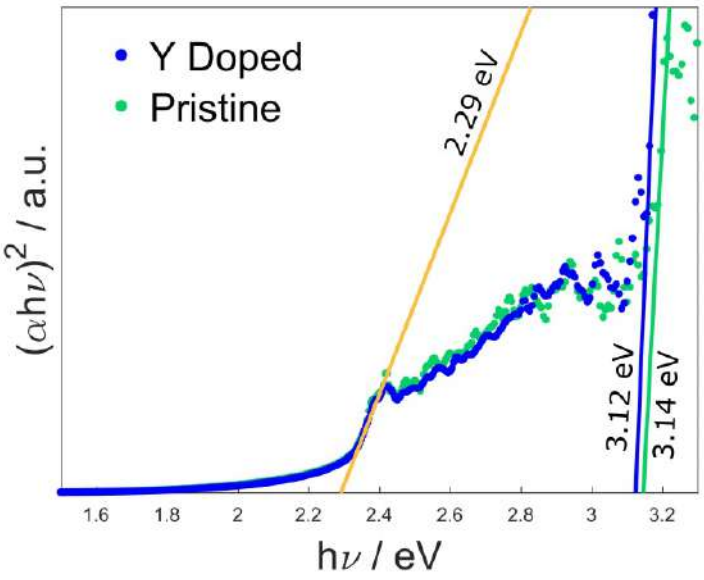


Figure S7.5: Tauc plot from UV-Vis absorption data for the yttrium doped and pristine samples, displaying direct band gap for $CsPbBr_3$ and the two varieties of ZnO. Ytttrium doping showed a band gap narrowing of 0.02 eV.

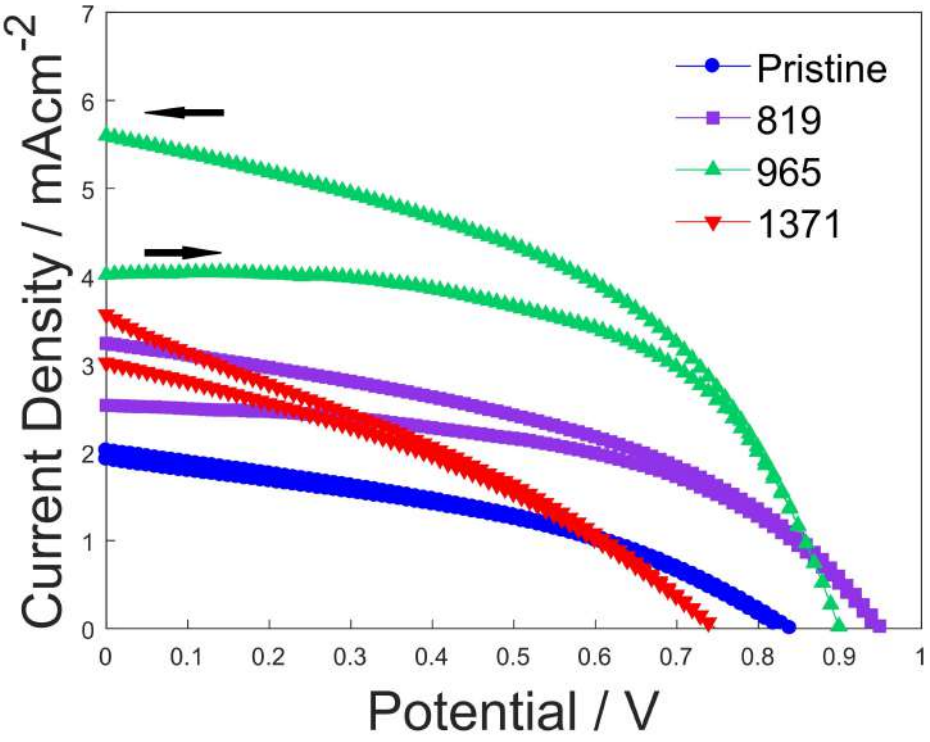


Figure S7.6: IV curves of the pristine and Y doped samples with length optimisation.

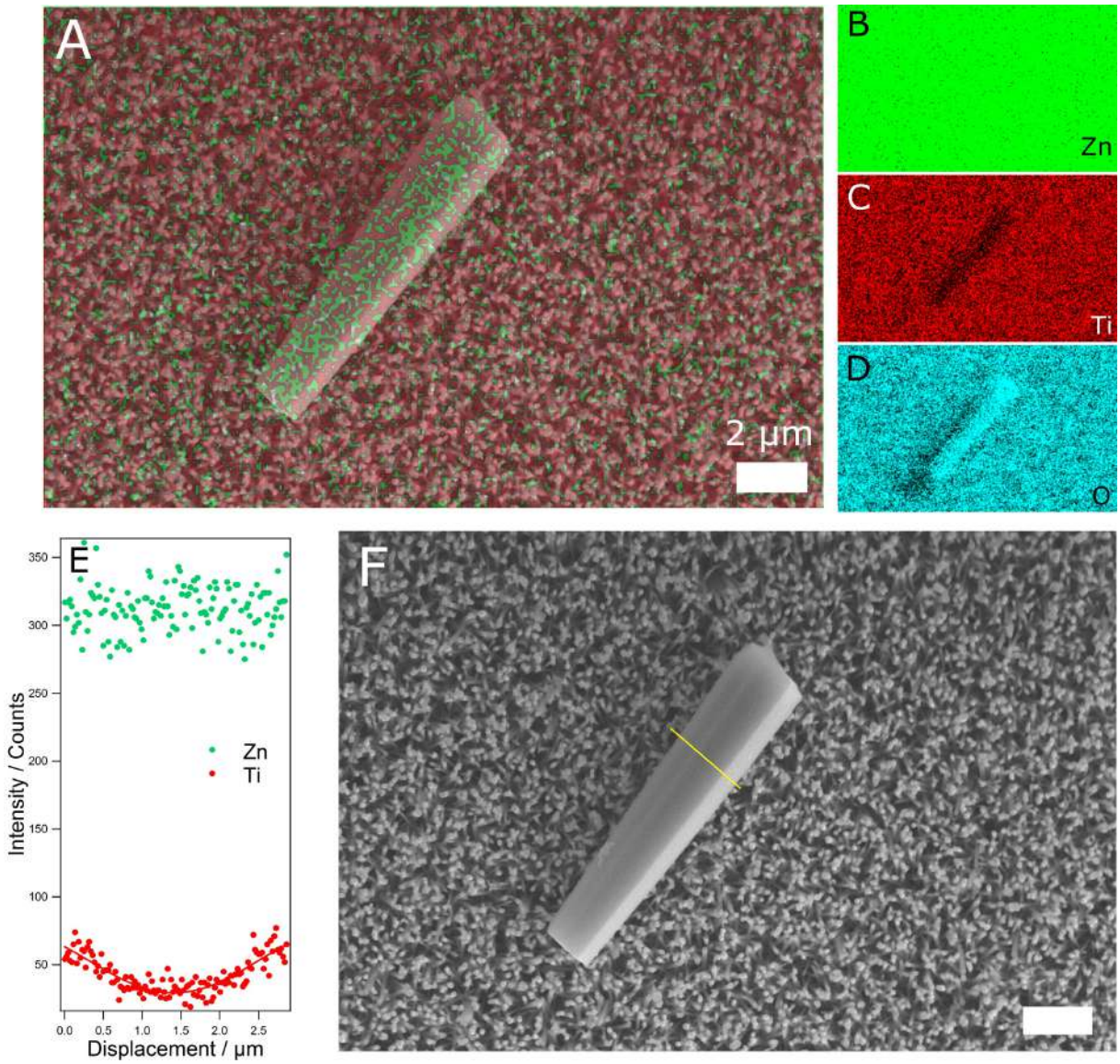


Figure S7.7: EDX data for the 3 dip cycle coated ZnO NRs, A) shows elemental mapping with B-D) showing individual elements. E) shows line scan data of the large NR profile shown in F).

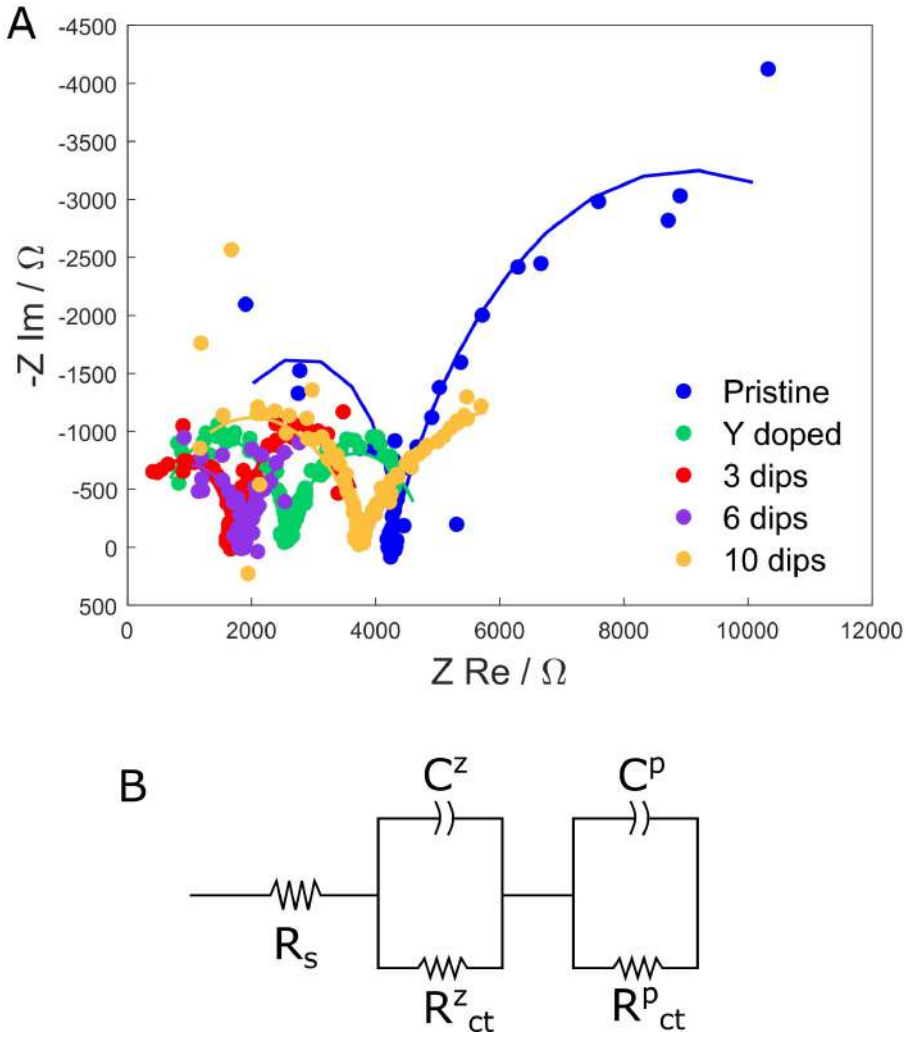


Figure S7.8: A) shows EIS data, from 50,000 to 0.1 Hz, along with simulated fitted curves, AC voltage of 10 mV, DC 0V under illuminated conditions. B) shows the equivalent circuit fit.

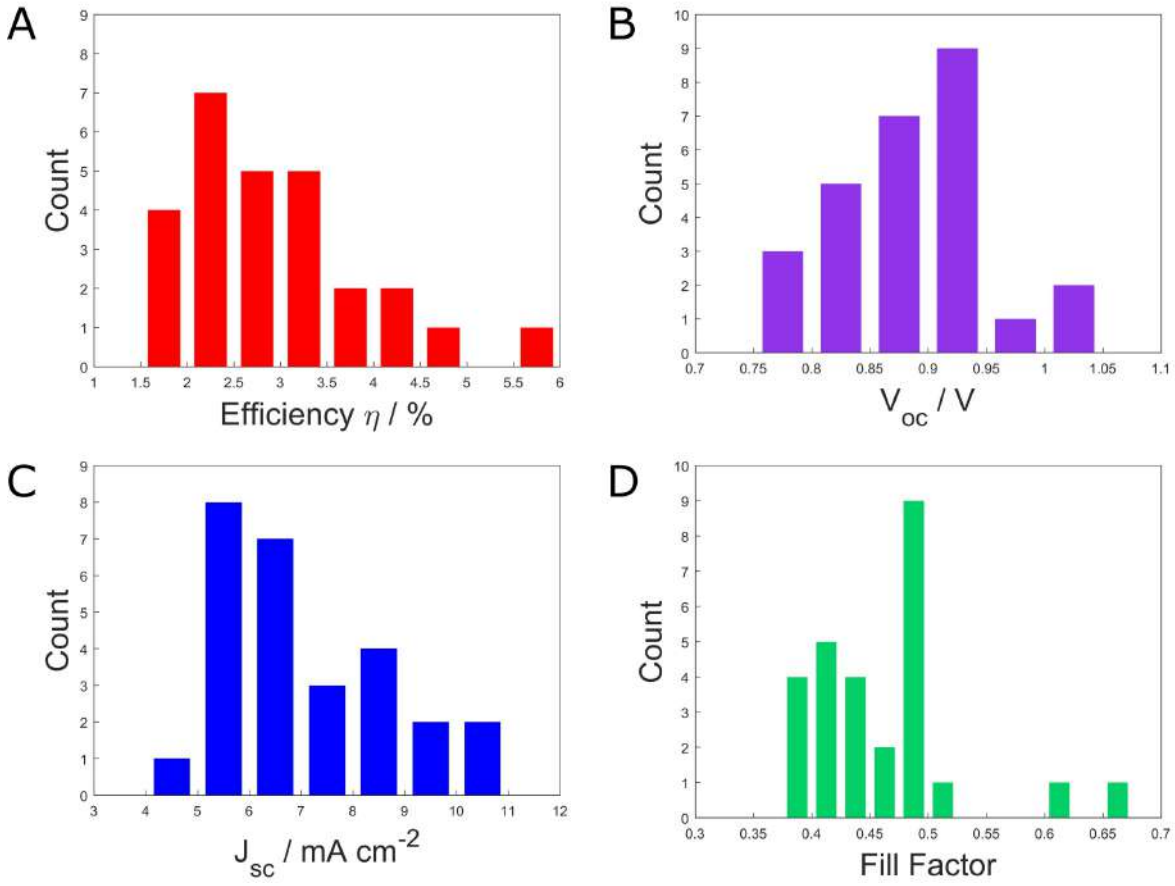


Figure S7.9: Solar cell parameters for 27 solar cells constructed under identical conditions, A) shows efficiency, B) shows the Voc, C) shows $J_{sc}$ and D) shows Fill Factor (FF)

# Chapter 8

# Dramatic Maturing Effects in All-Inorganic, $CsPbBr_3$ Perovskite Solar Cells

## 8.1 Abstract

As the growing interest in perovskite solar cell research has yielded impressive efficiency at a low cost, the focus has shifted to increase stability as they are plagued by degradation. Refreshingly, $CsPbBr_3$ solar cells built on ZnO nanowire electron transport layer with a graphite counter electrode not only avoid degradation but reverse the trend, showing significant maturation over time. In this work, this phenomenon is first confirmed as reproducible, as a large sample size showed on average a $51\pm10\%$ increase in efficiency after two weeks storage. In order to explain the mechanisms responsible for this maturing, samples were stored in a variety of different conditions and tested daily, by scanning electron microscopy, powder x-ray diffraction, IV curve and impedance spectroscopy. The sample stored in methanol atmosphere accelerated the effect, giving a four fold spike in efficiency after 2 days storage, whereas the saturated $H_2O$ environment degraded and stifled the device performance. By separating the various storage conditions into solvents, illumination and $N_2$, we suggest three complementary explanations. Firstly, that solvents can shift the equilibrium of crystal phase ratio of $CsPbBr_3$ to $CsPb_2Br_5$. Secondly, that

$CsPbBr_3$ grains are able to shrink between ZnO nanowires, increasing their electrical contact with the ETM. Finally ion migration and accumulation leads to localised p-n junctions at crystal grain boundaries aiding charge separation, evidenced by increased kinetic relaxation times on ionic time scales. Rather than degrading, these cells seem to imitate fine wine, increasing in value/efficiency over time. In this work we control this occurrence, elucidating the underlying mechanisms and explaining $CsPbBr_3$ device stability.

## 8.2 Introduction

Due to their meteoric rise in efficiency and solution based construction, inorganic-organic hybrid perovskite solar cells have been the subject of intense research.[67,68,71,74] The major limitation to these devices is stability, often requiring encapsulation to retain performance long term.[495,496] Recently, great stability increases have been achieved by exchanging the methylammonium cation with cesium, leading to the rapidly developing field of inorganic perovskite solar cells, achieving efficiencies as high as 13.4%.[163,441] Unencapsulated $CsPbBr_3$ is amongst the most stable, with some high humidity (90-95% RH) and high temperature (100°C) devices showed no performance loss after 2000 and 800 hours respectively.[448] In other typical examples, these cells tend to retain ∼90% of their performance after 10 - 130 days.[76,450,485] Despite large gains in long term stability, few works have reversed the trend of declining efficiency.

In order to understand the gain in stability with cation and halide substitution, several works aim to explain the mechanism by which degradation occurs. A key factor in the decline of efficiency is the generation of superoxide in the cell, which reacts with the perovskite to form its constituent reactants, evidenced by Aristidou *et al.*[497] This process requires oxygen, moisture and light to devastating effect, where the hydrophilic methyl ammonium cation causes $H_2O$ to rapidly infiltrate, and thereby damage, the cell. Cesium on the other hand, is both less hydrophilic and less volatile, leading to added stability.[450] To date, the degradation mechanism in-

volved in $CsPbBr_3$, although occurring on a far longer time scale, is largely unexplored (though it is known to be accelerated by high humidity).

Modest gains in efficiency over time have been previously reported, and have been attributed to various effects. Oxygen vacancy generation in the $TiO_2$ electron transport layer was the mechanism responsible for an efficiency doubling by light soaking over 15 minutes, found by Liu *et al.*[498] This led to a reduction in the series resistance, leading to greater device performance, though this declined over a period of days. Ginting *et al.* observed a permanent $\sim$24% rise in efficiency after 24 hours storage in dark conditions under air, which they attributed to the oxidation of spiro-OMeTAD, leading to improved hole transport.[499] By thermally aging $CsPbBr_3$ at 45°C for 300 hours, Luchkin *et al.* saw an increase of 35% in PCE due to the formation of p-n junctions at the grain boundaries. These junctions occurred due to ion migration, promoting charge separation and, consequentially, reduced electron-hole recombination.[484] Finally a 30% increase was observed after 1000 hours of storage under $N_2$, in $CH_3NH_3PbI_3$ ($MAPbI_3$) solar cells, attributed to infiltration of the perovskite into the ZnO NW electron transport material.[252] Clearly, many different effects are at work that can lead to maturation under various storage conditions.

In this work, dramatic long term maturing effects are measured after the storing of CsPbBr for 14 days, leading to a PCE increase of $51\pm10\%$. As the solar cells were constructed using ZnO ETM and graphite HTM, the explanations of increased oxygen vacancies and oxidation of spiro-OmeTAD cannot apply. In order to determine the mechanism behind this phenomenon, a wide range of storage conditions was used here. Solar cells in the various conditions were characterised by several techniques which tentatively confirm further infiltration of perovskite into the ZnO, establishing a crystallographic mechanism. The effects of ion migration and crystal phase ratio of triclinic to orthorhombic phase were also established to contribute. Finally we demonstrate control over maturation and understanding of degradation in these devices by

subjecting the sample to saturated moisture and solvent atmospheres, along with light/dark and $N_2$/air environments. This leads to either a fourfold increase in performance in MeOH storage, or complete destruction in $H_2O$ after 48 hours.

## 8.3 Experimental Method

### 8.3.1 Device Construction

Full details of device construction can be found in chapter seven. Briefly, etched and cleaned FTO-glass substrates were spin coated with 0.1 M zinc acetate solution, followed by annealing to convert the layer to zinc oxide seeds. Substrates were then placed face down in a growth solution overnight of 20 mM zinc nitrate, 20 mM hexamethylenetetramine for chemical bath deposition of ZnO NRs, the electron transport layer (ETM). These were then subjected to light acid treatment and passivated with dip coated $TiO_2$ as optimised in the previous chapter. Following this, $CsPbBr_3$ perovskite was deposited by a two step method: A spin-coated deposition of $PbBr_2$ in dimethylformamide, and then reaction with CsBr in methanol for 40 minutes at 50°C. The samples were completed by first drop casting a controlled area of multi-layer graphite suspended in chlorobenzene for the back contact and hole transport layer (HTM), then finally annealed at 250°C for five minutes.

### 8.3.2 Storage

For the initial study the completed cells were kept in ambient conditions in the dark, tested on the day of completion and then 14 days later. For the study of various storage effects tracked day by day, samples were each stored in phials, covered by aluminium foil to block out light in the dark samples, and stored in an illuminated room in the contrasting setting. The containers were filled with $N_2$ gas for the dry samples, sealed with fresh parafilm. The phials containing the samples to be exposed to solvent were placed in larger sealed jars, containing 20 ml volume

of the appropriate solvent (see Figure S8.1). Methanol and chlorobenzene were selected due to their presence in the device construction.

### 8.3.3 Characterisation

Samples were removed from their storage conditions in order to be characterised by top down scanning electron microscopy (SEM, JSM 820M, Jeol) and powder x-ray diffraction (XRD, Siemens D500) to track morphological and crystallographic evolution respectively. To analyse the device performance alongside optoelectronic charge transfer effects, cells were measured by IV curve followed by electrical impedance spectroscopy (EIS) under illuminated conditions, using a solar simulator (Oriel LCS-100, Newport) with built-in AM 1.5G filter callibrated to $100\,\mathrm{mW\,cm^{-2}}$. The current voltage curve used a scan speed of 20 $\mathrm{mV\,s^{-1}}$ and a cyclic scan to determine hysteresis, and EIS was performed with a 10 mV sinusoidal signal, with frequency varied from 50,000 to 0.1 $\mathrm{Hz}$, using a DC voltage at short circuit condition. Both these measurements were performed using a Palm Sens 3 electrochemical controller alongside PS trace 4.5 software (Palm Sense BV) and elchemea analytical to process the equivalent circuit fit.

## 8.4 Results and Discussion

### 8.4.1 Reproducible Maturing Effects

In previous work performed by the group, dramatic increases in efficiency were observed over a long time frame. As the effect of efficiency improvement in perovskite solar cells over time has never before been reported to such an extent, it is vital to display the reproducibility of such a result. Therefore, in order to confirm this phenomenon, a sample size of 24 solar cells was used, measured on the first day of construction (day 0), and then once again after 14 days of storage in dark ambient conditions. The results of this initial study are displayed in Figure 8.1, measuring the 5 core parameters of efficiency $\eta$, short circuit current $J_{sc}$, open circuit voltage

$V_{oc}$, Fill Factor FF, and degree of hysteresis DoH as defined by equation S1. This study confirms the regular occurrence of maturing, as 80% of the samples displayed an increase in power conversion efficiency, Figure 8.1A. This can be summarised by the 51±10% average growth in this value, the initial efficiency was 1.81±0.16% and the final was 2.53±0.19% for the solar cells. These values depend on the product of $J_{sc}$, $V_{oc}$ and FF, which shed light on the physical processes occurring in the cell(Figure 8.1B-D).

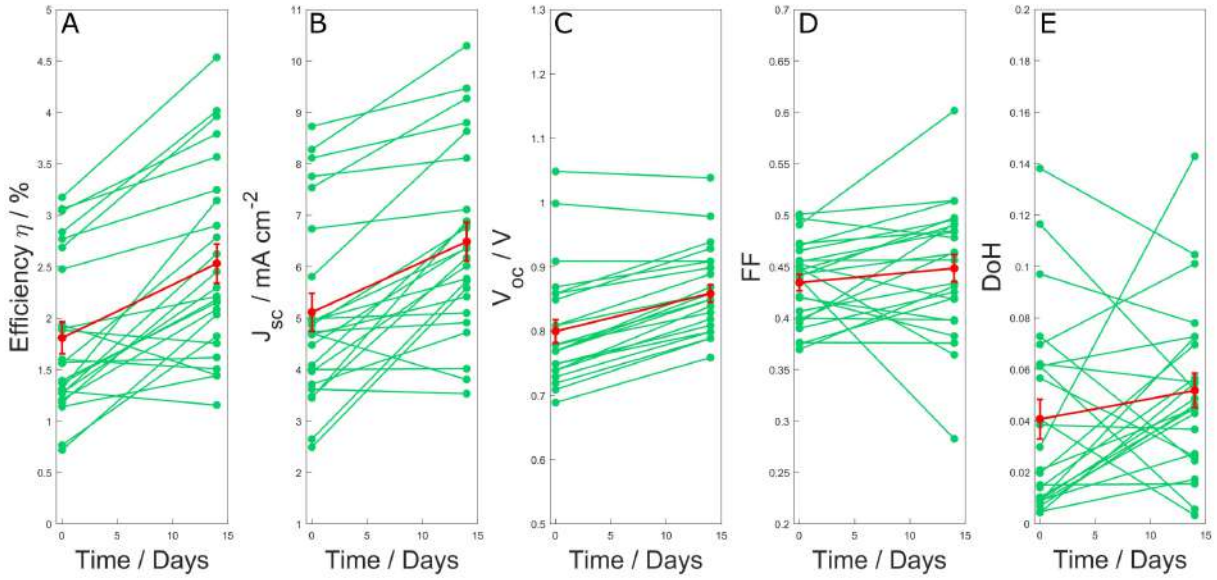


Figure 8.1: Solar cell parameters of a 24 cell sample size and their changes over 14 days. A) shows the solar cell efficiency, and the red plot the average value. B) shows the short circuit current, $J_{sc}$, C) the open circuit voltage, $V_{oc}$, D) the fill factor and finally E) the degree of hysteresis.

Although increases can be seen in all three parameters, the increase in FF is within the error on the mean, implying that the recombination in the bulk perovskite phase does not greatly change over time. Conversely, larger gains are seen in both $J_{sc}$ and $V_{oc}$ values which are responsible for the efficiency maturing effect. Firstly the average $J_{sc}$ shows an increase of 34 ± 8%, with one cell breaking beyond $10\,\mathrm{mA\,cm^{-2}}$, yielding the greatest contribution towards maturation. $J_{sc}$ is typically governed by light absorption and quantum efficiency, the latter of which

relies on efficient extraction of photogenerated charge at the ETM and HTM interfaces.[272] In the only other reporting of increased efficiency after large storage time in PSCs built on ZnO NWs, Wu *et al.* attributed this effect on the sinking of $MAPbI_3$ between the NW array over time to increase charge extraction contact.[252] This could be the case in this study explaining increased $J_{sc}$. A modest rise in $V_{oc}$ is also observed, by $8 \pm 1$ %: a parameter defined by the difference in quasi-Fermi levels in the intrinsic layer. Enhancements in $V_{oc}$ often accompany greater layer separation and reduced number of pin holes in the perovskite film, reducing numbers of deep states that occur at the edges of grain boundaries.[474]

Finally the degree of hysteresis DoH, was calculated for the study, quantifying the observed difference in IV plots' dependence on the direction of linear potential sweep. Despite being a vital factor in the degradation of $MAPbI_3$,[497] the value of DoH is initially much smaller in $CsPbBr_3$ solar cells, increasing on maturation by 7% after two weeks. This increase from 0.041 $\pm$ 0.008 is small, but may still be significant in explaining the maturing effects of storage.

### 8.4.2 Storage Conditions and Solar Cell Parameters

In order to isolate the causes of the maturing cells stored in dark conditions under air, different devices were stored in 7 situations reflecting these factors. To confirm solvent effects, cells were placed in saturated environments of methanol (MeOH), chlorobenzene (CB) and water ($H_2O$) with details found in the methods section. These solvents were chosen as they feature prominently in the device synthesis in the case of MeOH and CB, and could be trapped in the perovskite / NW layer, allowing further chemistry to occur in dark conditions under air. Also $H_2O$ was selected as it is often attributed to degradation in PSCs, and is available in atmospheric air.[497] In order to track the impact of exposure to light during PCE tests, along with effects of atmospheric $O_2$, the final four samples were kept in the following configurations: room light in air; room light in $N_2$ gas; dark in air and dark in $N_2$ gas. The samples stored under $N_2$

conditions are referred to as dry light and dry dark respectively. The tracking of the five solar cell parameters previously mentioned, for all seven situations can be found in Figure 8.2, tested daily for up to 26 days and averaged over the three cells on a single device. The raw IV curves from selected cells for each storage condition can be found in Figure S8.2 and Figure S8.3.

Surprisingly, all samples begin with an increase in power conversion efficiency $\eta$, after the first 24 hours of storage in various conditions. The most dramatic of which belongs to the sample stored in MeOH, which rose to nearly four times its original value after two days. This is explained by significant increases in all solar cell parameters, a threefold increase in $J_{sc}$ alongside $\sim$20% gains in $V_{oc}$ and FF. This is followed by an equally steep drop off in performance to day 6, implying that any residual MeOH left in the solar cell has a very strong effect on the core parameters. The sample stored in chlorobenzene on the other hand displayed a similar pattern of efficiency change, though far more modest- only $J_{sc}$ increased, while $V_{oc}$ and FF remained steady until significant degradation ruined device performance after four days. Despite a slight initial increase due to a temporary boost in FF, storage in a saturated $H_2O$ environment degraded device performance the fastest, with dramatically reduced efficiency on day two. It can be seen in Figure 8.2E that both $H_2O$ and CB caused dramatic increases in the hysteresis of the cells, a common feature in PSCs experiencing degradation.[500]

The other four samples (dry dark, dry light, air dark and air light) show far greater resistance to their respective storage conditions, with the samples stored under $N_2$ showing no decline in efficiency, even up to 26 days after construction. Both these samples had a slow rise in efficiency, likely due to the rapid removal of solvents which evaporated from the device. These enhancements cannot be explained in the same way, and so a different mechanism must be present, causing the dry dark sample to incur FF and $V_{oc}$ decreases whilst $J_{sc}$ increased. This could be due to the relaxation of the perovskite layer between the rods, increasing contact area whilst decreasing grain size. The dry light sample, comparatively held stable values for $J_{sc}$ and

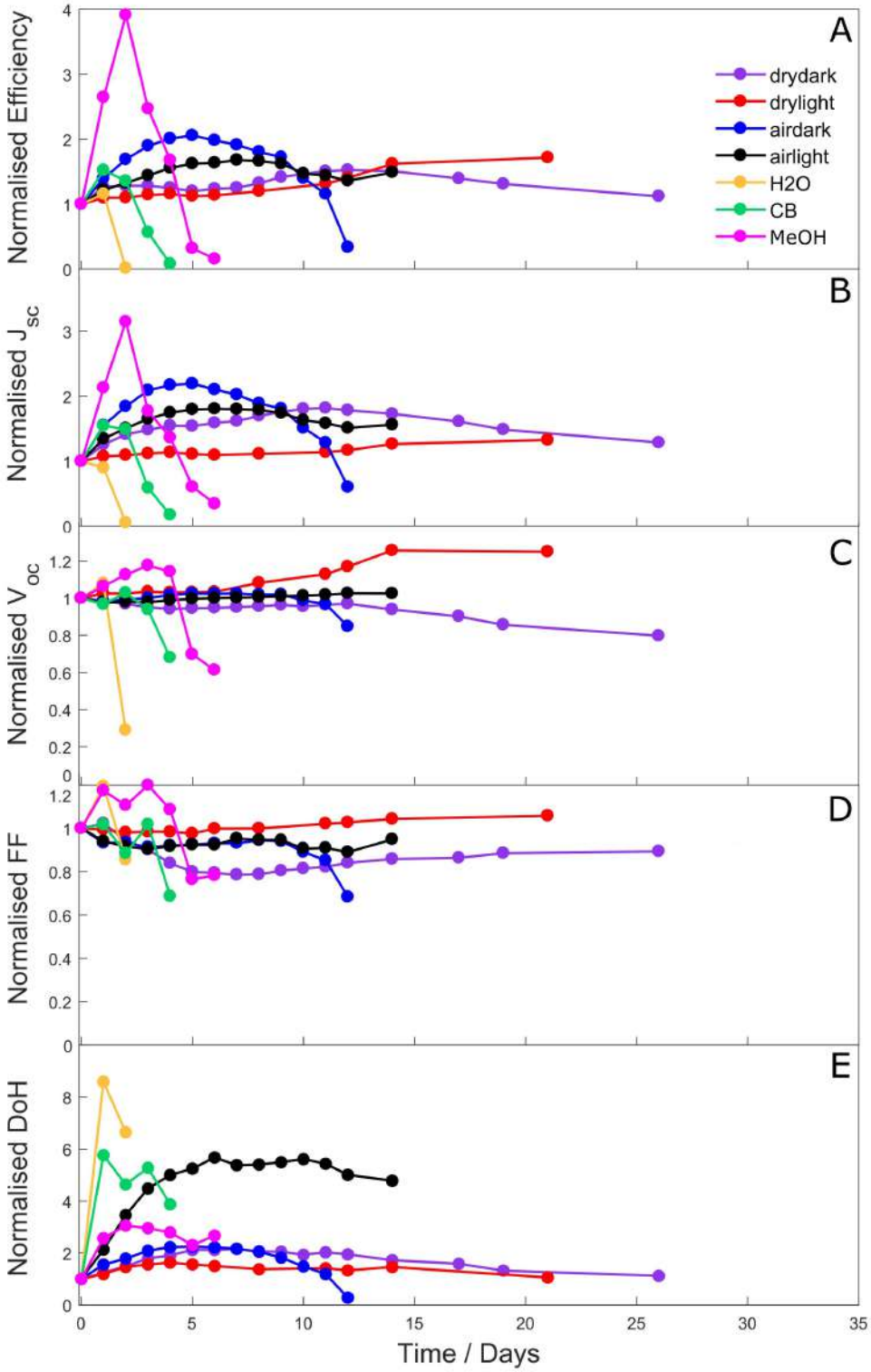


Figure 8.2: Averaged solar cell parameters of cells stored in various conditions, A) shows the solar cell efficiency, B) shows the short circuit current, $J_{sc}$, C) the open circuit voltage, $V_{oc}$, D) the fill factor and finally E) the degree of hysteresis.

FF with a significant increase in $V_{oc}$, potentially due to the filling of deep trap states. This would explain the gains in efficiency for the illuminated samples showing greater longevity, finishing higher than their corresponding dark samples. Tracking the parameters of the dark air sample day by day yields important information about the interim period performance of the samples in Figure 8.1. Strong increases in $J_{sc}$ are seen followed by a reduction on day 12, along with a collapse in FF. A clear difference is seen then, as enhancement for the first sample group is seen on day 14. This degradation is likely quickened due to damage caused by characterisation by powder XRD, SEM and the electric field imposed for IV curves. The positive effects are likely the sum of constituent conditions, that were investigated via SEM and powder XRD characterisation.

The stability of the cells over time is still comparatively high in comparison to organic inorganic hybrid perovskite cells. Many typical methyl ammonium lead iodide cells are destroyed within minutes or hours of exposure to moist air,[229,274] leading to exploration of capping and encapsulation.[374,447,501] There are several examples of long term stability shown in $CsPbBr_3$ which show unaltered device performance for longer than 100 days in high humidity.[229,443,459] However in many cases significant variability in the cell performance over time is observed, this work looks to uncover the potential causes for this within a 26 day window.[76,450,451,456]

### 8.4.3 Moisture and Solvent Effects

The storage condition with the most negative effect on device performance was the high humidity chamber ($H_2O$), the progress of which can be seen in Figure 8.3. On the day of construction, some CsBr is visible on the surface along with many pin holes, Figure 8.3A. Remarkably many of which are healed by day 1, Figure 8.3B. In fact, the self healing effect was remarkably rapid, the sample appeared bleach white in the high humidity container, and upon exposure to ambient humidity the standard yellow colour returned within 30 seconds. A demonstration of this is

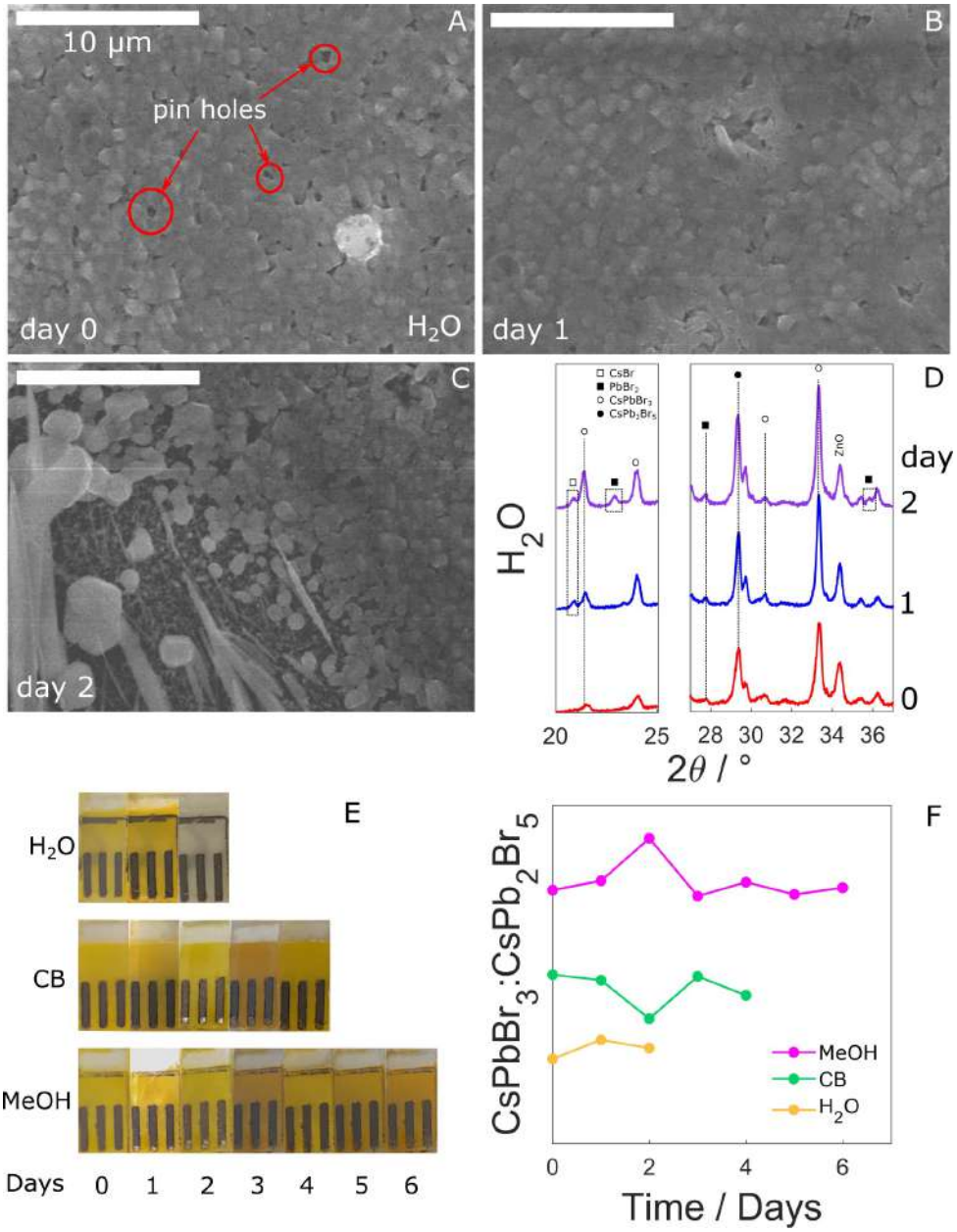


Figure 8.3: A-C) display top down SEM images from day 0, A), to day 2, C), displaying the sample displayed under saturated $H_2O$ conditions. D) $H_2O$ effects on the perovskite powder XRD plots, peaks indexed using orthorhombic $CsPbBr_3$ ICDD #30-0697,[502] and triclinic $CsPb_2Br_5$ #25-0211 of the solar cells displaying the solvent effects over time.[503] E) displays photographs taken daily of the samples, and F) summarises the ratio of phases based on the ratio of peak integral.

available in the ESI, taken 24 hours after $H_2O$ storage. However, with greater exposure the destruction of the $CsPbBr_3$ is seen on day 2, opening up the continuous film leaving rod structures and agglomerates, Figure 8.3C, and permanent bleaching found in the sample photos. Looking to the powder XRD, Figure 8.3D, it shows an initial growth in perovskite peaks at 33.5° and 22.0°, followed by the rise of new peaks at 21.5°, 22.7°, 27.9° and 35.8° assigned to CsBr and $PbBr_2$. Further peaks confirm the presence of $CsPb_2Br_5$ triclinic phase, common in $PbBr_2$ rich, 2 step reaction devices. Full XRD data can be found in Figure S8.4 and Figure S8.5. These results indicate that initially $H_2O$ promotes the formation of new $CsPbBr_3$, which is a known effect of moisture in the precursor solution.[504] This better quality, reduced pin-hole layer leads to the higher efficiency and FF observed on day 1 in Figure 8.2. Once saturated at day 2 however, the perovskite breaks down into its constituent components, CsBr and $PbBr_2$.

The devices stored in MeOH and CB were governed by an equilibrium between orthorhombic $CsPbBr_3$ and triclinic $CsPb_2Br_5$ crystal phase respectively via the two following reactions.

$$\mathrm{CsPbBr_3} + \mathrm{PbBr_2} \rightleftharpoons \mathrm{CsPb_2Br_5} \tag{8.1}$$

$$2\,\mathrm{CsPbBr_3} \rightleftharpoons \mathrm{CsPb_2Br_5} + \mathrm{CsBr} \tag{8.2}$$

Both the CsBr and $PbBr_2$ are available in excess, due to the incomplete reaction to $CsPbBr_3$, with bright particles of the former species visible at the surface for all the samples imaged on day 0. The presence of $PbBr_2$ has been confirmed by XRD, but is likely to be closer to the NWs, as it constitutes the first step of perovskite synthesis. The ratio of orthorhombic to triclinic phases was measured by the integration of the $CsPbBr_3$ peaks across the full diffractogram divided by the integration of the $CsPb_2Br_3$ peaks. The results are displayed in Figure 8.3E.

Interestingly, the phase ratios in the CB and MeOH samples are a mirror image of each other over the first four days, clarifying their differing performance over time. The ratio initially increases for the latter sample, implying a shift in the equilibrium towards $CsPbBr_3$, following

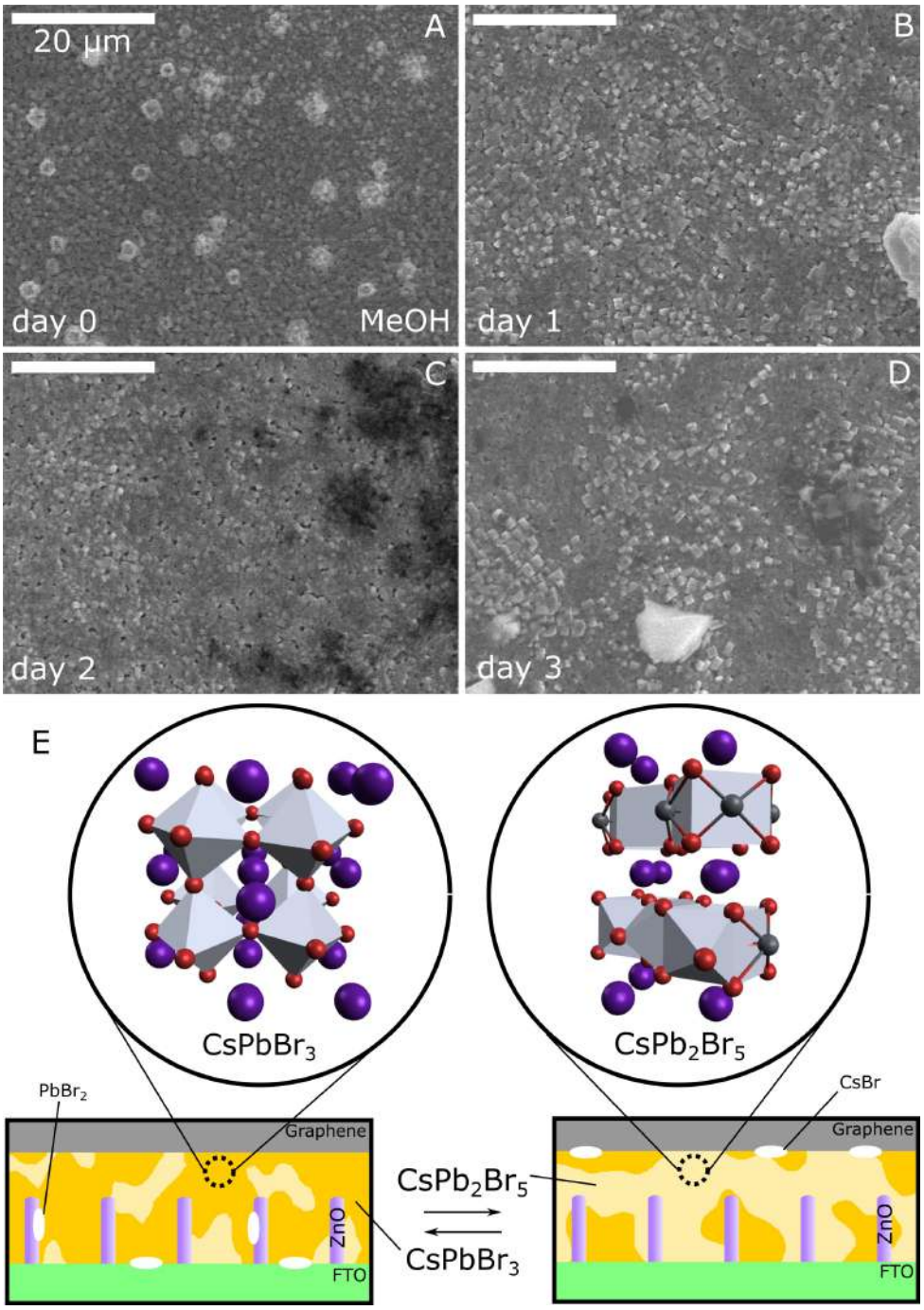


Figure 8.4: A-D) display top down SEM images from day 0, A, to day 3, D, of the sample stored in methanol conditions. E) shows the effect of the crystal phase ratio shifting from $CsPbBr_3$, left,[505] to $CsPb_2Br_5$,[506] right.

8.2. Despite evidence to show that a small quantity of $CsPb_2Br_5$ can be beneficial for the performance of PSCs in order to reduce electron hole recombination, the over abundance of this phase leads to great problems with light absorption in the device.[459] Finding methods to run the reaction further towards full perovskite phase has led to great increases in efficiency recently, for $CsPbBr_3$ solar cells using methods such as reacting the substrate face down or spin coating several times.[76,457] This work therefore, provides an elegant alternative to achieve this aim, by simply leaving in a saturated methanol atmosphere for 2 days. Conversely, chlorobenzene has the opposite effect, shifting the equilibrium to produce more $CsPb_2Br_5$, limiting device performance.

The reasons for this are unclear, however it is suggested that MeOH is more effective at dissolving CsBr as CB is, at dissolving $PbBr_2$. The films of these solvents adsorbed onto the perovskite surface allow the reactions of 8.1 and 8.2 to occur once they contain high enough concentration of either CsBr or $PbBr_2$, producing more $CsPbBr_3$ or $CsPb_2Br_5$ respectively. This is confirmed in Figure 8.4, as top down SEM images show a complete dissolution of surface CsBr, from day 0 to day 1, and the merging of $CsPbBr_3$ grains into day 2. Beyond this time, the solvent begins attacking the $CsPbBr_3$ phase, forming aggregates on surface as the reaction is reversed, visible in Figure 8.4C and D. This is further evidence by reversed phase shift visible in Figure 8.3F. The formation of a higher purity $CsPbBr_3$ explains the behaviour of device performance measured in Figure 8.2, as this will strongly improve the values of $J_{sc}$, $V_{oc}$ and FF.[76] The shifting of phase equilibrium mechanism is summarised in Figure 8.4E alongside their crystal structure models. The accompanying fall in $CsPbBr_3$:$CsPb_2Br_5$ ratio after day 2 degrades the performance. Conversely some CsBr is still visible on the surface of the CB sample through time. The top down SEM and powder XRD patterns can be found in Figure S8.6.

### 8.4.4 Light and Air Effects

The progression of solar cell parameters through time for dry dark, dry light, air dark and air light storage conditions was more gradual, although characterisation revealed key information on the maturation effect. The samples stored under $N_2$ conditions showed remarkable evolution in morphology over the study time, Figure 8.5, where significant merging of grains is seen in both light and dark samples. In the dry dark sample, Figure 8.5A-C, the ZnO became less visible, due to the large perovskite grains spreading out over the surface of the rods giving a smoother appearance up to day 14. Comparatively, the dry light sample, Figure 8.5D-F, showed an initial fusing of grains appearing amorphous on day 5, followed by their reformation and sinking between the ZnO NRs which become visible on day 14. This trend is complimented by information extracted from the prominent 33.6° $CsPbBr_3$ peak in the powder XRD. It is known that the nano crystalline domain size is proportional to the inverse of the Full Width Half Maximum (FWHM), as presented in the Scherrer equation.[259] This allows deviations in the domain size to be observed. These results are plotted against time in Figure 8.5G, displaying constantly increasing FWHM for the dry dark sample, and a reversible climb then fall for the dry light sample. This mirrors the SEM results, as the nano crystalline domain size is initially shrinking in both samples, allowing the large grains to fit between the NRs, which in turn increases surface contact and therefore reducing charge transfer resistance. Conversely, it is widely accepted that larger grains are more advantageous for PSCs, as the grain boundaries are where most of the electron-hole recombination occurs. This explains the dramatic increase in $J_{sc}$ for the dry dark sample as charge is more effectively transferred to ETM, alongside the fall in FF as smaller grains mean greater recombination in the bulk.

As far as the authors are aware, this is the first reported case of grain shrinking in any perovskite material, particularly when stored under dry inert conditions. The reasons for this effect are likely due to the combination of material and structure. $CsPbBr_3$ is a soft material able

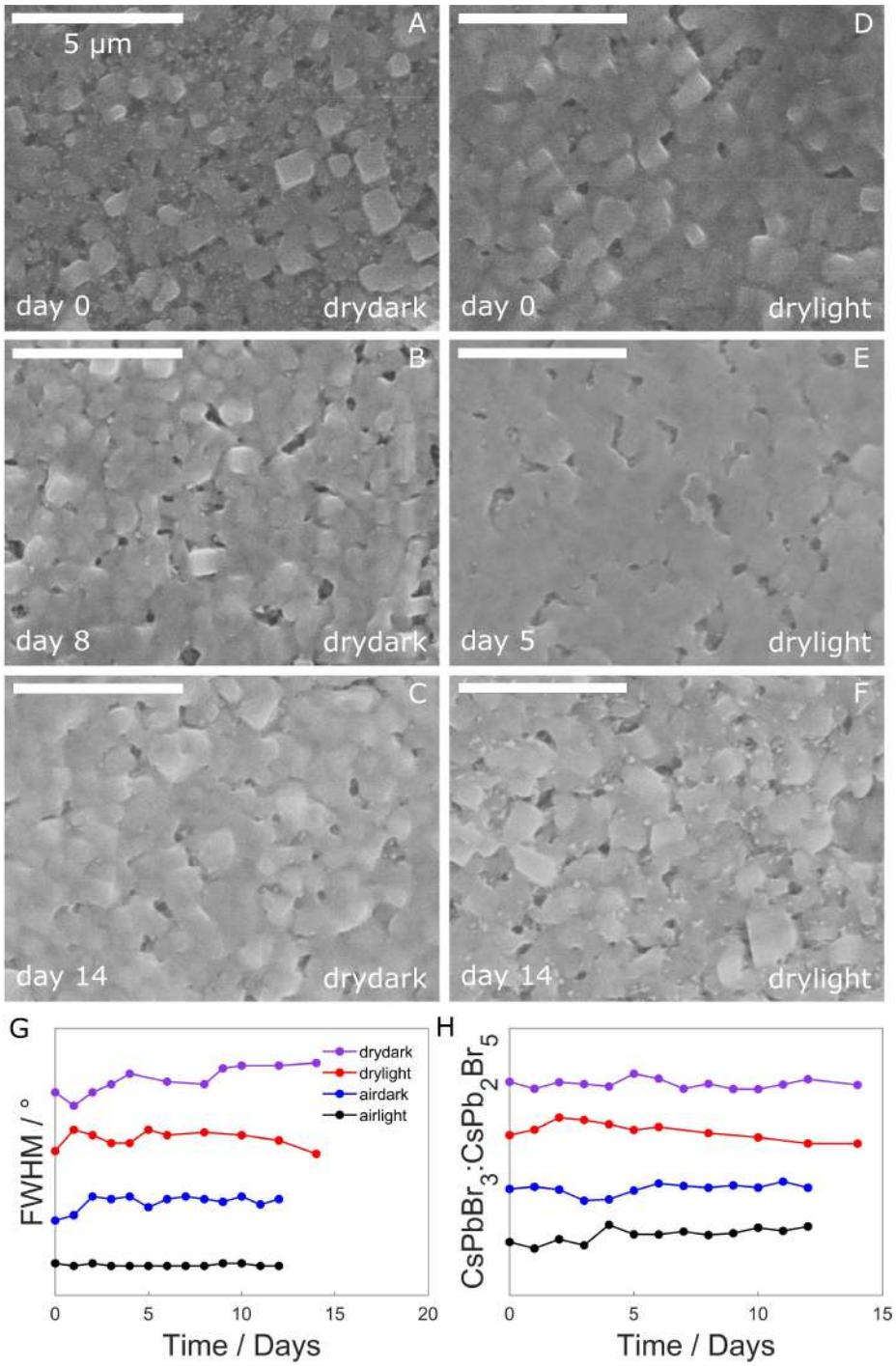


Figure 8.5: Top down SEM images for dry dark conditions through time, day 0, day 8 and day 14 in A), B) and C) respectively. SEM images for dry light conditions are found in D), E) and F) for day 0, 5 and 14 respectively. XRD peak full-width-half-maximum for $CsPbBr_3$ peak situated at 33.6°, for samples under dry, air, illuminated and dark conditions are found in G), alongside $CsPbBr_3$ to $CsPb_2Br_5$ ratio over time in H).

to contort to fill space, such as gaps in the zinc oxide nanorod structure.[507] Over time the grain sizes effectively shrink as they relax into the space between the NRs which act as separators. This process is likely aided by ionic migration and segregation, occurring when illumination and bias are applied simultaneously during IV tests, leading to the build up of mobile bromide ions at the boundaries and local n-type doping.[484] This would occur more strongly in the dry dark sample, as each IV sweep leads to greater ionic accumulation, weakening the crystal structure in the grain. Whereas, the dry light sample is given an unbiased 'rest', where sufficient energy is supplied for bromide migration (0.44 eV) but a lack of bias leads to its redistribution throughout the grain.[507,508] Also, the high content of $CsPb_2Br_5$ available may give the layer an amorphous character, due to the polycrystalline mixing of the two phases. The reversibility of this effect in the dry light sample explains why the FF and $J_{sc}$ do not change much over the experimental time frame. In fact the only parameter with a significant change is $V_{oc}$, which displaying a steady rise. This is likely to have occurred due to the filling of deep trap states within the $CsPbBr_3$ band gap, which occurs by visible light excitation of electrons and holes. With light soaking on a 24 hour time scale, nearly all these deep traps can be filled, negating their effect on $V_{oc}$.[509] As expected, when looking to the phase ratio in Figure 8.5H, the dark dry sample shows no significant swing either way, and therefore has no effect on device parameters. However, under illumination a swing to greater $CsPbBr_3$ content occurs, followed by a return and plateau at day 12. This reversible behaviour has been previously reported by Shen *et al.* in nanosheets of the same phases, where illumination provided sufficient energy for the conversion of $CsPb_2Br_5$ to $CsPbBr_3$.[503]

For the dark sample stood in ambient air, there is minimal change in the phase ratio, although a visible increase in FWHM is seen. This confirms the grain shrinking process is not hindered by $O_2$ or moisture. Conversely, the light air sample did not show any significant change in nano crystalline domain size, but did show a crystal phase shift towards the orthorhombic structure,

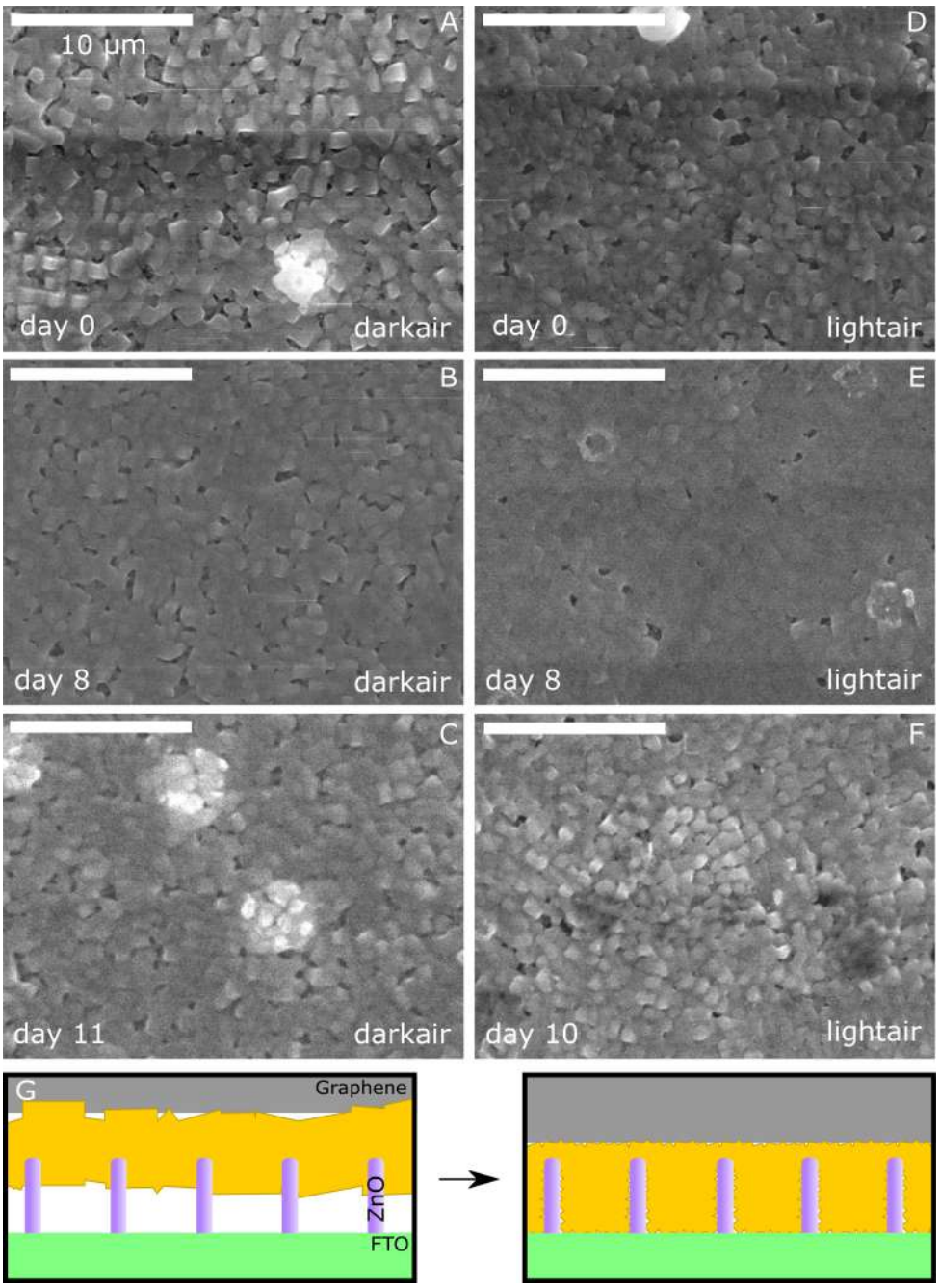


Figure 8.6: Top down SEM images for the conditions stored in air conditions, sample kept in the dark on day 0, day 8 and day 14 are shown in A), B) and C) respectively. The sample kept under constant illumination are shown in D), E) and F) for days 0, 5 and 10. The grain shrinking mechanism as determined by XRD FWHM, is displayed schematically in G).

which was not reversed. This permanent growth in $CsPbBr_3$ content is due to the availability of residual MeOH, alongside reported effects of atmospheric $H_2O$ and $O_2$ when combined with illumination, which has been shown to grow larger crystals of $CsPbBr_3$.[510] The SEM images found in Figure 8.6 agree with the XRD results, showing similar progress as the light dry and dry dark samples. The only major difference is that bright spots are observed for the dark air samples on day 11, which appear at the surface of the perovskite layer. This is due to ionic migration of $Br^-$ ions attracted to the cathode, forming an electrostatic double layer, and aggregating at the top surface and at grain boundaries. In contrast to the dry dark sample, the accumulated ions under dark air conditions are free to react with $H_2O$ to form HBr acid, which reacts with the $CsPbBr_3$ to yield the constituent $PbBr_2$ and CsBr.[511] This is the key disadvantage of the dark air sample, leading to its rapid degeneration in performance; as when illuminated and unbiased these ions are free to diffuse through the cell, preventing a build up. This causes the reduction of FF, $J_{sc}$ and $V_{oc}$ in the dark air sample. The cause of the large rise in hysteresis in the light air sample is still unexplained, though is likely due to increased concentration of mobile ions from light soaking.[499]

### 8.4.5 Storage Conditions and Impedance Parameters

In order to confirm and quantify the effects of ion migration and electron hole recombination on the solar cells during their storage, EIS was performed under illumination, at short circuit condition. On fresh construction, Nyquist plots displayed simple dual arcs for all the samples, however after 24 hours in all storage conditions a prominent induction loop feature became visible at intermediate frequency, with the exception of the $H_2O$ sample, Figure S8.7 and Figure S8.8. As far as the authors are aware, this is the first reported case of evolution to this well-known feature over time. The surface polarization model proposed by Ghahremanirad *et al.* was therefore used to fit the data.[512] This model explains the feature as additional potential

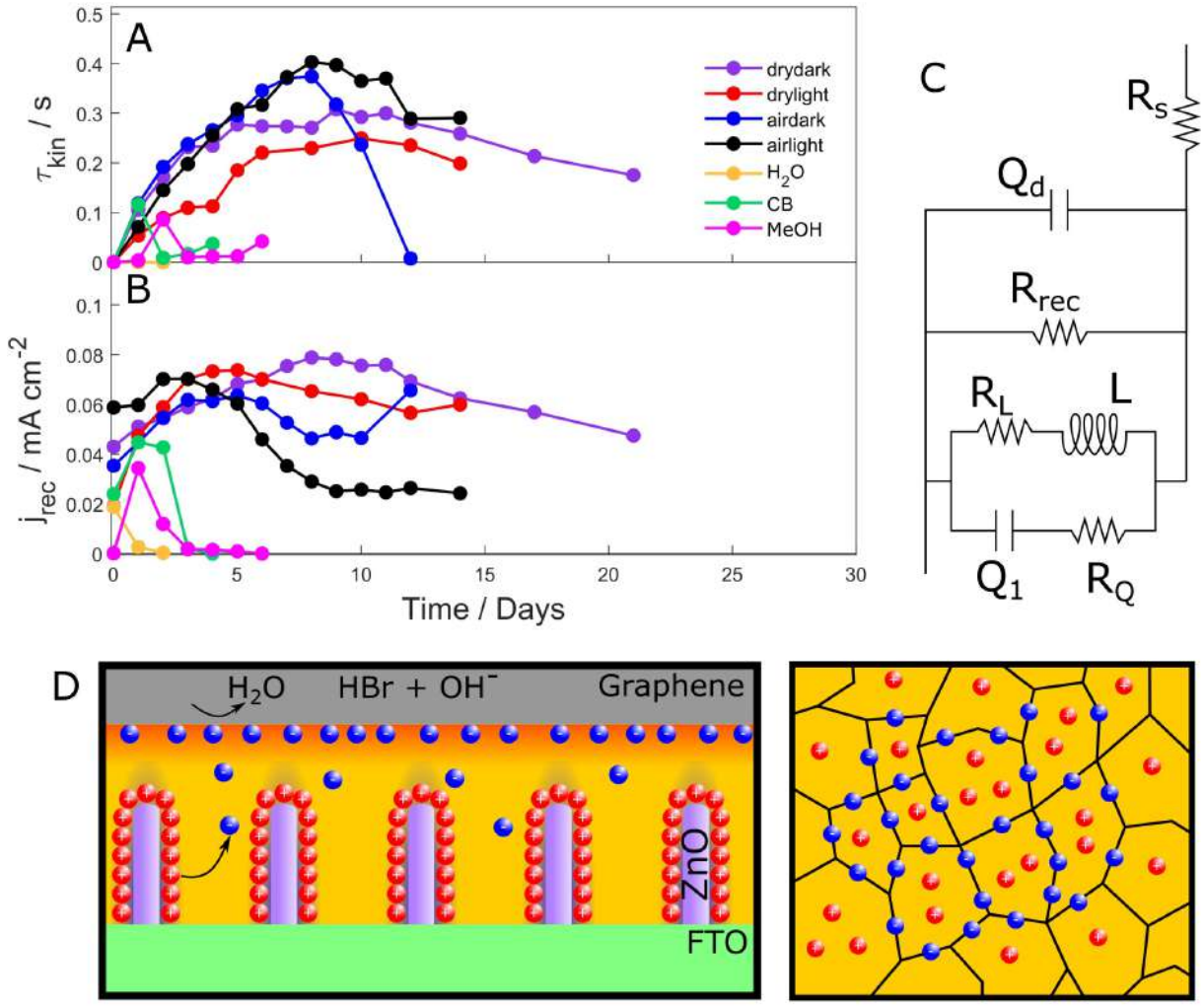


Figure 8.7: Impedance Spectroscopy values determined for the cells under different storage conditions, A) and B) show values of $\tau_{kin}$ and $j_{rec}$ respectively evolving through time. C) displays the lumped equivalent circuit used to fit the data and determine the values.[512] D) displays the ion migration and accumulation representation, with $Br^-$ accumulating at both the cathode (left) and at grain boundaries (right). Conversely, immobile $V_{Br}^+$ are formed at the anode interface and in the crystal grain bulk.

formed by the accumulation of positive charge at the anode, likely caused by ionic migration due to slow equilibration. Vitally, by using the model's lumped equivalent circuit, Figure 8.7C, the values of kinetic relaxation time of charge, $\tau_{kin}$, and steady state recombination current density, $j_{rec}$, were determined using the following formulae.

$$\tau_{kin} = \frac{L}{R_L} \tag{8.3}$$

$$j_{rec} = \frac{\beta k_B T}{q R_{rec}} \tag{8.4}$$

Where $k_B T$ is the thermal energy, $q$ is the elemental charge, $\beta$ is an ideality factor equal to unity and $L$, $R_L$ and $R_{rec}$ are parameters measured by the surface polarization equivalent circuit, Figure 8.7C. Also included are two capacitor elements, $Q_1$ and $Q_d$ corresponding to the various parallel contributions from the surface charging and the dielectric capacitance respectively. The model stipulates a polarized region at the ETM/perovskite interface occurs due to a highly localised collection of halide vacancies, which was confirmed by Weber *et al.* by time resolved Kelvin probe force microscopy.[513] This was observed alongside a diffuse space charge layer of halide ions distributed towards the electrostatic double layer at the HTM/perovskite interface. Greater $\tau_{kin}$ will therefore mean a slower rate of halide ions returning to the ETM interface becoming redistributed through the light sensitive layer. Furthermore, lower $j_{rec}$ will be beneficial to the solar cell due to less energy lost due to electron-hole recombination.

Figure 8.7A displays the effect of storage condition on kinetic relaxation over time. Other than the sample exposed to high humidity, all samples show a rise in $\tau_{kin}$ over the first few days. On day 0 there was no inductive effect, likely due to initial $Br^-$ ions moving rapidly through the sample, avoiding the slow accumulation that is caused by long term exposure to bias and illumination. For the samples in solvent saturated conditions, the small increases likely have a positive effect on the efficiency of the cell, but due to their rapid corrosion after day two, ion migration is stifled and therefore no significant surface polarisation can occur. This is clearly the

case for the $H_2O$ sample, in which no measurable $\tau_{kin}$ occurs, and the induction feature remains absent. The steady rise of $\tau_{kin}$ in the air and $N_2$ samples indicate the compound accumulation of $Br^-$ and $V_{Br}^+$ at the HTM and ETM respectively, over exposure to repeated IV sweep bias and illumination for PEC measurements. The concentration of liberated mobile ions congregating at the interfaces increases with the sample age, thereby reducing ion mobility, requiring a longer duration for the charge to distribute evenly.

The samples stored in air show the longest $\tau_{kin}$, which is likely due to the reaction of $Br^-$ at the surface with adsorbed $H_2O$, delaying their return to the bulk perovskite.[513] In the dark air sample this is more extreme. As previously described, the ions are largely immobile in storage, therefore HBr will quickly build up and react with the cell, as seen with the samples exposed to solvent. The removal of $Br^-$ and corrosion of the cell will once again lead to quick relaxation, as the remaining ions are more mobile, and so less polarisation occurs. This results in the collapse of $\tau_{kin}$ in the dark sample alongside its decline in efficiency, reaffirming the results from Figure 8.6. Conversely, for the light air sample, relaxation time increases to its largest recorded value due to the high mobile ion concentration coupled with surface reactions, without the same corrosion. This explains the large degree of hysteresis observed in this sample, due to the slow kinetic relaxation. This same mechanism at work is in the $N_2$ samples, leading to similar rises in $\tau_{kin}$, but in the absence of air and moisture localised increased ion concentration doesn't lead to corrosion in the dark dry sample. Finally, within an $N_2$ atmosphere when illuminated the ions are free to migrate, reducing the time taken for relaxation from surface polarisation.

The recombination current shown in Figure 8.7B confirms the local p-n junctions along grain boundaries in the light air sample. The formation of these junctions is closely tied to the surface polarisation and ion migration, reducing electron hole recombination by increasing charge separation rate. This follows the reduction in $j_{rec}$ with the increase in $\tau_{kin}$. As expected, the recombination current increases with the reduction in crystal grain size in Figure 8.5, as

recombination occurs predominantly along the grain boundaries within the perovskite layer. The fact that $j_{rec}$ so closely follows $j_{sc}$ indicates there is great potential in optimising the material interfaces within the cells, requiring passivation to more efficiently extract charge.

## 8.5 Conclusion

In summary, reproducible and significant maturing effects were observed in $CsPbBr_3$ solar cells with ZnO NW electron transport layers and graphite back contacts. The efficiency on average rose $51\pm10\%$ after two weeks of storage under ambient dark conditions, the largest reported in literature to date. These gains were constituted by a $34 \pm 8\%$ gain in $j_{sc}$ alongside an $8 \pm 1\%$ increase in $V_{oc}$. In order to isolate the causes of maturing, solar cells were kept in various storage conditions representing key solvents used in their manufacture, atmospheric moisture and illumination, alongside control samples kept under $N_2$. It was found that storage in a methanol atmosphere accelerated the maturing process, yielding efficiency four times greater than the fresh sample. Conversely, high humidity storage prevented this effect and critically damaged performance after two days. In order to gain new insights into the underlying processes, the samples were observed by powder XRD, SEM and EIS leading to three key mechanisms responsible. Changes in the dynamic crystal phase ratio between $CsPbBr_3$ and $CsPb_2Br_5$ had the strongest effect, followed by grain shrinking, allowing the perovskite to make better contact with the ZnO ETM. Finally ionic migration of $Br^-$, aided charge separation by forming p-n junctions at grain boundaries. This was confirmed by EIS, showing large changes in kinetic relaxation time within a window associated with ionic transport time scale. These results not only point to a permanent increase in efficiency based on particular storage conditions, leading these solar cells closer to commercialisation, but they also expand the understanding of degradation resistance in inorganic perovskite solar cells, shedding light on an unexplored field.

## 8.6 Supporting Information: Dramatic Maturing Effects Under Different Storage Conditions in All-Inorganic, $CsPbBr_3$ Perovskite Solar Cells

The degree of hysteresis (DoH) was calculated from the current density value at $0.6V_{oc}$ (the open circuit voltage), for the reverse scan $J_{RS}$ and the forward scan $J_{sc}$.[499]

$$DoH = \frac{J_{RS}(0.6V_{OC}) - J_{FS}(0.6V_{OC})}{J_{RS}(0.6V_{OC})} \tag{S6.1}$$

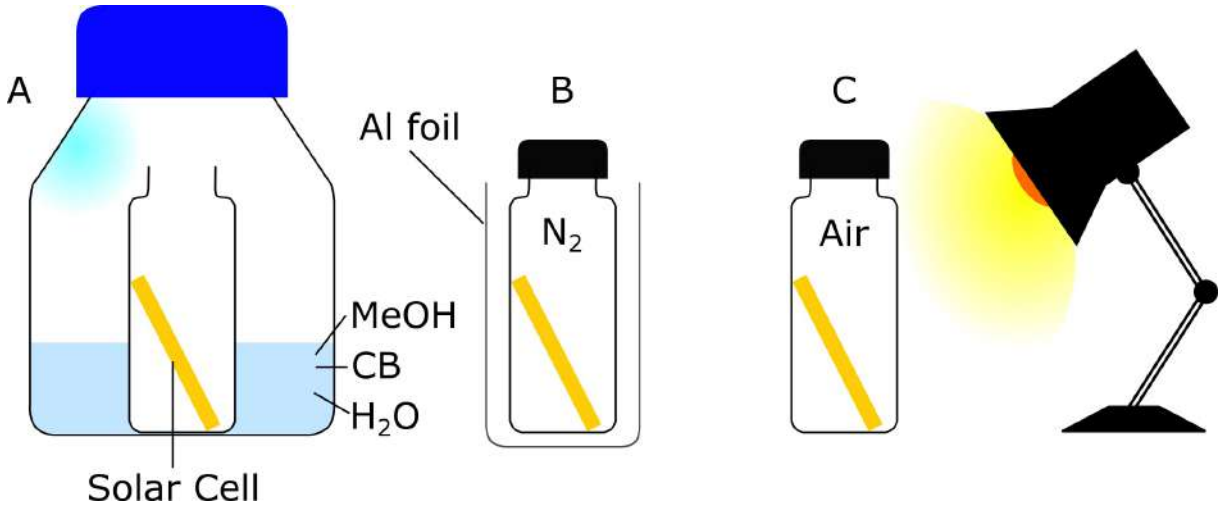


Figure S8.1: The setup of different storage conditions, A) shows the storage in either $H_2O$, chlorobenzene or methanol (covered in Al foil to keep dark). B) and C) display the set up for the dry dark sample and light air sample, respectively.

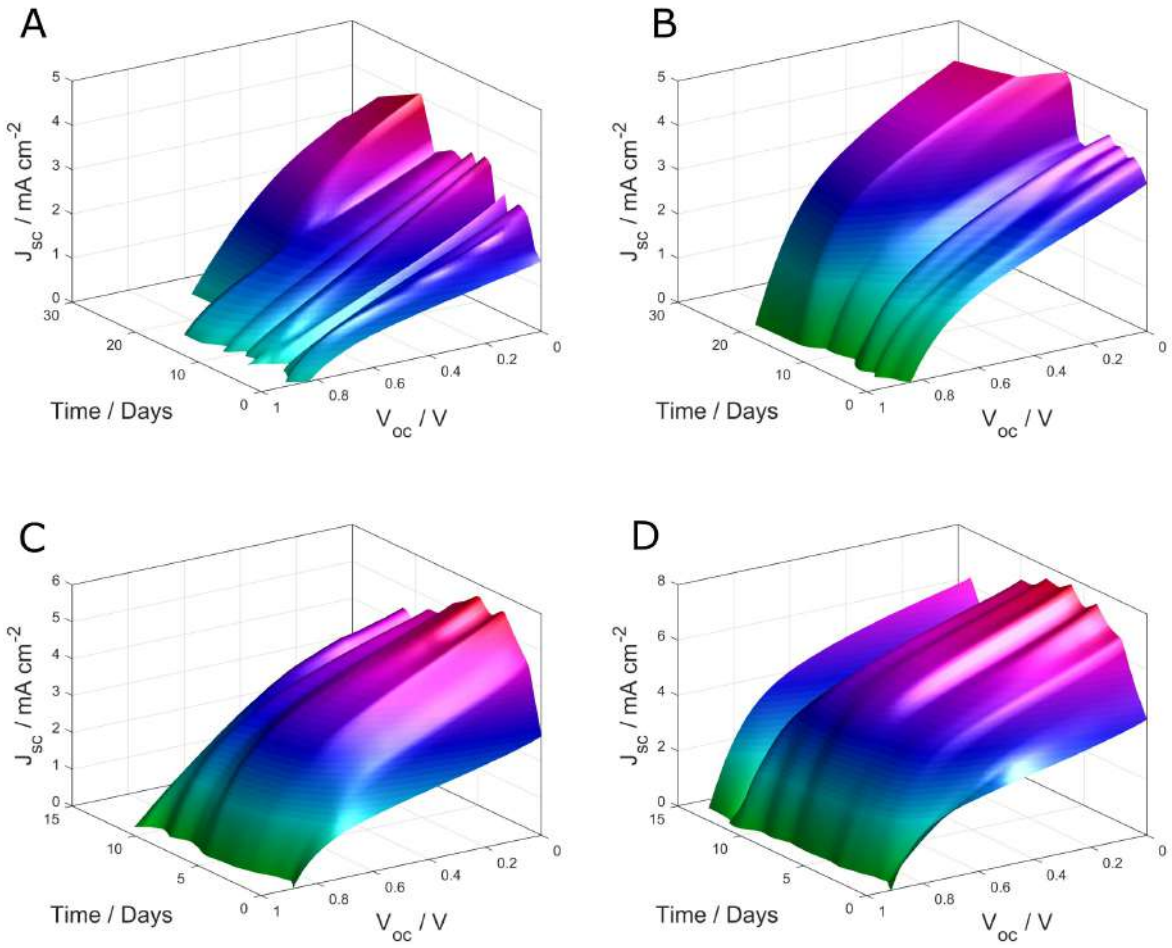


Figure S8.2: The evolution of IV curves over storage time, used to determine solar cell parameters. These are measured from one of the three cells on the device surface, averaged in order to determine the device parameters in Figure 8.2. A) shows the sample stored in dry dark conditions; B) shows the dry light sample; C) shows the air dark sample and D) shows the air light sample.

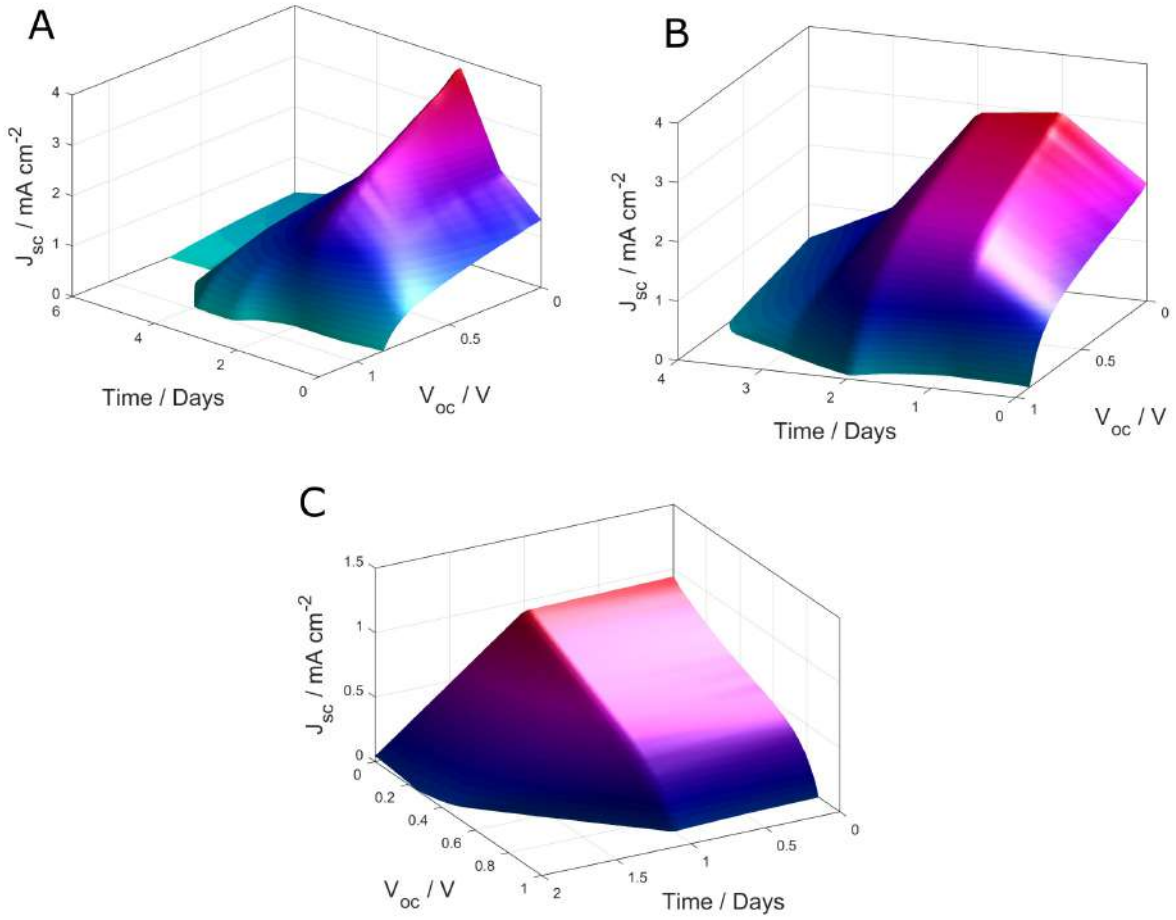


Figure S8.3: The evolution of IV curves over storage time, used to determine solar cell parameters. These are measured from one of the three cells on the device surface, averaged in order to determine the device parameters in Figure 8.2. A) shows the sample stored in saturated methanol conditions; B) shows the chlorobenzene sample and C) shows the $H_2O$ sample.

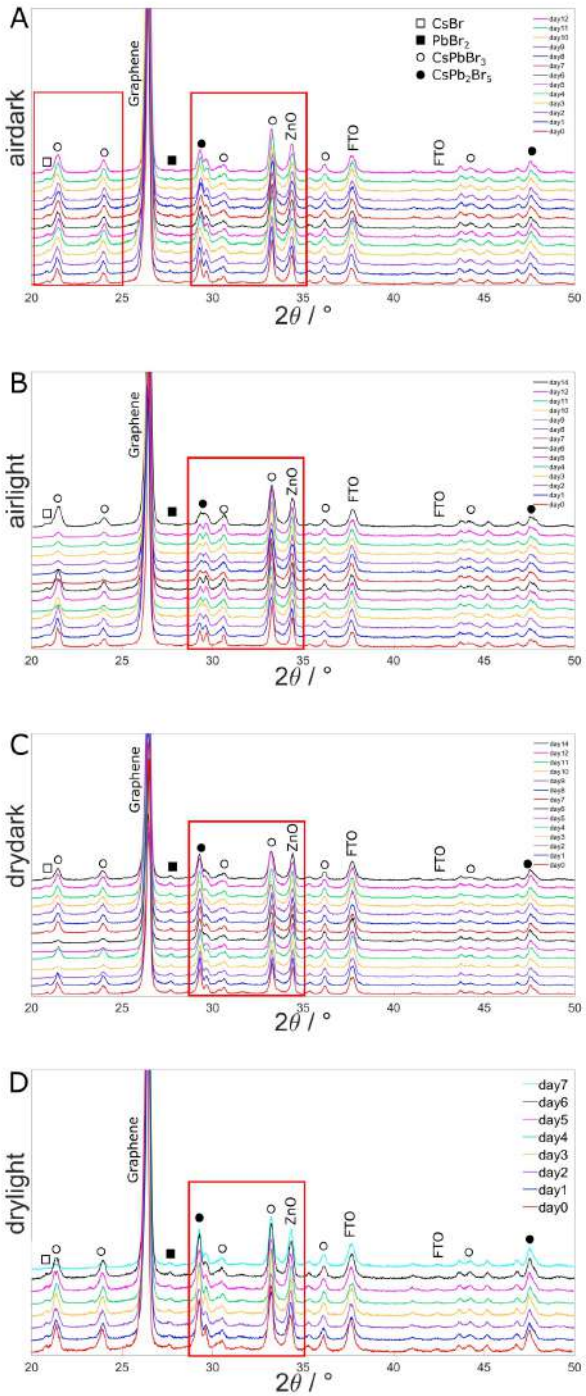


Figure S8.4: The full powder XRD patterns of samples in the following storage conditions: A) air and dark; B) air and light; C) dry and dark and D) dry light. The 33.6° peak was used for FWHM values in the main text, all the peaks assigned to $CsPbBr_3$ and $CsPb_2Br_5$ were integrated for phase ratio calculations.

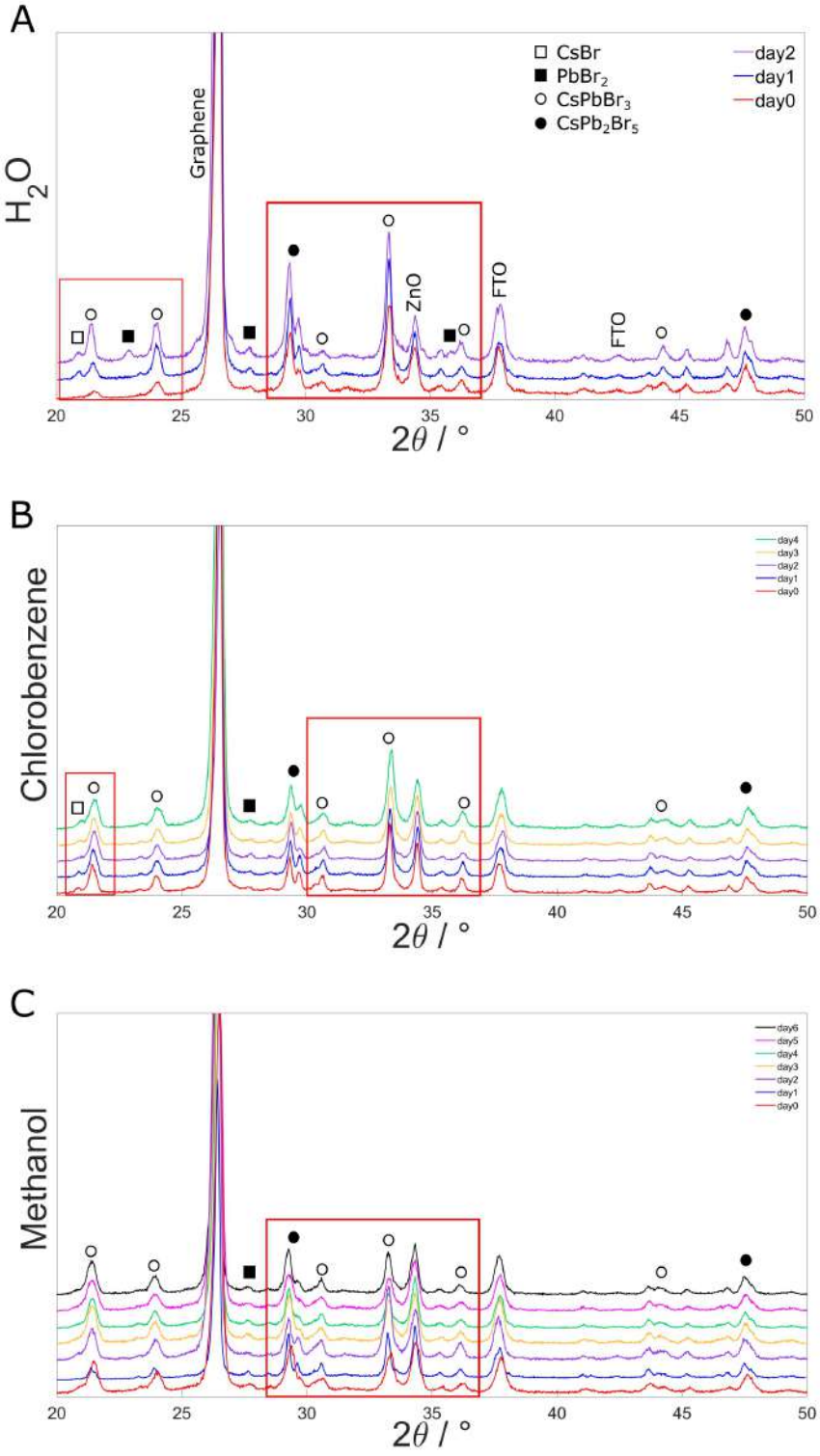


Figure S8.5: The full powder XRD patterns of samples in the following storage conditions, A) $H_2O$, B) chlorobenzene and C) methanol.

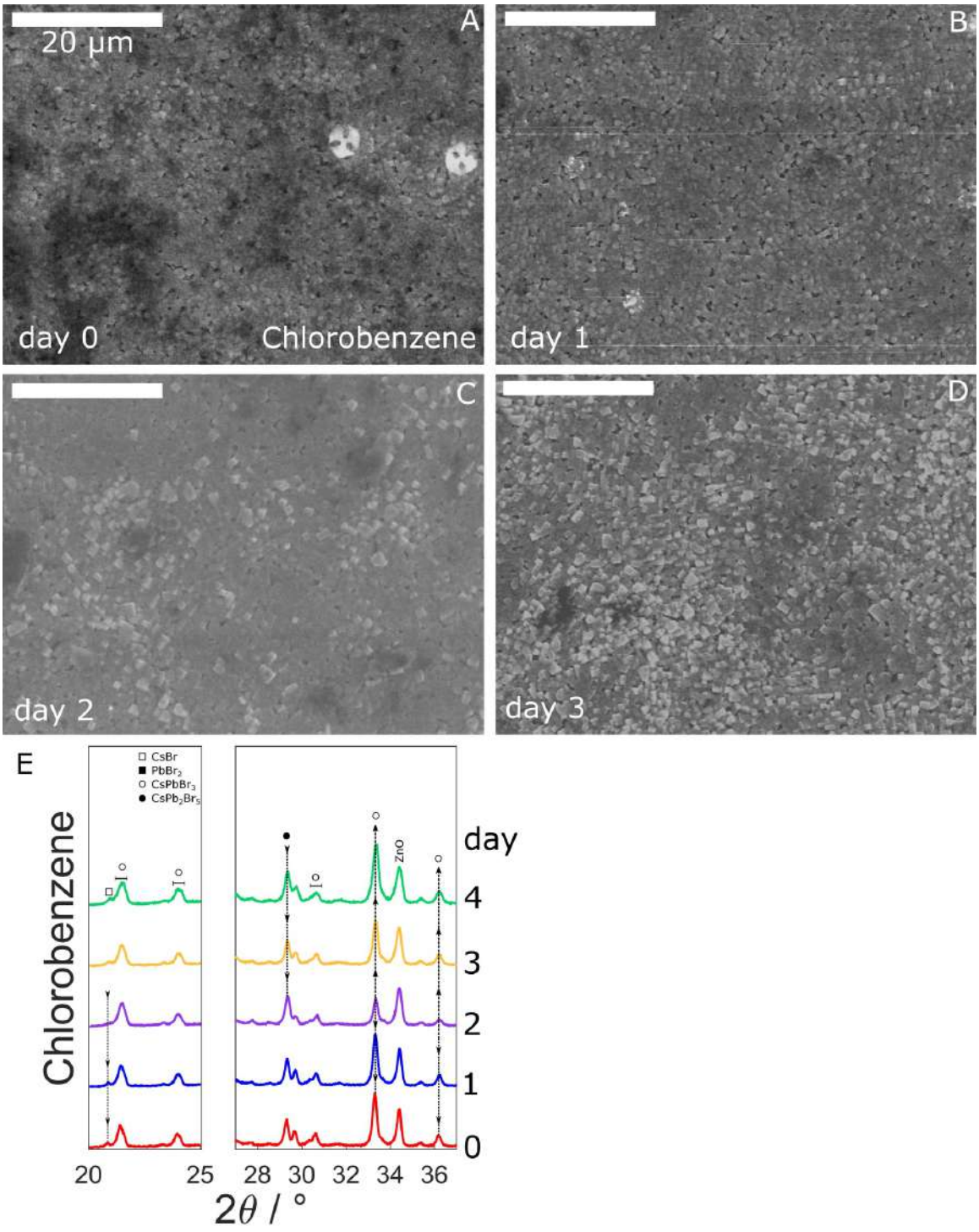


Figure S8.6: The effects of chlorobenzene on solar cell morphology and crystal structure, A) through D) show top down SEM images of the sample day by day. E) shows the change in primary peaks over time.

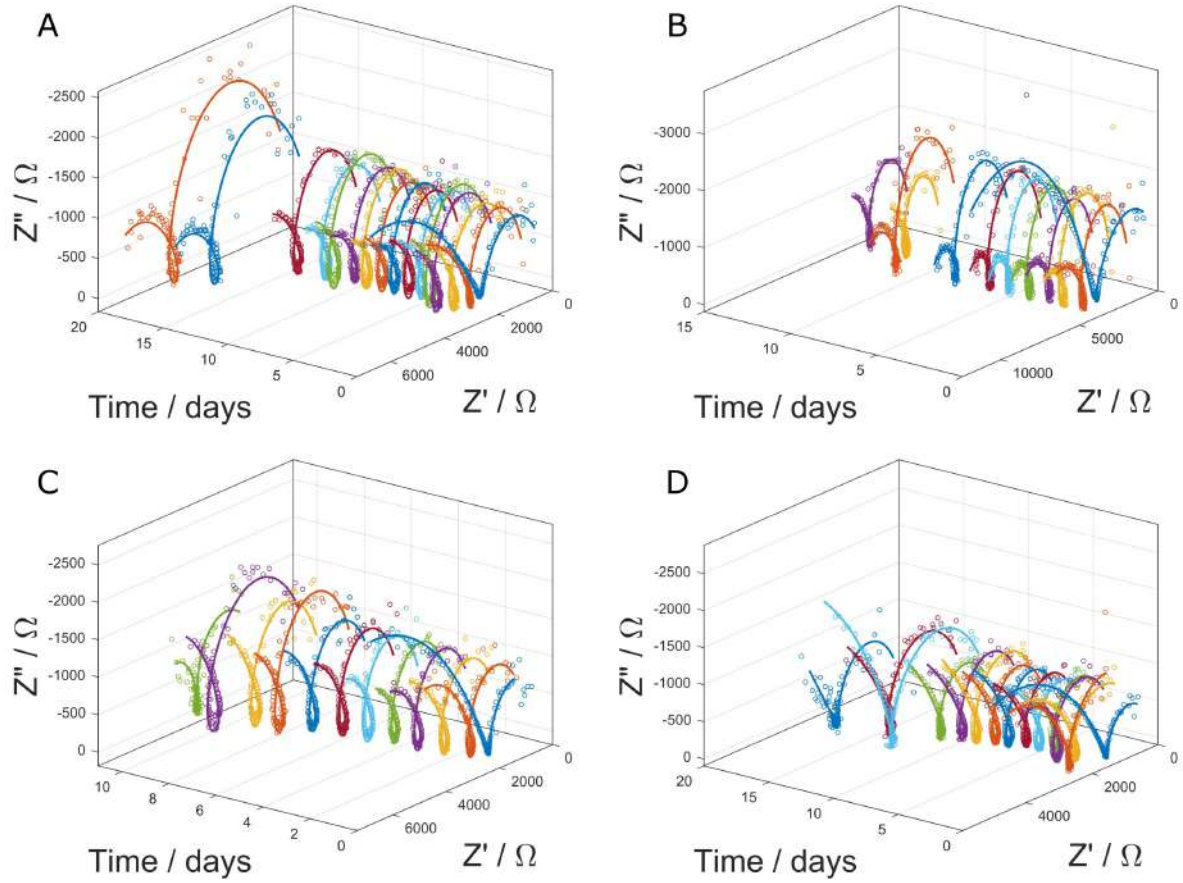


Figure S8.7: The evolution of the impedance spectroscopy data over time, with experimental data (circles) with surface polarization model fits (lines). A) shows the dry dark sample, B) shows the dry light sample, C) shows the dark air sample and finally D) shows the light air sample.

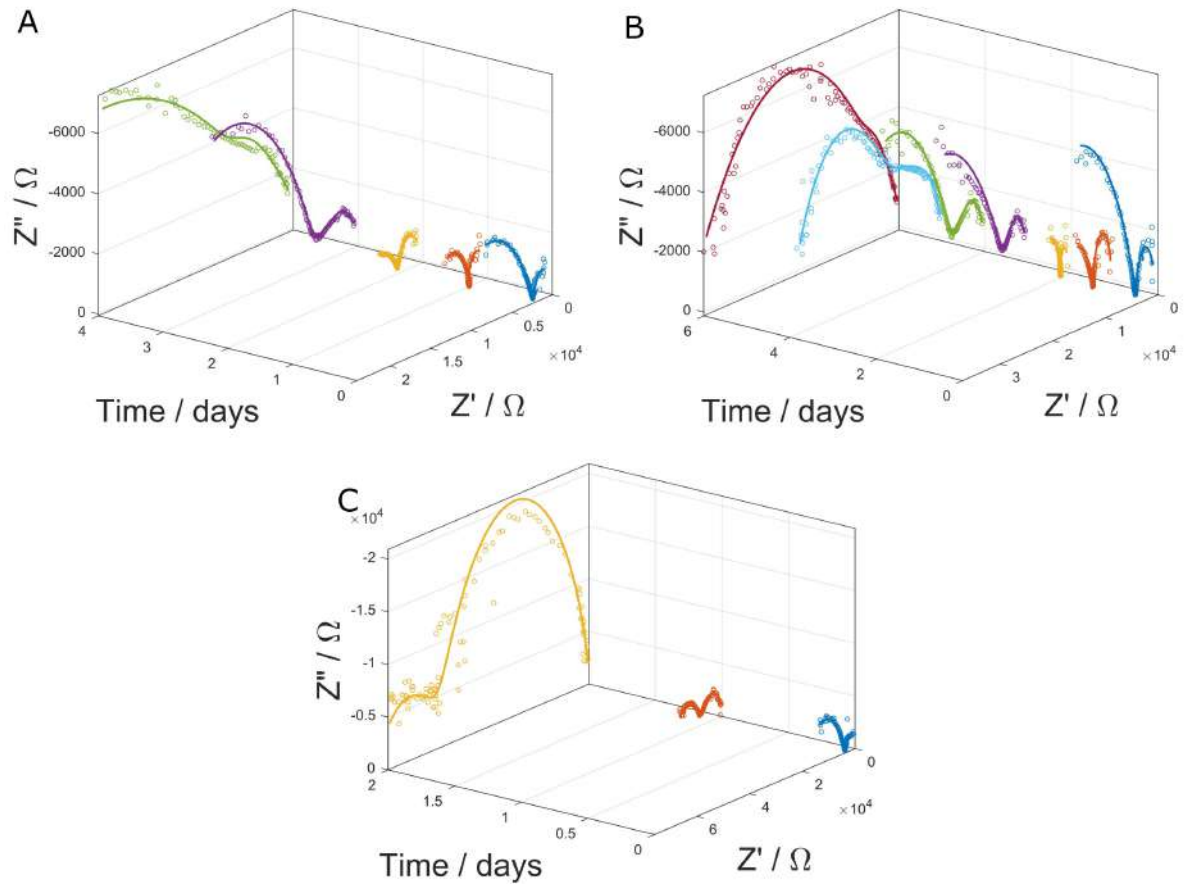


Figure S8.8: The evolution of the impedance spectroscopy data over time, with experimental data (circles) with surface polarization model fits (lines). A) shows the chlorobenzene sample, B) shows methanol sample and finally C) shows the sample stored in $H_2O$.

# Chapter 9

# Conclusion

In this thesis, vertically aligned ZnO nanorods were modified and applied to PEC water splitting and inorganic perovskite photovoltaics. The modifications including microwave synthesis, yttrium doping, $\alpha$-$Fe_2O_3$ and $TiO_2$ nanoscale coatings led to enhanced performance in both systems. These beneficial results are summarised in the following tables and explained by improved charge transport, charge transfer, light absorption and reduced electron hole recombination. These effects were measured by various forms of characterisation, such as IPCE, photoluminescence spectroscopy and EIS. Water splitting architectural strategies implemented through chapters three to six are summarised in Table 1, displaying photocurrent density at 1.23 $V_{RHE}$ alongside IPCE at 400 and 515 nm. Improvements to photovoltaic performance are included in Table 2, as implemented in chapter seven, displaying power-conversion efficiency and IPCE at the same wavelengths.

The various strategies employed to improve performance worked effectively, starting with more rapid synthesis. The microwave (MW) method not only slashed growth time from 16 hours to 2.5, but a high population of defects led to greater conductivity. Optimisation of this population using annealing yielded a photocurrent density of 0.71 mA $cm^{-2}$. The introduction of yttrium dopant atoms in chapter four, reduced the electronic band gap, increased aspect ratio, and grew conductivity 1,000 times. The dopant concentration was optimised to 0.1% content,

Table 9.1: PEC water splitting performances of variously synthesised, doped and electrochemically coated ZnO NR arrays.

| Sample | Photocurrent Density / mA $cm^{-2}$ | $IPCE_{400}$ / % | $IPCE_{515}$ / % |
|---|---|---|---|
| CBD | 0.14 | - | - |
| Microwave | 0.71 | - | - |
| 0.1%Y MW | 0.84 | 0.00 | 0.00 |
| Cathodic $Fe_2O_3$ | 1.59 | 8.96 | 2.25 |
| Anodic $Fe_2O_3$ | 1.22 | 7.02 | 0.43 |

maturing the performance further. Calculating the dopant density to a high accuracy was key to understanding the role of yttrium, leading to the implementation of a more accurate cylindrical charging model for Mott-Schottky analysis.[363] This model leads to $N_D$ values orders of magnitude different to those determined by the typical planar model in chapter three. This model was retroactively applied to the impedance data from said chapter for better comparison, the results are recorded in Table 9.2. Reassuringly, the values become far closer to those measured in chapter four (Undoped $N_D$ of $7.5 \times 10^{17}$ $\mathrm{cm}^{-2}$), with more reasonable changes in dopant density rather than swings in order of magnitude. The monotonic trend of increased temperature with decreased dopant density is maintained while flat band potential varies little.

Transforming the NR arrays into transparent conductive waveguides proved an ideal foundation for hematite based water splitting. Hematite has a suitable band gap for both water photolysis and visible light absorption. However, sluggish polaron hopping based minority charge transport means pure $Fe_2O_3$ is defeated by critically high recombinative losses. Growing electrochemically deposited nanoscale structures on the surface of conductive nanowires overcomes this problem, as holes are immediately transferred to the solution. Furthermore, suitable conduction band alignment means rapid electron transport to the counter electrode via the YZnO NRs. The contribution of a $ZnFe_2O_4$ interphase layer aids further charge separation.

Table 9.2: Mott-Schottky values derived from the two different models used in this thesis, applied to data from Chapter three.

| | Planar Model | | Cylindrical Model | |
|---|---|---|---|---|
| Sample | $V_{FB}$ / $V_{Ag/AgCl}$ | $N_D$ / $cm^{-3}$ | $V_{FB}$ / $V_{Ag/AgCl}$ | $N_D$ / $cm^{-3}$ |
| CBD | $-0.38$ | $7.61 \times 10^{18}$ | $-0.54$ | $2.58 \times 10^{17}$ |
| MW | $-0.47$ | $3.12 \times 10^{20}$ | $-0.51$ | $2.45 \times 10^{18}$ |
| 300°C | $-0.48$ | $2.18 \times 10^{20}$ | $-0.53$ | $2.15 \times 10^{18}$ |
| 400°C | $-0.46$ | $4.45 \times 10^{19}$ | $-0.42$ | $1.81 \times 10^{18}$ |
| 500°C | $-0.32$ | $1.68 \times 10^{19}$ | $-0.35$ | $9.71 \times 10^{17}$ |
| 550°C | $-0.01$ | $3.88 \times 10^{18}$ | $-0.25$ | $4.45 \times 10^{17}$ |

Electrochemical deposition using cathodic and anodic currents led to the highest water splitting photocurrents in this thesis, 1.59 and 1.22 mA $cm^{-2}$ respectively. Overall, this achieved a 10 times increase over the first synthetic method, due to visible light sensitisation as measured by IPCE.

Table 9.3: Solar cell performance of modified ZnO NR arrays, including Y doping of various lengths and dip coating cycles of $TiO_2$

| Sample | $\eta$ / % | $IPCE_{400}$ / % | $IPCE_{515}$ / % |
|---|---|---|---|
| Pristine | 0.63 | 18.12 | 14.37 |
| Y1195 | 0.83 | - | - |
| Y917 | 2.10 | 44.53 | 31.18 |
| Y625 | 1.22 | - | - |
| 3 dips $TiO_2$ | 5.83 | 77.79 | 66.29 |
| 6 dips $TiO_2$ | 4.10 | 67.73 | 53.67 |
| 10 dips $TiO_2$ | 2.81 | - | - |

Incorporating the conductive ZnO nanowires into inorganic $CsPbBr_3$ perovskite solar cells

yielded a similar enhancement, allowing more rapid electron transport to the anode. Once the nanorod lengths were optimised to 917 nm the efficiency increased from 0.63 to 2.10%. As the perovskite acted as light absorber, passivation was selected as a coating strategy rather than sensitisation. Therefore, $TiO_2$ was chosen as a charge selective coating, preventing interfacial recombination. Nanoscale coatings of the n-type material were applied to the Y doped ZnO by a dipping technique, adsorbing then hydrolysing TTIP. The thickness of the $TiO_2$ yielded a steep optimisation curve, with only the lightest coating giving the highest efficiency of 5.83% in the champion device. Further layer thickness, caused higher recombination due to the build up of the $TiO_2$ powder layer with poor electrical connectivity to the nanorods. The higher PCE performance is reflected by far greater IPCE in the visible light region between 400 to 515 nm.

In conclusion, the work in this thesis further cements ZnO as a high performance anode material for both solar water splitting, and as electron transport material in photovoltaic cells. The PVs constructed in this work, also utilise a liquid phase exfoliated graphite material for drop cast cathodes never previously applied to inorganic perovskite solar cells before.

## 9.1 Future Work

In order to finish the work performed in this thesis, several further investigations are required. Firstly, more evidence confirming photoelectrochemical water splitting rates could be attained by directly measuring output gases using gas chromatography with a thermal conductivity detector. Directly measuring the concentration of $O_2$ and $H_2$ would prove the evolution of said gases, rather than the indirect evidence of photocurrent density. Furthermore, this would allow the Faradaic charge transfer efficiency to be determined, indicating how well holes are injected into the solution at the anode surface.

The next step in the development of ZnO / $\alpha$-$Fe_2O_3$ hybrids would be the in situ doping of the hematite with 4+ ions such as $Si^{4+}$ and $Ti^{4+}$. This strategy has proven highly effective at

enhancing the performance of the single phase anodes, and would therefore be the next point of investigation. The anodes were still limited by high electron hole recombination in the iron oxide layer, therefore increasing its conductivity would improve charge transfer. More conductive hematite would allow thicker layers due to longer charge path lengths, absorbing more light. The advantage of the 3D hybrids constructed in this thesis, is that there is plenty of room for further enhancement, such as using passivating layers of MgO or noble metal nanoparticles for further light absorption. These methods have shown to be fertile routes for improvement in literature, especially optimisation of the solid liquid junction through passivation.

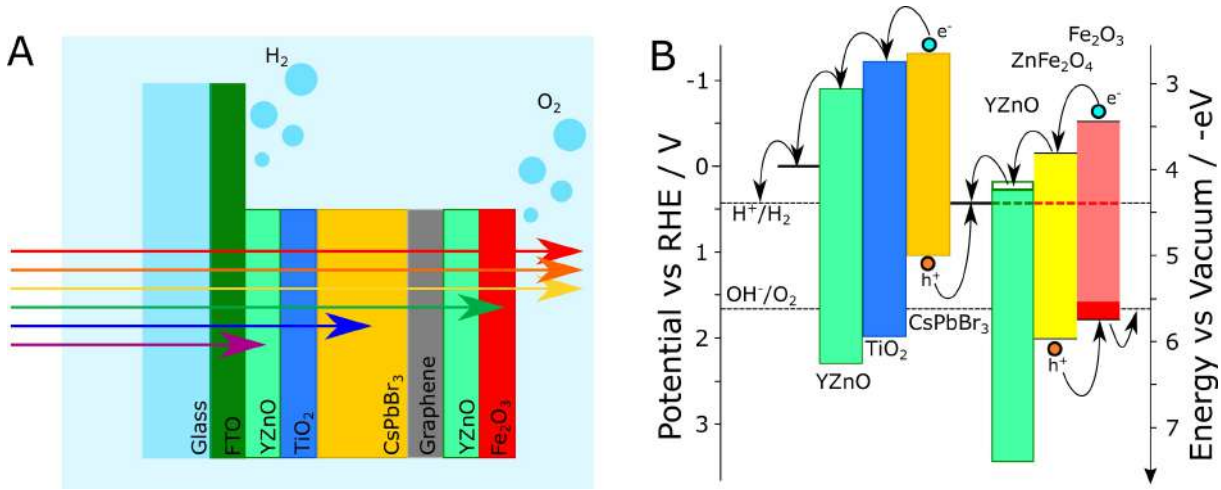


Figure 9.1: A) shows the proposed architecture for the solar water splitting device in future work. B) shows an energy diagram of how such an unbiased device would evolve oxygen and hydrogen.

The future of perovskite photovoltaics produced in this thesis would be optimisation of the $CsPbBr_3$ layer itself. Recent attention to this material has led to a growing number of publications with various improvements to the two step deposition utilised here. Depositing using multiple spin coats of CsBr leads to higher purity $CsPbBr_3$, alternately physical vapour deposition could be used or even just performing the CsBr submersion with the substrate face down yield higher quality perovskite phase with less tetragonal $CsPb_2Br_5$. Furthermore, a controlled

environment such as a dry room or glove box would allow the deposition of more moisture sensitive phases with lower band gaps for higher efficiencies. Alternately, the wide band gap $CsPbBr_3$ could be integrated into a multijunction device for great effect, especially with a higher quality CVD deposited, transparent layer graphite cathode. This assembly could then be printed on top of low band gap silicon solar cells. This would prevent vibrational losses incurred due to electronic relaxation to the conduction band edge by absorbing the higher energy photons in the $CsPbBr_3$. This would allow the cells to perform higher than the Shockley-Queisser limit of 33.7% for single junction cells.[514]

Finally, the full culmination of this thesis could result in a solar water splitting device, free from any external bias. This could utilise a hydrogen evolution catalyst such as Fe-OOH and an oxygen evolving counterpart such as iridium oxide immobilised on anode and cathode respectively. The photoanode utilised would be the iron oxide coated hybrid synthesised in chapter five, facing away from the light source, with FTO glass acting as a cathode on the converse side. Said electrodes would be driven at a fixed bias by a $CsPbBr_3$ solar cell sandwiched between the layers, protected from the water by the metal oxide layers. Though somewhat ambitious, a similar design was used to break the record of photoelectrochemical water splitting, bringing such technology closer to commercialisation.[34] Although, this device would still leave much visible light unabsorbed, an improvement would involve a tandem photovoltaic cell, and a lower band gap coating on the hematite. Perhaps with a final push to reduce material cost and increase efficiency, solar water splitting could play a key role in the fight against climate change.

# Bibliography


(1) Summary for Policymakers of IPCC Special Report on Global Warming of 1.5ºC approved by governments, *http://www.ipcc.ch/report/sr15/*, (Accessed October 2018).

(2) J. Patz, D. Campbell-Lendrum, T. Holloway and J. Foley, *Nature*, 2005, **438**, 310–317.

(3) B. W. Lavery, S. Kumari, H. Konermann, G. L. Draper, J. Spurgeon and T. Druffel, *ACS Appl. Mater. Interfaces*, 2016, **8**, 8419–8426.

(4) J. a. Turner, *Science*, 1999, **285**, 687–689.

(5) Adoption of the Paris Agreement, *https//ec.europa.eu/clima/policies/international/ Negot.*, (Accessed September 2019).

(6) J. Chakraborty and S. Banerji, *IOP Conf. Ser. Earth Environ. Sci.*, 2018, **127**, 012002.

(7) S. Punia Sindhu, V. Nehra and S. Luthra, *Energy*, 2016, **100**, 332–348.

(8) D. D. d. S. Carstens and S. K. da Cunha, *Energy Policy*, 2019, **125**, 396–404.

(9) National Statistics Energy Trends, *https://www.gov.uk/government/statistics/energy-trends-section-6-renewables*, (Accessed March 2019).

(10) D. Newbery, *Energy Policy*, 2018, **120**, 684–696.

(11) C. M. Lan, H. P. Wu, T. Y. Pan, C. T. Chen, C. W. Chang, W. S. Chao, C. L. Wang, C. Y. Lin and E. W. G. Diau, *Energy Environ. Sci.*, 2012, **5**, 6460–6464.

(12) S. Rühle, A. Y. Anderson, H. N. Barad, B. Kupfer, Y. Bouhadana, E. Rosh-Hodesh and A. Zaban, *J. Phys. Chem. Lett.*, 2012, **3**, 3755–3764.

(13) A. Islam, M. Akhtaruzzaman, T. H. Chowdhury, C. Qin, L. Han, I. M. Bedja, R. Stalder, K. S. Schanze and J. R. Reynolds, *ACS Appl. Mater. Interfaces*, 2016, **8**, 4616–4623.

(14) P. Hohne, K. Kusakana and B. Numbi, *Energy Reports*, 2019, **5**, 1–19.

(15) F. Rovense, *Energy Procedia*, 2015, **82**, 978–985.

(16) W. Wang, B. Guan, X. Li, J. Lu and J. Ding, *Sol. Energy Mater. Sol. Cells*, 2019, **194**, 36–46.

(17) A. Demirbas, *Energy Sources, Part B Econ. Planning, Policy*, 2017, **12**, 172–181.

(18) Y. Wang and S. Zhang, *Energy Sources, Part B Econ. Planning, Policy*, 2017, **12**, 1022–1029.

(19) Basic Hydrogen Strategy, *https://www.meti.go.jp/english/press/2017/pdf/1226_003b.pdf*, (Accessed March 2019).

(20) A. J. Bard and M. A. Fox, *Acc. Chem. Res*, 1995, **28**, 141–145.

(21) D. G. Nocera, *Acc. Chem. Res.*, 2012, **45**, 767–76.

(22) C. Sattler, M. Roeb, C. Agrafiotis and D. Thomey, *Sol. Energy*, 2017, **156**, 30–47.

(23) C. N. R. Rao and S. Dey, *Proc. Natl. Acad. Sci.*, 2017, **114**, 13385–13393.

(24) A. Fujishima and K. Honda, *Nature*, 1972, **238**, 37–38.

(25) S. R. Nagel and J. Tauc, *Phys. Rev. Lett.*, 1975, **35**, 380–383.

(26) F. Bloch, *Zeitschrift für Phys.*, 1929, **52**, 555–600.

(27) S. H. Simon, *The Oxford Solid State Basics*, Oxford, Oxford, 1st Editio, 2013.

(28) L. Brillouin, *J. Phys. le Radium*, 1930, **1**, 377–400.

(29) M. Y. Hsieh, F. I. Lai, W. C. Chen, M. C. Hsieh, H. Y. Hu, P. Yu, H. C. Kuo and S. Y. Kuo, *Nanoscale*, 2016, **8**, 5478–5487.

(30) J. Xu, Z. Chen, J. A. Zapien, C.-S. Lee and W. Zhang, *Adv. Mater.*, 2014, **26**, 5337–5367.

(31) S. J. a. Moniz, S. a. Shevlin, D. J. Martin, Z.-X. Guo and J. Tang, *Energy Environ. Sci.*, 2015, **8**, 731–759.

(32) M. G. Walter, E. L. Warren, J. R. McKone, S. W. Boettcher, Q. Mi, E. A. Santori and N. S. Lewis, *Chem. Rev.*, 2010, **110**, 6446–6473.

(33) O. Khaselev, *Science*, 2002, **280**, 425–427.

(34) J. Luo, J.-H. Im, M. T. Mayer, M. Schreier, M. K. Nazeeruddin, N.-G. Park, S. D. Tilley, H. J. Fan and M. Gratzel, *Science*, 2014, **345**, 1593–1596.

(35) M. M. May, H. J. Lewerenz, D. Lackner, F. Dimroth and T. Hannappel, *Nat. Commun.*, 2015, **6**, 1–7.

(36) J. L. Young, M. A. Steiner, H. Döscher, R. M. France, J. A. Turner and T. G. Deutsch, *Nat. Energy*, 2017, **2**, 1–8.

(37) W.-H. Cheng, M. H. Richter, M. M. May, J. Ohlmann, D. Lackner, F. Dimroth, T. Hannappel, H. A. Atwater and H.-J. Lewerenz, *ACS Energy Lett.*, 2018, **3**, 1795–1800.

(38) M. Radecka, M. Rekas, A. Trenczek-Zajac and K. Zakrzewska, *J. Power Sources*, 2008, **181**, 46–55.

(39) Y. Zhang, Z. Xing, X. Liu, Z. Li, X. Wu, J. Jiang, M. Li, Q. Zhu and W. Zhou, *ACS Appl. Mater. Interfaces*, 2016, **8**, 26851–26859.

(40) J. Schneider, M. Matsuoka, M. Takeuchi, J. Zhang, Y. Horiuchi, M. Anpo and D. W. Bahnemann, *Chem. Rev.*, 2014, **114**, 9919–9986.

(41) A. E. Becquerel, *Comptes Rendus L´Academie des Sci.*, 1839, **9**, 145–149.

(42) G. Adams, W. and E. Day, R., *Proc. R. Soc.*, 1877, **25**, 113.

(43) C. E. Fritts, *Am. J. Sci.*, 1883, **26**, 465.

(44) L. O. Grondahl, *Rev. Mod. Phys.*, 1877, **5**, 113.

(45) F. C. Nix and A. W. Treptwo, *J. Opt. Soc. Am.*, 1939, **29**, 457.

(46) R. Ohl, *U.S. Pat.*, 1941, **2**, 602.

(47) E. F. Kingsbury and R. S. Ohl, *Bell Syst. Tech. J.*, 1952, **31**, 802–815.

(48) D. M. Chapin, C. S. Fuller and G. L. Pearson, *J. Appl. Phys.*, 1954, **25**, 676–677.

(49) B. O'Regan and M. Grätzel, *Nature*, 1991, **353**, 737–740.

(50) J. Lu, H. Li, S. Liu, Y.-C. Chang, H.-P. Wu, Y.-B. Cheng, E. Wei-Guang Diau and M. Wang, *Phys. Chem. Chem. Phys.*, 2016, **18**, 6885–6892.

(51) H. C. Su, Y. Y. Wu, J. L. Hou, G. L. Zhang, Q. Y. Zhu and J. Dai, *Chem. Commun.*, 2016, **52**, 4072–4075.

(52) G. Magnano, D. Marinotto, M. P. Cipolla, V. Trifiletti, A. Listorti, P. R. Mussini, G. Di Carlo, F. Tessore, M. Manca, A. Orbelli Biroli and M. Pizzotti, *Phys. Chem. Chem. Phys.*, 2016, **18**, 9577–9585.

(53) E. Sheibani, L. Zhang, P. Liu, B. Xu, E. Mijangos, G. Boschloo, A. Hagfeldt, L. Hammarström, L. Kloo and H. Tian, *RSC Adv.*, 2016, **6**, 18165–18177.

(54) H. Wang, Y. Liu, M. Li, H. Huang, H. M. Xu, R. J. Hong and H. Shen, *Optoelectron. Adv. Mater. Rapid Commun.*, 2010, **4**, 1166–1169.

(55) H. Tributsch and M. Calvin, *Photochem. Photobiol.*, 1971, **14**, 95–112.

(56) Y. Li, J. Zhu, H. Chu, J. Wei, F. Liu, M. Lv, J. Tang, B. Zhang, J. Yao, Z. Huo, L. Hu and S. Dai, *Sci. China Chem.*, 2015, **58**, 1489–1493.

(57) G. Hodes, *J. Phys. Chem. C*, 2008, **112**, 17778–17787.

(58) S. S. Khalili and H. Dehghani, *RSC Adv.*, 2016, **6**, 10880–10886.

(59) J. Zhang, J. Gao, E. M. Miller, J. M. Luther and M. C. Beard, *ACS Nano*, 2014, **8**, 614–622.

(60) Z. Pan, I. Mora-Seró, Q. Shen, H. Zhang, Y. Li, K. Zhao, J. Wang, X. Zhong and J. Bisquert, *J. Am. Chem. Soc.*, 2014, **136**, 9203–9210.

(61) W. Feng, Y. Li, J. Du, W. Wang and X. Zhong, *J. Mater. Chem. A*, 2016, **4**, 1461–1468.

(62) J. M. Luther, M. Law, M. C. Beard, Q. Song, M. O. Reese, R. J. Ellingson and A. J. Nozik, *Nano Lett.*, 2008, **8**, 3488–3492.

(63) W. Zhang, X. Zeng, H. Wang, R. Fang, Y. Xu, Y. Zhang and W. Chen, *RSC Adv.*, 2016, **6**, 33713–33722.

(64) K. Zhao, Z. Pan and X. Zhong, *J. Phys. Chem. Lett.*, 2016, **7**, 406–417.

(65) B. Zhang, J. Zheng, X. Li, Y. Fang, L.-W. Wang, Y. Lin and F. Pan, *Chem. Commun.*, 2016, **52**, 5706–5709.

(66) B. Ding, Y. Li, S. Y. Huang, Q. Q. Chu, C. X. Li, C. J. Li and G. J. Yang, *J. Mater. Chem. A*, 2017, **5**, 6840–6848.

(67) M. M. Lee, J. Teuscher, T. Miyasaka, T. N. Murakami and H. J. Snaith, *Science*, 2012, **338**, 643–7.

(68) J. Burschka, N. Pellet, S. J. Moon, R. Humphry-Baker, P. Gao, M. K. Nazeeruddin and M. Grätzel, *Nature*, 2013, **499**, 316–9.

(69) N.-G. Park, *Mater. Today*, 2015, **18**, 65–72.

(70) S. Bag and M. F. Durstock, *ACS Appl. Mater. Interfaces*, 2016, **8**, 5053–5057.

(71) A. Kojima, K. Teshima, Y. Shirai and T. Miyasaka, *J. Am. Chem. Soc.*, 2009, **131**, 6050–1.

(72) H. S. Kim, C. R. Lee, J. H. Im, K. B. Lee, T. Moehl, A. Marchioro, S. J. Moon, R. Humphry Baker, J. H. Yum, J. E. Moser, M. Grätzel and N. G. Park, *Sci. Rep.*, 2012, **2**, 591.

(73) S. Paek, P. Schouwink, E. N. Athanasopoulou, K. T. Cho, G. Grancini, Y. Lee, Y. Zhang, F. Stellacci, M. K. Nazeeruddin and P. Gao, *Chem. Mater.*, 2017, **29**, 3490–3498.

(74) M. Saliba, T. Matsui, K. Domanski, J. Y. Seo, A. Ummadisingu, S. M. Zakeeruddin, J. P. Correa-Baena, W. R. Tress, A. Abate, A. Hagfeldt and M. Gratzel, *Science*, 2016, **354**, 206–209.

(75) NREL Best Research-Cell Efficiency Chart, *https://www.nrel.gov/pv/cell-efficiency.html*, (Accessed March 2019).

(76) J. Duan, Y. Zhao, B. He and Q. Tang, *Angew. Chemie Int. Ed.*, 2018, **57**, 3787–3791.

(77) J. Duan, Y. Zhao, X. Yang, Y. Wang, B. He and Q. Tang, *Adv. Energy Mater.*, 2018, **8**, 1802346.

(78) M. Kulbak, D. Cahen and G. Hodes, *J. Phys. Chem. Lett.*, 2015, **6**, 2452–2456.

(79) G. E. Moore, *Proc. IEEE*, 1998, **86**, 82–85.

(80) F. L. Yang, D. H. Lee, H. Y. Chen, C. Y. Chang, S. D. Liu, C. C. Huang, T. X. Chung, H. W. Chen, C. C. Huang, Y. H. Liu, C. C. Wu, C. C. Chen, S. C. Chen, Y. T. Chen, Y. H. Chen, C. J. Chen, B. W. Chan, P. F. Hsu, J. H. Shieh, H.-J. Tao, Y.-C. Yeo, Y. Li, J. W. Lee, P. Chen, M. S. Liang and C. Hu, *Dig. Tech. Pap. Symp. VLSI Technol.*, 2004, 196–197.

(81) J. R. Morones, J. L. Elechiguerra, A. Camacho, K. Holt, J. B. Kouri, J. T. Ramírez and M. J. Yacaman, *Nanotechnology*, 2005, **16**, 2346–2353.

(82) P. Poizot, S. Laruelle, S. Grugeon, L. Dupont and J.-m. Tarascon, *Nature*, 2000, **407**, 496–499.

(83) *US Pat.* 5455489, 1994.

(84) Y. M. Liu and W. P. Hu, *Adv. Mater. Res.*, 2012, **573-574**, 135–139.

(85) Jubilee Church - Richard Meier & Partners Architects LLP, *https://www.richardmeier.com/?projects=jubilee-church-2*, (Accessed March 2019).

(86) M. Wu and S. Huang, *Mol. Clin. Oncol.*, 2017, 738–746.

(87) E. S. Arinze, B. Qiu, G. Nyirjesy and S. M. Thon, *ACS Photonics*, 2016, **3**, 158–173.

(88) K. Kolwas and A. Derkachova, *J. Phys. Chem. C*, 2017, **121**, 4524–4539.

(89) M. Wu, W. J. Chen, Y. H. Shen, F. Z. Huang, C. H. Li and S. K. Li, *ACS Appl. Mater. Interfaces*, 2014, **6**, 15052–15060.

(90) Y. Cheng, C. Chen, X. Chen, J. Jin, H. Li, H. Song and Q. Dai, *J. Mater. Chem. A*, 2017, **5**, 6515–6521.

(91) S. Mokkapati and K. R. Catchpole, *J. Appl. Phys.*, 2012, **112**, 101101.

(92) A. Niv, M. G. Koren, H. Dotan, G. Bartal and A. Rothschild, *J. Mater. Chem. A*, 2016, **4**, 3043–3051.

(93) S. Zhou, R. Tang and L. Yin, *Adv. Mater.*, 2017, **29**, 1703682.

(94) E. Garnett and P. Yang, *Nano Lett.*, 2010, **10**, 1082–1087.

(95) H. S. Kim, M. Patel, H. H. Park, A. Ray, C. Jeong and J. Kim, *ACS Appl. Mater. Interfaces*, 2016, **8**, 8662–8669.

(96) S. Baruah and J. Dutta, *Sci. Technol. Adv. Mater.*, 2009, **10**, 013001.

(97) E. S. Babu, S. K. Hong, T. S. Vo, J. R. Jeong and H. K. Cho, *Electron. Mater. Lett.*, 2015, **11**, 65–72.

(98) Y. Hu, X. Yan, Y. Gu, X. Chen, Z. Bai, Z. Kang, F. Long and Y. Zhang, *Appl. Surf. Sci.*, 2015, **339**, 122–127.

(99) W. C. Lee, Y. Fang, R. Kler, G. E. Canciani, T. C. Draper, Z. T. Al-Abdullah, S. M. Alfadul, C. C. Perry, H. He and Q. Chen, *Mater. Chem. Phys.*, 2015, **149-150**, 12–16.

(100) W. C. Lee, G. E. Canciani, B. O. Alwhshe and Q. Chen, *Int. J. Hydrogen Energy*, 2016, **41**, 123–131.

(101) M. Law, L. E. Greene, J. C. Johnson, R. Saykally and P. D. Yang, *Nat. Mater.*, 2005, **4**, 455–459.

(102) S.-F. Leung, Q. Zhang, M. M. Tavakoli, J. He, X. Mo and Z. Fan, *Small*, 2016, **12**, 2536–2548.

(103) Z. Fan, H. Razavi, J. Do, A. Moriwaki, O. Ergen, J. L. Chueh, P. W. Leu, J. C. Ho, T. Takahashi, L. A. Reichertz, S. Neale, K. Yu, M. Wu, J. W. Ager and A. Javey, *Nat. Mater.*, 2009, **8**, 648–653.

(104) X. Ma, H. Elbohy, S. Sigdel, C. Lai, Q. Qiao and H. Fong, *RSC Adv.*, 2016, **6**, 11481–11487.

(105) *Zinc Oxide Bulk, Thin Films and Nanostructures*, ed. Jagadish and Pearton, Elsevier Science, Oxford, 2006.

(106) D. C. Look and R. J. Molnar, *Appl. Phys. Lett.*, 1997, **70**, 3377–3379.

(107) G. Yin, J. Ma, H. Jiang, J. Li, D. Yang, F. Gao, J. Zeng, Z. Liu and S. F. Liu, *ACS Appl. Mater. Interfaces*, 2017, **9**, 10752–10758.

(108) W. Ming, S. Chen and M. H. Du, *J. Mater. Chem. A*, 2016, **4**, 16975–16981.

(109) M. Skompska and K. Zarbska, *Electrochim. Acta*, 2014, **127**, 467–488.

(110) R. Tena-Zaera, J. Elias, C. Lévy-Clément, I. Mora-Seró, Y. Luo and J. Bisquert, *Phys. status solidi*, 2008, **205**, 2345–2350.

(111) M. Skompska and K. Zarbska, *Electrochim. Acta*, 2014, **127**, 467–488.

(112) S. Xu, C. Lao, B. Weintraub and Z. L. Wang, *J. Mater. Res.*, 2008, **23**, 2072–2077.

(113) M. Baek, D. Kim and K. Yong, *ACS Appl. Mater. Interfaces*, 2017, **9**, 2317–2325.

(114) D. Commandeur, G. Brown, E. Hills, J. Spencer and Q. Chen, *ACS Appl. Nano Mater.*, 2019, **2**, 1570–1578.

(115) F. Xu, Y. Lu, Y. Xie and Y. Liu, *Mater. Des.*, 2009, **30**, 1704–1711.

(116) H. Parangusan, D. Ponnamma, M. A. A. Al-Maadeed and A. Marimuthu, *Photochem. Photobiol.*, 2018, **94**, 237–246.

(117) X. Ren, A. Sangle, S. Zhang, S. Yuan, Y. Zhao, L.-Y. Shi, R. L. Z. Hoye, S. Cho, D. Li and J. L. MacManus-Driscoll, *J. Mater. Chem. A*, 2016, **4**, 10203–10211.

(118) P. Zhang, J. Wu, T. Zhang, Y. Wang, D. Liu, H. Chen, L. Ji, C. Liu, W. Ahmad, Z. D. Chen and S. Li, *Adv. Mater.*, 2018, **30**, 1–20.

(119) R. Lv, T. Wang, F. Su, P. Zhang, C. Li and J. Gong, *Nano Energy*, 2014, **7**, 143–150.

(120) F. Dehghan Nayeri, M. Kolahdouz, E. Asl-Soleimani and S. Mohajerzadeh, *J. Alloys Compd.*, 2015, **633**, 359–365.

(121) Y. Cao, S. Deng, Q. Hu, Q. Zhong, Q. P. Luo, L. Yuan and J. Zhou, *RSC Adv.*, 2015, **5**, 85969–85973.

(122) C. Li, X. Zhu, H. Zhang, Z. Zhu, B. Liu and C. Cheng, *Adv. Mater. Interfaces*, 2015, **2**, 1500428.

(123) J. Lü, K. Huang, J. Zhu, X. Chen, X. Song and Z. Sun, *Phys. B Condens. Matter*, 2010, **405**, 3167–3171.

(124) A. Janotti and C. G. Van de Walle, *Reports Prog. Phys.*, 2009, **72**, 126501.

(125) S. Chu, G. Wang, W. Zhou, Y. Lin, L. Chernyak, J. Zhao, J. Kong, L. Li, J. Ren and J. Liu, *Nat. Nanotechnol.*, 2011, **6**, 506–510.

(126) S. Tabassum, E. Yamasue, H. Okumura and K. N. Ishihara, *Appl. Surf. Sci.*, 2016, **377**, 355–360.

(127) N. Kaur, S. K. Sharma, D. Y. Kim and N. Singh, *Phys. B Condens. Matter*, 2016, **500**, 179–185.

(128) L. Xiao, E. Li, J. Yi, W. Meng, S. Wang, B. Deng and J. Liu, *J. Alloys Compd.*, 2018, **764**, 545–554.

(129) X. He, J. E. Yoo, M. H. Lee and J. Bae, *Nanotechnology*, 2017, **28**, 245402.

(130) N. R. Shanmugam, S. Muthukumar, A. P. Selvam and S. Prasad, *Nanomedicine*, 2016, **11**, 1345–1358.

(131) A. Ali, A. A. Ansari, A. Kaushik, P. R. Solanki, A. Barik, M. K. Pandey and B. D. Malhotra, *Mater. Lett.*, 2009, **63**, 2473–2475.

(132) B. Baruwati, D. K. Kumar and S. V. Manorama, *Sensors Actuators B Chem.*, 2006, **119**, 676–682.

(133) W. C. Lee, Y. Fang, J. F. Turner, J. S. Bedi, C. C. Perry, H. He, R. Qian and Q. Chen, *Sensors Actuators, B Chem.*, 2016, **237**, 724–732.

(134) D. Bhatia, H. Sharma, R. Meena and V. Palkar, *Sens. Bio-Sensing Res.*, 2016, **9**, 45–52.

(135) S. Baruah, M. A. Mahmood, M. T. Z. Myint, T. Bora and J. Dutta, *Beilstein J. Nanotechnol.*, 2010, **1**, 14–20.

(136) R. Pagano, A. Quarta, S. Pal, A. Licciulli, L. Valli and S. Bettini, *J. Phys. Chem. C*, 2017, **121**, 27199–27206.

(137) A. Serrà, Y. Zhang, B. Sepúlveda, E. Gómez, J. Nogués, J. Michler and L. Philippe, *Appl. Catal. B Environ.*, 2019, **248**, 129–146.

(138) A. Hernández-Ramírez, M. d. L. Maya-Treviño, L. Hinojosa-Reyes, M. Villanueva-Rodríguez, R. E. Núñez-Salas and J. L. Guzmán-Mar, *Catal. Today*, 2018, **328**, 202–209.

(139) Z. J. Wang, H. Song, H. Pang, Y. Ning, T. D. Dao, Z. Wang, H. Chen, Y. Weng, Q. Fu, T. Nagao, Y. Fang and J. Ye, *Appl. Catal. B Environ.*, 2019, **250**, 10–16.

(140) D. Yang, Q. Zhu, C. Chen, H. Liu, Z. Liu, Z. Zhao, X. Zhang, S. Liu and B. Han, *Nat. Commun.*, 2019, **10**, 677.

(141) N. M. Vuong, J. L. Reynolds, E. Conte and Y. I. Lee, *J. Phys. Chem. C*, 2015, **119**, 24323–24331.

(142) Z. Han, M. Wang, X. Chen and S. Shen, *Phys. Chem. Chem. Phys.*, 2016, **18**, 11460–11466.

(143) X. Yang, A. Wolcott, G. Wang, A. Sobo, R. C. Fitzmorris, F. Qian, J. Z. Zhang and Y. Li, *Nano Lett.*, 2009, **9**, 2331–2336.

(144) Y. Qiu, K. Yan, H. Deng and S. Yang, *Nano Lett.*, 2012, **12**, 407–413.

(145) H. J. Lee, S. H. Shin, K. T. Nam, J. Nah and M. H. Lee, *J. Mater. Chem. A*, 2016, **4**, 3223–3227.

(146) W. S. Chang, Y. C. Chang, H. M. Chen, K. H. Chen, S. F. Hu, C. W. Tsai, R. S. Liu and C. K. Chen, *Angew. Chemie Int. Ed.*, 2010, **49**, 5966–5969.

(147) Y. G. Lin, Y. K. Hsu, Y. C. Chen, S. B. Wang, J. T. Miller, L. C. Chen and K. H. Chen, *Energy Environ. Sci.*, 2012, **5**, 8917.

(148) L. Liu, W. Wang, J. Long, S. Fu, Y. Liang and J. Fu, *Sol. Energy Mater. Sol. Cells*, 2019, **195**, 330–338.

(149) X. Liu, X. Li, Y. Li, C. Song, L. Zhu, W. Zhang, H. Q. Wang and J. Fang, *Adv. Mater.*, 2016, **28**, 7405–7412.

(150) S. B. Ambade, R. B. Ambade, S. H. Eom, M. J. Baek, S. S. Bagde, R. S. Mane and S.-H. Lee, *Nanoscale*, 2016, **8**, 5024–5036.

(151) R. Parize, A. Katerski, I. Gromyko, L. Rapenne, H. Roussel, E. Kärber, E. Appert, M. Krunks and V. Consonni, *J. Phys. Chem. C*, 2017, **121**, 9672–9680.

(152) G. Gao, L. Yu, A. Vinu, J. G. Shapter, M. Batmunkh, C. J. Shearer, T. Yin, P. Huang and D. Cui, *RSC Adv.*, 2016, **6**, 109406–109413.

(153) P. Tiwana, P. Docampo, M. B. Johnston, H. J. Snaith and L. M. Herz, *ACS Nano*, 2011, **5**, 5158–5166.

(154) H. Zhao, F. Huang, J. Hou, Z. Liu, Q. Wu, H. Cao, Q. Jing, S. Peng and G. Cao, *ACS Appl. Mater. Interfaces*, 2016, **8**, 26675–26682.

(155) Y. Cao, Y. J. Dong, H. Y. Chen, D. B. Kuang and C. Su, *RSC Adv.*, 2016, **6**, 78202–78209.

(156) M. H. Kumar, N. Yantara, S. Dharani, M. Graetzel, S. Mhaisalkar, P. P. Boix and N. Mathews, *Chem. Commun.*, 2013, **49**, 11089.

(157) D. Bi, G. Boschloo, S. Schwarzmüller, L. Yang, E. M. J. Johansson and A. Hagfeldt, *Nanoscale*, 2013, **5**, 11686.

(158) P. Chen, X. Yin, M. Que, Y. Yang and W. Que, *RSC Adv.*, 2016, **6**, 57996–58002.

(159) K. Mahmood, B. S. Swain and A. Amassian, *Adv. Energy Mater.*, 2015, **5**, 1500568.

(160) Z. Liu, T. He, H. Wang, S. M. Jain, K. Liu, J. Yang, N. Zhang, H. Liu and M. Yuan, *J. Power Sources*, 2018, **401**, 303–311.

(161) J. You, L. Meng, T. B. Song, T. F. Guo, Y. Yang, W. H. Chang, Z. Hong, H. Chen, H. Zhou, Q. Chen, Y. Liu, N. De Marco and Y. Yang, *Nat. Nanotechnol.*, 2016, **11**, 75–81.

(162) M. Aamir, T. Adhikari, M. Sher, N. Revaprasadu, W. Khalid, J. Akhtar and J. M. Nunzi, *New J. Chem.*, 2018, **42**, 14104–14110.

(163) C. Liu, W. Li, C. Zhang, Y. Ma, J. Fan and Y. Mai, *J. Am. Chem. Soc.*, 2018, **140**, 3825–3828.

(164) H. J. Ahn, M. J. Kwak, J. S. Lee, K. Y. Yoon and J. H. Jang, *J. Mater. Chem. A*, 2014, **2**, 19999–20003.

(165) A. G. Tamirat, J. Rick, A. A. Dubale, W. N. Su and B. J. Hwang, *Nanoscale Horizons*, 2016, **1**, 243–267.

(166) P. Liao, M. C. Toroker and E. A. Carter, *Nano Lett.*, 2011, **11**, 1775–1781.

(167) B. Klahr, S. Gimenez, F. Fabregat-Santiago, T. Hamann and J. Bisquert, *J. Am. Chem. Soc.*, 2012, **134**, 4294–4302.

(168) L. Steier, J. Luo, M. Schreier, M. T. Mayer, T. Sajavaara and M. Grätzel, *ACS Nano*, 2015, **9**, 11775–11783.

(169) X. Li, P. S. Bassi, P. P. Boix, Y. Fang and L. H. Wong, *ACS Appl. Mater. Interfaces*, 2015, **7**, 16960–16966.

(170) R. Córdova, L. A. Ballesteros, P. Grez, J. R. Ramos-Barrado, H. Gómez, R. Schrebler, R. Schrebler, E. A. Dalchiele and E. Muñoz, *J. Electrochem. Soc.*, 2014, **161**, H903–H908.

(171) A. Kay, I. Cesar and M. Grätzel, *J. Am. Chem. Soc.*, 2006, **128**, 15714–15721.

(172) R. S. Schrebler, L. Ballesteros, A. Burgos, E. C. Muñoz, P. Grez, D. Leinen, F. Martín, J. Ramón Ramos-Barrado and E. a. Dalchiele, *J. Electrochem. Soc.*, 2011, **158**, D500.

(173) S. R. Pendlebury, X. Wang, F. Le Formal, M. Cornuz, A. Kafizas, S. D. Tilley, M. Grätzel and J. R. Durrant, *J. Am. Chem. Soc.*, 2014, **136**, 9854–9857.

(174) X. Zhao, J. Feng, S. Chen, Y. Huang, T. C. Sum and Z. Chen, *Phys. Chem. Chem. Phys.*, 2017, **19**, 1074–1082.

(175) K. Y. Yoon, H. J. Ahn, M. J. Kwak, S. I. Kim, J. Park and J. H. Jang, *J. Mater. Chem. A*, 2016, **4**, 18730–18736.

(176) D. Wang, Y. Zhang, J. Wang, C. Peng, Q. Huang, S. Su, L. Wang, W. Huang and C. Fan, *ACS Appl. Mater. Interfaces*, 2014, **6**, 36–40.

(177) J. Yang, C. Bao, T. Yu, Y. Hu, W. Luo, W. Zhu, G. Fu, Z. Li, H. Gao, F. Li and Z. Zou, *ACS Appl. Mater. Interfaces*, 2015, **7**, 26482–26490.

(178) Y. K. Hsu, Y. C. Chen and Y. G. Lin, *ACS Appl. Mater. Interfaces*, 2015, **7**, 14157–14162.

(179) X. Wang, K. Q. Peng, Y. Hu, F. Q. Zhang, B. Hu, L. Li, M. Wang, X. M. Meng and S. T. Lee, *Nano Lett.*, 2014, **14**, 18–23.

(180) M. T. Mayer, C. Du and D. Wang, *J. Am. Chem. Soc.*, 2012, **134**, 12406–12409.

(181) J. Li, S. K. Cushing, P. Zheng, F. Meng, D. Chu and N. Wu, *Nat. Commun.*, 2013, **4**, 2651.

(182) C. W. Marean, *J. Hum. Evol.*, 2010, **59**, 425–443.

(183) P. Li, D. E. Miser, S. Rabiei, R. T. Yadav and M. R. Hajaligol, *Appl. Catal. B Environ.*, 2003, **43**, 151–162.

(184) R. Mecozzi, L. Di Palma, D. Pilone and L. Cerboni, *J. Hazard. Mater.*, 2006, **137**, 886–892.

(185) O. Shekhah, W. Ranke, A. Schüle, G. Kolios and R. Schlögl, *Angew. Chemie Int. Ed.*, 2003, **42**, 5760–5763.

(186) W. S. Choi, H. Y. Koo, Z. Zhongbin, Y. Li and D.-Y. Kim, *Adv. Funct. Mater.*, 2007, **17**, 1743–1749.

(187) X. Gou, G. Wang, J. Park, H. Liu and J. Yang, *Nanotechnology*, 2008, **19**, 125606.

(188) T. M. Bandhauer, S. Garimella and T. F. Fuller, *J. Electrochem. Soc.*, 2011, **158**, 1–25.

(189) L. Wang, K. Liang, G. Wang and Y. Yang, *J. Mater. Chem. A*, 2018, **6**, 13968–13974.

(190) Q. Hou, J. Ren, H. Chen, P. Yang, Q. Shao, M. Zhao, X. Zhao, H. He, N. Wang, Q. Luo and Z. Guo, *ChemElectroChem*, 2018, **5**, 726–731.

(191) M. Grätzel, *Inorg. Chem.*, 2005, **44**, 6841–6851.

(192) M. Shahpari, A. Behjat, M. Khajaminian and N. Torabi, *Sol. Energy*, 2015, **119**, 45–53.

(193) W. Hu, T. Liu, X. Yin, H. Liu, X. Zhao, S. Luo, Y. Guo, Z. Yao, J. Wang, N. Wang, H. Lin and Z. Guo, *J. Mater. Chem. A*, 2017, **5**, 1434–1441.

(194) D. R. Kennedy, M. Ritchie and J. Mackenzie, *Trans. Faraday Soc.*, 1958, **54**, 119.

(195) M. Itakura, N. Niizeki, H. Toyoda and H. Iwasaki, *Jpn. J. Appl. Phys.*, 1967, **6**, 311–317.

(196) Y. Bai, I. Mora-Seró, F. De Angelis, J. Bisquert and P. Wang, *Chem. Rev.*, 2014, **114**, 10095–10130.

(197) P. Zhang, T. Tachikawa, M. Fujitsuka and T. Majima, *J. Phys. Chem. Lett.*, 2016, **7**, 1173–1179.

(198) W. Zhang, R. Zhu, B. Liu and S. Ramakrishna, *Aust. J. Chem.*, 2011, **64**, 1282.

(199) K. Zhu, T. B. Vinzant, N. R. Neale and A. J. Frank, *Nano Lett.*, 2007, **7**, 3739–3746.

(200) B. O'Regan and M. Grätzel, *Nature*, 1991, **353**, 737–740.

(201) A. Yella, H. W. Lee, H. N. Tsao, C. Yi, A. K. Chandiran, M. K. Nazeeruddin, E. W. G. Diau, C. Y. Yeh, S. M. Zakeeruddin and M. Grätzel, *Science*, 2011, **334**, 629–634.

(202) E. J. W. Crossland, N. Noel, V. Sivaram, T. Leijtens, J. A. Alexander-Webber and H. J. Snaith, *Nature*, 2013, **495**, 215–219.

(203) H. P. Wu, C. M. Lan, J. Y. Hu, W. K. Huang, J. W. Shiu, Z. J. Lan, C. M. Tsai, C. H. Su and E. W. G. Diau, *J. Phys. Chem. Lett.*, 2013, **4**, 1570–1577.

(204) D. R. Baker and P. V. Kamat, *Adv. Funct. Mater.*, 2009, **19**, 805–811.

(205) I. Robel, V. Subramanian, M. Kuno and P. V. Kamat, *J. Am. Chem. Soc.*, 2006, **128**, 2385–2393.

(206) V. González-Pedro, C. Sima, G. Marzari, P. P. Boix, S. Giménez, Q. Shen, T. Dittrich and I. Mora-Seró, *Phys. Chem. Chem. Phys.*, 2013, **15**, 13835–13843.

(207) J. Yang, Q. Tang, Q. Meng, Z. Zhang, J. Li, B. He and P. Yang, *J. Mater. Chem. A*, 2017, **5**, 2143–2150.

(208) Y. Xiao, G. Han, Y. Li, M. Li, Y. Chang and J. Wu, *J. Mater. Chem. A*, 2014, **2**, 16531–16537.

(209) K. Sveinbjörnsson, K. Aitola, J. Zhang, M. B. Johansson, X. Zhang, J. P. Correa-Baena, A. Hagfeldt, G. Boschloo and E. M. Johansson, *J. Mater. Chem. A*, 2016, **4**, 16536–16545.

(210) Z. Yu, F. Qi, P. Liu, S. You, K. K. Kondamareddy, C. Wang, N. Cheng, S. Bai, W. Liu, S. Guo and X. Zhao, *Nanoscale*, 2016, **8**, 5847–5851.

(211) Y. Huang, J. Zhu, Y. Ding, S. Chen, C. Zhang and S. Dai, *ACS Appl. Mater. Interfaces*, 2016, acsami.5b08421.

(212) Y. Xiao, G. Han, Y. Li, M. Li and J. Wu, *J. Mater. Chem. A*, 2014, **2**, 16856–16862.

(213) M. Shalom, S. Dor, S. Rühle, L. Grinis and A. Zaban, *J. Phys. Chem. C*, 2009, **113**, 3895–3898.

(214) B. Ding, S. Y. Huang, Q. Q. Chu, Y. Li, C. X. Li, C. J. Li and G. J. Yang, *J. Mater. Chem. A*, 2018, **6**, 10233–10242.

(215) Y. Zhao, Y. Zhang, W. Xing and N. Xu, *Chem. Eng. J.*, 2005, **111**, 31–38.

(216) A. Jaroenworaluck, W. Sunsaneeyametha, N. Kosachan and R. Stevens, *Surf. Interface Anal.*, 2006, **38**, 473–477.

(217) D. Angmo, N. Espinosa and F. Krebs, *Low-cost Nanomaterials*, ed. Z. Lin and J. Wang, Springer London, Springer-Verlag London, 2014.

(218) C. Hou, B. Hu and J. Zhu, *Catalysts*, 2018, **8**, 575.

(219) Y. Paz, Z. Luo, L. Rabenberg and A. Heller, *J. Mater. Res.*, 1995, **10**, 2842–2848.

(220) K. Li, B. Li, J. Wu, F. Kang, J. K. Kim and T. Y. Zhang, *ACS Appl. Mater. Interfaces*, 2017, **9**, 35917–35926.

(221) A. J. Gardecka, M. Lübke, C. F. Armer, D. Ning, M. Reddy, A. S. Williams, A. Lowe, Z. Liu, I. P. Parkin and J. A. Darr, *Solid State Sci.*, 2018, **83**, 115–121.

(222) M. Catti, I. Pinus, R. Ruffo, M. M. Salamone and C. M. Mari, *Solid State Ionics*, 2016, **295**, 72–77.

(223) K. Gelderman, L. Lee and S. W. Donne, *J. Chem. Educ.*, 2007, **84**, 685.

(224) Z. Kang, H. Si, S. Zhang, J. Wu, Y. Sun, Q. Liao, Z. Zhang and Y. Zhang, *Adv. Funct. Mater.*, 2019, **29**, 1808032.

(225) Y. Ooyama, K. Furue, T. Enoki, M. Kanda, Y. Adachi and J. Ohshita, *Phys. Chem. Chem. Phys.*, 2016, **18**, 30662–30676.

(226) S. Al-Hilli and M. Willander, *Sensors*, 2009, **9**, 7445–7480.

(227) H. Kanda, A. Uzum, A. K. Baranwal, T. A. Peiris, T. Umeyama, H. Imahori, H. Segawa, T. Miyasaka and S. Ito, *J. Phys. Chem. C*, 2016, **120**, 28441–28447.

(228) B. X. Wang, T. F. Liu, Y. B. Zhou, X. Chen, X. B. Yuan, Y. Y. Yang, W. P. Liu, J. M. Wang, H. W. Han and Y. W. Tang, *Phys. Chem. Chem. Phys.*, 2016, **18**, 27078–27082.

(229) J. Liang, C. Wang, Y. Wang, Z. Xu, Z. Lu, Y. Ma, H. Zhu, Y. Hu, C. Xiao, X. Yi, G. Zhu, H. Lv, L. Ma, T. Chen, Z. Tie, Z. Jin and J. Liu, *J. Am. Chem. Soc.*, 2016, **138**, 15829–15832.

(230) T. W. Hamann, *Dalt. Trans.*, 2012, **41**, 7830.

(231) M. J. Katz, S. C. Riha, N. C. Jeong, A. B. F. Martinson, O. K. Farha and J. T. Hupp, *Coord. Chem. Rev.*, 2012, **256**, 2521–2529.

(232) R. Schrebler, C. Llewelyn, F. Vera, P. Cury, E. Muñoz, R. del Río, H. Gómez Meier, R. Córdova and E. A. Dalchiele, *Electrochem. Solid-State Lett.*, 2006, **9**, C110–C113.

(233) Y. Hou, C. Zheng, Z. Zhu and X. Wang, *Chem. Commun.*, 2016, **52**, 6888–6891.

(234) D. K. Zhong, M. Cornuz, K. Sivula, M. Grätzel and D. R. Gamelin, *Energy Environ. Sci.*, 2011, **4**, 1759.

(235) K. J. McDonald and K. S. Choi, *Chem. Mater.*, 2011, **23**, 4863–4869.

(236) R. Kant, S. Pathak and V. Dutta, *Sol. Energy Mater. Sol. Cells*, 2018, **178**, 38–45.

(237) A. Hankin, J. C. Alexander and G. H. Kelsall, *Phys Chem Chem Phys*, 2014, **16**, 16176–16186.

(238) X. Yin, Z. Xu, Y. Guo, P. Xu and M. He, *ACS Appl. Mater. Interfaces*, 2016, **8**, 29580–29587.

(239) M. Kwiatkowski, R. Chassagnon, O. Heintz, N. Geoffroy, M. Skompska and I. Bezverkhyy, *Appl. Catal. B Environ.*, 2017, **204**, 200–208.

(240) J. Duan, J. Wu, J. Zhang, Y. Xu, H. Wang, D. Gao and P. D. Lund, *Int. J. Energy Res.*, 2016, **40**, 806–813.

(241) X. Chen, S. Shen, L. Guo and S. S. Mao, *Chem. Rev.*, 2010, **110**, 6503–6570.

(242) W. Ke, C. C. Stoumpos, J. L. Logsdon, M. R. Wasielewski, Y. Yan, G. Fang and M. G. Kanatzidis, *J. Am. Chem. Soc.*, 2016, **138**, 14998–15003.

(243) J. Yu, G. Dai and B. Huang, *J. Phys. Chem. C*, 2009, **113**, 16394–16401.

(244) R. Yu, Q. Lin, S. F. Leung and Z. Fan, *Nano Energy*, 2012, **1**, 57–72.

(245) D. Koushik, W. J. Verhees, Y. Kuang, S. Veenstra, D. Zhang, M. A. Verheijen, M. Creatore and R. E. Schropp, *Energy Environ. Sci.*, 2017, **10**, 91–100.

(246) J. J. Li, J. Y. Ma, J. S. Hu, D. Wang and L. J. Wan, *ACS Appl. Mater. Interfaces*, 2016, **8**, 26002–26007.

(247) E. Belarbi, M. Vallés-Pelarda, B. Clasen Hames, R. S. Sanchez, E. M. Barea, H. Maghraoui-Meherzi and I. Mora-Seró, *Phys. Chem. Chem. Phys.*, 2017, **19**, 10913–10921.

(248) H. Sutiono, A. M. Tripathi, H. M. Chen, C. H. Chen, W. N. Su, L. Y. Chen, H. Dai and B. J. Hwang, *ACS Sustain. Chem. Eng.*, 2016, **4**, 5963–5971.

(249) M. C. K. Sellers and E. G. Seebauer, *Thin Solid Films*, 2011, **519**, 2103–2110.

(250) H. N. Hieu, N. Q. Dung, J. Kim and D. Kim, *Nanoscale*, 2013, **5**, 5530–8.

(251) M. Zhong, L. Chai and Y. Wang, *Appl. Surf. Sci.*, 2019, **464**, 301–310.

(252) N. Wu, C. Shi, N. Li, Y. Wang and M. Li, *Mater. Res. Innov.*, 2016, **20**, 338–342.

(253) J. William Strutt and L. Rayleigh, *Philos. Mag. Ser. 5*, 1880, **9:53**, 40–55.

(254) K. Kanaya and H. Kawakatsu, *J. Phys. D. Appl. Phys.*, 1972, **5**, 1727–1742.

(255) H. Seiler, *J. Appl. Phys.*, 1983, **54**, R1–R18.

(256) M. R. Khan and M. Karimi, *X-Ray Spectrom.*, 1980, **9**, 32–35.

(257) Z. L. Wang, *J. Phys. Chem. B*, 2000, **104**, 1153–1175.

(258) W. H. Bragg and W. L. Bragg, *Proc. R. Soc. A Math. Phys. Eng. Sci.*, 1913, **88**, 428–438.

(259) U. Holzwarth and N. Gibson, *Nat. Nanotechnol.*, 2011, **6**, 534–534.

(260) D. F. Swinehart, *J. Chem. Educ.*, 1962, **39**, 333.

(261) J. Tauc, *Mater. Res. Bull.*, 1968, **3**, 37–46.

(262) A. B. Murphy, *Sol. Energy Mater. Sol. Cells*, 2007, **91**, 1326–1337.

(263) W. C. Lee, Ph.D. Thesis, University of Sussex, 2015, pp. 1–279.

(264) G. Gilliland, *Mater. Sci. Eng. R Reports*, 1997, **18**, 99–399.

(265) C. A. Parker and W. T. Rees, *Analyst*, 1962, **87**, 83.

(266) Y. R. Ryu, T. S. Lee and H. W. White, *Appl. Phys. Lett.*, 2003, **83**, 87–89.

(267) L. Armelao, D. Barreca, G. Bottaro, S. Gross, A. Gasparotto, C. Maragno, E. Tondello and A. Zattin, *Surf. Sci. Spectra*, 2003, **10**, 137–142.

(268) C. C. Chang, *Surf. Sci.*, 1971, **25**, 53–79.

(269) R. Reay, S. Kounaves and G. Kovacs, *Proc. IEEE Int. Solid-State Circuits Conf. - ISSCC '94*, 1994, 162–163.

(270) A. S. Feiner, *J. Chem. Educ.*, 1994, **71**, 493–494.

(271) C. T. Dervos, P. D. Skafidas, J. A. Mergos and P. Vassiliou, *Sensors*, 2004, **4**, 58–70.

(272) A. Huang, L. Lei, J. Zhu, Y. Yu, Y. Liu, S. Yang, S. Bao, X. Cao and P. Jin, *ACS Appl. Mater. Interfaces*, 2017, **9**, 2016–2022.

(273) J. L. Garrett, E. M. Tennyson, M. Hu, J. Huang, J. N. Munday and M. S. Leite, *Nano Lett.*, 2017, **17**, 2554–2560.

(274) J. Jin, C. Chen, H. Li, Y. Cheng, L. Xu, B. Dong, H. Song and Q. Dai, *ACS Appl. Mater. Interfaces*, 2017, **9**, 14518–14524.

(275) T. T. Hien, N. D. Quang, C. Kim and D. Kim, *Nano Energy*, 2019, **57**, 660–669.

(276) F. Fabregat-Santiago, G. Garcia-Belmonte, J. Bisquert, P. Bogdanoff and A. Zaban, *J. Electrochem. Soc.*, 2003, **150**, 293–298.

(277) D.-Y. Son, J.-H. Im, H.-S. Kim and N.-G. Park, *J. Phys. Chem. C*, 2014, **118**, 16567–16573.

(278) R. Memming, *Semiconductor Electrochemistry*, Wiley-VCH Verlag GmbH, Weinheim, Germany, 2000.

(279) B. Pettinger, H.-R. Schöppel, T. Yokoyama and H. Gerischer, *Bericht der Bunsengesellschaft für Phys. Chemie*, 1974, **78**, 1024–1030.

(280) C. Wang, T. Hisatomi, T. Minegishi, M. Nakabayashi, N. Shibata, M. Katayama and K. Domen, *J. Mater. Chem. A*, 2016, **4**, 13837–13843.

(281) J. Bisquert, *J. Phys. Chem. B*, 2002, **106**, 325–333.

(282) F. Fabregat-Santiago, G. Garcia-Belmonte, J. Bisquert, A. Zaban and P. Salvador, *J. Phys. Chem. B*, 2002, **106**, 334–339.

(283) Y. Feng, J. Bian, M. Wang, S. Wang, C. Zhang, Q. Dong, B. Zhang and Y. Shi, *Mater. Res. Bull.*, 2018, **107**, 74–79.

(284) S. Ravishankar, O. Almora, C. Echeverría-Arrondo, E. Ghahremanirad, C. Aranda, A. Guerrero, F. Fabregat-Santiago, A. Zaban, G. Garcia-Belmonte and J. Bisquert, *J. Phys. Chem. Lett.*, 2017, **8**, 915–921.

(285) R. J. Millar, J. S. Fuglestvedt, P. Friedlingstein, J. Rogelj, M. J. Grubb, H. D. Matthews, R. B. Skeie, P. M. Forster, D. J. Frame and M. R. Allen, *Nat. Geosci.*, 2017, **10**, 741–747.

(286) A. Wolcott, W. A. Smith, T. R. Kuykendall, Y. Zhao and J. Z. Zhang, *Adv. Funct. Mater.*, 2009, **19**, 1849–1856.

(287) P. Mishra, P. Shukla and O. Srivastava, *Int. J. Hydrogen Energy*, 2007, **32**, 1680–1685.

(288) L. Cai, F. Ren, M. Wang, G. Cai, Y. Chen, Y. Liu, S. Shen and L. Guo, *Int. J. Hydrogen Energy*, 2015, **40**, 1394–1401.

(289) S. Mukhopadhyay, I. Mondal, U. Pal and P. S. Devi, *Phys. Chem. Chem. Phys.*, 2015, **17**, 20407–20415.

(290) X. Li, J. Li, C. Cui, Z. Liu and Y. Niu, *J. Phys. Chem. C*, 2016, **120**, 4183–4188.

(291) J. Lu, H. Wang, S. Dong, F. Wang and Y. Dong, *J. Alloys Compd.*, 2014, **617**, 869–876.

(292) G. Zhou, X. Xu, T. Ding, B. Feng, Z. Bao and J. Hu, *ACS Appl. Mater. Interfaces*, 2015, **7**, 26819–26827.

(293) C. Zhang, M. Shao, F. Ning, S. Xu, Z. Li, M. Wei, D. G. Evans and X. Duan, *Nano Energy*, 2015, **12**, 231–239.

(294) M. Wang, F. Ren, J. Zhou, G. Cai, L. Cai, Y. Hu, D. Wang, Y. Liu, L. Guo and S. Shen, *Sci. Rep.*, 2015, **5**, 12925.

(295) M. Wang, F. Ren, G. Cai, Y. Liu, S. Shen and L. Guo, *Nano Res.*, 2014, **7**, 353–364.

(296) S. Shao, P. Jia, S. Liu and W. Bai, *Mater. Lett.*, 2008, **62**, 1200–1203.

(297) L. V. Podrezova, S. Porro, V. Cauda, M. Fontana and G. Cicero, *Appl. Phys. A*, 2013, **113**, 623–632.

(298) S. Cao, X. Yan, Z. Kang, Q. Liang, X. Liao and Y. Zhang, *Nano Energy*, 2016, **24**, 25–31.

(299) V. Polshettiwar, M. N. Nadagouda and R. S. Varma, *Aust. J. Chem.*, 2009, **62**, 16–26.

(300) M. N. Nadagouda, T. F. Speth and R. S. Varma, *Acc. Chem. Res.*, 2011, **44**, 469–478.

(301) C. O. Kappe, D. Dallinger and S. S. Murphree, *Practical Microwave Synthesis for Organic Chemists*, Wiley-VCH Verlag GmbH & Co. KGaA, Weinheim, Germany, 2008.

(302) W. W. Wang and Y. J. Zhu, *Inorg. Chem. Commun.*, 2004, **7**, 1003–1005.

(303) J. Huang, C. Xia, L. Cao and X. Zeng, *Mater. Sci. Eng. B Solid-State Mater. Adv. Technol.*, 2008, **150**, 187–193.

(304) M. G. Ma, Y. J. Zhu, G. F. Cheng and Y. H. Huang, *Mater. Lett.*, 2008, **62**, 507–510.

(305) N. Uma Sangari and S. Chitra Devi, *J. Solid State Chem.*, 2013, **197**, 483–488.

(306) K. Ocakoglu, S. Mansour, S. Yildirimcan, A. A. Al-Ghamdi, F. El-Tantawy and F. Yakuphanoglu, *Spectrochim. Acta Part A Mol. Biomol. Spectrosc.*, 2015, **148**, 362–368.

(307) T. Sin Tee, T. Chun Hui, C. Wu Yi, Y. Chi Chin, A. A. Umar, G. Riski Titian, L. Hock Beng, L. Kok Sing, M. Yahaya and M. M. Salleh, *Sensors Actuators B Chem.*, 2016, **227**, 304–312.

(308) S. E. Harrison, *Phys. Rev.*, 1954, **93**, 52–62.

(309) A. F. Kohan, G. Ceder, D. Morgan and C. G. Van de Walle, *Phys. Rev. B*, 2000, **61**, 15019–15027.

(310) D. Reynolds, D. Look, B. Jogai, J. Van Nostrand, R. Jones and J. Jenny, *Solid State Commun.*, 1998, **106**, 701–704.

(311) M. J. Alam and D. C. Cameron, *J. Vac. Sci. Technol. A Vacuum, Surfaces, Film.*, 2001, **19**, 1642–1646.

(312) I. Kara, A. Yildiz, G. Yildiz, B. Dogan, N. Serin and T. Serin, *J. Mater. Sci. Mater. Electron.*, 2016, **27**, 6179–6182.

(313) K. J. Kim and Y. R. Park, *Appl. Phys. Lett.*, 2002, **81**, 1420–1422.

(314) J. M. Li, H. Y. Cheng, Y. H. Chiu and Y. J. Hsu, *Nanoscale*, 2016, **8**, 15720–15729.

(315) Q. Yu, W. Fu, C. Yu, H. Yang, R. Wei, Y. Sui, S. Liu, Z. Liu, M. Li, G. Wang, C. Shao, Y. Liu and G. Zou, *J. Phys. D. Appl. Phys.*, 2007, **40**, 5592–5597.

(316) B. Lin, Z. Fu and Y. Jia, *Appl. Phys. Lett.*, 2001, **79**, 943.

(317) C. Chen, Q. H. Yang, Y. Yang, W. Lv, Y. Wen, P. X. Hou, M. Wang and H. M. Cheng, *Adv. Mater.*, 2009, **21**, 3007–3011.

(318) P. Cheng, S. Li, L. Zhang and J. Li, *Appl. Phys. Lett.*, 2008, **93**, 111–114.

(319) A. Janotti and C. G. Van De Walle, *Phys. Rev. B - Condens. Matter Mater. Phys.*, 2007, **76**, 1–22.

(320) T. Sekiguchi, N. Ohashi and Y. Terada, *Jpn. J. Appl. Phys.*, 1997, **36**, L289–L291.

(321) J. Cui, *J. Phys. Chem. C*, 2008, **112**, 10385–10388.

(322) H. Zeng, G. Duan, Y. Li, S. Yang, X. Xu and W. Cai, *Adv. Funct. Mater.*, 2010, **20**, 561–572.

(323) A. Allagui, H. Alawadhi, M. Alkaaby, M. Gaidi, K. Mostafa and Y. Abdulaziz, *Phys. Status Solidi Appl. Mater. Sci.*, 2016, **213**, 139–145.

(324) J. E. A. M. Van Den Meerakker, E. A. Meulenkamp and M. Scholten, *J. Appl. Phys.*, 1993, **74**, 3282–3288.

(325) B. Choi, H. Im, J. Song and K. Yoon, *Thin Solid Films*, 1990, **193-194**, 712–720.

(326) Y. Liu, X. Yan, Z. Kang, Y. Li, Y. Shen, Y. Sun, L. Wang and Y. Zhang, *Sci. Rep.*, 2016, **6**, 29907.

(327) F. Meng, J. Li, S. K. Cushing, J. Bright, M. Zhi, J. D. Rowley, Z. Hong, A. Manivannan, A. D. Bristow and N. Wu, *ACS Catal.*, 2013, **3**, 746–751.

(328) K.-S. Ahn, S. Shet, T. Deutsch, C.-S. Jiang, Y. Yan, M. Al-Jassim and J. Turner, *J. Power Sources*, 2008, **176**, 387–392.

(329) B. S. Wang, R. Y. Li, Z. Y. Zhang, W. Xing, X. L. Wu, G. A. Cheng and R. T. Zheng, *Catal. Today*, 2019, **321-322**, 100–106.

(330) B. Jin, Z. Jiao and Y. Bi, *J. Mater. Chem. A*, 2015, **3**, 19702–19705.

(331) S. Shen, C. X. Kronawitter, J. Jiang, P. Guo, L. Guo and S. S. Mao, *Nano Energy*, 2013, **2**, 958–965.

(332) S. Xie, X. Lu, T. Zhai, W. Li, M. Yu, C. Liang and Y. Tong, *J. Mater. Chem.*, 2012, **22**, 14272.

(333) T. Majumder, J. Hmar, S. Dhar and S. Mondal, *Chem. Phys.*, 2017, **490**, 1–6.

(334) M. Wang, F. Ren, J. Zhou, G. Cai, L. Cai, Y. Hu, D. Wang, Y. Liu, L. Guo and S. Shen, *Sci. Rep.*, 2015, **5**, 12925.

(335) Y. Qiu, K. Yan, H. Deng and S. Yang, *Nano Lett.*, 2012, **12**, 407–413.

(336) A. Ballestas-Barrientos, X. Li, S. Yick, A. F. Masters and T. Maschmeyer, *Sustain. Energy Fuels*, 2018, **2**, 1463–1473.

(337) Y. Fang, X. Li and X. Wang, *ACS Catal.*, 2018, **8**, 8774–8780.

(338) Q. Yu and C. B. Cao, *J. Nanosci. Nanotechnol.*, 2012, **12**, 3984–3989.

(339) J. B. Baxter and C. A. Schmuttenmaer, *J. Phys. Chem. B*, 2006, **110**, 25229–25239.

(340) S. Y. Choi, C. D. Kim, D. S. Han and H. Park, *J. Mater. Chem. A*, 2017, **5**, 10165–10172.

(341) A. B. Martinson, M. S. Goes, F. Fabregat-Santiago, J. Bisquert, M. J. Pellin and J. T. Hupp, *J. Phys. Chem. A*, 2009, **113**, 4015–4021.

(342) Y. F. Xu, H. S. Rao, X. D. Wang, H. Y. Chen, D. B. Kuang and C. Su, *J. Mater. Chem. A*, 2016, **4**, 5124–5129.

(343) R. Kaur, a. V. Singh and R. M. Mehra, *Phys. status solidi*, 2005, **202**, 1053–1059.

(344) L.-N. Bai, H.-M. Sun, J.-S. Lian and Q. Jiang, *Chinese Phys. Lett.*, 2012, **29**, 117101.

(345) J. Q. Wen, J. M. Zhang and Z. Q. Li, *Opt. - Int. J. Light Electron Opt.*, 2018, **156**, 297–302.

(346) S. Heo, S. K. Sharma, S. Lee, Y. Lee, C. Kim, B. Lee, H. Lee and D. Y. Kim, *Thin Solid Films*, 2014, **558**, 27–30.

(347) Y. Z. Tsai, N. F. Wang, M. R. Tseng and F. H. Hsu, *Mater. Chem. Phys.*, 2010, **123**, 300–303.

(348) N. Üzar, G. Algün, N. Akçay, D. Akcan and L. Arda, *J. Mater. Sci. Mater. Electron.*, 2017, **28**, 11861–11870.

(349) N. F. Wang, Y. Z. Tsai, M. R. Tseng and F. H. Hsu, *Integr. Ferroelectr.*, 2013, **143**, 17–23.

(350) J. Zheng, J. Song, Q. Jiang and J. Lian, *Appl. Surf. Sci.*, 2012, **258**, 6735–6738.

(351) J. H. Zheng, S. F. Niu, R. Y. Zheng, W. X. Zhang and P. F. Yu, *Optoelectron. Adv. Mater. Rapid Commun.*, 2016, **10**, 222–227.

(352) J. Huo, L. Fang, Y. Lei, G. Zeng and H. Zeng, *J. Mater. Chem. A*, 2014, **2**, 11040–11044.

(353) C. Y. Cummings, F. Marken, L. M. Peter, K. G. Upul Wijayantha and A. A. Tahir, *J. Am. Chem. Soc.*, 2012, **134**, 1228–1234.

(354) G. Garcia-Belmonte, A. Munar, E. M. Barea, J. Bisquert, I. Ugarte and R. Pacios, *Org. Electron. physics, Mater. Appl.*, 2008, **9**, 847–851.

(355) Q. Wang, S. Ito, M. Grätzel, F. Fabregat-Santiago, I. Mora-Seró, J. Bisquert, T. Bessho and H. Imai, *J. Phys. Chem. B*, 2006, **110**, 25210–25221.

(356) A. Sacco, *Renew. Sustain. Energy Rev.*, 2017, **79**, 814–829.

(357) F. Fabregat-Santiago, J. Bisquert, G. Garcia-Belmonte, G. Boschloo and A. Hagfeldt, *Sol. Energy Mater. Sol. Cells*, 2005, **87**, 117–131.

(358) A. Dualeh, T. Moehl, N. Tétreault, J. Teuscher, P. Gao, M. K. Nazeeruddin and M. Grätzel, *ACS Nano*, 2014, **8**, 362–373.

(359) T. Nakajima, A. Hagino, T. Nakamura, T. Tsuchiya and K. Sayama, *J. Mater. Chem. A*, 2016, **4**, 17809–17818.

(360) M. A. Modestino, S. M. H. Hashemi and S. Haussener, *Energy Environ. Sci.*, 2016, **9**, 1533–1551.

(361) P. Kumar, V. Singh, V. Sharma, G. Rana, H. K. Malik and K. Asokan, *Ceram. Int.*, 2015, **41**, 6734–6739.

(362) R. D. Shannon, *Acta Crystallogr. Sect. A*, 1976, **32**, 751–767.

(363) I. Mora-Seró, F. Fabregat-Santiago, B. Denier, J. Bisquert, R. Tena-Zaera, J. Elias and C. Lévy-Clément, *Appl. Phys. Lett.*, 2006, **89**, 203117.

(364) Y. Zhao, Z. Liu, H. Yang, T. Li and P. Yang, *RSC Adv.*, 2016, **6**, 110943–110950.

(365) E. Sachet, C. T. Shelton, J. S. Harris, B. E. Gaddy, D. L. Irving, S. Curtarolo, B. F. Donovan, P. E. Hopkins, P. A. Sharma, A. L. Sharma, J. Ihlefeld, S. Franzen and J. P. Maria, *Nat. Mater.*, 2015, **14**, 414–420.

(366) K. P. Kelley, E. Sachet, C. T. Shelton and J.-P. Maria, *APL Mater.*, 2017, **5**, 076105.

(367) J. Qiu, X. Li, F. Zhuge, X. Gan, X. Gao, W. He, S. J. Park, H. K. Kim and Y. H. Hwang, *Nanotechnology*, 2010, **21**, 195602.

(368) E. Guillén, E. Azaceta, L. M. Peter, A. Zukal, R. Tena-Zaera and J. A. Anta, *Energy Environ. Sci.*, 2011, **4**, 3400.

(369) K. Wijeratne, V. Seneviratne and J. Bandara, *EPJ Appl. Phys.*, 2015, **69**, 10403.

(370) J. Bisquert and A. Zaban, *Appl. Phys. A Mater. Sci. Process.*, 2003, **77**, 507–514.

(371) J. Bisquert, I. Mora-Sero and F. Fabregat-Santiago, *ChemElectroChem*, 2014, **1**, 289–296.

(372) S. U. Park and J. H. Koh, *Electron. Mater. Lett.*, 2013, **9**, 493–496.

(373) V. Jabbari, M. Hamadanian, M. Shamshiri and D. Villagrán, *RSC Adv.*, 2016, **6**, 15678–15685.

(374) Y.-H. Chiang, M.-H. Li, H.-M. Cheng, P.-S. Shen and P. Chen, *ACS Appl. Mater. Interfaces*, 2017, **9**, 2403–2409.

(375) Y. Fang, Y. Xu, X. Li, Y. Ma and X. Wang, *Angew. Chemie Int. Ed.*, 2018, **57**, 9749–9753.

(376) Z. Li, C. Yao, Y. Yu, Z. Cai and X. Wang, *Adv. Mater.*, 2014, **26**, 2262–2267.

(377) G. P. Sharma and S. Prasad, *Energy*, 2006, **31**, 1921–1926.

(378) H. Zhou, Y. Qu, T. Zeid and X. Duan, *Energy Environ. Sci.*, 2012, **5**, 6732.

(379) M. Grätzel, *Nature*, 2001, **414**, 338–344.

(380) F. Creutzig, B. Fernandez, H. Haberl, R. Khosla, Y. Mulugetta and K. C. Seto, *Annu. Rev. Environ. Resour.*, 2016, **41**, 173–198.

(381) L. Kavan and M. Grätzel, *Electrochim. Acta*, 1995, **40**, 643–652.

(382) W. Zhen, X. Ning, B. Yang, Y. Wu, Z. Li and G. Lu, *Appl. Catal. B Environ.*, 2018, **221**, 243–257.

(383) U. Gupta and C. Rao, *Nano Energy*, 2017, **41**, 49–65.

(384) Y. Fang, W. C. Lee, G. E. Canciani, T. C. Draper, Z. F. Al-Bawi, J. S. Bedi, C. C. Perry and Q. Chen, *Mater. Sci. Eng. B*, 2015, **202**, 39–45.

(385) K. Maeda and K. Domen, *J. Phys. Chem. C*, 2007, **111**, 7851–7861.

(386) H. S. Han, S. Shin, D. H. Kim, I. J. Park, J. S. Kim, P. S. Huang, J. K. Lee, I. S. Cho and X. Zheng, *Energy Environ. Sci.*, 2018, **11**, 1299–1306.

(387) R. F. G. Gardner, R. L. Moss and D. W. Tanner, *Br. J. Appl. Phys.*, 1966, **17**, 55–61.

(388) B. Warnes, F. Aplan and G. Simkovich, *Solid State Ionics*, 1984, **12**, 271–276.

(389) N. A. Jayah, H. Yahaya, M. R. Mahmood, T. Terasako, K. Yasui and A. M. Hashim, *Nanoscale Res. Lett.*, 2015, **10**, 1–10.

(390) K. Sivula, F. Le Formal and M. Grätzel, *ChemSusChem*, 2011, **4**, 432–49.

(391) A. G. Joly, J. R. Williams, S. A. Chambers, G. Xiong, W. P. Hess and D. M. Laman, *J. Appl. Phys.*, 2006, **99**, 053521.

(392) Y. Lin, G. Yuan, S. Sheehan, S. Zhou and D. Wang, *Energy Environ. Sci.*, 2011, **4**, 4862.

(393) A. Subramanian, A. Annamalai, H. H. Lee, S. H. Choi, J. Ryu, J. H. Park and J. S. Jang, *ACS Appl. Mater. Interfaces*, 2016, **8**, 19428–19437.

(394) H. Gao, C. Liu, H. E. Jeong and P. Yang, *ACS Nano*, 2012, **6**, 234–240.

(395) Y. Hou, C. Zheng, Z. Zhu and X. Wang, *Chem. Commun.*, 2016, **52**, 1–4.

(396) D. Commandeur, G. Brown, P. McNulty, C. Dadswell, J. Spencer and Q. Chen, *J. Phys. Chem. C*, 2019, **123**, 18187–18197.

(397) S. Peulon, H. Antony, L. Legrand and A. Chausse, *Electrochim. Acta*, 2004, **49**, 2891–2899.

(398) M. Lorenz, M. Brandt, K. Mexner, K. Brachwitz, M. Ziese, P. Esquinazi, H. Hochmuth and M. Grundmann, *Phys. status solidi - Rapid Res. Lett.*, 2011, **5**, 438–440.

(399) T. Srinivasulu, K. Saritha and K. R. Reddy, *Mod. Electron. Mater.*, 2017, **3**, 76–85.

(400) C. Zhang, W. Fan, H. Bai, X. Yu, C. Chen, R. Zhang and W. Shi, *ChemElectroChem*, 2014, **1**, 2089–2097.

(401) L. Zhang, L. Sun, Z. Guan, S. Lee, Y. Li, H. D. Deng, Y. Li, N. L. Ahlborg, M. Boloor, N. A. Melosh and W. C. Chueh, *Nano Lett.*, 2017, **17**, 5264–5272.

(402) S. Kumar, P. Sahare and S. Kumar, *Mater. Res. Bull.*, 2018, **105**, 237–245.

(403) H. Chen, Z. Wei, X. Zheng and S. Yang, *Nano Energy*, 2015, **15**, 216–226.

(404) Y. C. Chen, C. L. Kuo and Y. K. Hsu, *J. Alloys Compd.*, 2018, **768**, 810–816.

(405) X. L. Zheng, C. T. Dinh, F. P. G. de Arquer, B. Zhang, M. Liu, O. Voznyy, Y. Y. Li, G. Knight, S. Hoogland, Z. H. Lu, X.-W. Du and E. H. Sargent, *Small*, 2016, **12**, 3181–3188.

(406) N. Helaili, G. Mitran, I. Popescu, K. Bachari, I. C. Marcu and A. Boudjemaa, *J. Electroanal. Chem.*, 2015, **742**, 47–53.

(407) S. S. Kalanur, I. H. Yoo, J. Park and H. Seo, *J. Mater. Chem. A*, 2016, **5**, 1455–1461.

(408) J. Li, F. Meng, S. Suri, W. Ding, F. Huang and N. Wu, *Chem. Commun.*, 2012, **48**, 8213–8215.

(409) I. Doron-Mor, A. Hatzor, A. Vaskevich, T. Van Der Boom-Moav, A. Shanzer, I. Rubinstein and H. Cohen, *Nature*, 2000, **406**, 382–385.

(410) Z. Zhang, J. Li, X. Wang, J. Qin, W. Shi, Y. Liu, H. Gao, Y. Mao, P. Sun, T. B. Song, H. Chen, Y. Yang, M. A. Alam, G. V. Gupta, J. Lou, P. M. Ajayan, M. J. Bedzyk, M. G. Kanatzidis and A. D. Mohite, *RSC Adv.*, 2017, **7**, 13325–13330.

(411) A. Ikram, S. Sahai, S. Rai, S. Dass, R. Shrivastav and V. R. Satsangi, *Int. J. Hydrogen Energy*, 2015, **40**, 5583–5592.

(412) M. Chakraborty, D. Roy, A. Biswas, R. Thangavel and G. Udayabhanu, *RSC Adv.*, 2016, **6**, 75063–75072.

(413) D. D. Qin and C. L. Tao, *RSC Adv.*, 2014, **4**, 16968.

(414) A. Sheikh, A. Yengantiwar, M. Deo, S. Kelkar and S. Ogale, *Small*, 2013, **9**, 2091–2096.

(415) Ü. Özgür, Y. I. Alivov, C. Liu, A. Teke, M. A. Reshchikov, S. Doğan, V. Avrutin, S. J. Cho and H. Morko, *J. Appl. Phys.*, 2005, **98**, 1–103.

(416) I. N. Sokolik and O. B. Toon, *J. Geophys. Res. Atmos.*, 1999, **104**, 9423–9444.

(417) K. F. Palmer and D. Williams, *J. Opt. Soc. Am.*, 1974, **64**, 1107.

(418) J. Skaar, *Phys. Rev. E*, 2006, **73**, 026605.

(419) R. Misho and W. Murad, *Sol. Energy Mater. Sol. Cells*, 1992, **27**, 335–345.

(420) Y. W. Phuan, W. J. Ong, M. N. Chong and J. D. Ocon, *J. Photochem. Photobiol. C Photochem. Rev.*, 2017, **33**, 54–82.

(421) Q. Yu, X. Meng, L. Shi, G. Liu, P. Li and J. Ye, *RSC Adv.*, 2016, **6**, 62263–62269.

(422) R. R. Rangaraju, A. Panday, K. S. Raja and M. Misra, *J. Phys. D. Appl. Phys.*, 2009, **42**, 135303.

(423) M. Al-Kuhaili, M. Saleem and S. Durrani, *J. Alloys Compd.*, 2012, **521**, 178–182.

(424) T. S. Atabaev, H. H. T. Vu, M. Ajmal, H.-K. Kim and Y.-H. Hwang, *Appl. Phys. A*, 2015, **119**, 1373–1377.

(425) S. Shen, C. X. Kronawitter, J. Jiang, S. S. Mao and L. Guo, *Nano Res.*, 2012, **5**, 327–336.

(426) S. H. Tamboli, G. Rahman and O. S. Joo, *J. Alloys Compd.*, 2012, **520**, 232–237.

(427) R. L. Spray and K. S. Choi, *Chem. Mater.*, 2009, **21**, 3701–3709.

(428) C. Yilmaz and U. Unal, *RSC Adv.*, 2015, **5**, 16082–16088.

(429) L. Y. Zhang, D. S. Xue, X. F. Xu, A. B. Gui and C. X. Gao, *J. Phys. Condens. Matter*, 2004, **16**, 4541–4548.

(430) L. Fu, H. Yu, Y. Li, C. Zhang, X. Wang, Z. Shao and B. Yi, *Phys. Chem. Chem. Phys.*, 2014, **16**, 4284.

(431) T. J. LaTempa, X. Feng, M. Paulose and C. A. Grimes, *J. Phys. Chem. C*, 2009, **113**, 16293–16298.

(432) Z. Zhang, M. F. Hossain and T. Takahashi, *Appl. Catal. B Environ.*, 2010, **95**, 423–429.

(433) R. R. Rangaraju, K. S. Raja, A. Panday and M. Misra, *J. Phys. D. Appl. Phys.*, 2010, **43**, 445301.

(434) H. E. Prakasam, O. K. Varghese, M. Paulose, G. K. Mor and C. A. Grimes, *Nanotechnology*, 2006, **17**, 4285–4291.

(435) Z. Fan, Z. Xu, S. Yan and Z. Zou, *J. Mater. Chem. A*, 2017, **5**, 8402–8407.

(436) D. D. Qin, D. L. Shan, C. L. Tao, Y. Yan, C. H. He, Q. H. Wang, J. J. Quan, J. Gu, J. Chen, X. Q. Lu, Y. Li and A. C. Trammel, *ChemSusChem*, 2017, **10**, 2796–2804.

(437) L. Martinez, D. Leinen, F. Martín, M. Gabas, J. R. Ramos-Barrado, E. Quagliata and E. a. Dalchiele, *J. Electrochem. Soc.*, 2007, **154**, D126.

(438) W. Luo, C. Jiang, Y. Li, S. A. Shevlin, X. Han, K. Qiu, Y. Cheng, Z. Guo, W. Huang and J. Tang, *J. Mater. Chem. A*, 2017, **5**, 2021–2028.

(439) L. Bertoluzzi, P. Lopez-Varo, J. A. Jiménez Tejada and J. Bisquert, *J. Mater. Chem. A*, 2016, 1–9.

(440) C. Li, S. Tscheuschner, F. Paulus, P. E. Hopkinson, J. Kießling, A. Köhler, Y. Vaynzof and S. Huettner, *Adv. Mater.*, 2016, **28**, 2446–2454.

(441) M. Kulbak, S. Gupta, N. Kedem, I. Levine, T. Bendikov, G. Hodes and D. Cahen, *J. Phys. Chem. Lett.*, 2016, **7**, 167–172.

(442) J. Duan, Y. Zhao, B. He and Q. Tang, *Small*, 2018, **14**, 1704443.

(443) H. Yuan, Y. Zhao, J. Duan, B. He, Z. Jiao and Q. Tang, *Electrochim. Acta*, 2018, **279**, 84–90.

(444) Y. Xu, Y. Wang, J. Yu, B. Feng, H. Zhou, J. Zhang, J. Duan, X. Fan, P. A. van Aken, P. D. Lund and H. Wang, *IEEE J. Photovoltaics*, 2016, **6**, 1530–1536.

(445) R. Zhang, C. Fei, B. Li, H. Fu, J. Tian and G. Cao, *ACS Appl. Mater. Interfaces*, 2017, **9**, 9785–9794.

(446) J. Song, L. Liu, X. F. Wang, G. Chen, W. Tian and T. Miyasaka, *J. Mater. Chem. A*, 2017, **5**, 13439–13447.

(447) J. Cao, B. Wu, R. Chen, Y. Wu, Y. Hui, B. W. Mao and N. Zheng, *Adv. Mater.*, 2018, **30**, 1–9.

(448) J. Liang, C. Wang, Y. Wang, Z. Xu, Z. Lu, Y. Ma, H. Zhu, Y. Hu, C. Xiao, X. Yi, G. Zhu, H. Lv, L. Ma, T. Chen, Z. Tie, Z. Jin and J. Liu, *J. Am. Chem. Soc.*, 2016, **138**, 15829–15832.

(449) J. Liu, Y. Wu, C. Qin, X. Yang, T. Yasuda, A. Islam, K. Zhang, W. Peng, W. Chen and L. Han, *Energy Environ. Sci.*, 2014, **7**, 2963–2967.

(450) X. Chang, W. Li, L. Zhu, H. Liu, H. Geng, S. Xiang, J. Liu and H. Chen, *ACS Appl. Mater. Interfaces*, 2016, **8**, 33649–33655.

(451) J. Duan, T. Hu, Y. Zhao, B. He and Q. Tang, *Angew. Chemie Int. Ed.*, 2018, **57**, 5746–5749.

(452) D. Commandeur, J. McGuckin and Q. Chen, *Nanotechnol.*, 2019.

(453) A. Manekkathodi, Y. J. Wu, L. W. Chu, S. Gwo, L. J. Chou and L. J. Chen, *Nanoscale*, 2013, **5**, 12185.

(454) H. Xu, J. Duan, Y. Zhao, Z. Jiao, B. He and Q. Tang, *J. Power Sources*, 2018, **399**, 76–82.

(455) J. Duan, D. Dou, Y. Zhao, Y. Wang, X. Yang, H. Yuan, B. He and Q. Tang, *Mater. Today Energy*, 2018, **10**, 146–152.

(456) G. Liao, J. Duan, Y. Zhao and Q. Tang, *Sol. Energy*, 2018, **171**, 279–285.

(457) P. Teng, X. Han, J. Li, Y. Xu, L. Kang, Y. Wang, Y. Yang and T. Yu, *ACS Appl. Mater. Interfaces*, 2018, **10**, 9541–9546.

(458) Z. Liu, B. Sun, X. Liu, J. Han, H. Ye, T. Shi, Z. Tang and G. Liao, *Nano-Micro Lett.*, 2018, **10**, 34.

(459) X. Zhang, Z. Jin, J. Zhang, D. Bai, H. Bian, K. Wang, J. Sun, Q. Wang and S. F. Liu, *ACS Appl. Mater. Interfaces*, 2018, **10**, 7145–7154.

(460) A. Nikolakopoulou, D. Tasis, L. Sygellou and P. Lianos, *Electrochim. Acta*, 2014, **139**, 54–60.

(461) C. M. Hansen and A. L. Smith, *Carbon N. Y.*, 2004, **42**, 1591–1597.

(462) Z. Liu, C. Fan, L. Chen and A. Cao, *J. Nanosci. Nanotechnol.*, 2010, **10**, 7382–7385.

(463) Y. Hernandez, M. Lotya, D. Rickard, S. D. Bergin and J. N. Coleman, *Langmuir*, 2010, **26**, 3208–3213.

(464) A. Ciesielski and P. Samorì, *Chem. Soc. Rev.*, 2014, **43**, 381–398.

(465) Y. Arao and M. Kubouchi, *Carbon N. Y.*, 2015, **95**, 802–808.

(466) S. Nemala, S. Prathapani, P. Kartikay, P. Bhargava, S. Mallick and S. Bohm, *IEEE J. Photovoltaics*, 2018, **8**, 1252–1258.

(467) J. Holovský, S. De Wolf, J. Werner, Z. Remeš, M. Müller, N. Neykova, M. Ledinský, L. Černá, P. Hrzina, P. Löper, B. Niesen and C. Ballif, *J. Phys. Chem. Lett.*, 2017, **8**, 838–843.

(468) C. M. Long, M. A. Nascarella and P. A. Valberg, *Environ. Pollut.*, 2013, **181**, 271–286.

(469) C. Petridis, G. Kakavelakis and E. Kymakis, *Energy Environ. Sci.*, 2018, **11**, 1030–1061.

(470) T. Mahmoudi, Y. Wang and Y. B. Hahn, *Nano Energy*, 2018, **47**, 51–65.

(471) U. Khan, A. O'Neill, M. Lotya, S. De and J. N. Coleman, *Small*, 2010, **6**, 864–871.

(472) J. T.-W. Wang, J. M. Ball, E. M. Barea, A. Abate, J. A. Alexander-Webber, J. Huang, M. Saliba, I. Mora-Sero, J. Bisquert, H. J. Snaith and R. J. Nicholas, *Nano Lett.*, 2014, **14**, 724–730.

(473) A. Agresti, S. Pescetelli, B. Taheri, A. E. Del Rio Castillo, L. Cinà, F. Bonaccorso and A. Di Carlo, *ChemSusChem*, 2016, **9**, 2609–2619.

(474) C. H. Ng, T. S. Ripolles, K. Hamada, S. H. Teo, H. N. Lim, J. Bisquert and S. Hayase, *Sci. Rep.*, 2018, **8**, 2482.

(475) Q. A. Akkerman, M. Gandini, F. Di Stasio, P. Rastogi, F. Palazon, G. Bertoni, J. M. Ball, M. Prato, A. Petrozza and L. Manna, *Nat. Energy*, 2017, **2**, 16194.

(476) Z. Serbetçi, H. El-Nasser and F. Yakuphanoglu, *Spectrochim. Acta Part A Mol. Biomol. Spectrosc.*, 2012, **86**, 405–409.

(477) W. L. Lu, P. K. Hung, C. I. Hung, C. H. Yeh and M. P. Houng, *Mater. Chem. Phys.*, 2011, **130**, 619–623.

(478) J. C. Johnson, H. Yan, P. Yang and R. J. Saykally, *J. Phys. Chem. B*, 2003, **107**, 8816–8828.

(479) N. Islavath and G. Lingamallu, *Sol. Energy*, 2018, **170**, 158–163.

(480) S. R. Raga and Y. Qi, *J. Phys. Chem. C*, 2016, **120**, 28519–28526.

(481) K. M. Boopathi, R. Mohan, T. Y. Huang, W. Budiawan, M. Y. Lin, C. H. Lee, K. C. Ho and C. W. Chu, *J. Mater. Chem. A*, 2016, **4**, 1591–1597.

(482) Y. C. Shih, L. Y. Wang, H. C. Hsieh and K. F. Lin, *J. Mater. Chem. A*, 2015, **3**, 9133–9136.

(483) S. Hernández, V. Cauda, A. Chiodoni, S. Dallorto, A. Sacco, D. Hidalgo, E. Celasco and C. F. Pirri, *ACS Appl. Mater. Interfaces*, 2014, **6**, 12153–12167.

(484) S. Y. Luchkin, A. F. Akbulatov, L. A. Frolova, S. A. Tsarev, P. A. Troshin and K. J. Stevenson, *Sol. Energy Mater. Sol. Cells*, 2017, **171**, 205–212.

(485) Y. Jiang, J. Yuan, Y. Ni, J. Yang, Y. Wang, T. Jiu, M. Yuan and J. Chen, *Joule*, 2018, **2**, 1356–1368.

(486) J. Liang, P. Zhao, C. Wang, Y. Wang, Y. Hu, G. Zhu, L. Ma, J. Liu and Z. Jin, *J. Am. Chem. Soc.*, 2017, **139**, 14009–14012.

(487) B. Li, Y. Zhang, L. Zhang and L. Yin, *J. Power Sources*, 2017, **360**, 11–20.

(488) M. M. Rahman, N. Uekawa, F. Shiba, Y. Okawa, M. Sakai, K. Yamamoto, K. Kudo and T. Konishi, *Jpn. J. Appl. Phys.*, 2016, **55**, 01AE09.

(489) C. M. Pelicano and H. Yanagi, *J. Energy Chem.*, 2018, **27**, 455–462.

(490) D. A. Afanasyev, K. Y. Mirzoev and N. K. Ibrayev, *IOP Conf. Ser. Mater. Sci. Eng.*, 2018, **289**, 012001.

(491) H. Wang, L. Yan, J. Liu, J. Li and H. Wang, *J. Mater. Sci. Mater. Electron.*, 2016, **27**, 6872–6880.

(492) P. Ruankham, D. Wongratanaphisan, A. Gardchareon, S. Phadungdhitidhada, S. Choopun and T. Sagawa, *Appl. Surf. Sci.*, 2017, **410**, 393–400.

(493) F. A. Cataño, L. Allende and H. Gómez, *J. Chil. Chem. Soc.*, 2015, **60**, 2940–2943.

(494) Q. Yang, J. Li, Y. Cheng, H. W. Li, Z. Guan, B. Yu and S. W. Tsang, *J. Mater. Chem. A*, 2017, **5**, 9852–9858.

(495) Q. Luo, H. Ma, Y. Zhang, X. Yin, Z. Yao, N. Wang, J. Li, S. Fan, K. Jiang and H. Lin, *J. Mater. Chem. A*, 2016, **4**, 5569–5577.

(496) J. Liu, G. Wang, Z. Song, X. He, K. Luo, Q. Ye, C. Liao and J. Mei, *J. Mater. Chem. A*, 2017, **5**, 9097–9106.

(497) N. Aristidou, C. Eames, M. S. Islam and S. A. Haque, *J. Mater. Chem. A*, 2017, **5**, 25469–25475.

(498) G. Liu, B. Yang, B. Liu, C. Zhang, S. Xiao, Y. Yuan, H. Xie, D. Niu, J. Yang, Y. Gao and C. Zhou, *Appl. Phys. Lett.*, 2017, **111**, 153501.

(499) R. T. Ginting, M. K. Jeon, K. J. Lee, W. Y. Jin, T. W. Kim and J. W. Kang, *J. Mater. Chem. A*, 2017, **5**, 4527–4534.

(500) G. Yang, H. Lei, H. Tao, X. Zheng, J. Ma, Q. Liu, W. Ke, Z. Chen, L. Xiong, P. Qin, Z. Chen, M. Qin, X. Lu, Y. Yan and G. Fang, *Small*, 2017, **13**, 1601769.

(501) Y. Zhang, P. Wang, X. Yu, J. Xie, X. Sun, H. Wang, J. Huang, L. Xu, C. Cui, M. Lei and D. Yang, *J. Mater. Chem. A*, 2016, **4**, 18509–18515.

(502) M. Yang, H. shang Peng, F. long Zeng, F. Teng, Z. Qu, D. Yang, Y. quan Wang, G. xiang Chen and D. wei Wang, *J. Colloid Interface Sci.*, 2018, **509**, 32–38.

(503) W. Shen, L. Ruan, Z. Shen and Z. Deng, *Chem. Commun.*, 2018, **54**, 2804–2807.

(504) G. E. Eperon, G. M. Paternò, R. J. Sutton, A. Zampetti, A. A. Haghighirad, F. Cacialli and H. J. Snaith, *J. Mater. Chem. A*, 2015, **3**, 19688–19695.

(505) C. C. Stoumpos, C. D. Malliakas, J. A. Peters, Z. Liu, M. Sebastian, J. Im, T. C. Chasapis, A. C. Wibowo, D. Y. Chung, A. J. Freeman, B. W. Wessels and M. G. Kanatzidis, *Cryst. Growth Des.*, 2013, **13**, 2722–2727.

(506) Z. Zhang, Y. Zhu, W. Wang, W. Zheng, R. Lin and F. Huang, *J. Mater. Chem. C*, 2018, **6**, 446–451.

(507) D. Pan, Y. Fu, J. Chen, K. J. Czech, J. C. Wright and S. Jin, *Nano Lett.*, 2018, **18**, 1807–1813.

(508) D. W. DeQuilettes, W. Zhang, V. M. Burlakov, D. J. Graham, T. Leijtens, A. Osherov, V. Bulović, H. J. Snaith, D. S. Ginger and S. D. Stranks, *Nat. Commun.*, 2016, **7**, 11683.

(509) S. W. Lee, S. Kim, S. Bae, K. Cho, T. Chung, L. E. Mundt, S. Lee, S. Park, H. Park, M. C. Schubert, S. W. Glunz, Y. Ko, Y. Jun, Y. Kang, H. S. Lee and D. Kim, *Sci. Rep.*, 2016, **6**, 38150.

(510) S. Huang, Z. Li, B. Wang, N. Zhu, C. Zhang, L. Kong, Q. Zhang, A. Shan and L. Li, *ACS Appl. Mater. Interfaces*, 2017, **9**, 7249–7258.

(511) X. Chen, F. Zhang, Y. Ge, L. Shi, S. Huang, J. Tang, Z. Lv, L. Zhang, B. Zou and H. Zhong, *Adv. Funct. Mater.*, 2018, **28**, 1–7.

(512) E. Ghahremanirad, A. Bou, S. Olyaee and J. Bisquert, *J. Phys. Chem. Lett.*, 2017, **8**, 1402–1406.

(513) S. A. L. Weber, I. M. Hermes, S.-H. Turren-Cruz, C. Gort, V. W. Bergmann, L. Gilson, A. Hagfeldt, M. Graetzel, W. Tress and R. Berger, *Energy Environ. Sci.*, 2018, **11**, 2404–2413.

(514) W. Shockley and H. J. Queisser, *J. Appl. Phys.*, 1961, **32**, 510–519.